UNIVERSITAT DE BARCELONA

# Tectonic evolution of the São Vicente area and tsunamigenic potential of the active structures in the SW Iberian margin: Implications for hazard assessment

Cristina Sánchez Serra

# Tectonic evolution of the São Vicente area and tsunamigenic potential of the active structures in the SW Iberian margin: Implications for hazard assessment


Memòria de tesi doctoral presentada per:

**Cristina Sánchez Serra**

Per optar al Grau de Doctora per la Universitat de Barcelona


Aquesta memòria s'ha dut a terme dins el Programa de Doctorat de Ciències de la Terra de la Universitat de Barcelona sota la direcció de:

Dra. Eulàlia Gràcia Mont i Dr. Roger Urgeles Esclasans

I la tutela de:

Dra. Eulàlia Masana Closa

Barcelona, Maig de 2021

*“Educating the mind without educating*

*the heart is no education at all”*

*-Aristotle-*

# Agraïments / Acknowledgements

Sempre he pensat que la millor part d'una Tesi són els agraïments, entre les seves línies es pot apreciar el que ha sigut realment el desenvolupament d'aquesta, en tots els seus nivells, però especialment a nivell humà. Per això vull començar donant les gràcies al valent lector que ha obert aquesta Tesi doctoral i en llegeix les seves línies.

El primer agraïment el vull dedicar als meus directors de la Tesi, la Laia i en Roger. Gràcies per confiar en mi i donar-me l'oportunitat de viure aquesta aventura. Gràcies pel vostre recolzament al llarg de tot aquest temps. Gràcies al Roger per el seu bon rotllo i bromes constants i a la Laia per la seva energia i positivisme infinits.

A la Sara, moltes gràcies per guiar-me, aconsellar-me, i il·luminar-me el camí quan més ho necessitava.

A la meva tutora, l'Eulàlia, per les xerrades i els ànims que sempre m'ha donat quan l'anava a veure a la UB.

A tutti i colleghi italiani dell'INGV, Roberto, Stefano, Francesco, Fabrizio, Manuela, Alessio e Antonio. Grazie per avermi accolta durante il mio soggiorno a Roma, per avermi accompagnata nei miei inizi nel campo della modellazione, ma soprattutto grazie per l'energia positiva. È stato un piacere lavorare con voi.

A Laura, por acompañarme y apoyarme durante mi experiencia italiana. Por nuestros días de turismo, nuestras cenas caseras y los Aperol en las terrazas. ¡¡Gràcias!!

A los chicos del P-91, Slaven y Davide, por ser los mejores compañeros de despacho que hubiera podido tener. Por vuestra fe en mi, por todas las conversaciones, por escucharme y entenderme. Davide, por las campañas que hemos vivido, sin duda mucho más llevaderas en tu compañia.

A les meves *Girlies*, Estela, Clàudia, Marta, Irene, sens dubte una de les millors coses que m'emporto d'aquesta experiència ha sigut conèixer-vos! Gràcies per tots els moments viscuts, *los días de largo*, els sopars, els esmorzars post-ioga, tantes i tantes coses...però sobretot gràcies per estar sempre allà. Irene, vam començar juntes i acabem juntes, gràcies per ser un pilar per a mi, recolzar-me i acompanyar-me en tot aquest camí. Al Sergio, quasi una *grily* més, per totes les converses, les bromes, els ànims...ara et toca a tu anar a per la Tesis!

També vull agrair tots els moments viscuts amb tota la gent que he conegut per l'Institut i que m'han aportat el seu granet de sorra, en Miquel, el Jaume, l'Hector, l'Anaïs, el Jhonny, l'Shray, l'Alci, el Sergi, la Sònia...

A nivell més personal vull agrair el suport constant, les xerrades diàries i els ànims del meu amic i company de fatigues, l'Octavi, sens dubte tot això no hagués sigut el mateix sense tu! Sempre recordaré Malta...i el que ens queda!

A l'Amanda, la Nia, el Kevin, i les nenes de Badalona, gràcies per la confiança, per animar-me, escoltar-me, en resum, per ser-hi sempre.

A la meva família, els meus pares, els meus germans i la meva àvia, no tinc paraules que puguin agrair tot el que m'heu aportat. Gràcies a vosaltres he arribat fins aquí. Heu patit amb mi, heu rigut amb mi, us heu emocionat amb mi...Sempre us he sentit a prop, per molt lluny o ocupada que estigués. El vostre recolzament, ajuda i estima sempre m'han acompanyat en aquesta aventura i m'han donat les forces que necessitava per seguir...Sempre endavant!

I per últim, la persona que més de prop ha viscut tot aquest procés i que més n'ha patit les últimes conseqüències, en Lluís. Gràcies per fer que tot sigui fàcil, per la teva paciència, admiració i suport incondicional. Gràcies per creure en mi i fer-me sentir invencible.

A tots, aquesta Tesi també és vostre.

## Funding:

The author of this PhD thesis has been supported by a four-year Pre-Doc FPI "Formación de Personal Investigador" grant (ref. BES-2016-078877) from "Ministerio de Ciencias e Innovación" between 2017 and 2021. This fellowship was granted and carried out within the framework of the INSIGHT (CTM2015-70155-R) project.

This work was carried out within the "Laboratori de Processos Geològics del Sòl i Subsòl Oceànics" research group in the "Institut de Ciències del Mar – CSIC (Consell Superior d'Investigacions Científiques)".

# Contents

# SUMMARY

The southwestern margin of the Iberian Peninsula, which includes the Gulf of Cadiz, is characterized by a present-day active deformation mainly driven by the NW-SE trending convergence between the African and Eurasia plates. In addition, this area hosts some of the largest earthquakes occurred in Western Europe. The issue in the SW Iberian margin, which this thesis aims to solve, is that there is not an overall understanding of the active tectonics and contemporary sedimentary processes that occur in some areas of the study region. In addition, there is a lack of detailed fault-models of the main active faults, high-quality earthquake ruptures and tsunami propagation models.

For this reason, in this PhD Thesis, the following points are studied: **1)** Analysis of the Cape São Vicente area to identify the sedimentary and the tectonic processes developed in the study region and the interaction between both. **2)** High-resolution data analysis of two of the most important faults of the SW Iberian margin, the Marquês de Pombal fault and the Lineament South fault to infer their current activity. **3)** Carry Out 3D fault-plane models of the main active structures in the study area to evaluate the sensitivity of the tsunami impact on the coast of SW Iberia and NW Morocco to the fault geometry and slip distribution for local earthquakes. The main findings of my PhD Thesis related with the previous points are the follow:

**1)** A multi-scale dataset consisting of multi-beam echo-sounder, 2D multi-channel seismic and high-resolution sidescan sonar (TOBI) data allow to identify a large variety of morphologies, as well as sedimentary and tectonic structures along the São Vicente Canyon, the largest submarine canyon developed in the external part of the Gulf of Cadiz. The São Vicente Canyon and their dynamics are highly conditioned by the convergence between the Eurasian and African plates. The origin of the canyon is fully tectonic, as it shows a strong structural control. The São Vicente Canyon is mainly conditioned by three current-active thrust faults: the Marquês de Pombal Fault, the São Vicente Fault and the Horseshoe Fault. No major rivers feed sediment to the canyon head, and therefore, the main sediment source is related to the disintegration of canyon flanks and the Mediterranean Overflow Water sedimentary deposits. Due to the canyon retrogressive erosion, submarine slides and scars are the main seafloor morphologies. The São Vicente Canyon is a clear example of a diachronic and segmented canyon developed since the Late Miocene in an area of active plate tectonics.

**2)** By integrating the most advanced technologies in marine geosciences covering different scales of resolution, such as: multibeam echosounder, sub-bottom profiler, Autonomous Underwater Vehicle (AUV) "Abyss" and, high-resolution 2D multichannel seismic profiles, it has been possible to characterize, in detail, the Lineament South and the Marquês de Pombal faults. The Lineament South strike-slip fault is the longest active structure in the study area that may generate one of the most powerful earthquakes in the SW Iberian margin. Both ends of the Lineament South Fault raise the seafloor and generate positive and negative floor-like structures, demonstrating its current activity. The main motion component of the fault is right-lateral, as the rake and the dislocated structures in both extremes of the fault suggest. The Marquês de Pombal fault is an active left-lateral reverse fault. As isochore maps and the distribution of the vertical slip evidenced, this structure was active from the Middle-Miocene until nowadays where its uplift control the incision and the activity of the São Vicente Canyon.

**3)** To identify the most vulnerable areas to be affected by a tsunami in SW Iberia and NW Morocco, realistic tsunami models have been built modelling in detail the main active faults in the region, including: the Gorringe Bank, Marquês de Pombal, Horseshoe, North Coral Patch and South Coral Patch thrust faults, and the Lineament South strike-slip fault. Based on a large dataset of 2D multi-channel seismic profiles, 3D sub-surface models that involves dimensional complexities of the fault planes have been generated. Additionally, with the aim to know the influence of the slip distribution along the fault plane in tsunami simulations, various heterogeneous slip-distributions have been considered in the Horseshoe fault tsunami scenario. The results show that using more complex fault geometries and slip distributions, the peak wave height (about the mean sea level) at the coastline can double compared to simpler tsunami source scenarios from planar fault geometries. Therefore, complex fault geometries and non-uniform slip distribution should be considered in future tsunami hazard updates. Tsunami simulations also show that the presence of submarine canyons attenuates the wave heights that reach the coastline, while the submarine ridges and the shallow shelf increase it. The tsunami simulations done, reveal that the most dangerous faults for the Moroccan coast are the Horseshoe, Gorringe Bank and South Coral Patch, for the Spanish and the Algarve coasts is the Lineament South fault and for the western coast of Portugal, the Gorringe Bank fault.

# STRUCTURE AND ORGANIZATION OF THIS PhD THESIS

In order to achieve the objectives and to present the results in a clear structure, the dissertation of this PhD Thesis has been organized as a classic volume in four parts. Each of these parts is subdivided into chapters that are focused on different topics. This volume includes the following Parts and Chapters.

| | |
|---|---|
| **Part I: Introduction** | Chapter 1: Objectives and general concepts<br>Chapter 2: Geological setting<br>Chapter 3: Data and methods |
| **Part II: Results** | Chapter 4: Characterization of the Cape São Vicente area<br>Chapter 5: The Lineament South and the Marquês de Pombal faults: high-resolution data<br>Chapter 6: Seismogenic and tsunamigenic potential of the active faults of the SW Iberian margin |
| **Part III: Discussion** | Chapter 7: Discussion |
| **Part IV: Conclusions and Forward look** | Chapter 8: Conclusions<br>Chapter 9: Forward look |
| **Part V: References** | List of acronyms<br>References |
| **Annexes** | Scientific output related to this thesis |

# PART I

# INTRODUCTION

# CHAPTER 1

# Objectives and general concepts

## 1.1. Introduction

Earthquakes, tsunamis and submarine landslides are geo-hazards that can inflict significant damage in the population and coastal areas around the world. Furthermore, they may cause an important impact in societies as well as global economies at distances of thousands of kilometres (Morgan et al., 2009; Satake, 2015). Dramatic examples are the recent 2011 $M_w$ 9.1 Tohoku-Oki and the 2004 $M_w$ 9.3 Sumatra-Andaman earthquakes, which generated a series of massive tsunami-waves. They grew-up to 30-40 m high heading towards land, travelling at 700 km/h for up to 10 km (Mori et al., 2011; Stein & Okal, 2005). These tsunamis killed a total of 220.000 people in 14 countries in Southeast Asia, and a total of 15.000 people in Japan, which demonstrates that these events were some of the deadliest natural disasters in history, although their consequences varied significantly depending on the level of preparedness (Koshimura & Shuto, 2015).

Large earthquakes and tsunamis are infrequent events, however, the high number of missing and injured people and the casualties that they can cause make them one of the most dangerous phenomena in nature (Lay et al., 2005; Stein & Okal, 2005). Despite large earthquakes and tsunamis are recurrent events in active plate boundaries with high-deformation rates (i.e., the Ring of Fire in the Pacific), they can also occur in relatively slow tectonic deformation areas with long-recurrence intervals, such as the SW Iberian margin (Fig. 1.1).

The SW Iberian margin (Fig. 1.2) contains the plate-boundary between Africa and Eurasia, which is characterized by slow NW-SE trending convergence (3.8-5.6 mm/yr). This is one of the most seismogenic areas in Western Europe, where large destructive earthquakes and tsunamis have occurred. Historical chronicles refer to 16 tsunamis that have affected the Iberian and Moroccan Atlantic coasts since 218 B.C. (Campos, 1991). The most destructive historical event in this area was the 1755 Lisbon Earthquake ($M_w$ > 8.5) and Tsunami (Fig. 1.1), which hit several coastal cities along southwest Iberia

and North Africa, destroying the city of Lisbon by the combined effect of the earthquake, fires and tsunami waves (Baptista et al., 1998). In 1969, a large earthquake nucleated in the Horseshoe Abyssal Plain with a magnitude $M_w$ 8.0 (Fukao, 1973), one of the largest events in recent times (Fig. 1.2). Therefore, to carry out a detailed hazard assessment in the SW Iberian margin is essential.

***Figure 1.1.*** *Image of the destruction of Lisbon after the 1st of November 1755 earthquake and tsunami (Image from Higgins Art Gallery & Museum, 2020).*

To implement earthquake and tsunami hazard assessment, the following items are essential: a) An accurate knowledge of the geodynamics and stress field of the area; b) A detailed characterization of the main active faults, high-quality earthquake rupture and tsunami propagation models, and a good constraint on the required fault parameters; c) A good knowledge of the interaction between the tectonic structures, together with geomorphological elements of the study area (Geist, 1998; Satake, 2015; Yamashita & Sato, 1974).

Since the mid-90s, several geological and geophysical surveys have been carried out in the region, compiling data of the main geomorphological features, seismo-stratigraphy and active faults of the SW Iberian margin. Regarding the geodynamic evolution of SW Iberia, the most recent and outstanding findings defined the nature of the basement of the Gorringe Bank as a serpentinized exhumed mantle (Sallarès et al., 2013). Moreover, Martínez-Loriente et al., (2014) recognize three different oceanic Basement domains: the Seine Abyssal Plain domain made of oceanic crust generated in the NE Central Atlantic spreading centre; the Gulf of Cadiz domain constituted by oceanic crust from the Alpine-Tethys rifting system; and the Gorringe Bank domain made of exhumed mantle rocks form the first stages of North Atlantic opening. Regarding active tectonics, recent works (e.g., Bartolome et al., 2012; Martínez-Loriente et al., 2014) demonstrate the tectonic activity of the Lineament South strike-

slip fault and Martínez-Loriente et al., (2013, 2018) show the tectonic evolution of the Coral Patch Ridge area, the Seine Abyssal hills and the neighbouring Horseshoe Fault (Fig. 1.2). Previous works (i.e. Gràcia et al., 2003a; Gràcia et al., 2003b; Zitellini et al., 2004) already demonstrated the activity of the northern segment of the Horseshoe Fault that constitutes part of the southern flank of the São Vicente Canyon, one of the largest submarine canyon of the Atlantic continental margin. Silva et al., (2017) demonstrated the occurrence of a seismic cluster parallel to the São Vicente Canyon, which may be related to the seismic structures of the Cape of São Vicente region (Fig. 1. 2). However, there is a - lack of - understanding the geomorphology and tectono-sedimentary evolution of the Cape São Vicente area in the SW Iberian margin and their relationship with the Canyon (Fig. 1.2).

Past tsunami simulations and hazard assessment studies in the SW Iberian margin already demonstrate the seismogenic and tsunamigenic potential of active structures in the SW Iberian and NW Moroccan coasts (Baptista et al., 2011; Lima et al., 2010; Matias et al., 2013; Omira et al., 2013, 2012). Focusing on the tsunami scientific field, Tonini et al., (2020), shows that the imprint of the fault geometry is evident in the waveform and suggested that oversimplified fault models may not represent the real coastal impact of tsunamis.

Unfortunately, there is a lack in the realistic characterization of main fault ruptures. Prior to this Thesis, the worst-case tsunami scenarios that each fault in the study area may generate were considered roughly from rectangular-planar fault surfaces. In addition, these studies did not take into account the geomorphological elements of the seafloor that may have a direct implication in the wave-height and tsunami propagation. In view of current knowledge gaps, the main motivations of this Thesis are to advance in the understanding of the active tectonics and contemporary sedimentary processes that occur in the area of the Cape São Vicente (Fig. 1.2), as well as to establish realistic fault-models of the main active structures in SW Iberia to carry out detailed tsunami simulations allowing to analyse the complexities of tsunami genesis.

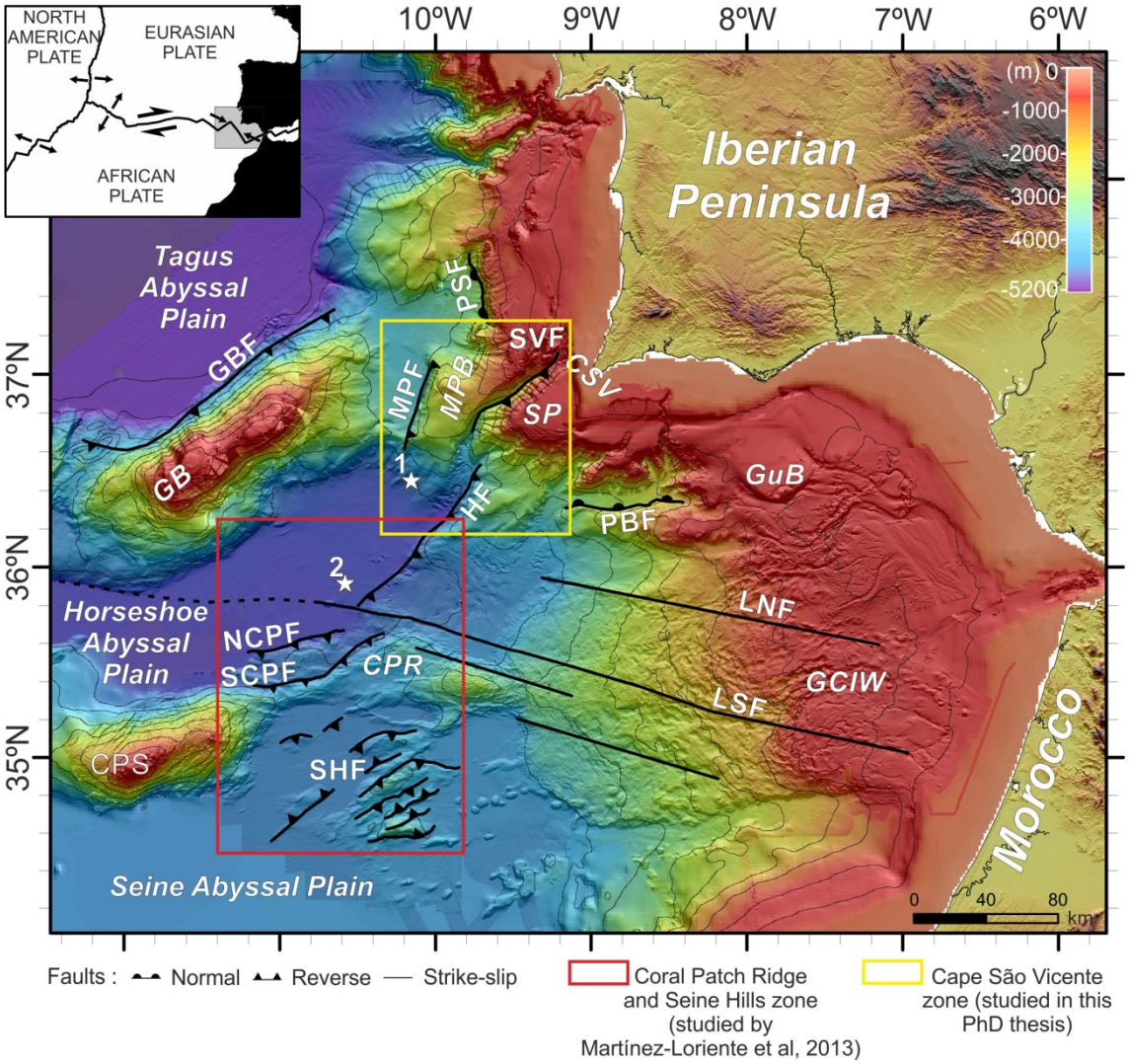


***Figure 1.2.*** *Topographic and bathymetric map of the SW Iberian margin, obtained from the SWIM multibeam compilation (Zitellini et al., 2009). White stars correspond to the epicentres of: 1) 1755 Lisbon earthquake and Tsunami. 2) 1969 Horseshoe earthquake (Buforn et al., 2004). Inset: Plate tectonic setting of the SW Iberian margin. CPR: Coral Patch Ridge; CPS: Coral Patch Seamount; CSV: Cape São Vicente; GB: Gorringe Bank; GBF: Gorringe Bank Fault; GCIW: Gulf of Cadiz Imbricated Wedge; GuB: Guadalquivir Bank; HF: Horseshoe Fault; LNF: Lineament North fault; LSF: Lineament South fault; MPF: Marques de Pombal Fault; MPB: Marques de Pombal Fault Block; NCPF: North Coral Patch Fault; PBF: Portimao Bank Fault; PSF: Pereira de Sousa Fault; SCPF: South Coral Patch Fault; SHF: Seine Hills Faults; SP: Sagres Plateau; SVF: São Vicente Fault.*

## 1.2. Hypotheses

On the basis of the text explained above, the main hypotheses to test in this Doctoral Thesis are the following:

1) The Marquês de Pombal fault plays a key role in the evolution of the Cape São Vicente area. Furthermore, the main active faults in this zone (i.e., Marquês de Pombal Fault, São Vicente Fault and Horseshoe Fault) controlled the development of one of the largest submarine canyon, in the Atlantic continental margins: the São Vicente Canyon.

2) The accuracy of the fault models has a considerable influence on the resulting tsunami propagation pattern and the wave-height and improves significantly the simulation of the worst-case tsunami scenarios. Therefore, accurate parameters, realistic fault-planes and heterogeneous slip-distributions need to be taken into account during the tsunami hazard assessment process.

## 1.3. Objectives

This PhD Thesis has been developed in the framework of the INSIGHT project "ImagiNg large SeismogenIc and tsunamiGenic structures of the Gulf of Cadiz with ultra-High resolution Technologies" granted in year 2016. The INSIGHT project (P.I.: R. Urgeles and E. Gràcia) was a national project belonging to the Spanish National Plan of Research, Development and Innovation (R+D+I), leaded by the Marine Science Institute (ICM-CSIC) in Barcelona. The project mainly focuses on imaging and characterizing the main fault systems with the highest possible resolution, and their relationship with fluid flow systems and large slope failures. The aim is to accurately determine the seismic parameters of these faults and evaluate the seismogenic and tsunamigenic potential of the largest tectonic sources.

In line with the objectives of the project and, based on the sections above (1.1- 1.2), the main goals of this PhD Thesis are:

***1) To characterize the geomorphological and tectonic evolution of the Cape of São Vicente zone and improve the knowledge on the origin and interplay between active tectonics and the dynamics of submarine canyons.***

The geomorphology and seismo-stratigraphy of the São Vicente canyon and the neighbouring areas have been refined and the main tectonic structures that condition it

are identified. Detailed analyses of the area were performed using bathymetric data, TOBI (Towed ocean bottom instrument) sidescan sonar images and TOPAS (TOpographic PArametric Sounder) subbottom data, together with Multi-Channel Seismic (MCS) profiles. Moreover, the tectonic evolution of the main faults in the area and their relationship with the timing of formation of the Canyon has been explained. In addition, the interconnection of the sediment sources of the canyon with the high-seismicity rate of the area is also exposed.

***2) Characterization of active structures using high-resolution technologies: High-resolution Multi-Channel Seismic and Autonomous Underwater Vehicle (AUV) datasets.***

Three AUV images and high-resolution MCS profiles of the Marquês de Pombal fault and the Lineament South fault are analysed in this Thesis to define in detail the morphological expression of the faults on the seafloor and their characteristics. The three AUV images (i.e. one for Marquês de Pombal fault, one for the western side and another for the eastern side, at each end of the Lineament South fault) proved the current tectonic activity of the fault along their entire length.

***3) Tsunami hazard assessment in the SW Iberian margin based on realistic 3D fault plane geometries of the main active structures:***

***a) Seismogenic potential of the main active faults.***

***b) Tsunamigenic potential of the main active faults.***

***c) Evaluation of the bathymetric effects on the wave-height and tsunami propagation.***

In this thesis, complex 3D-fault planes (i.e., based on an extensive dataset of TOPAS and MCS profiles) have been generated following the main active faults of the SW Iberian margin, in order to model the worst-case tsunami scenario that each individual fault may produce. In addition, different heterogeneous slip-distributions are taken into account to verify the relevance of using a realistic slip in the tsunami simulations. Furthermore, the importance of seafloor structures, such as the São Vicente canyon or the Gorringe Bank seamount, in the tsunami wave-height and tsunami propagation has also been studied. Finally, a compilation of all the relevant information (i.e., tsunami

propagation, wave-height and, bathymetry features) is carried out to analyse the most affected cities in each tsunami scenario.

## 1.4. General concepts

Basic and general concepts, essential to understand the geological setting and other fundamental topics, such as plate tectonics, plate boundaries and fault systems, earthquakes, tsunamis, geological hazards and submarine canyons will be presented in the following sections of this PhD Thesis.

### *1.4.1. Fundamentals of plate tectonics*

The Earth is a complex system in continuous evolution constituted by a series of concentric layers with different chemical and mechanical properties (Turcotte & Schubert, 2002). To understand the Earth-dynamics model, the German meteorologist Alfred Wegener proposed the Theory of the Continental Drift in 1912 (Turcotte & Schubert, 2002). He argued that the continents on both sides of the Atlantic Ocean were separating. Many years later, in the 1960s Mary Tharp and Bruce Heezen discovered that the ocean floor was not flat but covered with various kinds of geological features, such as canyons, ridges and mountains, just like on the Earth's above-ground continents. These oceanic geological features were much large and deeper than anything seen on the planet surface. Mary Tharp and Bruce Heezen demonstrated that the ocean floor was a vast world more complex that anyone had dared to imagine up until then (Kenyon, 1982; Le Pichon, 1968; Wilson, 1963).

In the plate tectonics framework, the lithosphere (i.e., external part of the Earth), is composed by the crust and the upper mantle (Cox & Hart, 1986; Hamblin & Christiansen, 2003) (Fig 1.3), and divided into a small number of rigid plates under brittle deformation, which we refer to as the tectonic plates (Fig 1.4). The tectonic plates are in relative motion with respect to one another above a highly viscous, mechanically weak and deeper part of the upper mantle with plastic behaviour, the asthenosphere (Hamblin & Christiansen, 2003; Turcotte & Schubert, 2002) (Fig 1.3). The mechanism of the motion is controversial, but the most accepted theory is the presence of convection currents in the mantel (Kearey, 1994). Tectonic interactions between plates

occur at the plate boundaries where most of the deformation, seismic and volcanic activity takes place (Fig 1.3).

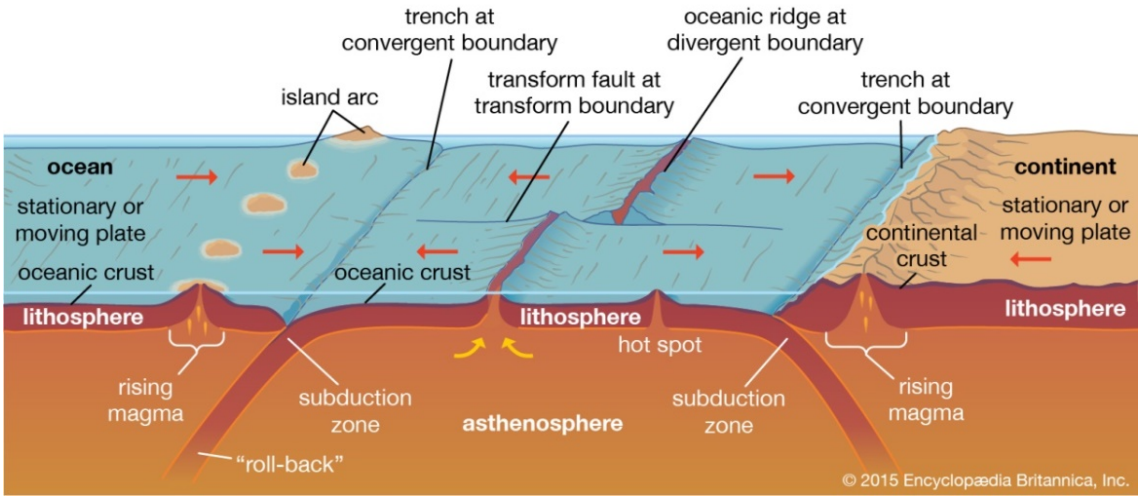


***Figure 1.3.*** *Diagram of the different interactions between tectonic plates and their boundaries. The diagram depicts the continent and oceans, with the Transform faults at transform boundaries, Mid-ocean ridges at divergent boundaries and Trenches at convergent boundaries. Below the seafloor, the picture shows the thin lithosphere (i.e. oceanic and continental crust) and below the thick asthenosphere in the upper mantle, where oceanic plates subduct by the slab roll-back mechanism. Extracted from Encyclopaedia Britannica, (2015).*

On the basis of plate motion, there are three types of plate boundaries (Figs 1.3 and 1.4):

a) **Transform or conservative boundaries**: The plates slide horizontally and move laterally to each other, generating transform fault systems predominantly horizontal. The lithosphere plate is not created nor destroyed. Most such faults are found in oceanic crust, where they accommodate a lateral offset between segments of divergent boundaries, forming a zigzag pattern. This is a result of oblique seafloor spreading, where the direction of motion is not perpendicular to the trend of the overall divergent boundary (Kearey, 1994).

b) **Convergent or destructive boundaries**: The plates are approaching and collide to each other. One plate slides beneath the other, a process known as subduction. The subduction zone can be defined by a plane where many earthquakes would occur, referred to as the Wadati-Benioff zone. When there is a density variation in between the plates, the densest lithosphere sinks underneath the less dense one towards the mantle

and is destroyed. This type of boundary generates a subduction process represented by oceanic trench and islands arc systems. When the two lithospheres have the same density, the collision may generate a mountain ridge *(*Kearey, 1994)

c) **Divergent or constructive boundaries**: The plates move away from each other, the lithosphere progressively gets thin and new oceanic lithosphere is created by magma pushing up from the mantle. These types of boundaries are represented by mid-ocean ridges systems or continental rifts (Kearey, 1994)

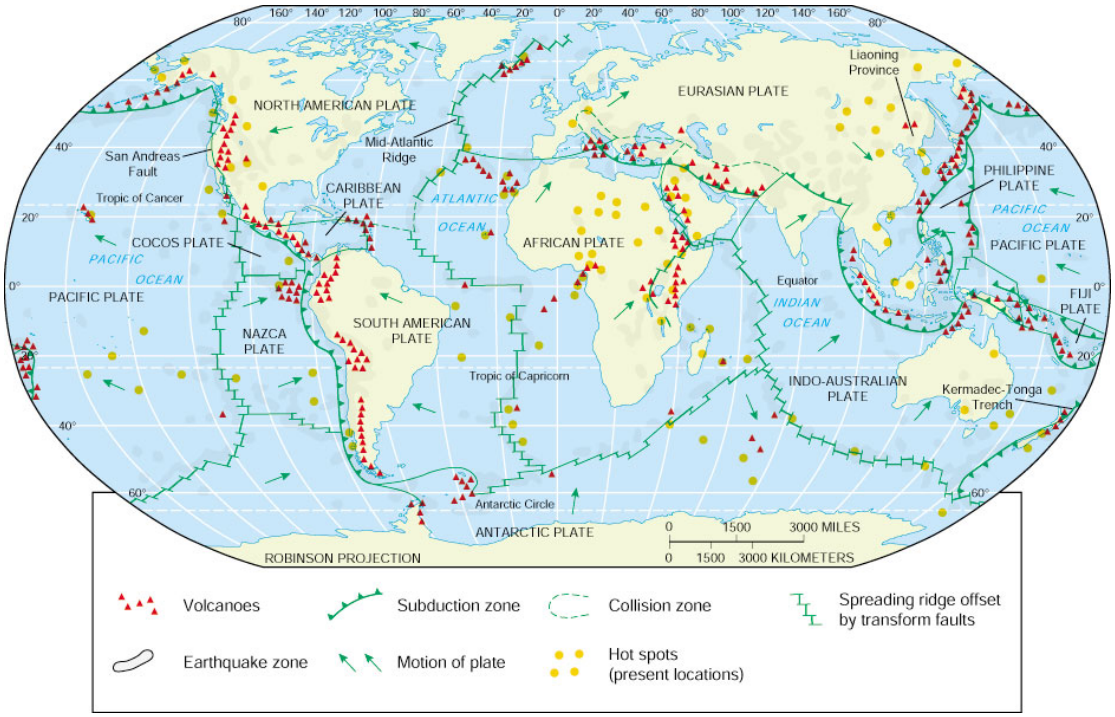


***Figure 1.4.*** *World map of the main tectonic plates with the diverse plate boundaries Subduction zones, spreading centers and transform faults have been identified. In addition, volcanoes (onland & submerged), hotspots and earthquake zones are also depicted. Plate boundaries are the zones where most of the seismic and volcanic activity occur. Extracted from Arboleya, (2018).*

The **oceanic crust** is the uppermost layer that is created or destroyed at plate boundaries. It is generated at Mid-Ocean Ridges and destroyed in the mantle at subduction zones. Therefore, it has a high relevance in the dating and reconstruction of the plate tectonic motions throughout the history of the Earth. The oceanic crust has a mean thickness of 6-7 km and an average density of 3.0 g/cm$^3$ (Turcotte & Schubert, 2002). This type of crust is characterized by a layered structure, where each layer has a different composition. From the most shallow to the deepest layer: basaltic pillow lavas, sheeted diabase dike complex, isotropic Gabbroic rocks, layered gabbroic rocks and

layered peridotites (Fig. 1.5). In contrast, the **continental crust** has a mean thickness of 35 km and an average density of 2.7 g/cm$^3$. This type of crust can be divided in two layers, one above of granodiorite composition and another below of granulite composition.

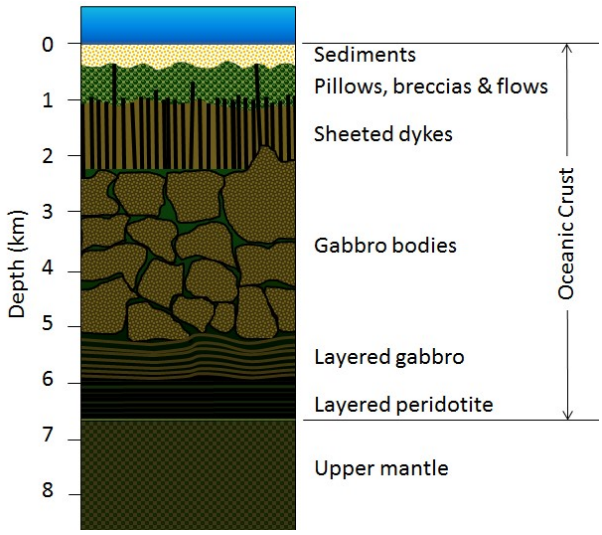


***Figure 1.5.*** *Schematic layered structure of the oceanic crust. It includes sediments, pillow lavas, breccias and flows, sheeted dykes, gabbros, layered gabbros and layered peridotite. The detailed thickness and horizontal contacts are based on standard ophiolite complexes. Extracted from Earle, (2015).*

### *1.4.2. Fault types and basic parameters*

A **fault** is a fracture or a discontinuity in a volume of rock, which has produced a significant displacement, as a result of rock movements. Two blocks of rock separated by a fault are displaced relatively to each other (Keller & Pinter, 2002) . The motion of the faults can be rapid, and may originate an earthquake or can slowly occur in the form of creeping (Press et al., 1986). To define and characterize a fault system, their motion and seismic potential, a series of mechanical parameters are used (Fig 1.6a) (Keller & Pinter, 2002). They are the following:

a) **Strike**: Direction of the line, relative to North, formed by the intersection of the fault plane and the ground.

b) **Rake**: Direction of the fault motion with respect to the strike line of the plane that defines the tectonic behaviour of the fault (Fig 1.6b).

c) **Dip-angle**: Angle at which the fault is inclined to the horizontal plane.

d) **Fault geometry**: Length and width of the fault plane.

e) **$M_w$**: Moment magnitude is a measure of an earthquake size based on the seismic moment, with the latter being a function of the fault slip and area involved in the earthquake.

f) **Focal depth**: Depth of an earthquake hypocentre.

g) **Slip**: Relative movement of both sides of the fault plane. The slip is fundamentally related to the stress-drop on the fault (i.e. difference between the stress across a fault before and after the occurrence of an earthquake) and the material properties of the medium (Hirono et al., 2016; Scholz, 2002).

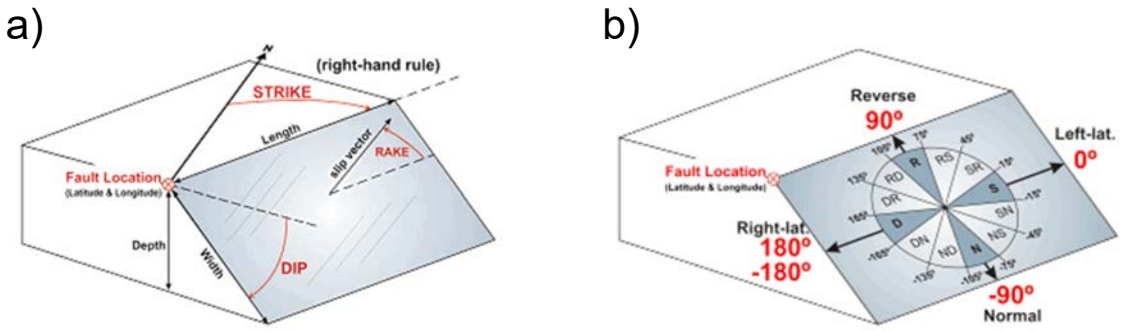


***Figure 1.6.*** *Diagram of the standard conventions to define faults. a) Diagram of the fault plane parameters (i.e. length, width, depth, strike, rake and dip). b) Diagram of the fault types in function of the rake. Extracted from IGME, (2015).*

On the basis of the Anderson stress model, the faults can be classified in three main types, depending on the direction of the three principal stresses $\sigma_1 > \sigma_2 > \sigma_3$ to the horizontal plane: normal faults, reverse faults and strike-slip faults (Lowrie, 2007) (Fig. 1.6, 1.7). The principal stresses are consequence of the state of the stress of an area, produced by the motion of the tectonic plates. The Anderson's stress model, to explain the fault-type ruptures, considers an isotropic deforming rock and a coaxial deformation (Lowrie, 2007). The $\sigma_1$ represents the axis of maximum tensional stress (T-axis) and $\sigma_3$ represents the axis of maximum compressional stress (P-axis) (Fig. 1.7). When the motion of the faults occurs up or down the fault plane, it is called as a dip-slip fault, and when the motion is horizontal, parallel to the strike of the fault plane, it is referred to a strike-slip fault. These are the three types of fault systems (Lowrie, 2007):

- **Normal faults**: Dip-slip fault in which the block above (the hanging-wall) has moved downward relative to the block below (footwall). The T-axis is horizontal and the P-axis is vertical (Fig. 1.7).
- **Reverse fault or thrust fault**: Dip-slip fault in which the hanging-wall moves upward and over the footwall. The T-axis is vertical and the P-axis is horizontal (Fig. 1.7).
- **Strike-slip or transcurrent fault**: The fault surface is usually near vertical, and the footwall moves laterally either left or right, with little vertical motion. The T- and P- axis lie in the horizontal plane. If the observer perceives that the opposite side of the fault moves to the left, the fault is said to be sinistral or left-lateral. If the observer perceives that the opposite side moves to the right, the fault is dextral or right-lateral (Fig. 1.7).

On the basis of the interpretation of principal axes of stress that led to an earthquake, seismologists can calculate the orientation and direction of slip of a seismogenic fault that it is called as **focal mechanism** and it is displayed on maps as a "beach ball" symbol (Fig. 1.7). Focal mechanisms are computed using a method that tries to find the best fit to the direction of the first P-wave motions of an earthquake observed at different seismic stations (Fowler, 2005).

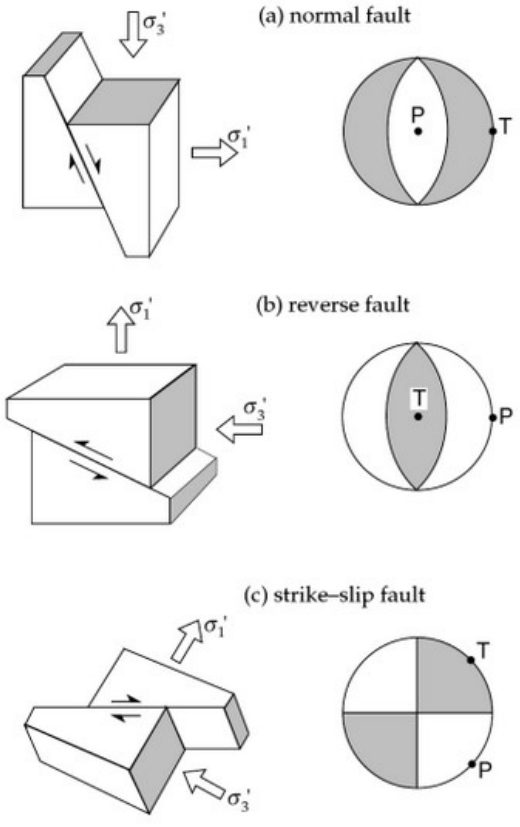


***Figure 1.7.*** *Schema of the three basic types of faults (right) and their associated focal mechanisms (left). P: orientation of the P-axis; T: orientation of T-axis. Extracted from Lowrie, (2007).*

### *1.4.3. Seismicity concepts*

An **earthquake** is the sudden slip on a fault and the resulting trembling in the ground, caused by the released stress that radiates energy throughout a seismic-wave (Keller & Pinter, 2002). Most of the earthquakes are the result of a fault rupture (i.e. the strain energy is stored until the stress accumulated at the fault is enough to overcome the block), but they can also be generated by landslides, volcanism or magmatic activity (Gràcia et al., 2019; Sallarès & Ranero, 2019). The **hypocentre** (or focus) is the point on the fault plane where the earthquake rupture starts. The **epicentre** is the point on the surface located vertically above the hypocentre.

The faults that are able to generate ruptures and therefore earthquakes are defined as **active faults**. The first widely active fault definition refers to a fault that is currently moving (Wallace, 1981), however this definition is an ambiguous and strongly dependent on the location and interest of the study. In regions with high motion plate boundaries and high-recurrence of events, such as California, between North American and Pacific plates, a fault is considered active if it has tectonic activity during the Holocene (Machette, 2000). Whereas, in slow motion plate boundaries, such as the SW Iberian margin, a fault is considered active if it has moved during the Quaternary and the time-span of concern to society (Machette, 2000). To know when an active fault is likely to produce an earthquake, it is necessary to calculate the average time-interval between earthquakes, which is called **average recurrence interval** (Keller & Pinter, 2002). To calculate this, three different methods may be used:

a) **Seismic data**: Uses historical and instrumental earthquakes and an average time-interval between the seismic events.

b) **Paleoseismic data**: Studies the geological record (e.g. paleo-turbidites) to identify and evaluate the prehistorical earthquakes, as well as the time-interval between a sequence of consecutive events (Gràcia et al., 2010).

c) **Slip rate**: How fast two sides of a fault are slipping relative to one another (mm/yr) (Keller & Pinter, 2002) . Assuming a given displacement per event (slip per event in mm) and dividing that number by the slip rate (mm/yr), the recurrence period is obtained (yr).

### *1.4.3.1. Seismic zones and seismic data offshore*

To study in detail the seismicity of a region, such seismicity needs to be related with past, current and future earthquakes events and the active tectonic structures of the area in order to identify the **seismic zones** (i.e., areas where earthquakes tend to focus) (Fowler, 2005).

The definition of a **seismic zone** is based on the interpretation of the geological, geophysical and seismological data. The delimitation of the seismic zones is important not only for theoretical reasons such as, understanding the geodynamics of a region, but also for practical reasons. One of the main reasons is to predict earthquake ground-motion resulting from the largest earthquake that could shake a given region (Keller & Pinter, 2002).

To determine the tectonic framework of offshore areas and the characteristics of individual faults is not an easy task because these tectonic structures are located at large water-depths. The main difficulty is to obtain the geological data, which is based on indirect methods (i.e., seismic and acoustic data), mainly because of the inaccessibility to offshore faults and the difficulties related to direct *in situ* observations. Punctually, it is possible to obtain direct information from the material that constitutes the area under investigation by sediment sampling using coring devices that usually do not exceed 2 to 3 m in length. Less frequently piston coring devices may allow for sedimentary sequences up to 50 m below sea floor to be sampled. Using rarely available drilling techniques it is possible to retrieve sediments and fault related materials from several hundred/km below the seafloor (Chester et al., 2012). Direct observations at the seafloor can sometimes be performed using ROVs (Remotely Operated Vehicle), AUVs and submersibles (Szitkar et al., 2019; Yoerger et al., 2007).

In the same way, assigning specific earthquakes to a particular fault system is also a complex task. The main difficulty is to relate the earthquake epicentres with the active faults. To locate the epicentre of an earthquake it is necessary to have a wide-coverage (360º) of the seismic stations around the epicentre, capable to record the event, triangulate it and locate it with as high precision as possible. The main problem is that seismic stations are often located onshore, far away from the earthquake source. Therefore, there is a significant lack of seismic event records, which may induce errors in the location of the epicentres located at tens of kilometres away (Engdahl &

Villasenor, 2002). Finally, it is very important to gather all the seismic data of a given study region in order to properly define their seismic behaviour. The main sources of seismic information are the following:

a) **Instrumental and macro-seismic catalogues**: Throughout the last Century, the way to record the seismicity of a given region has evolved due to the fast development in seismic instrumentation. Before the XX$^{th}$ Century, all the located epicentres were determined from macro-seismic information, which was based on the perception that the society had of an earthquake through inquest and assessment of the damage and social effects that it caused. **Macroseismic catalogues** are exclusively based on intensity data (Susagna i Vidal & Goula i Suriñach, 1999). The development of seismological instrumentation that took place at the beginning of the XX$^{th}$ Century is a point from which the science evolved from macroseismic epicentres to instrumental epicentres. However, there are few instrumental records from the beginning of the XX$^{th}$ Century. It was not until the middle of that Century that several networks of instrumental seismic stations began to be deployed. The **instrumental catalogues** allowed a broad and precise knowledge of the earthquakes that occurred in a given region during the last 40 years (Susagna i Vidal & Goula i Suriñach, 1999).

b) **Historical chronicles:** Documenting the historical seismicity is based on different types of written information of large/great earthquakes that occurred before the XX$^{th}$ Century. The main dilemma of this type of information is that there are important inaccuracies that require the participation of expert's historians that know the particularities of each epoch in the study area (Campos, 1991; Escorza, 2007).

c) **Submarine paleoseismology:** Paleoseismology is based on the study of the geological record to evaluate pre-historical and historical earthquakes. The aim of paleo-seismology is to extend the seismic catalogue back in time. This is especially important in slow slip-rate regions that host large earthquakes with long recurrence periods ($<10^3$ yr), and regions where the historical catalogues are shorter than the recurrence interval (e.g., the SW Iberian margin) (Santanach i Prat & Masana, 2001). In the case of the offshore SW Iberian margin, the instrumental period is relatively short (< 100 yr) and the historical earthquake catalogues are not sufficient, considering the high magnitude earthquakes and the long recurrence interval in this region (Gràcia et al., 2010; Masana et al., 2004). The submarine paleoseismic approach allows us to determine past seismic activity and their recurrence rate for large magnitude events ($M_w$

> 6.0). Recent investigations by Gràcia et al. (2010) tested the "turbidite paleoseismology" in the SW Iberian margin. The study was based on the coeval deposition of turbidites in distal depositional areas as a proxy for paleo-earthquakes during the high-stand of the Holocene period (Fig. 1.8).

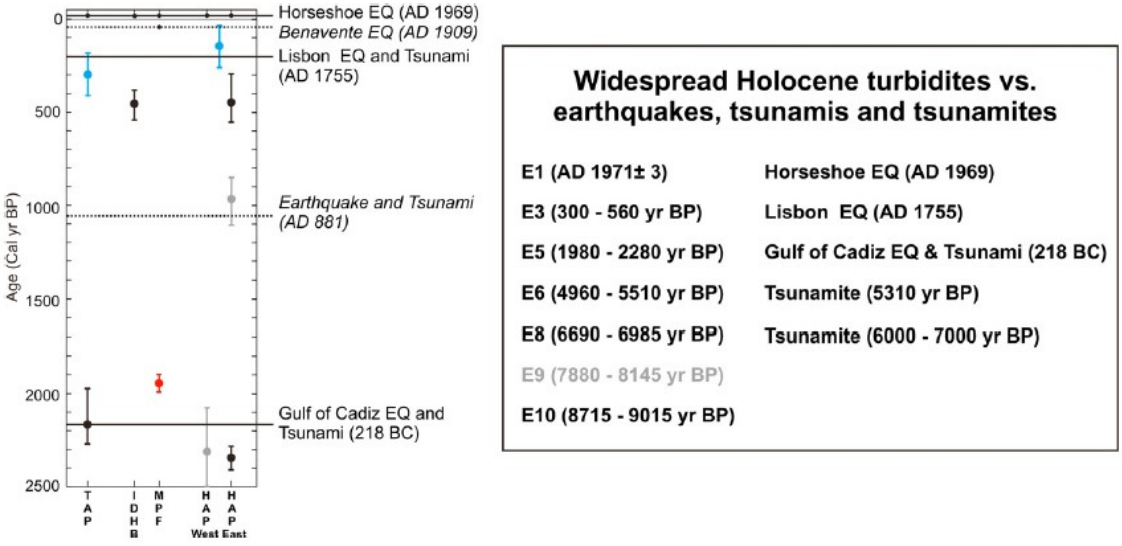


***Figure 1.8.*** *Turbidite ages recorded in different areas of the SW Iberian margin for the last 2500 years. Black lines correspond to the ages of instrumental and historical earthquakes and tsunamis of $M_w \geq 8.0$. Dashed lines: historical earthquakes and tsunamis of $6.0 \leq M_w \geq 8.0$. In red, turbidity event from Vizcaino et al., 2006. Depicted in blue, turbidites ages from Thomson and Weaver (1994). IDHB: Infante Don Henrique Basin; MPF: Marquês de Pombal Fault; HAP: Horseshoe Abyssal Plain; TAP: Tagus Abyssal Plain. Inside the box: turbidite events linked to the instrumental and historical earthquakes. E9, in grey, is not considered for calculating the regional recurrence. Extracted from Gràcia et al., (2010).*

### *1.4.3.2. Seismic scales to measure earthquakes*

To describe the released energy of an earthquake there are two types of scales, one more quantitative and another more qualitative. The former are **magnitude scales,** which are logarithmic and based on measurements of the seismic-wave recorded on a seismogram (e.g. Richter scale, Table 1.1), the latter are **intensity scales**, which are subjective and are based on the shaking, damage to buildings and social impact of an earthquake (e.g. MSK scale or Mercalli scale, Table 1.1) (Fowler, 2005). Intensity scales should be taken into account in respect to the different building codes and the socio-economic features of different world areas.

| Richter magnitude | Modified Mercalli intensity | Description |
|---|---|---|
| 1.0–3.0 | I | Not felt except by a very few under especially favorable conditions. |
| 3.0–3.9 | II | Felt only by a few persons at rest, especially on upper floors of buildings. |
| | III | Felt quite noticeably by persons indoors, especially on upper floors of buildings. Many people do not recognize it as an earthquake. Standing motor cars may rock slightly. Vibrations similar to the passing of a truck. Duration estimated. |
| 4.0–4.9 | IV | Felt indoors by many, outdoors by few during the day. At night, some awakened. Dishes, windows, doors disturbed; walls make cracking sound. Sensation like heavy truck striking building. Standing motor cars rocked noticeably. |
| | V | Felt by nearly everyone; many awakened. Some dishes, windows broken. Unstable objects overturned. Pendulum clocks may stop. |
| 5.0–5.9 | VI | Felt by all, many frightened. Some heavy furniture moved; a few instances of fallen plaster. Damage slight. |
| | VII | Damage negligible in buildings of good design and construction; slight to moderate in well-built ordinary structures; considerable damage in poorly built or badly designed structures; some chimneys broken. |
| 6.0–6.9 | VIII | Damage slight in specially designed structures; considerable damage in ordinary substantial buildings with partial collapse. Damage great in poorly built structures. Fall of chimneys, factory stacks, columns, monuments, walls. Heavy furniture overturned. |
| | IX | Damage considerable in specially designed structures; well-designed frame structures thrown out of plumb. Damage great in substantial buildings, with partial collapse. Buildings shifted off foundations. |
| 7.0 and higher | X | Some well-built wooden structures destroyed; most masonry and frame structures destroyed with foundations. Rails bent. |
| | XI | Few, if any (masonry) structures remain standing. Bridges destroyed. Rails bent greatly. |
| | XII | Damage total. Lines of sight and level are distorted. Objects thrown into the air. |

***Table 1.1.*** *Comparison table of the Ritcher magnitude and modified Mercalli intensity scales. From Tendürüs et al., (2010).*

The **magnitude of an earthquake** is a number that characterizes the relative size of an earthquake. There are different scales of magnitude deriving from identifying specific body wave (P- and S- waves) of the ground motion on a seismogram. Some of the scales defined are the local or Richter magnitude ($M_L$), surface-wave magnitude ($M_s$), body-wave magnitude ($m_b$ for short period, $m_B$ for long period), and **moment magnitude ($M_w$)**. The $\mathbf{M_w}$ is the most recent and useful scale obtained from the **seismic moment ($M_0$)** and is a more reliable measure of the magnitude of an earthquake than is either $M_L$, $M_s$ or $m_b$ (Fowler, 2005). The $\mathbf{M_0}$ measures the sizes of an earthquake considering fault parameters such as the shear modulus (strain necessary to overcome the friction force), the fault rupture area and the average displacement of the fault (slip) (Fowler, 2005). In addition, to link physical fault parameters with earthquake released energy the $M_w$ can be easily calculated with modern instruments and can be estimated by geodetic and geological data. For all these reasons, nowadays the $M_w$ is the most used worldwide magnitude scale (Kanamori, 1977).

### *1.4.4. Basic concepts of tsunamis*

#### *1.4.4.1. Tsunami definition and generation*

Tsunami is a Japanese word that means "harbour wave". It has been known since ancient times that this type of wave, different from the usual ones produced by wind and tides, can inflict significant damage to the coasts.

In scientific terms, a **tsunami** is a series of giant gravity waves in a water body caused by the displacement of a large volume of water (Satake, 2015). This work focuses on tsunamis generated by earthquakes (earthquake tsunamis), when the energy released by an underwater earthquake triggers an abruptly seafloor vertical deformation. The vertically deformation immediately displaces the overlying water losing its equilibrium position (Satake, 2015) (Fig 1.9). Due to the small compressibility of seawater, it is assumed that the initial wave height of a tsunami is set by the amount of uplift or dropdown produced by the seafloor rupture (Satake, 2015). Gravity restores mean sea level by converting the energy of the local sea surface displacement into a gravity wave. Offshore, earthquake-induced tsunamis have a small wave height, a very long wavelength (much longer than ocean depth) and travel at high velocity (over 800 km/h) across ocean basins with negligible speed loss (Fig 1.9. and Table 1.2.)

The waves grow in height when they reach shallower waters (shoaling effect), because the banks and the continental shelf compress the wave and its velocity decreases drastically (below 80 km/h) (Table 1.2.). Its wavelength diminishes and its amplitude grows enormously (Satake, 2015). The most important tsunamis are produced by large and shallow earthquakes ($M_w$ > 7 and 10-50 km depth in the crust) associated to the movement of tectonic plates (Bryant, 2008).

There are different processes, besides the earthquakes, that can generate a tsunami such as, volcanic eruptions, landslides and other underwater disturbances like glacier calvings, detonations or meteorite impacts (e.g. Keating & McGuire, 2000; Latter, 1981; Stein & Okal, 2005) (Fig 1.9).

Within the tsunami earthquakes, there are two different types: the tsunamigenic earthquakes and the tsunami earthquakes. A **tsunamigenic earthquake** is an earthquake that generates a tsunami, while a **tsunami earthquake** is an earthquake that excites much larger tsunamis than expected from the seismic waves (Kanamori, 1977; Satake, 2015).

a)

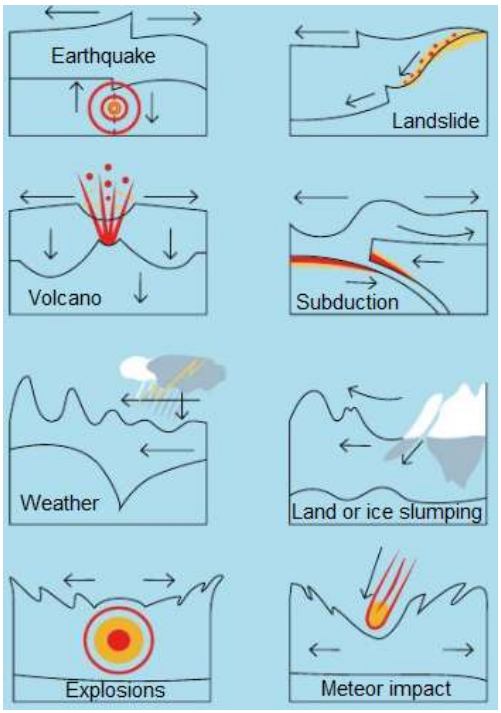


b)

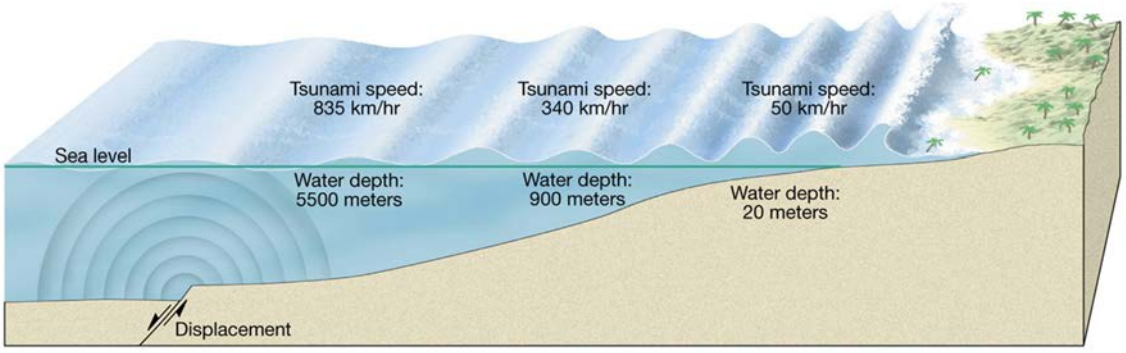


***Figure 1.9.*** *Tsunami generation and propagation. a) Different processes that may generate a tsunami (modified from SalvagdorGali/Shutterstock.com in Sallarès & Ranero, (2020)); b) Diagram of tsunami evolution from the source point until the coastline. From Tarbuck et al., (2005).*

| **Depth (meters)** | 7000 | 4000 | 2000 | 200 | 50 | 10 |
|---|---|---|---|---|---|---|
| **Velocity (km/h)** | 943 | 713 | 504 | 159 | 79 | 36 |
| **Wave length (km)** | 282 | 213 | 151 | 48 | 23 | 10.6 |

***Table 1.2.*** *Relationship between Depth, Velocity and Wave length of a tsunami. Tsunami speed and wave length are reduced in shallow waters as wave height increase rapidly modified from International Tsunami Information Center, (2020).*

### *1.4.4.2. Tsunami propagation*

Tsunamis propagate in all directions from the source area, with the direction of propagation of the main energy, generally being orthogonal to the direction of the earthquake rupture, and hence it depends on the orientation and dimensions of the fault on which the earthquake originates. Variations in tsunami propagation energy can occur where regional bathymetric and topographic elements modify the waveform. The tsunami-wave may experiment refractions, reflections and dispersion throughout its propagation (Levin & Nosov, 2015):

- **Reflections** occur when the tsunami-wave bounce back against shorelines and returns into the medium, creating a complex wave-pattern. Tsunamis can reflect off in topographic features, mainly in coastal areas (Levin & Nosov, 2015).
- **Refraction** is the variation of the direction (bending) of wave-propagation caused by segments of the tsunami-wave that move at different velocities, as the water-depth changes along the wave front. The difference in wave-velocity may occur because the wave-velocity decreases in the shallow water. When part of the tsunami-wave is in shallower water than another part, the wave bends (Levin & Nosov, 2015). This effect is possible mainly because the tsunami wavelength is much larger than the water-depth and the horizontal motion of water-mass is uniform through the entire water column (i.e. from the ocean bottom to the surface) (Satake, 2015).
- **Dispersion** occur when the longer wavelength components of the waves, propagate faster than the shorter wavelength components, therefore, the wave not reaches long distance with the initial profile (Satake et al., 2015).

Tsunami-waves can act as shallow water-waves or long-waves. For shallow water or long waves, the wave velocity (v) depends on the water depth (d) according to the formula:

$$V = \sqrt{g \cdot d}$$

where g is the acceleration of gravity (Bryant, 2008).

### *1.4.4.3. Tsunami metrics*

To describe a tsunami and the impact that may have on the coast, a series parameters, offshore and on-land, describing the tsunami characteristics are needed. In the former case, the most used parameters are the amplitude, the wave-height and the wavelength; in the latter, the most used parameters are the run-up, the inundation height, the inundation distance and the flow depth. The definitions of each parameters are as follow (Satake, 2015):

*Offshore* (Fig 1.10)

- **Amplitude:** Is the measure from a zero value to a negative or positive peak (crest or trough) of a wave. The zero measure is an estimation of the tidal level. The initial motion (negative or positive peak) carries the information on the tsunami source.
- **Wave-height:** Is the measure from a trough to a crest of a wave. It is also called as "range" or "double amplitude". It is measured using tide gauges.
- **Wavelength:** Distance between two consecutive crest or trough.

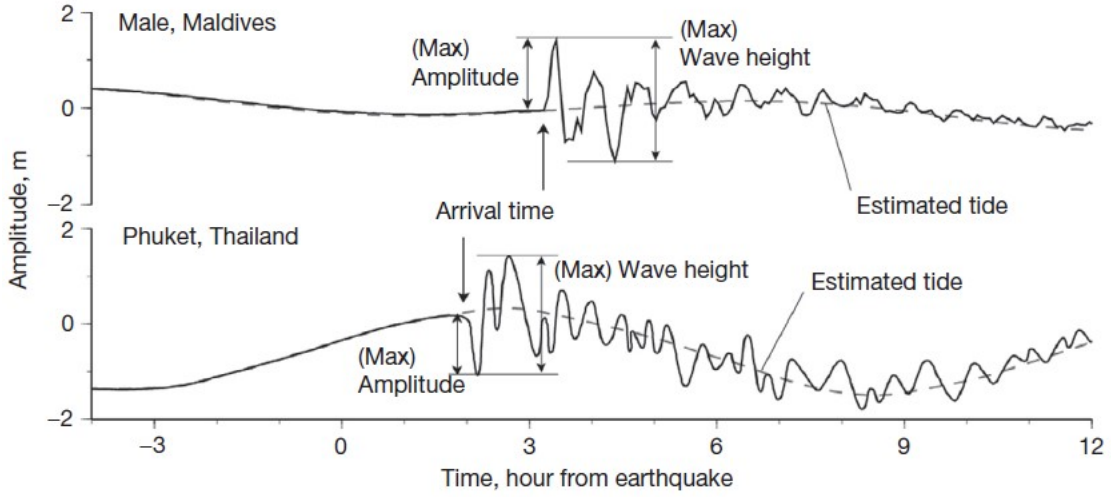


***Figure 1.10**. 2004 Sumatra-Andaman waveforms recorded by a gauge stations in Male (Maldives) and Phuket (Thailand) showing amplitude and wave-height. From Satake (2015).*

*On-land* (Fig 1.11.)*:*

- **Flow depth:** Is the height of a tsunami on-land measured from the ground level.
- **Inundation height:** Relative measure of the sea level on the tsunami arrival time.

- **Inundation distance:** Horizontal water penetration distance measured from the coast.
- **Run-up height:** Maximum inundation height, where the velocity and the kinetic energy of the tsunami become zero.

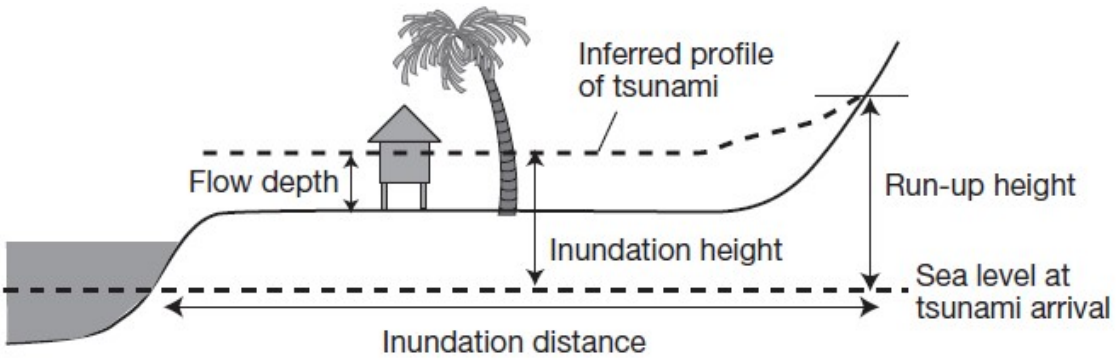


***Figure 1.11.*** *Graphical definitions of the tsunami parameters measurements on-land. From Satake, (2015).*

#### *1.4.4.4. Tsunami observations*

**Tsunami observations and measurements** are very important since they allow to create extensive databases that are very useful to benchmark tsunami models and tsunami early warning systems. They can be instrumental measurements or geological observations (Satake, 2015).

There are different **instrumental measurements**. The most common method used for more than a century is the tide gauge at ports and harbours that measures sea-level coastal heights. The classic **tide gauge** is mechanical and detects the sea-level changes by a float in a well. The most recent gauges include pressure (i.e., they measure water pressure that is converted to sea-level height), acoustic and radar measurements (i.e., they send ultrasonic waves to measure sea-level changes) (Satake, 2015). Offshore wave-gauges are very important to detect tsunamis before they arrive to the shore. This type of wave-gauge uses ultrasonic waves to measure water height and wave period. For deep-ocean measurements, bottom pressure gauges are used. They also records ground motion and work as ocean-bottom seismograph. These gauges send signals to a surface buoy which in turn send the information via satellite to a land station (González et al., 2005).

On the one hand, **geological observations** not usually provide direct information on the metrics of tsunamis; on the contrary they can contribute with important information in terms of sizes and recurrence interval of earthquakes and tsunamis. The **geological observations** are based in the study of **prehistoric tsunami deposits** (Bryant, 2008). These deposits result from a short and rare episode where multiple waves transport suspended load, which is rapidly deposited in sheets characterized by graded bedding. The identification and dating of this type of sedimentary deposit allows to calculate the amount of tsunamigenic events that occurred in specific areas and time intervals in the past (Bryant, 2008). On the other hand, when a tsunami occurs in a remote area, is common to carry out more or less immediately a tsunami survey that provides metrics of the tsunamis (e.g. flooding parameters) (Borrero, 2005; Okal et al., 2015).

### *1.4.5. Geological Risk and related concepts*

A **natural hazard** is a natural phenomenon that may have a potential threat to society (i.e., fatalities, damage to property and infrastructure) (Keller & DeVecchio, 2015). Natural hazards are characterized by their magnitude (energy released) and intensity (strength of the event on the environment), as well as their frequency (number of events occurred on average) and probability (a number between 0 and 1, which indicate the chance of happening of an event). The natural phenomena itself is not a risk, but it may prompt risk due to the human use of the land. In this regard, the increase in world population, together with **poor land-use**, can lead to the occurrence of phenomena that may lead to disasters and eventually become huge catastrophes (ICGC, 2008). The consequences of a natural phenomenon can be considered a **disaster** if the hazardous event occurring in a limited time and on a defined area causes injured or fatalities and the state of emergency is declared and international assistance is required. A **catastrophe** is a devastating event that requires a long time and expenditure of a lot of money to recover the damaged place (Keller & DeVecchio, 2015).

Natural hazards may affect millions of people around the world and it is calculated that each year about 80.000 people die in natural disasters or catastrophes (Keller & DeVecchio, 2015). When a natural phenomenon interacts with human activity, the concept of a geological risk takes place. Therefore, the concept of **risk** can be defined as the combination of a **natural hazard** and the **vulnerability** (i.e., exposure and level of expected damage of people or elements of the affected area) (Fig 1.12) (ICGC).


**RISK = Natural Hazard x Vulnerability**

***Figure 1.12.*** *Diagram of the risk function. This is not only depending on the exposure to natural processes that may impact on society. Impacts from catastrophic events are directly related to human decisions and policies made before, during and after it. Modified from Wood, (2011).*

#### *1.4.5.1. Prevention, mitigation and prediction*

Natural hazards cannot be predicted, although, it is sometimes possible to predict when a hazardous natural event will occur in the short term, especially in natural events linked to weather (flooding, coastal floods...). However, most of the natural events such as earthquakes and tsunamis, which are studied in this thesis, are not possible to predict, especially because they are relatively unusual phenomena and without previous precursors. For this reason, prevention and mitigation strategies are basic for society. **Prevention strategies** are those dedicated to avoiding an event from becoming a disaster (i.e., monitoring, warning systems, evacuation strategies…). While **mitigation strategies** are aimed at any action that reduces vulnerability, such as safety-conscious engineering, safe building structures or contention structures (Keller & DeVecchio, 2015).

In the case of the tsunami hazard, the way to prevent and mitigate the effects of tsunamis in terms of loss of human life is to develop vulnerability studies to **adapt urban plans and build protection structures** (sea level barriers and walls in front of the coast), use an early warning system and educate the coastal population on the best

way to evacuate the affected area. **Early warning systems** are based on seismic and sea-level monitoring and comparison of the data with past tsunami events and numerical tsunami simulations. If the recorded data is compatible with a tsunami earthquake, a tsunami warning message is sent to the population in a few minutes (Satake, 2015). Therefore, to protect vulnerable coastal areas from tsunamis, a precise monitoring network of tide gauges, a good network of seismic stations, and a good knowledge and characterization of active tectonic structures that can generate tsunamis are necessary to carry out tsunami hazard assessments. In general terms, to have high-quality earthquake rupture and tsunami propagation models, a good constraint on the fault parameters is required (Tonini et al., 2020).

### *1.4.6. Alongslope and downslope sediment transport processes in mid-latitude continental margins*

From the lower course of a fluvial system until sedimentary particles enter the submarine geological record, they experiment one or more transport cycles of transfer, deposition and reactivation. Understanding sediment transfer processes is key to properly recognize the morphologies and deposits in continental margins. The sediment transfer between continental shelf, continental slope and abyssal plain is at the origin of relief generation and sedimentary deposits (Hamblin & Christiansen, 2003). Sedimentary flows occur on mid-latitude continental margins embrace four major marine processes:

a) Much of the material entering the sea from the continents does so in the form of **coastal fluvial plumes** (Pratson et al., 2007) (Fig 1.13). These plumes are usually hypopycnal (i.e., they have lower density than sea-water) and spread forming a surface nepheloid layer (Biscaye & Eittreim, 1977). This nepheloid layer can sink to the seafloor and gradually deposit the suspended clay portion of the sediment load through the process of flocculation. When fluvial plumes are rather hyperpycnal (i.e., denser than the sea-water), they propagate along the seafloor in the form of a turbulent gravity flow, which follows the direction of maximum slope (Parsons et al., 2001). During the low-stand periods, large rivers can directly connect to submarine canyons, where the sediment material from the fluvial course will be mainly transferred by hyperpycnal flows (Khripounoff et al., 2009; Mauffrey et al., 2017).

***Figure 1.13.*** *Copernicus Sentinel-2B satellite image of a coastal fluvial plume from the Tiber River. Modified from ESA, (2019).*

b) **Hemipelagic sediment** is sourced from multiple processes and materials, including nepheloid layers and biogenic pelagic (i.e., material of organisms living in the water-column), that settles on the continental slope and abyssal plains (Stow & Tabrez, 1998) (Fig 1.14).

c) **Bottom currents** have an important role in the transport and redistribution of sediments throughout the oceans, especially at the edges of the slope and deep basins (Piper & Normark, 2009; Weaver et al., 2000). On the one hand, these currents may generate erosive landforms on the seafloor, such as furrows and depressions. On the other hand, they play an important role generating depositional forms and deposits, such as **contourites and sedimentary waves**. Four types of bottom currents are identified: a) Thermohaline-induced geostrophic bottom currents, b) wind-driven bottom currents, c) tidal bottom-currents, and d) baroclinic bottom currents (Shanmugam, 2012) (Fig 1.14).

d) **Mass transport movements** (mass movements, mass transport or mass wasting processes) are an important source of material driven from the slope. They can occur in multiple forms such as block falls, glides and slides, debris flows and turbidity currents (Thierry Mulder & Cochonat, 1996), being the latter the most important mass-transport mechanism (Pratson et al., 2007). **Turbidity currents** (Fig 1.14) are sediment-laden

flows (i.e., hyperpycnal flows) which are usually channelled (confined flows) within submarine canyons and submarine channels, flowing under the action of gravity. These density flows are one of the main causes for the development of **submarine canyons**.

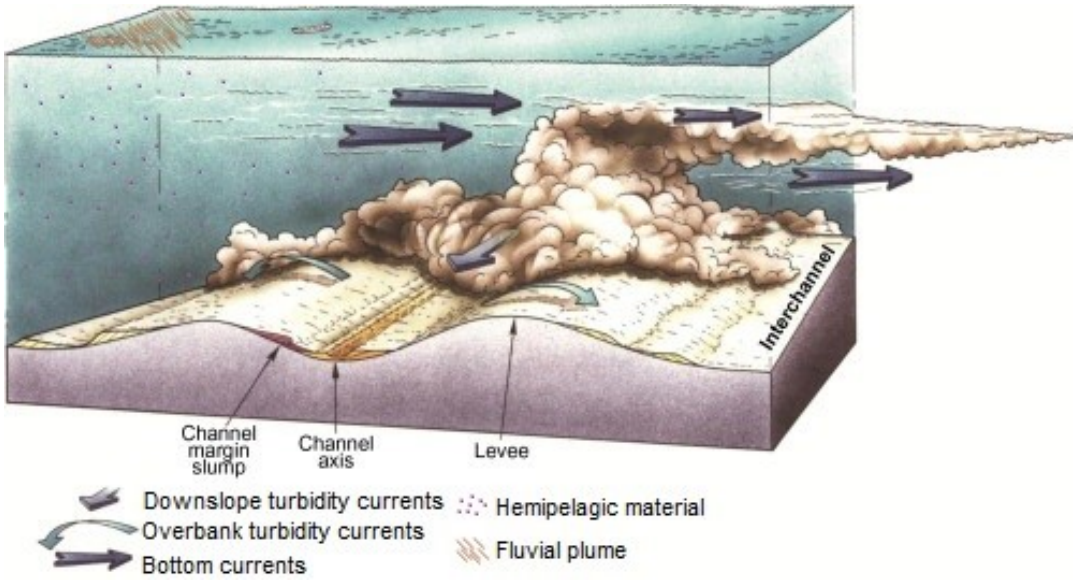


***Figure 1.14.*** *Conceptual model of the generalized distribution and interaction between the four main sedimentary processes. Channelized turbidity currents, bottom currents, hemipelagic material and fluvial plumes. Modified from Shanmugam, (2012).*

### *1.4.6.1. Submarine canyons*

Submarine canyons are major sediment pathways that link shallow continental shelves to the deep sea. They play an important global role in the development of continental margins. Submarine canyons do not only act as conduits for sediments, but also they play a role as main transport corridor for associated nutrients, organic carbon, litter and pollutants travelling from the continental shelves to the abyssal plains (Amblas et al., 2012; Lastras et al., 2009; Micallef et al., 2014; Serra et al., 2020; Shepard, 1981). Erosion and sediment remobilization induced by sediment-laden gravity flows (e.g., turbidity currents), which travel from the head and flanks of the canyon towards the deep oceanic basins (Lewis & Barnes, 1999), are the main factors in the generation of submarine canyons. Temporary sediment accumulations near the canyon head may become unstable due to a number of factors, such as over-steepening, earthquake-triggered deformation, sediment liquefaction and basal erosion of canyon flanks (Arzola et al., 2008; Sultan et al., 2007). However, other flows such as hyperpycnal flows also generate erosion at the canyon head (Canals et al., 2006; Palanques et al., 2006; Puig et al., 2014) and transport large sediment volumes along the

entire canyon. The onset of canyon development and their subsequent evolution is determined by a number of factors, including sediment sources and the resulting sedimentary and erosive processes that shape the canyon-floor and their flanks (Amblas et al., 2011; Mauffrey et al., 2017). Moreover, structural control has also been proposed (Micallef et al., 2014). Morphologically, submarine canyons can be divided into three parts: a) the head or upper part, b) the central part, and c) the lower part. The **upper part** is generated near to the shelf-break region, and the canyon is entrenched between slopping canyon walls. In the **central part**, the relief is smooth, and in the **lower part**, the flanks are gentle and the canyon is open to the depositional fan or abyssal plain (Shepard, 1981).

According to the submarine canyon classification by Harris & Whiteway, (2011), three different submarine canyons typologies can be distinguished: a) **Type 1**, shelf-incision with connection to a major river system, this type of canyons usually extend from the continental shelf to the abyssal plain; b) **Type 2**, shelf-incision without a connection to a major river system; and c) **Type 3**, blind canyons, the upper part of this type of canyons is located in upper slope.

# CHAPTER 2

# Geological setting

The SW Iberian margin hosts the present-day Eurasian-African plate boundary. This boundary extends to the West, until it connects to the Azores Triple Junction that includes: North America, Eurasia and Nubia plates at the eastern part of the Straits of Gibraltar. This complex structure bordering Africa and Eurasia is referred to as the Azores Gibraltar Fault Zone (AGFZ) (Fig. 2.1). Different kinematics and stress regimes occur along AGFZ, therefore, three different tectonic domains have been identified (Omira, Neres, & Batista, 2019). To the East of the Azores Triple Junction, the plate boundary coincides with the Terceira Rift, considered an active hyper-slow spreading oceanic rift, with diffuse deformation distributed along a series of horsts and grabens (Hildenbrand et al., 2014; Marques et al., 2013; Vogt & Jung, 2004). The nexus between the Terceira Rift and the SW Iberian margin is a relatively discrete Transform Zone, the dextral strike-slip Gloria Fault, which becomes diffuse as it approaches to the SW Iberian margin (Neres et al., 2016). Present-day tectonic deformation in the SW Iberian margin is mainly driven by NW-SE trending convergence, with an estimated velocity of 3.8–5.6 mm $a^{-1}$ (Neres et al., 2016; Nocquet & Calais, 2004) (Fig. 2.1). Sartori et al., (1994) describe the plate boundary in the SW Iberian margin as a diffused boundary distributed in a broad area of about 200 km wide. Zitellini et al., (2009) proposed the SWIM fault zone as the new transcurrent plate-boundary and (Martínez-Loriente et al., 2014) describe the main structure of the SWIM fault zone, the strike-slip Lineament South Fault (LSF), which can be considered as the present-day African-Eurasian plate-boundary.

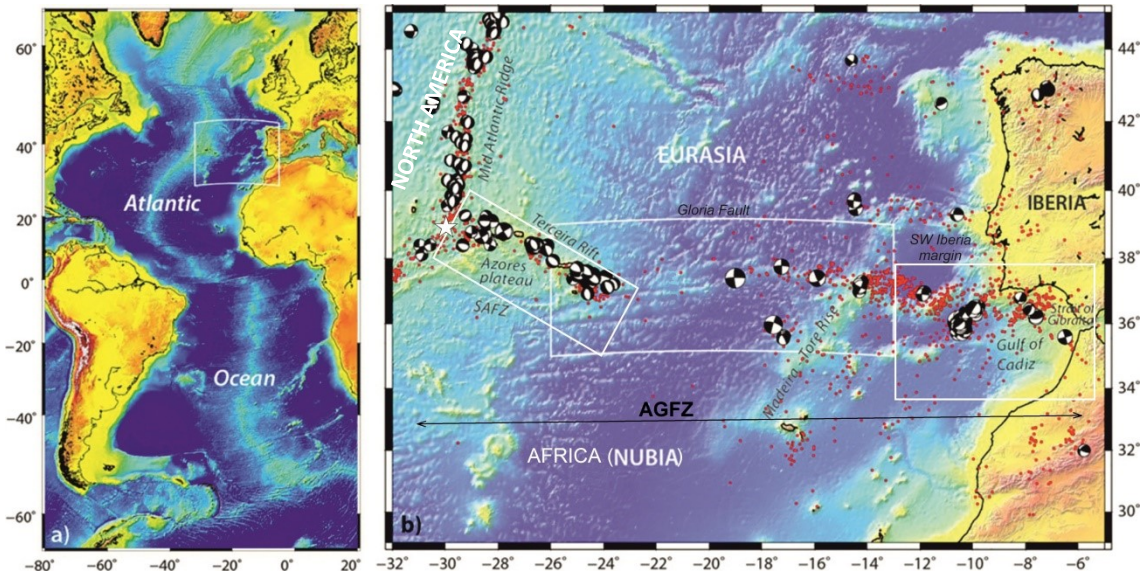


***Figure 2.1.*** *a) Location of the Azores Gibraltar Fault Zone (AGFZ) in the Atlantic Ocean. b) Coloured bathymetric map of the plate boundaries between Eurasia, Africa (Nubia) and North America. The white star is located at the triple junction. Red dots correspond to epicentres of M > 4 from the International Seismological Centre (ISC) for the period 1970-2017. Focal mechanisms (M > 5) from the database compiled by Custódio et al., (2015). SAFZ: South Azores Fracture Zone. Modified from Omira et al., (2019).*

## 2.1. Geodynamic evolution

The SW Iberian margin has undergone a complex geodynamic history involving different extensional and compressional episodes since the initial brake-up of Pangea that constrain the present morphology and tectonic structure of the study area. During the last two decades several authors (Labails et al., 2010; Malod & Mauffret, 1990; Olivet, 1996; Roest & Srivastava, 1991; Sahabi et al., 2004; Schettino & Turco, 2009; Srivastava et al., 1990; Tortella et al., 1997; Tucholke et al., 2007) have proposed different kinematic reconstructions of the geodynamic evolution of the SW Iberian margin. These reconstructions differ in specific events, but they all agree in the evolution of the major tectonic stages, which are the following:

1. Initial stage of the opening of the Central Atlantic in the Lower Jurassic (Malod & Mauffret, 1990; Sahabi et al., 2004; Schettino & Turco, 2009).

2. Oblique rifting phases between Africa and Iberia from Late Jurassic to Lower Cretaceous (Malod & Mauffret, 1990).

3. Jumping of the plate boundary to the Pyrenees and tectonic quiescence in SW Iberia in the Upper Cretaceous (Tortella et al., 1997) until the Oligocene, when the convergence in the Pyrenean belt ceased and the AGFZ became the boundary between Africa and Iberia (Srivastava et al., 1990).

4. N-S compression and subduction of the African plate under the South Sardinian Domain, resulting in closure of the western Mediterranean and westward migration of the Internal Zones of the Betic and Rif Cordilleras (Maldonado et al., 1999).

5. Emplacement of large allochthonous units and reactivation of old extensional structures during the Tortonian when the trend of compression rotated towards NNW-SSE (Gràcia et al., 2003b; Martínez-Loriente et al., 2013, 2018; Medialdea et al., 2004; Torelli et al., 1997).

On the basis of these major tectonic stages and in comparison with new wide-angle seismic (WAS) data, Martínez-Loriente et al., (2014) proposed a more detailed framework for the geodynamic evolution of the area, describing the presence of three different oceanic domains offshore SW Iberia (Fig. 2.2): (1) the Seine Abyssal Plain (SAP) domain, underlay by Jurassic oceanic crust; (2) the Gulf of Cadiz domain, made of Jurassic-age oceanic crust (Sallarès et al., 2011); and (3) the Gorringe Bank (GB) domain, made of exhumed mantle rocks underlying the Gorringe Bank, southern Tagus and northern Horseshoe abyssal plains.

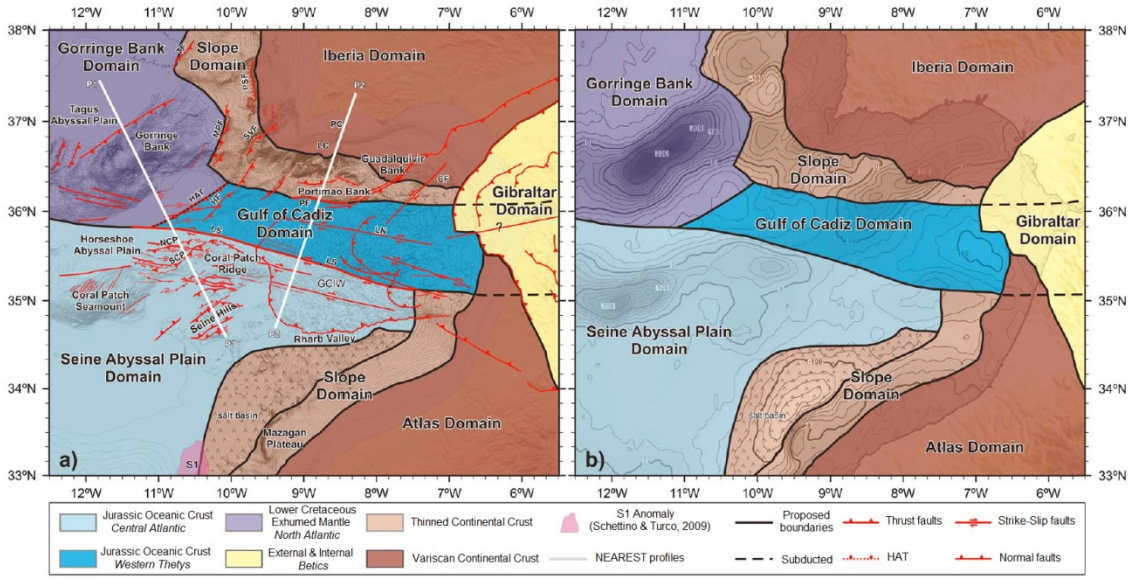


***Figure 2.2.*** *Distribution map of the different geological domains offshore the SW Iberian margin. a) Bathymetric map made with the SWIM compilation of Zitellini et al., (2009) and GEBCO digital atlas. Main tectonic structures of the region after several authors (Bartolome et*

*al., 2012; Iribarren et al., 2007; Martínez-Loriente et al., 2013; Zitellini et al., 2009). White lines labeled P1 and P2 correspond to the WAS profiles acquired during the NEAREST-SEIS survey (Sallarès et al., 2011, 2013). Purple band displays magnetic anomaly S1 (e.g. Schettino & Turco, 2009); b) Free-air anomaly map (contours each 100 mGal) (Smith & Sandwell, 1997). CF: Cadiz Fault; GCIW: Gulf of Cadiz imbricated wedge; HAT: Horseshoe Abyssal Plain Thrust; HF: Horseshoe Fault; LC: Lagos Canyon; LN: Lineament North; LS: Lineament South; MPF: Marquês de Pombal Fault; NCP: North Coral Patch Ridge Fault; PC: Portimão Canyon; PF: Portimão Fault; PSF: Pereira de Sousa Fault; SCP: South Coral Patch Ridge Fault; SVF: São Vicente Fault. From Martínez-Loriente et al., (2014).*

The newest geodynamic evolution that Martínez-Loriente et al., (2014) proposed is as follows:

**Stage 1**: During the Late Triassic, the rift system that cut Pangea from the Caribbean to the Tethys, generated rift structures in NE America (Schlische et al., 2002), S Iberia (Martin-Rojas et al., 2009), NW Africa (Le Roy & Piqué, 2001), western Morocco and especially in the Atlas region (Schettino & Turco, 2009). In the Lower Jurassic (190 Ma), the seafloor spreading centre started at the CAO (Central Atlantic Ocean) (~8 mm/yr the first 20 Ma). The rift structures became more important in northern Morocco, separating this microplate from Iberia and Newfoundland. Around 183 Ma (Fig. 2.3a) in the CAO and incipient Alpine-Tethys system, the first oceanic crust was generated and the rift in the Atlas closed (Schettino & Turco, 2009).

**Stage 2**: With the Atlas extension being inactive and the Moroccan plate fixed to NW Africa (Schettino & Turco, 2009), the deformation was transferred to the Gibraltar Fault (GiF), a transform margin which was a pre-existing plate boundary between Iberia and Morocco. Around 155 Ma, in the Upper Jurassic, the transform margin becomes an oblique seafloor-spreading system, that generated a narrow basin between Iberia and NW Africa (Schettino & Turco, 2009). At this time, the oceanic crust of SW Iberia was generated by two different but simultaneous spreading systems: a) The Central Atlantic system that now conforms the Jurassic oceanic crust of the SAP domain; and b) The Alpine-Tethys oblique-spreading system between Iberia and Africa (i.e. Western Tethys) that now conforms the Jurassic-age oceanic crust of the Gulf of Cadiz domain (Fig. 2.3b).

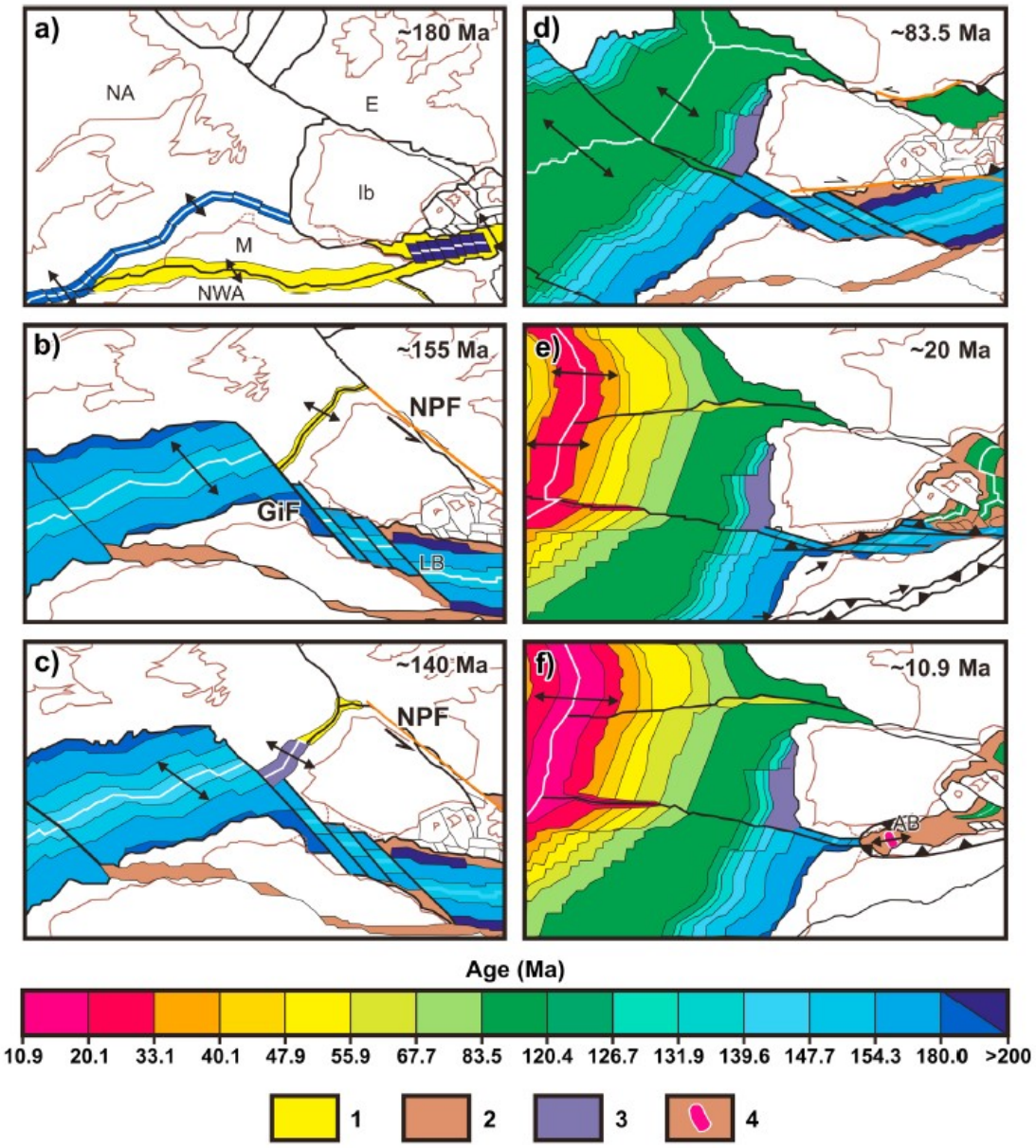


***Figure 2.3.*** *Schematic maps displaying the kinematic evolution of the African, Iberian, Eurasian and American Plates. Primarily reconstruction based on Schettino and Turco (2011), although other works (e.g. Booth-Rea et al., 2007; Labails et al., 2010; Sahabi et al., 2004; Schettino & Turco, 2009; Stampfli & Borel, 2002) have also been used. AB: Alboran Basin; E: Eurasia; GiF: Gibraltar Fault; Ib: Iberia; LB: Ligurian Basin; M: Morocco; NA: North America; NPF: North Pyrenean Fault Zone; NWA: Northwest Africa; (1) areas affected by active rifting and thinning; (2) areas with thinned crust; (3) exhumed mantle rocks; (4) active volcanic arc; transform faults are shown in orange. White lines are spreading centres. From Martínez-Loriente et al., (2014).*

**Stage 3**: In the Upper Jurassic, between 150-147.7 Ma the plate boundary jumped from the Atlantic-Tethys transfer zone to the North Pyrenean fault zone. As a result, the oblique Alpine-Tethys spreading centre stopped, and a new rift originated between North America and Iberia (Tucholke et al., 2007). During the earlier North Atlantic opening phase (until 122 Ma), the exhumed continental mantle, now underlain the GB, southern Tagus and northern Horseshoe abyssal plains and conforms the GB domain (Fig. 2.3c).

**Stage 4**: In the Lower Cretceous (120 Ma) a counter-clockwise rotation of Iberia with respect to Eurasia and Africa generated the rift of the Bay of Biscay (Sibuet et al., 2004). The rates of expansion of the CAO spreading centre dropped and the western Tethys started to subduct underneath the Eurasian margin (Schettino & Turco, 2009). In the Upper Cretaceous (83.5 Ma), the boundary between Eurasia and Iberia became convergent (i.e., beginning the Pyrenean orogeny), the Bay of Biscay rift disappeared and the transform boundary between Iberia and Morocco was inactive (Fig. 2.3d) (Schettino & Turco, 2009).

**Stage 5**: In the early Cenozoic and until the Eocene, the convergence in the Pyrenees was interrupted. At 56 Ma, the convergence was reactivated with slow rates until 33.1 Ma. The Pyrenean belt ceased to be a major plate boundary (Iberia fixed to Eurasia) and a subduction zone originated at the South and East of Iberia, where Alpine-Tethys oceanic lithosphere started to be consumed (Schettino & Turco, 2009). In the Atlantic Ocean, a ridge-ridge-transform triple junction developed and high spreading rates in respect to NW Africa, generated the reactivation of the Triassic-Jurassic Atlas rift structures as reverse faults (Beauchamp et al., 1999; Piqué et al., 2002). Around 19 Ma, the Atlas uplifted and the Alpine-Tethys extension finished (Fig. 2.3e) (Schettino & Turco, 2009).

**Stage 6**: In the Tortonian (10.9 Ma), the subduction front migrated to the west generating a slab rollback. The Alboran back-arc basin originated and large allochthonous units and gravitational units were emplaced in the Gulf of Cadiz (Laura Gómez de la Peña et al., 2020). The NW-SE trending convergence of the SW Iberian margin produced the reactivation of WNW-ESE structures of the Jurassic Alpine-Tethys systems, as well as a series of NE-SW thrust structures (Fig. 2.3f).

## 2.2. Morphology of the SW Iberian margin

The SW Iberian margin can be divided in three parts: a) the continental shelf and coastal areas, b) the external part of the Gulf of Cadiz; and c) the internal part of the Gulf of Cadiz (Martínez-Loriente et al., 2013; Tortella et al., 1997).

The external part of the Gulf of Cadiz is the region comprised between the GB and the Cape of São Vicente (CSV). This part is characterized by three deep abyssal plains bounded by large seamounts and massive ridges (i.e., NE-SW-trending structural highs), formed during the NW-SE trending compression of the latest stages of Eurasia-Africa convergence (Gràcia et al., 2003a; Gràcia et al., 2003b; Terrinha et al., 2003; Zitellini et al., 2009). The GB is by far the most prominent structure of the external part of the Gulf of Cadiz. It is a 5000 m high topographic relief (with respect to the surrounding areas) of 220 km-long and 80 km-wide (Jiménez-Munt et al., 2010). The two major elevations of the GB are the Gettysburg (20 m.b.s.l. (i.e. below sea level)) and Ormonde (30 m.b.s.l.) seamounts. The GB, together with the Hirondelle Seamount, the Infante Don Henrique slope basin (IDHB) and the Marquês de Pombal fault Block (MPB), acts as the boundary between the Tagus Abyssal Plain (TAP) at 5150 m depth to the north and the Horseshoe Abyssal Plain (HAP) at 4850 m depth to the south. The HAP is bounded to the west by the Madeira-Tore Rise, to the east by the continental slope and to the south by the Ampere and Coral Patch Seamounts (CPS) and the Coral Patch Ridge (CPR) (Lebreiro et al., 1997). The structures to the south of the HAP separate it from the Seine Abyssal Plain (SAP) at 4400 m depth. The main structure in the continental slope of the external part of the Gulf of Cadiz is the São Vicente Canyon (SVC) that links the continental shelf with the HAP. This is the largest canyon in the SW Iberian area and one of the most important canyons of the Atlantic continental margins (Fig. 2.4).

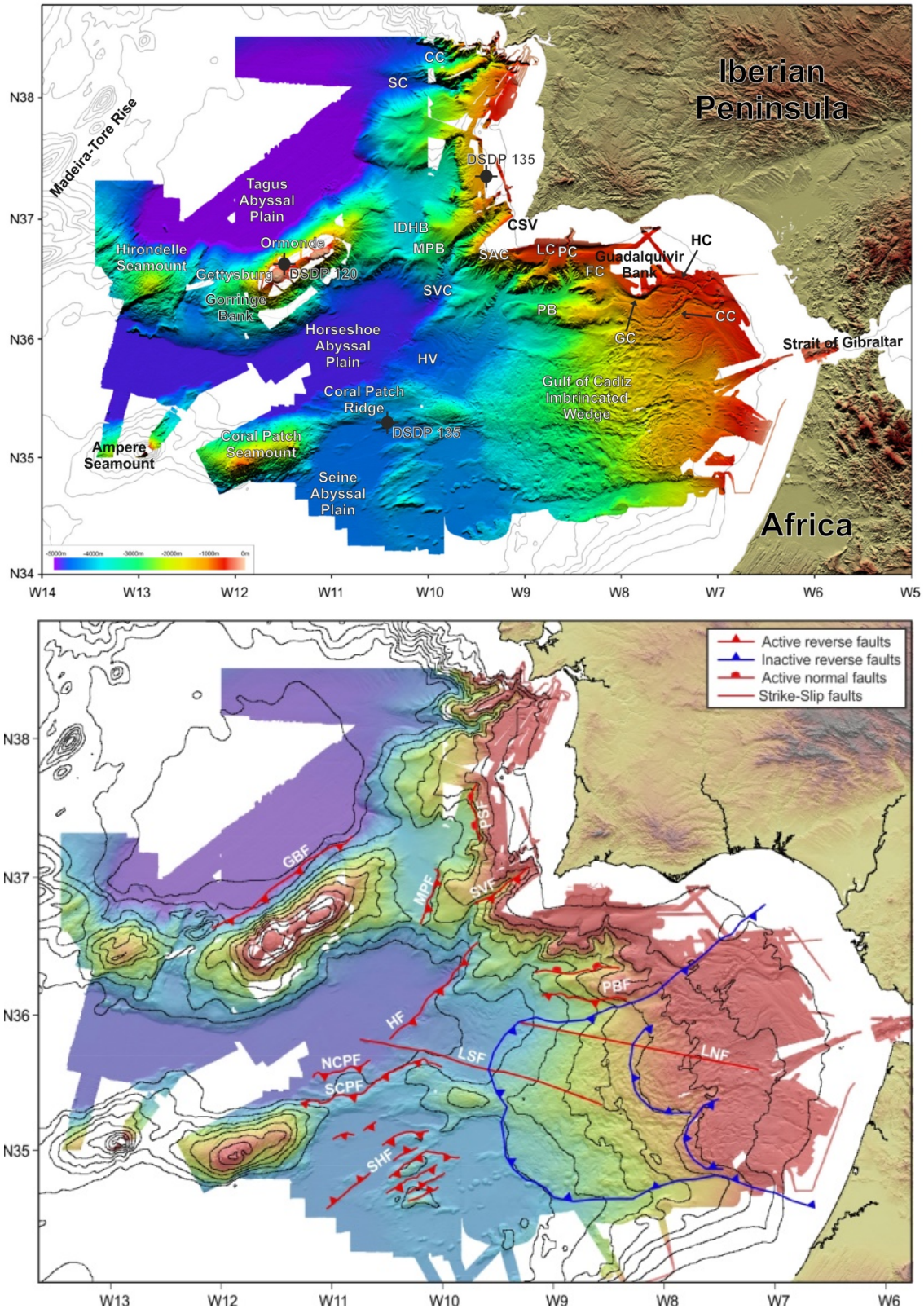


***Figure 2.4.*** *Top: Bathymetric map of the SW Iberian margin resulting from the SWIM multibeam compilation (Zitellini et al., 2009). CC: Cadiz channel; CSV: Cape São Vicente; FC: Faro canyon; GC: Guadalquivir channel; HC: Huelva channel; IDHB: Infante Don Henrique Basin; LC: Lagos canyon; MPB: Marques de Pombal Fault Block; PB: Portimão Bank; PC:*

*Portimão canyon; SC: Sagres canyon; SVC: São Vicente Canyon (Gràcia et al., 2003a; Hernández-Molina et al., 2003; Zitellini et al., 2009). Bottom: Tectonic map derived from the swath bathymetry (Zitellini et al., 2009) and main fault systems after Martínez-Loriente et al., (2013, 2018). GBF: Gorringe Bank Fault; HF: Horseshoe Fault; LNF: Lineament North Fault; LSF: Lineament South Fault; MPF: Marquês de Pombal Fault; NCPF: North Coral Patch Fault; PBF: Portimão Bank Fault; PSF: Pereira da Sousa Fault; SCPF: South Coral Patch Fault; SHF: Seine Hills Faults; SVF: São Vicente Fault.*

The internal part of the Gulf of Cadiz is the region comprised between the CSV and the Straits of Gibraltar (Fig. 2.4). Between the CSV and the Guadalquivir Bank (GuB), the Gulf of Cadiz is characterized by two complex drainage systems. The north-south drainage system consists of an organized network of gullies and submarine canyons (Terrinha et al., 2009), such as the Sagres canyon (SC), the Lagos canyon (LC), the Portimão canyon (PC) and the Faro canyon (FC). The east-west drainage system (i.e. the inner part of the Gulf of Cadiz drains toward the Atlantic Ocean) consists in valleys (e.g. Horseshoe valley) and channels (e.g. Huelva channel, Cadiz channel and Guadalquivir channel) produced by the erosion and sedimentation related to bottom currents, in this case the MOW (Mediterranean Outflow Water) and downslope associated gravity processes (Hernández-Molina et al., 2003; Terrinha et al., 2009). In this part of the Gulf of Cadiz, there are two main promontories, the Portimão Bank (PB) and the GuB (Fig. 2.4), which are morphological expressions of a Mesozoic horst inverted during the Neogene compressional stage (Gràcia et al., 2003b). Large sub-surface diapiric processes are important morphological elements in the PB.

The most characteristic morphological element in the internal part of the Gulf of Cadiz is the Gulf of Cadiz Imbricated Wedge (GCIW) (e.g. Iribarren et al., 2007) or also referred as the Gulf of Cadiz Accretionary Wedge (e.g. Gutscher et al., 2002). The GCIW is defined as a west-dipping U-shaped body that extends over the Gulf of Cadiz with 300 km-length, 200 km-width and depths ranging from 200 m to 4300 m (Duarte et al., 2011; Gràcia et al., 2003b; Iribarren et al., 2007; Torelli et al., 1997). The GCIW occupies about 58000 $km^2$ in the NW Africa and SW Iberia margins (Iribarren et al., 2007). During the Neogene convergence allochthonous units in front of the GCIW, such as the Horseshoe Gravitational Unit (HGU) (a massive and rapid succession of large submarine landslides) were emplaced (Gràcia et al., 2003b; Iribarren et al., 2007; Maldonado et al., 1999; Torelli et al., 1997). The GCIW contains a number of elements and associated morphologies related to fluid flow, such as salt diapirs, subsurface fluid

migration structures, pockmarks, mud volcanoes, gas hydrates and free gas (e.g. Hensen et al., 2015; Pinheiro et al., 2003; Somoza et al., 2002).

### *2.2.1. Continental shelves and coastal areas*

The geodynamic evolution and the coastal hydrodynamic processes (i.e. waves, currents and tides) have configured the continental shelf and the coastal morphologies of the SW Iberian and NW Moroccan margins.

#### *2.2.1.1 SW Iberia*

The physiography of the South-West Iberian margin is characterized by a 600 km-long and an average of 40 km-width shelf (Lobo et al., 2014). Furthermore, the presence of numerous submarine canyons on the slope, such as, the Cascais canyon (CC), Setúbal canyon (SC), SVC, LC, PC and FC is relevant. These canyons act as a sediment corridor between the continental shelf and abyssal plains (Gaudin et al., 2006; Serra et al., 2020) (Fig. 2.4).

The SW Iberian costal area can be divided in four sections: a) the Lisbon section; b) the Algarve section; c) the Huelva section and d) the Cadiz section (Benavente et al., 2015; Lobo et al., 2014) (Fig. 2.5). The Lisbon section is a 200 km-long, N-S trending coastal stretch between Lisbon and the CSV. The coast in **the Lisbon section** is characterized by cliffs and interrupted by few narrow beaches, with the exception on the coastal areas of the Tagus and Sado estuaries and the Santo André coastal Lagoon, where low topography, sandy beaches and sand barriers predominate (Ramos-Pereira et al., 2005). In this section, the width of the continental shelf is narrowest at the Cape Espichel and CSV (about 7-9 km), and increases towards the Sines area where the continental shelf reaches widths up to 50 km. The shelf break is located at 130 m water depth and the slope average is about 0.4º. **The Algarve section** is a 150 km-long, W-E trending coastal stretch between the CSV and Guadiana River, where Mesozoic rocky cliffs are progressively substituted to the East by unconsolidated Miocene formations, where sandy beaches predominate (Stanley, 1982). The area is locally interrupted by small fluvio-estuarine systems (Lobo et al., 2014). The continental shelf of the Algarve section shows significant width variability, with a minimum of 7 km in the Faro area and about 25 km elsewhere. The Algarve continental shelf has an average slope of 0.4º and a maximum value up to 1.5º (Roque, 1998), while the shelf-break is located at water depths of 110-150 m. **The Huelva section** is a 100 km-long, WNW-ESE treading coastal stretch, between the Guadiana and Guadalquivir rivers, where low relief sandy

coasts, marshes and sand barriers predominate (Lobo et al., 2014). In this section, the continental shelf increases progressively in width from 25 km to 40 km from West to East. The slope of the shelf is relatively constant around 0.2º-0.3º and the shelf break is located at water depths of 130 m (Maldonado et al., 2003). **The Cadiz section** is 150 km-long, NNW-SSE trending, extending from the Guadalquivir River to the Straits of Gibraltar, where extensive low-relief beaches are interrupted by small cliffs and promontories (Benavente et al., 2015). The average shelf width in this section is 35 km and progressively decreases towards the Straits of Gibraltar to 15 km. The shelf gradient is around 0.2º while the shelf break is located at water depths of 120-140 m and 100 m near the Straits of Gibraltar (Maldonado et al., 2003).

#### *2.2.1.2. NW Morocco*

The Atlantic Moroccan margin is a 530 km-long shelf with a mean width of 45 km. The coastal area can be divided in three sections: a) the western Rif section; b) the Rharb section, and c) the Meseta section (Fig. 2.5). **The western Rif section** is 110 km-long and NNE-SSW trending, extending between the city of Moulay-Bouselham and the Straits of Gibraltar. The northern half of the section is composed by abrupt cliffs while the southern half is dominated by sandy beaches and large sand dunes. In this section, the continental shelf is 25-30 km wide, the slope is < 1º and the shelf break is located at 150 m depth (Lobo et al., 2014). **The Rharb section** is 120 km-long, NNE-SSW trending section, which extends from the city of Moulay-Bouselham to Rabat, where low coasts with dune complexes and marshes predominate. The Rharb section is characterized by a 20-35 km-wide and 0,5º dipping shelf with the shelf-break located at 120-150 m depth (Lobo et al., 2014). **The Meseta section** is 310 km-long, NE-SW trending and extends between Safi and Rabat. In the northern part of the section low cliff, narrow beaches and massive sand dunes predominate. In the southern part until Safi, the coastline is surrounded by cliffs (Lobo et al., 2014; Scheffers, 2010). The Meseta shelf is 40 km wide, dipping 0.1º-0.6º and the shelf break is located at 150 m depth (Ruellan, 1985).

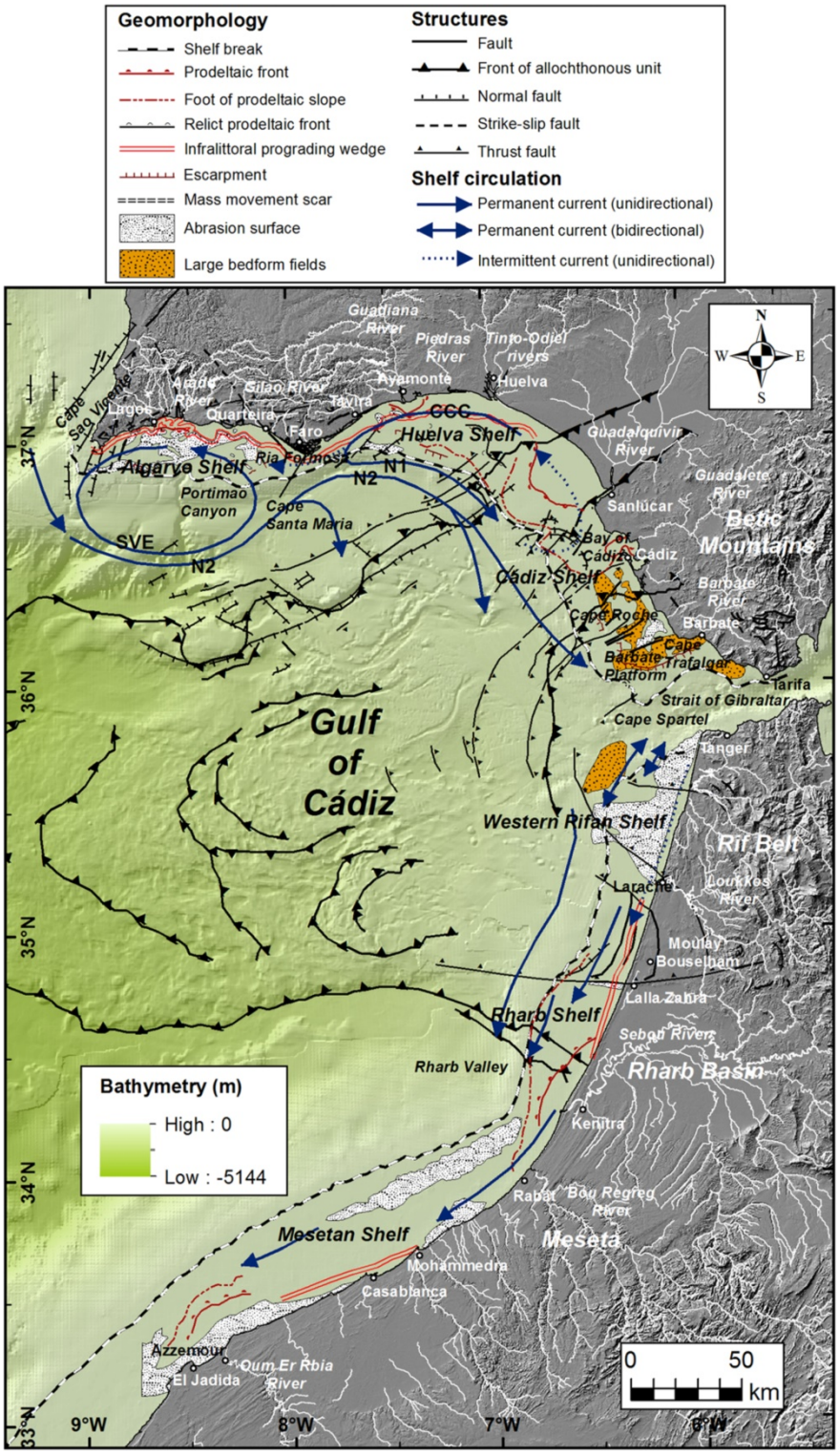


***Figure 2.5.*** *Shelf geomorphology and current patterns of the Gulf of Cadiz. Tectonic features are synthesized from several sources: Gràcia et al., (2003a); Maad et al., (2010); Medialdea et al., (2009). Shallow circulation information modified from García-Lafuente et al., (2006). N1: shelf-break (Huelva) front; N2: branch of the Portuguese–Canary Eastern Boundary Current; SVE: cyclonic eddy off Cape São Vicente; CCC: coastal counter-current. From Lobo et al., (2014).*

## 2.3. Main geological structures

As a result of the Neogene collision, Mesozoic extensional faults were reactivated and new fault systems appeared in weakened areas. There are two main families of active faults that will be described in this study: a) NE-SW trending reverse faults, such as the Gorringe Bank fault (GBF), the Marquês de Pombal fault (MPF), the Horseshoe fault (HF), the North Coral Patch fault (NCPF), the South Coral Patch fault (SCPF) and the Seine Hills faults (SHF); and b) WNW-ESE trending dextral strike-slip faults, such as the Lineament South (LSF) and the Lineament North (LNF). In addition, the Pereira de Souza normal fault will also be described.

### *2.3.1. The Pereira de Souza Fault*

The Pereira de Souza fault (PSF) is a west-dipping, N-S trending, 70 km-long extensional fault. This fault cuts the basement and the sedimentary sequence above until the seafloor forming a 1800 m high prominent scarpment (Cunha et al., 2009; Gràcia et al., 2003a; Terrinha et al., 2003). The PSF (Fig. 2.6) originated during the Mesozoic rifting and segmentation phases of the SW Iberian margin, creating accommodation space until the Plio-Quaternary (Cunha et al., 2009). The activity of the fault is evidenced by the well-developed fault scarp with prominent active gullies along the crest and the presence of levee-type deposits, that can be recognized along the footwall for a length of 20 km (Terrinha et al., 2003).

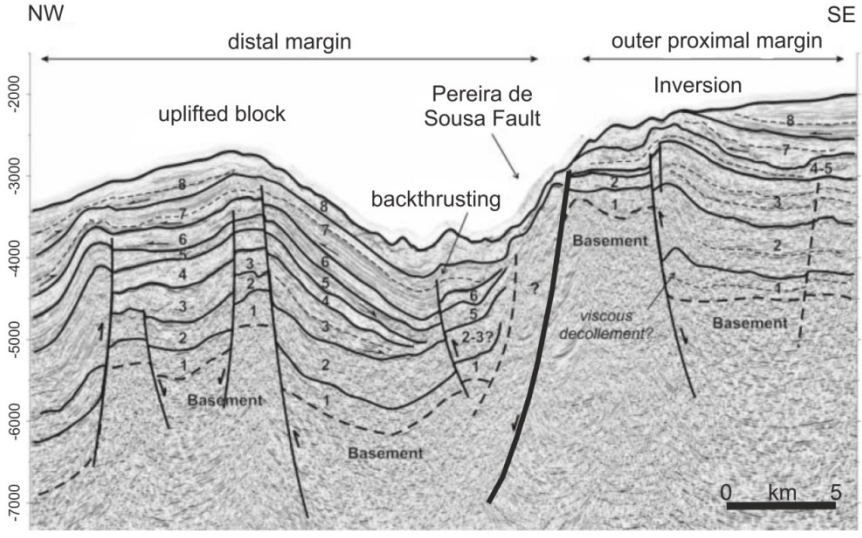


***Figure 2.6.*** *Multichannel seismic profile across the Pereira de Souza fault (PSF). 1: Late Triassic; 2: Early-Middle Jurassic; 3: Late Jurassic; 4: Early Cretaceous, 5: Early-Late Cretaceous, 6: Paleocene- Middle Eocene; 7: Middle Eocene-Oligocene; Miocene-PlioQuaternary. Modified from Pereira & Alves, (2011).*

In addition, the middle Miocene compressional phase deformed the hanging-wall of the PSF (Gràcia et al., 2003a) and a discreet uplift of the footwall resulted in the formation of minor reverse faults and a small local backthrust (Pereira & Alves, 2011) (Fig. 2.6).

### *2.3.2. The Portimão and Guadalquivir Bank faults*

The PB is an E-W asymmetric and elongated 93 km-long and 20 km wide relief, that deepens westward from 1400 m to 3400 m water depth (Silva et al., 2020). The PB is the natural continuity of the 28 km-long, 12 km-wide GuB that outcrops on the seafloor at 550 m depth (Fig. 2.4). The GuB is made up of Variscan metamorphic flysch and shows a strong positive, up to 130 mGal, gravimetric anomaly (Gràcia et al., 2003a). The PB is interpreted as a pop-up structure bounded by two E-W trending reverse faults. The northern fault of the PB links with the southern part of the Guadalquivir Bank, as well as the Guadalquivir Bank Fault (GuBF) (Fig. 2.7).

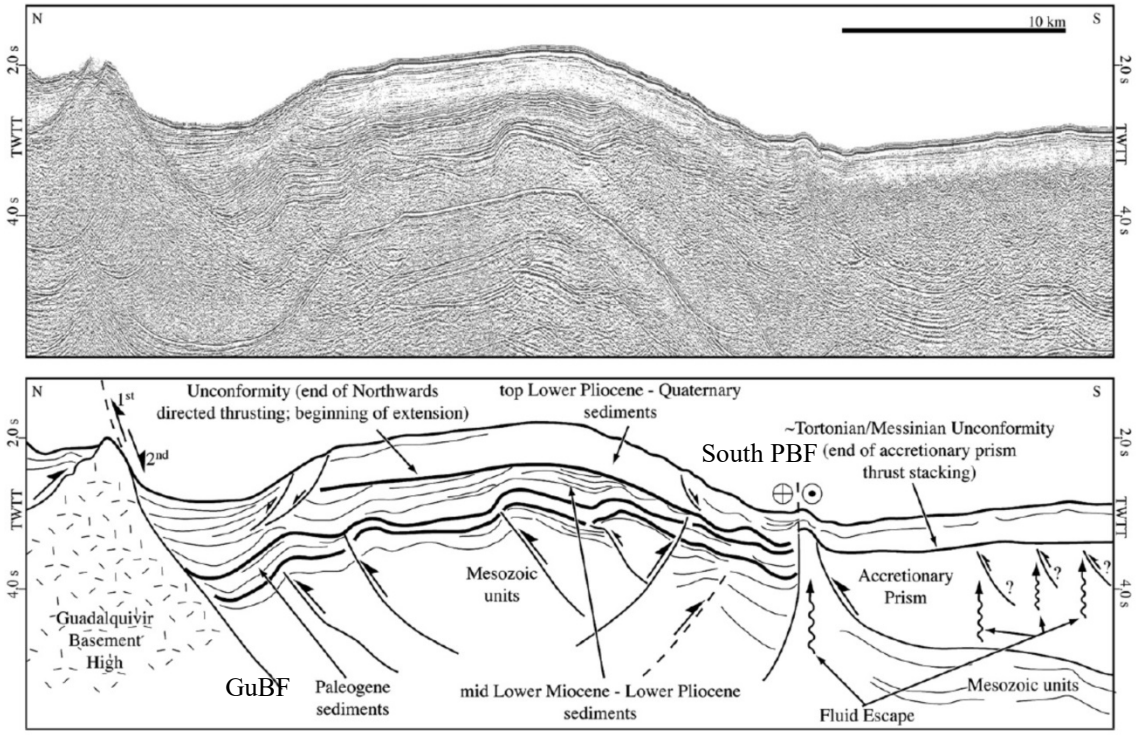


***Figure 2.7.*** *Uninterpreted multichannel seismic profile (VOLTAIRE 3) and line-drawing of the Guadalquivir Basement High and Portimão Bank faults (GuBF: Guadalquivir Bank Fault; South PBF: South Portimão Bank Fault). From Terrinha et al., (2009).*

During the Mesozoic rifting processes, the PB evolved as a graben structure, bounded by two E-W extensional faults, which were reactivated as a pop-up structure during the Neogene convergent stage (Gràcia et al., 2003a; Silva et al., 2020; Terrinha

et al., 2009). The drag of the uppermost sedimentary sequence and the presence of gravitational extensional faults, indicate that the northern boundary of the PB is experimenting local extension related to a releasing-bend generated by the basement fault (Terrinha et al., 2009). The southern fault of PB (PBF) is experimenting dextral transpressive strike-slip deformation since Early Pliocene times (Terrinha et al., 2009).

### *2.3.3. The Gulf of Cadiz Imbricated Wedge*

The GCIW is defined as a tectonic imbricated unit of the Betics and Rift belts of Alpine Orogeny above a basal detachment that climbs up above a low-angle footwall, with wedge geometry and radial tectonic transport (Gràcia et al., 2003b; Iribarren et al., 2007; Medialdea et al., 2004; Tortella et al., 1997) (Fig. 2.8). The GCIW is a 14-15 km thick seismically chaotic body. Its surface is irregular and covered by mud volcanos and salt diapirs (Duarte et al., 2011; Iribarren et al., 2007). According to observations and the correlation with the Betic and Rift outcrops, Iribarren et al., (2007) proposed that the GCIW is mainly composed of Triassic evaporites and a succession of Jurassic to Middle Miocene sedimentary rocks, as documented for the allochthonous units at the front of the Betic Cordillera. The origin and activity of the GCIW is presently debated. On the one hand, Duarte et al., (2011); Gutscher et al., (2002); Lonergan & White, (1997); Maldonado et al., (1999); Royden, (1993), considered the GCIW as an accretionary wedge originated in a plate boundary dominated by active roll-back subduction of an east-dipping lithospheric slab, nowadays positioned beneath the Gibraltar Arc. In addition, Duarte et al., (2011) and Gutscher et al., (2002) proposed that the roll-back subduction is still active and may be the source of the 1755 Lisbon Earthquake. However, the presence of a sedimentary sequence, from Plio-Quaternary to Tortonian age, sealing the structure (Betancourt et al., 2015; Gràcia et al., 2003; Iribarren et al., 2007; Zitellini et al., 2009), absence of significant seismic activity and lack of volcanic activity (Stich et al., 2005) rule-out this hypothesis.

On the other hand, the most accepted hypothesis considers that the GCIW is as an allochthonous body tectonically emplaced by the westward migration of the Gibraltar Arc, which occurred in the upper Miocene (Betancourt et al., 2015; Gràcia et al., 2003; Eulàlia Gràcia et al., 2003; Iribarren et al., 2007; Medialdea et al., 2004; Torelli et al., 1997; Tortella et al., 1997). The rapid growth of the GCIW could may generate numerous slope instabilities and slope failures producing large submarine gravitational deposits, such as the HGU in the HAP (Iribarren et al., 2007).

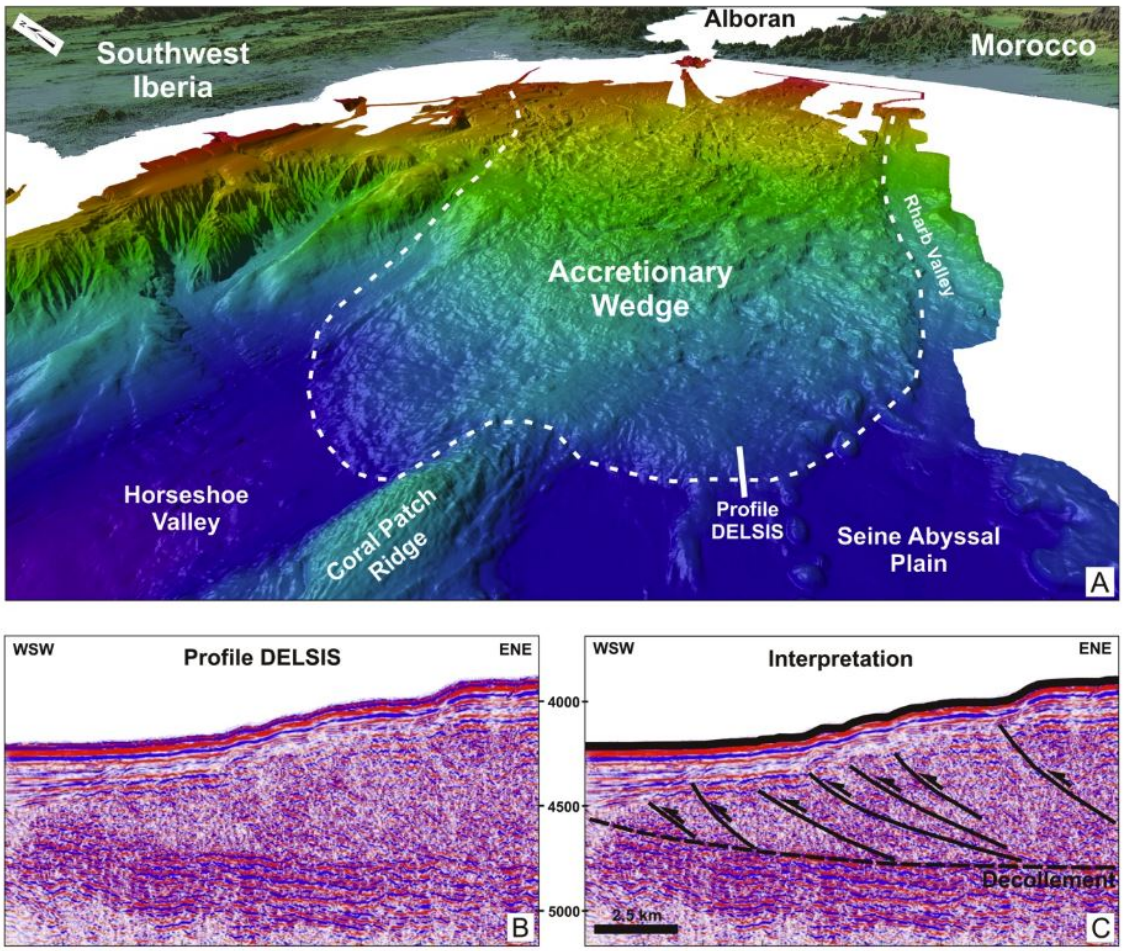


***Figure 2.8.*** *a) Southwest perspective view from the Gulf of Cadiz Imbricated Wedge (GCIW); b) DELSIS Multichannel seismic profile (MCS) along the front of the accretionary wedge; and c) Fault interpretation and basal decollement that separates the upper and lower units. From Duarte et al., (2011).*

### *2.3.4. The Gorringe Bank Fault*

The GB is, by far, the most prominent structure of the Gulf of Cadiz (Jiménez-Munt et al., 2010). The GBF is a 155 km-long, NW-verging thrust fault located in between the TAP and the HAP plains (Fig. 2.9). This large thrust fault of the north-western segment of the HAP, overthrusts the TAP for 4-5 km (Sallarès et al., 2013; Sartori et al., 1994; Tortella et al., 1997) and uplift the seafloor from 5000 m up to 24 m depth (Terrinha et al., 2009). The GB is characterized by a 9 m-high geoid anomaly, 120 mGal Bouguer anomaly (Jiménez-Munt et al., 2010) and ~300 mGal free-air gravity anomaly (Sallarès et al., 2013). On the basis of the DSDP Site 120 drilled at the Gorringe Bank (Ryan et al., 1973), it was evidenced that the GB is a massive exhumed mantle ridge composed by serpentinized peridotites with gabbroic intrusions and few tholeiitic extrusions (Auzende et al., 1978; Girardeau et al., 1998; Ryan et al., 1973). The different degree of

tectonic deformation that affects the GB is evidenced by the asymmetric steepness of the flanks, i.e. the northern flank is steeper than the southern, and hence, the tectonic deformation is more intense in the northern side (Terrinha et al., 2009).

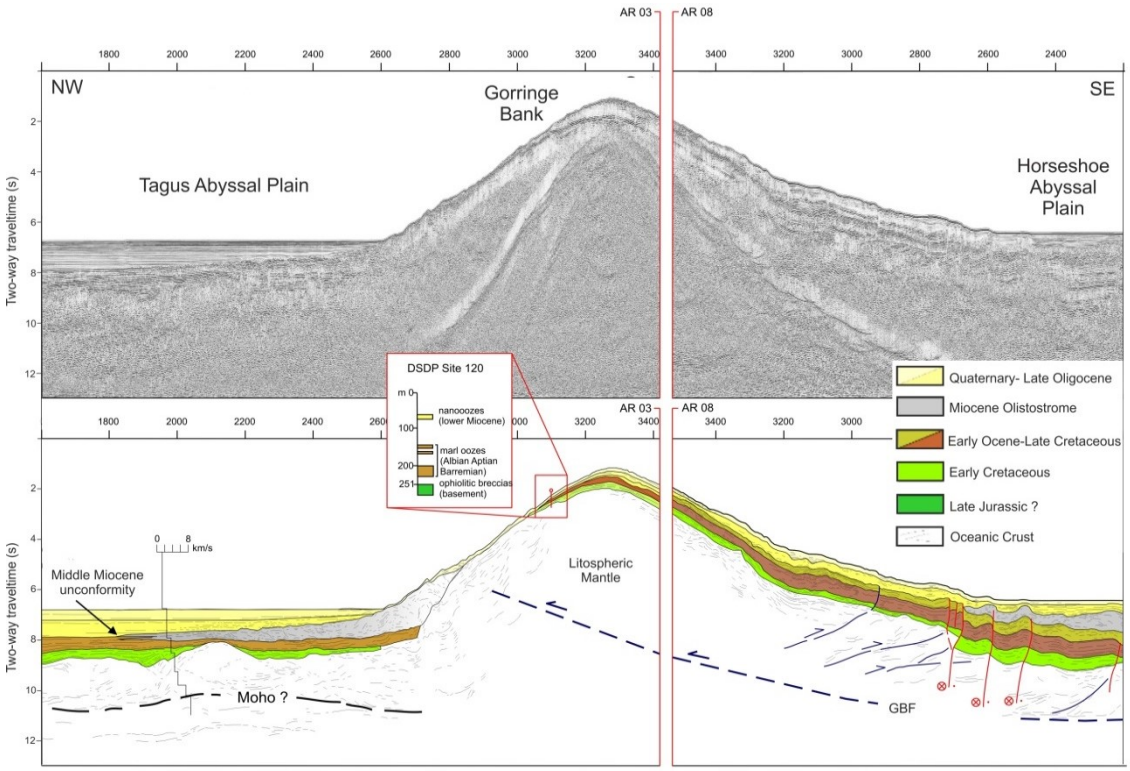


***Figure 2.9.*** *Section of the seismic reflection profile IAM-4 and schematic interpretation of the present-day structure of the Gorringe Bank Fault (GBF). Modified from Sartori et al., (1994) and Zitellini et al., (2009).*

Despite all the studies, there is a debate on the nature and origin of the GB and surrounding areas. Some authors consider it as a magmatically-intruded mantle block exhumed by tectonic mantle denudation (Jiménez-Munt et al., 2010). Sartori et al., (1994) and Tortella et al., (1997) consider it as an oceanic crust block, while others proposed that the GB corresponds to exhumed continental mantle rocks of a continent-ocean transition (COT) zone (Rovere et al., 2004) or to lithosphere from an ultra-slow oceanic spreading centre (Girardeau et al., 1998; Srivastava et al., 1990). Nowadays, the most accepted theory is the one proposed by the latest studies of Sallarès et al., (2013). Based on WAS data as well as gravity and velocity models, Sallarès et al., (2013) consider that the GB and adjacent segments of the HAP and TAP are mainly made of serpentinized peridotites (Fig. 2.10). In addition, the GB is part of a 150-180 km band of exhumed mantle rocks originated during the earliest phase of North-Atlantic opening, in the Earliest Cretaceous (147-133 Ma) constituting the oldest section of the West Iberian

margin COT. This configuration remained tectonically stable until the Oligocene-Early Miocene, when in response to the NW-SE trending convergence between Eurasia and Africa, large-scale thrusting developed and the GB was uplifted. The geometry of the fault is not clear in the seismic profiles due to the high degree of fracturing and consequent alteration (i.e., serpentinization) of the exhumed mantle that conforms the basement, but there is indirect evidence on the velocity models of a SE-dipping, low velocity-high serpentinization zone (Sallarès et al., 2013) (Fig. 2.10). The present-day activity of the GBF is also evidenced by the slight deformation of the Plio-Quaternary sediments associated to the main thrust (Sartori et al., 1994) and the seismic cluster associated with this structure (Silva et al., 2017). Fukao, (1973) and Gjevik et al., (1997) proposed the GBF as a possible tectonic source of the 1755 Lisbon Earthquake.

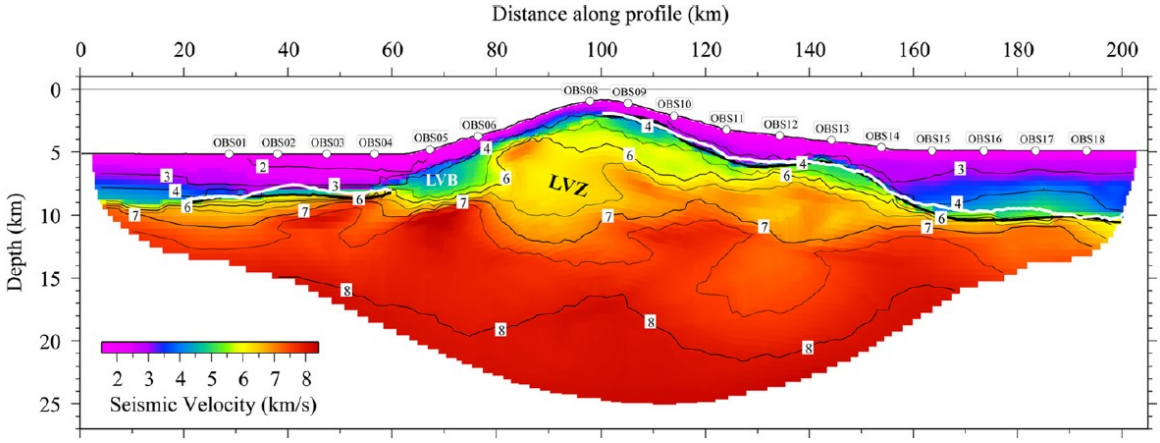


***Figure 2.10.*** *2D final velocity model obtained by inversion of arrival times of Ps (phases refracted within the sediments), PsP (sediment–basement reflections), Pb (phases refracted within the basement) phases. Thick solid black line displays the inverted sediment–basement boundary. White line corresponds to the horizon interpreted to be the base of the Mesozoic sediments along MCS profiles AR03-08 (Zitellini et al., 2009). White circles indicate OBS locations. LVZ: Low-velocity zone; LVB: Low-velocity body/olistostrome. From Sallarès et al., (2013).*

### *2.3.5. The Marquês de Pombal Fault*

The MPF is a 55 km-long, NE-SW trending, west-verging monocline thrust (Gràcia et al., 2003a; Terrinha et al., 2003; Zitellini et al., 2001, 2004), located about ~ 100 km to the west of CSV (Fig. 2.11). One of the most striking features of the MPF is the 1-km-high offset of the N20º-trending escarpment (Gràcia et al., 2003a; Zitellini et al., 2001) (Fig. 2.11). The northern and southern tips of the MPF are blind thrusts (Fig.

2.12). The MPF is the boundary between the MPB and the IDHB. At the northern sector of the MPB the maximum slope is of 23º, while at the southern sector the maximal slope is of 12º (Zitellini et al., 2001). The hanging-wall of the MPF shows an irregular upper surface due to abundant slope failures (Vizcaino et al., 2006) (Fig. 2.11). They may reach more than 20 km of runout and are likely triggered by the seismic activity associated to the fault system (Ford et al., 2021; Gràcia et al., 2003; Terrinha et al., 2003; Vizcaino et al., 2006). The style of deformation in the northern and southern parts of the MPF are different. This is corroborated by the strike of the escarpment that slightly changes in the southern part, where is more irregular and the slope is gentle (Gràcia et al., 2003a; Terrinha et al., 2003; Zitellini et al., 2004) (Fig. 2.11). It is possible to identify two scarps (Fig. 2.11), which are linked by a curved scarp, and may be associated with a restraining bend between the two fault segments (Terrinha et al., 2003). The morphological expression and trend of the thrust fault are related to the tectonic evolution of the pre-existing Mesozoic N-S trending rifting fault and its reactivation since the Middle Miocene to the present-day. The faulting and some folds affect the whole sedimentary sequence, including the Holocene sediments, which indicates present-day tectonic activity. The MPF has been proposed as the source structure of the 1755 Lisbon earthquake by several authors, such as Baptista et al., (1998) and Zitellini et al., (2001). However, the dimensions of the fault are too small to generate an earthquake of magnitude $M_w \geq 8.5$. For these reasons some authors, such as (Gràcia et al., 2003b) and Terrinha et al., (2003) proposed a complex rupture of the MPF together with the HF or the PSF.

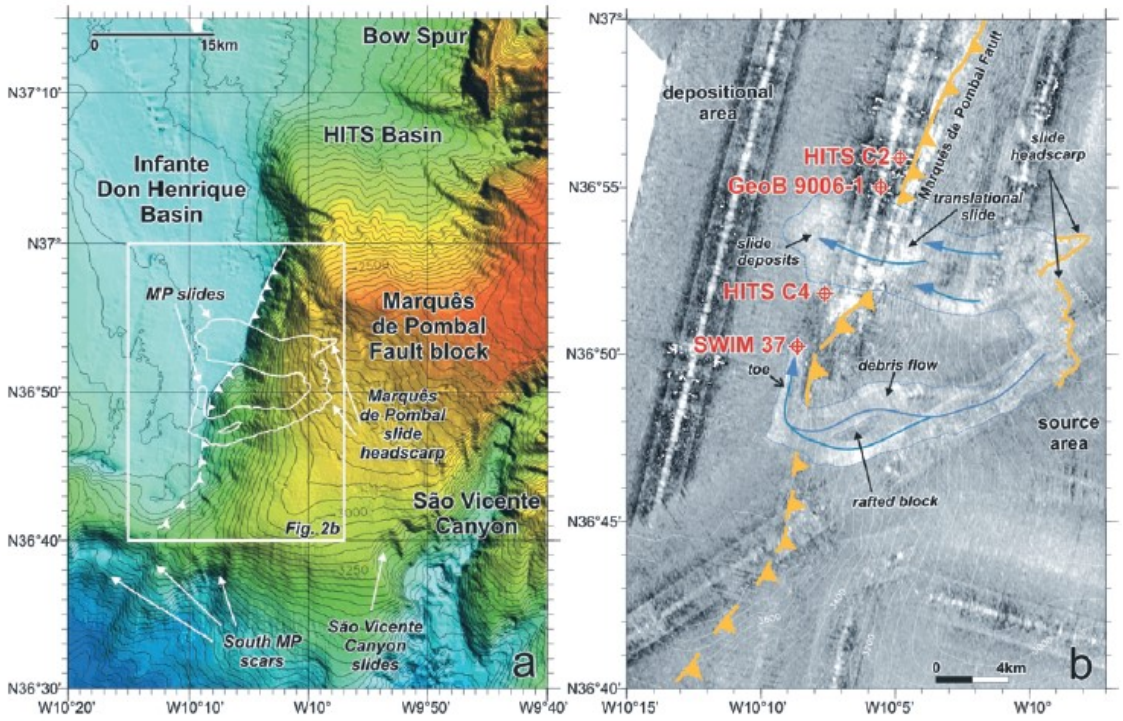


***Figure 2.11***. *a) Shaded-relief bathymetric map of the Marquês de Pombal fault displaying recent slope failure activity on the fault hanging-wall block. Contour interval is 50m. b) Interpreted acoustic-backscatter map. Sediment cores depicted in red. From Vizcaino et al., (2006).*

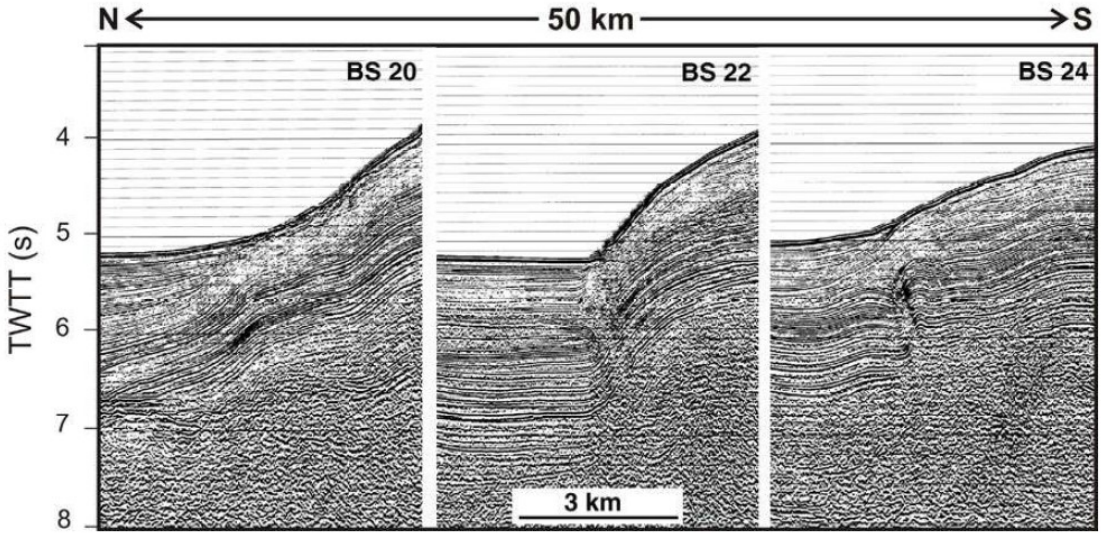


***Figure 2.12.*** *Multichannel seismic profiles after post-stack time-migration across the Marquês the Pombal Fault. The seismic profile BS20 is located in the northern sector of the fault, the profile BS22 is located in the central part of the fault, and the profile BS24 is located in the southern part of the fault. At both ends the fault deforms the shallower reflectors, while in the central section (BS22), the fault reaches the seafloor. Modified from Zitellini et al., (2001) in Martínez-Loriente, (2013).*

### *2.3.6. The São Vicente Fault*

The São Vicente fault (SVF) is a poorly-studied thrust-fault, mainly due to the lack of good-quality seismic profiles and the complex situation of the fault, hard to identify as it occurs on the flank of the syncline where the SVC develops (Gràcia et al., 2003a; Vizcaino et al., 2006). The SVF is a NE-SW trending and south-east dipping steep fault that reaches the seafloor along the northern section of the SVC (Gràcia et al., 2003a; Terrinha et al., 2003; Zitellini et al., 2001). On one hand, authors, such as Gràcia et al., (2003a) and Vizcaino et al., (2006) describe the SVF as the NNW extension of the HF. The SVF corresponds to a thrust-system, which together with the MPF, deforms a 100-km-wide region in the SW continental Iberian margin (Gràcia et al., 2003a). On the other hand, Terrinha et al., (2003) and Alves et al., (2003) related the SVF with the offshore prolongation of the left-lateral Variscan Odemira–Ávila fault (also known as the Messejana fault). The cluster of seismicity along the fault trend (Silva et al., 2017) suggest that the SVF is currently active.

In contrast with the previously described, Pereira & Alves, (2013) considered that the SVF is a N-S normal fault coinciding with the easternmost end of the Odemira-Ávila fault. The authors link the origin of the SVF with the transtension and oblique continental-rift during the Mesozoic. These authors consider that the area acts as a left-lateral releasing–restraining bend from the Late Cretaceous.

### *2.3.7. The Horseshoe Fault*

The HF is a ~100 km-long, NW-verging, east-dipping, anticline thrust-fault that separates the Horseshoe Valley from the HAP (Fig. 2.13). The anticline is characterized by a long back-limb that dips less than the fault-ramp, and by a narrow and steep forelimb, which may be generated by shear fault-bend folding (Martínez-Loriente et al., 2018). The fault trace extends from the WNW-ESE strike-slip LSF to the southern termination of the SVC (Gràcia et al., 2003a; Martínez-Loriente et al., 2018; Terrinha et al., 2009; Zitellini et al., 2001, 2004) and it is cut by WNW-ESE strike-slip faults (Terrinha et al., 2009) (Fig. 2.13). The average fault-dip is high in the first kms below the seafloor (~ 40º) and decreases to ~ 25º until the basement where it becomes listric (Martínez-Loriente et al., 2018; Zitellini et al., 2001). Martínez-Loriente et al., (2018) suggested that in the central and southern segments, the HF is rooted at the Moho (i.e., at about 9 km below the seafloor) or in the base of the serpentinized area in the uppermost mantle (i.e., about 14 km below the seafloor), while the northern segment is

rooted in the upper (18 km below the seafloor) or lower thinned crust (23 km below the seafloor). The HF displaces the late HGU "giant chaotic body" (Gràcia et al., 2003b; Iribarren et al., 2007; Torelli et al., 1997) and reaches up to the seafloor, affecting the whole sedimentary sequence evidenced by the growth-strata configuration and the generation of the Horseshoe fault scarp (Fig. 2.14). The HF scarp is characterized by a N55 E-trending relief of more than 1 km, which is well developed on the northern segment of the fault and is being eroded on its southern part by the E-W drainage system from the Horseshoe Valley (Fig 2.4) (Gràcia et al., 2003b; Terrinha et al., 2009; Zitellini et al., 2004). The low relief and the minor uplift in the southern segment, where the offset between the footwall and hanging-wall is less than in the central segment, suggest that the fault ends towards the LSF, where the deformation is transferred (Martínez-Loriente et al., 2018). Several authors (e.g. Gràcia et al., 2003b; Terrinha et al., 2009; Zitellini et al., 2004), describe the fault as an active system. Martínez-Loriente et al., (2018) calculated the Plio-Quaternary slip-rate, which is about 0.2 ± 0.01 mm/yr with a recurrence interval of about 6855 ± 250 years. In addition, ultra-high resolution subbottom profiles reveal a succession of mass-transport deposits (MTD) on the HF footwall, reinforcing the idea that the fault is presently active (Martínez-Loriente et al., 2018). The HF has been considered as a reactivated Mesozoic rifting structure (Gràcia et al., 2003b; Martínez-Loriente et al., 2018; Terrinha et al., 2009). Some authors proposed that the Horseshoe fault, simultaneously acted together with the MPF as a possible source of the 1755 Lisbon earthquake and tsunami (Gràcia et al., 2003a, b; Terrinha et al., 2003).

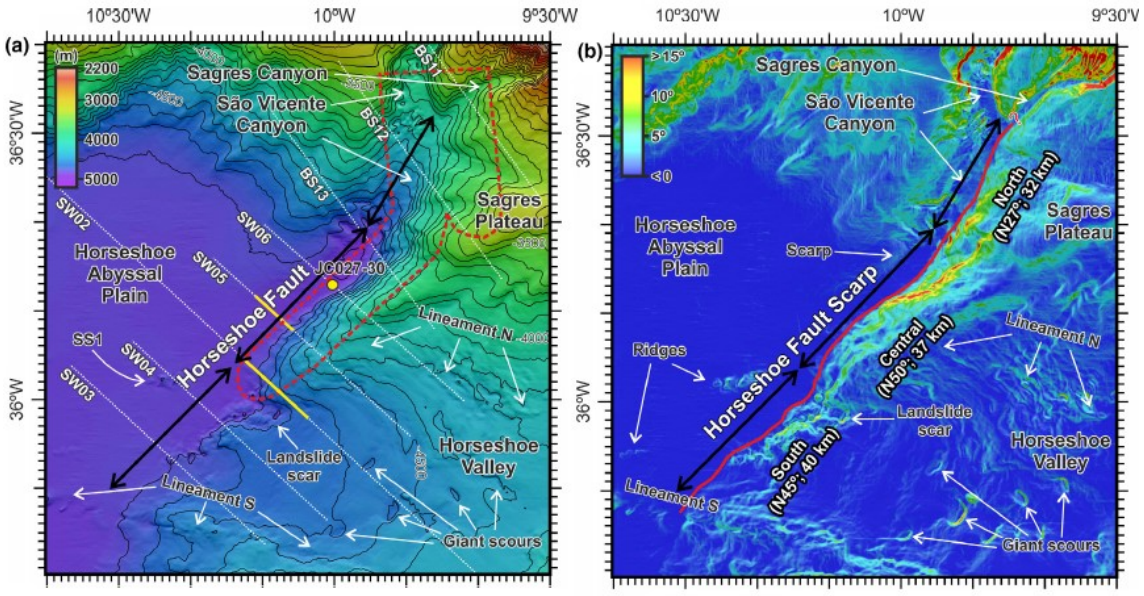


***Figure 2.13.*** *a) Colour-relief bathymetric map of the HF area. Contour interval is 100 m.*

*Multichannel seismic profiles are depicted as thin white dashed lines. Yellow dot: sediment core JC027-30. Red dashed polygon: TOBI sidescan sonar imaging. b) Slope map of the HF area. HF trace depicted in red. Modified from Martínez-Loriente et al., (2018).*

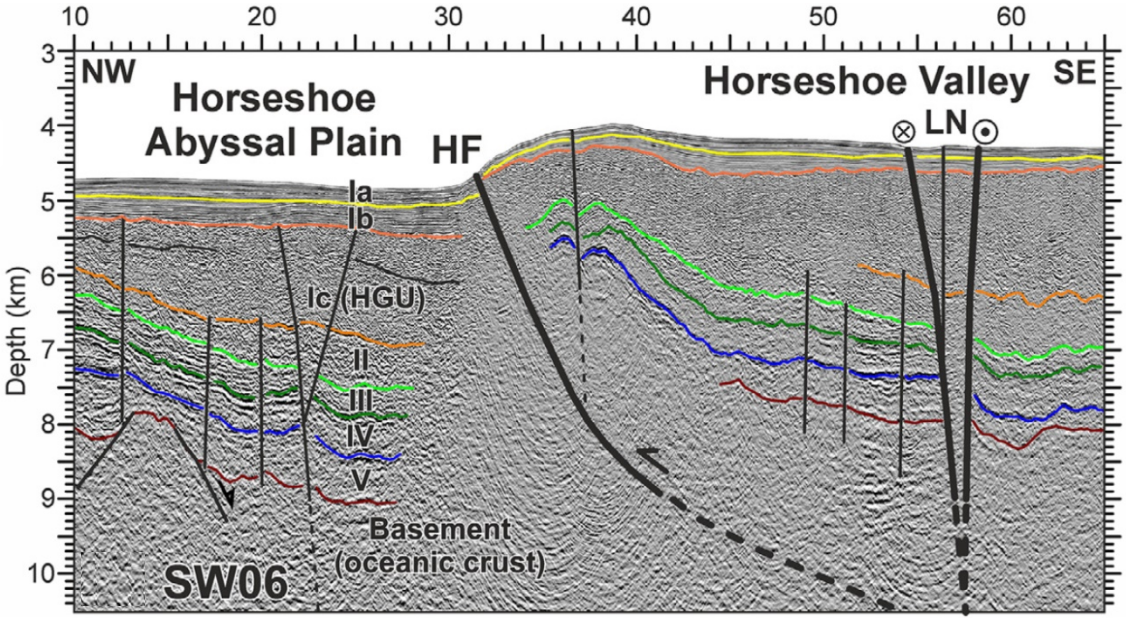


***Figure 2.14.*** *Interpreted pre-stack depth migrated SW06 seismic profile across the HF. Location of the seismic line is shown in the Fig. 2.13. Modified from Martínez-Loriente et al., (2018).*

### *2.3.8. The Horseshoe Abyssal Thrust*

On the basis of WAS profiles and velocity models, Martínez-Loriente et al., (2014, 2018) detected a SE dipping anomaly in the HAP, interpreted as the so-called Horseshoe Abyssal Plain Thrust (HAT). The HAT is a NE-SW trending, NW-verging tectonic structure (Martínez-Loriente et al., 2014), which according to the models by Martínez-Loriente et al., (2014) dips ~30º ± 20º (Fig. 2.15). Dip uncertainty of the this structure is mainly due to the fact that the authors only had a single WAS profile that crossed the structure; therefore, the ~30º could be an apparent dip. In the SW Iberian margin, the HAT acts as the boundary between the GB domain made of Cretaceous exhumed mantle rocks (Martínez-Loriente et al., 2014; Sallarès et al., 2013) and the Gulf of Cadiz domain, constituted by Western Tethys Jurassic oceanic crust (Martínez-Loriente et al., 2014). The HAT is oriented following the trend of the seismicity cluster located in the middle of the HAP, and the earthquake focal mechanisms show reverse moment-tensor and depths of 40-60 km (Geissler et al., 2010; Silva et al., 2017; Stich et al., 2006; Stich et al., 2010).

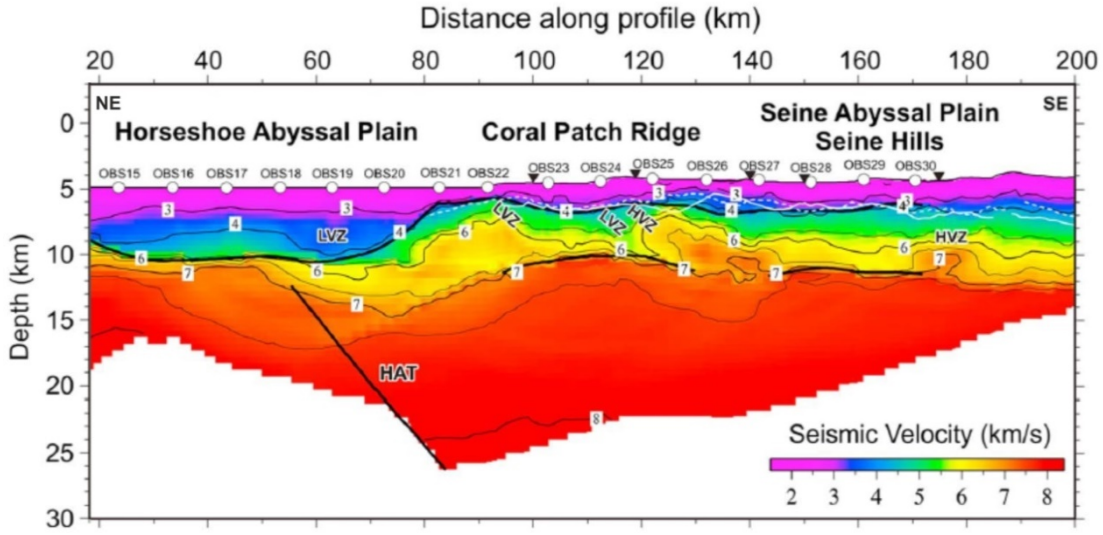


***Figure 2.15.*** *2D velocity model obtained by inversion of the dataset constituted by arrival times of Ps (phases refracted within the sediments), PsP (sediment–basement reflections) and Pb (phases refracted within the basement) phases. Thick solid black lines: inverted sediment-basement boundary, the crust-mantle boundary (i.e.,Moho), and the Horseshoe Abyssal plain Thrust (HAT). Dashed and solid white lines: horizons interpreted to be the base of the sediment cover in the SW12 and SW13 MCS profiles, respectively (Martínez-Loriente et al., 2013). White circles: OBS locations. HVZ: high-velocity zone; LVZ: low-velocity zone. Modified from Martínez-Loriente et al., (2014).*

### *2.3.9. The North Coral Patch Fault and South Coral Patch Fault*

The Coral Patch Ridge (CPR) is a 160 km-long structure with a rhomboidal shape, that separates the HAP and the SAP. It is composed by two NW-verging thrust faults that lift the CPR. The North Coral Patch Fault (NCPF) is 65 km-long and limits the northern part of the ridge at 4250 m depth. The South Coral Patch Fault (SCPF) is 83 km-long and bounds the southern part of the ridge, at 3080 m depth (Martínez-Loriente et al., 2013) (Fig. 2.16). Both thrusts show back-limbs that dip less than the fault-ramp and narrow forelimbs in relation to their long backlimbs that were generated by shear fault-bend folding. The two thrusts dip about ~ 40º during the first km below the seafloor and decrease to ~ 25º until the basement (Martínez-Loriente et al., 2013). These faults cut, fold and show growth-strata configuration in the recent-most sedimentary units of Holocene age, indicating present-day tectonic activity. In the western segment, the NCPF acts as a blind-thrust folding the whole sedimentary sequence, while it reaches up to the seafloor in the central segment with a stratal offset that decreases towards the surface.

The SCPF shows relatively constant vertical slip along the fault, cutting through the whole sedimentary sequence suggesting that it is a recent structure of Miocene-Late Pliocene age (Martínez-Loriente et al., 2013, 2014, 2018; Sartori et al., 1994). The NCPF and the SCPF root in a common detachment level in the serpentinized area of the upper mantle (12-13 km) or in the Moho about 7-8 km (Martínez-Loriente et al., 2013).

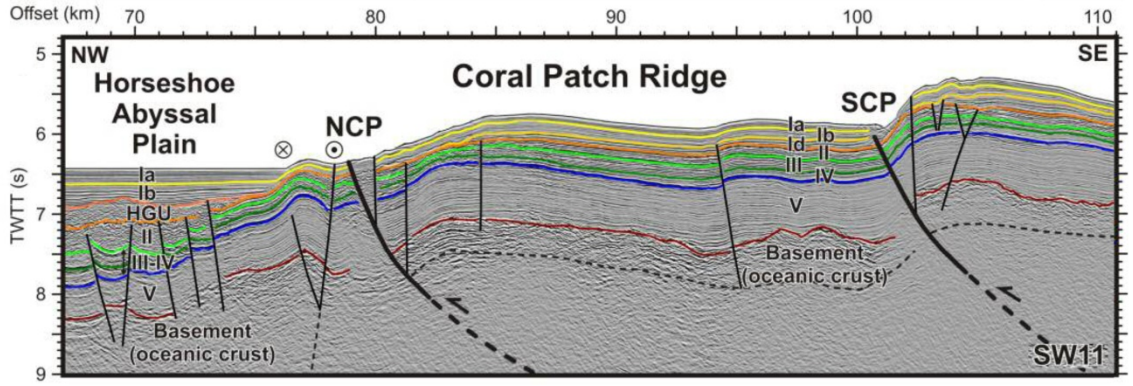


***Figure 2.16.*** *Interpreted section of the SW11 MCS profile across the central part of the Coral Patch Ridge, through the North Coral Patch fault (NCP) and the South Coral Patch Fault (SCP). Ia: Plio-Quaternary; Ib: Middle Miocene-Pliocene; HGU: Horseshoe Gravitational Unit; Id: Upper Oligocene-Middle Miocene; II: Upper Cretaceous-Lower Eocene; III: Cretaceous; IV: Lower Cretaceous; V: Upper Jurassic; TWTT: Two-way travel time. Modified from Martínez-Loriente et al., (2013).*

### *2.3.10. The Seine Abyssal Hills*

The Seine Abyssal Hills (SH) are a succession of elongated ridges (the larger is about 55 km long and the tallest is about 740 m above the surrounding seafloor) located in the northern part of the SAP. These ridges are constituted by NE-SW trending blind thrust-folds with NW and SE vergence (Martínez-Loriente et al., 2013) (Fig. 2.17). The fault-bend folding and fault-propagation folding are the two main mechanisms of deformation in the SH; therefore, the faults are associated to back-thrusts and kink folds that accommodate the deformation close to the seafloor (Martínez-Loriente et al., 2013). The SH thrust-faults dips about ~ 45º over the first kilometres in the subsurface and decreases towards the basement to ~ 25º, where it tends to flatten (Martínez-Loriente et al., 2013). The vertical offset of the SH is homogeneous suggesting that it is a recent structure, such as the SCPF originating in the Miocene-Late Pliocene age (Martínez-Loriente et al., 2013, 2014, 2018; Sartori et al., 1994). In general terms, the SH thrusts are rooted at the same common detachment level that the NCPF and SCPF, in the serpentinized area of the upper mantle (12-13 km) or in the Moho, about 7-8 km depth

(Martínez-Loriente et al., 2013). The deformation of all the seismo-stratigraphic sequence and the growth-strata configuration of the youngest seismo-stratigraphic units suggests that the SH thrusts faults (SHF) are currently active (Martínez-Loriente et al., 2013). The acoustic basement of the SH and CPR is constituted by oceanic crust tilted blocks that correspond to originally structured half-grabens (Martínez-Loriente et al., 2013). On the basis of the kinematic reconstruction by Martínez-Loriente et al., (2014), the oceanic crust (SAP domain) is considered as a slow-stage of seafloor spreading of the NE segment of the Central Atlantic.

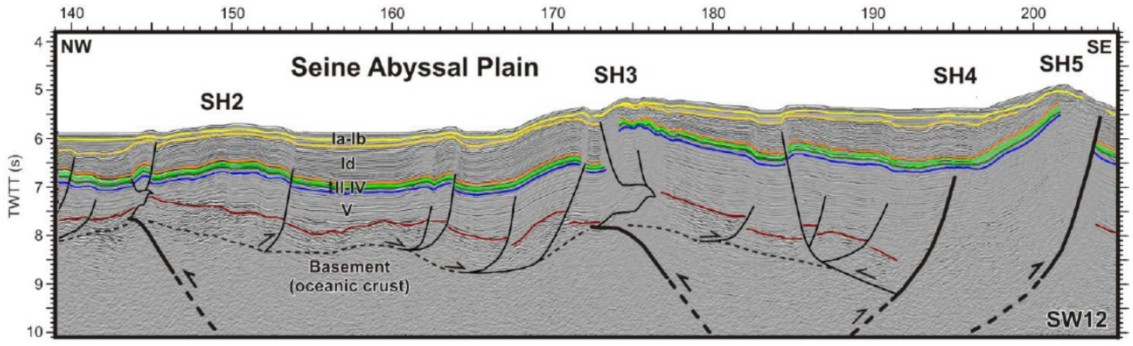


***Figure 2.17.*** *Interpreted section of the SW12 MCS profile across the Seine Abyssal Plain and the Seine Hills (SH). Ia: Plio-Quaternary; Ib: Middle Miocene-Pliocene; Id: Upper Oligocene-Middle Miocene; II: Upper Cretaceous-Lower Eocene; III: Cretaceous; IV: Lower Cretaceous; V: Upper Jurassic;TWTT: Two-way travel time. Modified from Martínez-Loriente et al., (2013).*

### *2.3.11. The Lineament South Fault and Lineament North Fault*

The LSF and LNF are the main WNW-ESE dextral strike-slip faults of the SW Iberian margin. These two faults are part of bathymetric lineations identified by Rosas et al., (2009); Terrinha et al., (2009); Zitellini et al., (2009) in the SW Iberian margin. The lineaments, known as SWIM faults based on the SWIM bathymetric compilation developed by Zitellini et al., (2009), cross the Gulf of Cadiz from the Hirondelle Seamount until the Moroccan continental shelf and conform a wide-deformation band, the SWIM Fault Zone (SFZ). The SWIM lineaments offset some thrust faults such as the HF (Martínez-Loriente et al., 2018; Terrinha et al., 2009; Zitellini et al., 2009), the Coral Patch Faults and the SHF (Martínez-Loriente et al., 2013), suggesting that the WNW-ESE strike-slip lineaments post-date the NE-SW thrusts. Some authors hypothesized that the SWIM faults initiated their activity during the Pliocene (Terrinha et al., 2009) or at 1.8 Ma as suggested by the analogue models of Rosas et al., (2012). Martínez-Loriente et al., (2014) suggest that due to their orientation, location and

behaviour the WNW-ESE strike-slip faults correspond to a reactivation of inherited structures from the Jurassic transfer zone. The LNF is a dextral strike-slip fault (Fig. 2.18), which has an average strike of 100º ± 2º, and is evident in the northern part of GCIW. It is a 130 km-long fault with deformation distributed within a 4.8 km wide zone (Bartolome et al., 2012). In the parametric profiles, a positive flower-like structure with a seafloor build-up of 120 m can be observed. The LSF is the longest fault in the Gulf of Cadiz, which acts as a boundary between the three types of basement present off SW Iberia (Martínez-Loriente et al., 2014). The LSF is a dextral strike-slip fault (strike 105º ± 2º) (Fig. 2.19) that extends from the HAP to the Moroccan continental shelf, along more than 350 km. This fault cuts the Quaternary sequence up to the seafloor and its morphological expression is a set of continuous crest-and-troughs with a width of hundreds of meters over the seafloor (Bartolome et al., 2012).

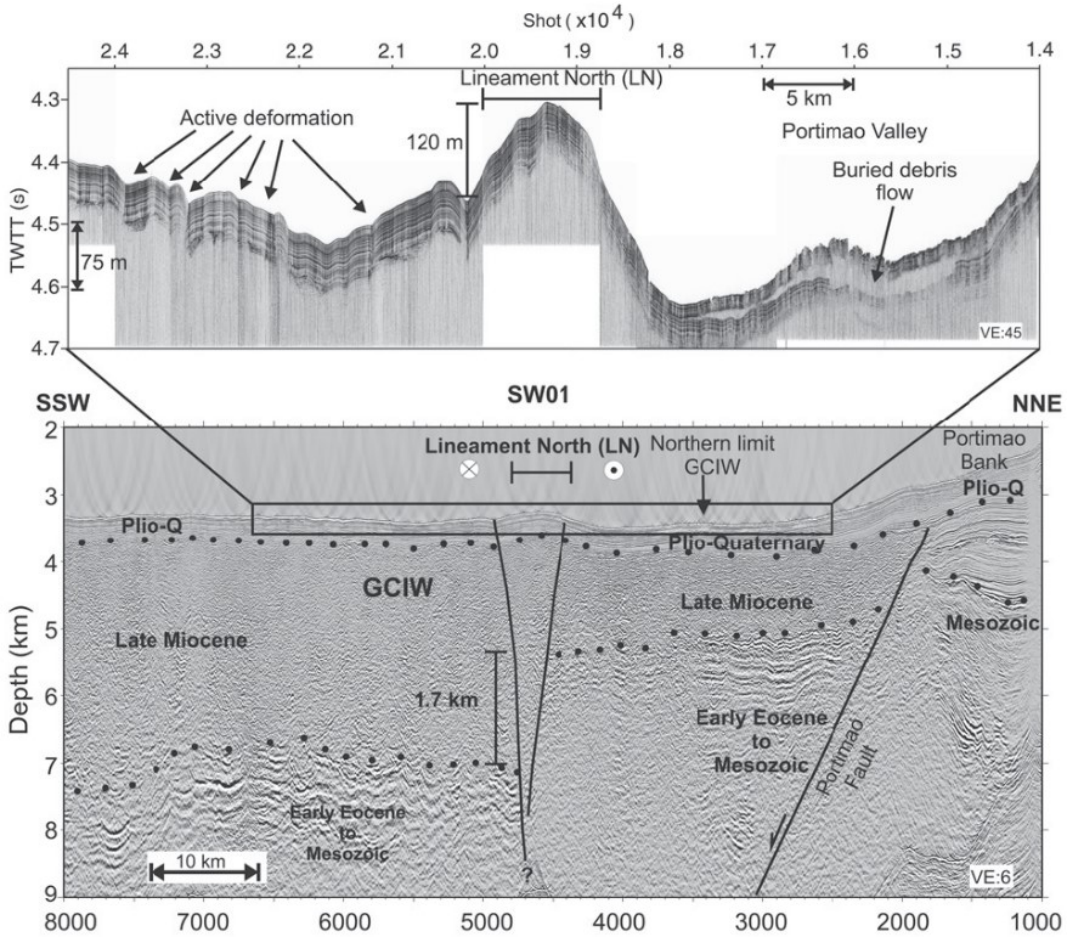


***Figure 2.18.*** *TOPAS (topographic parametric sounder) profile and interpreted section of the depth-migrated MCS profile SW01 across the Lineament North. GCIW: Gulf of Cadiz Imbricated Wedge. VE; Vertical exaggeration. From Bartolome et al., (2012).*

Several mud volcanoes can also be recognized along the LNF and LSF traces. Hensen et al., (2015) relate the presence of these structures with the strike-slip faults, since this type of fracture works as a permeable conduit serving as an important pathway for ascending fluids originated in the oceanic crust, which at this location is older than 140 Ma. Seismic moment tensors from the seismicity associated with the lineaments show WNW-ESE right-lateral strike-slip motions and vertical components at upper mantle depths (40-60 km) (Bartolome et al., 2012). In general terms, these strike-slip faults accommodate part of the deformation of the Eurasia-Africa plate boundary and are an important sources of seismicity (Bartolome et al., 2012; Zitellini et al., 2009).

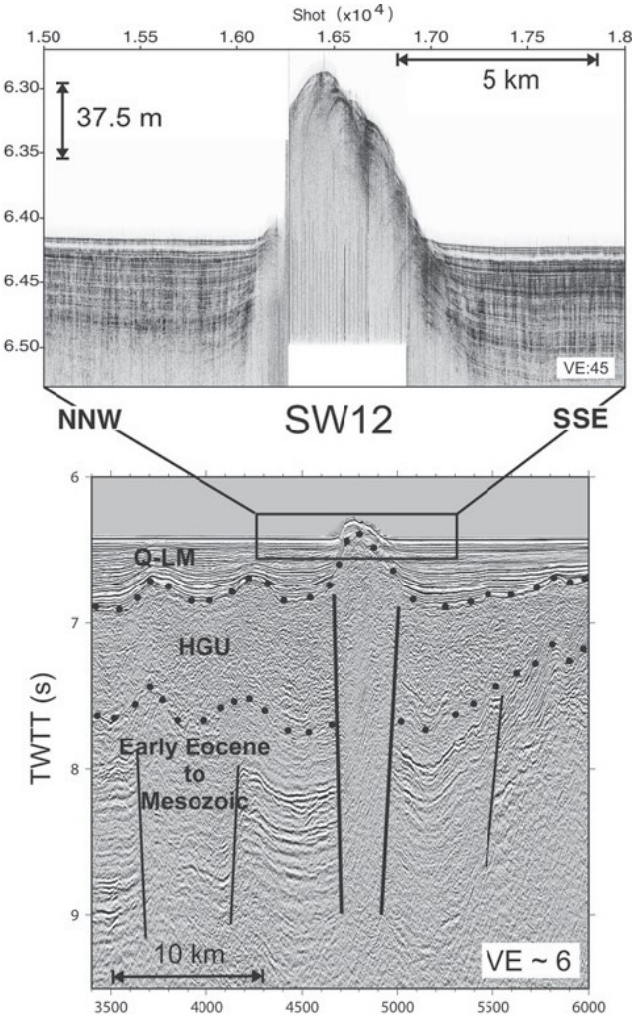


***Figure 2.19.*** *TOPAS (topographic parametric sounder) profile and interpreted section of the depth-migrated MCS profile SW12 across the Lineament South. HGU: Horseshoe Gravitational Unit; Q-LM: Quaternary-Late Miocene; TWTT: two-way travel-time; VE: Vertical exaggeration. From Bartolome et al., (2012).*

## 2.4. Seismicity of the SW Iberian margin

The SW Iberian margin is the most seismogenic area in western Europe. The convergent setting between the Eurasian and African plates (e.g. Martínez-Loriente et al., 2014; Zitellini et al., 2009) (Fig. 2.20) is the responsible of the large historical and instrumental destructive earthquakes and tsunamis that occurred in this region.

On the basis of the present-day NW-SE convergence, Africa is moving in a NW-WNW direction with respect to Iberia, at a rate of 3.8-5.6 mm $yr^{-1}$ (DeMets et al., 2010; Nocquet, 2012; Nocquet & Calais, 2004; Stich et al., 2006). SW Iberia is a seismically active area of low to intermediate magnitude ($M_w \leq 5.5$) earthquakes, punctured by high-magnitude events and shallow to deep seismicity (up to 60 km depth) (Fig. 2.20). In the SW Iberian margin, the deformation and the corresponding seismic activity is distributed in defined clusters (Custódio et al., 2015; Geissler et al., 2010; S. Silva et al., 2017) over a wide area where the deformation band of the SFZ acts as a boundary between a seismic area (to the north of the SFZ) and a non-seismic area (to the south) ( Zitellini et al., 2009) (Fig. 2.21). Focal mechanisms indicate compressional stress and/or strike-slip regime (Buforn et al., 1995; Stich et al., 2005, 2010), revealing a regional transpressive strain with the P-axes oriented (NW-SE) parallel to the maximum shortening between the Eurasian-African plate boundary (Geissler et al., 2010).

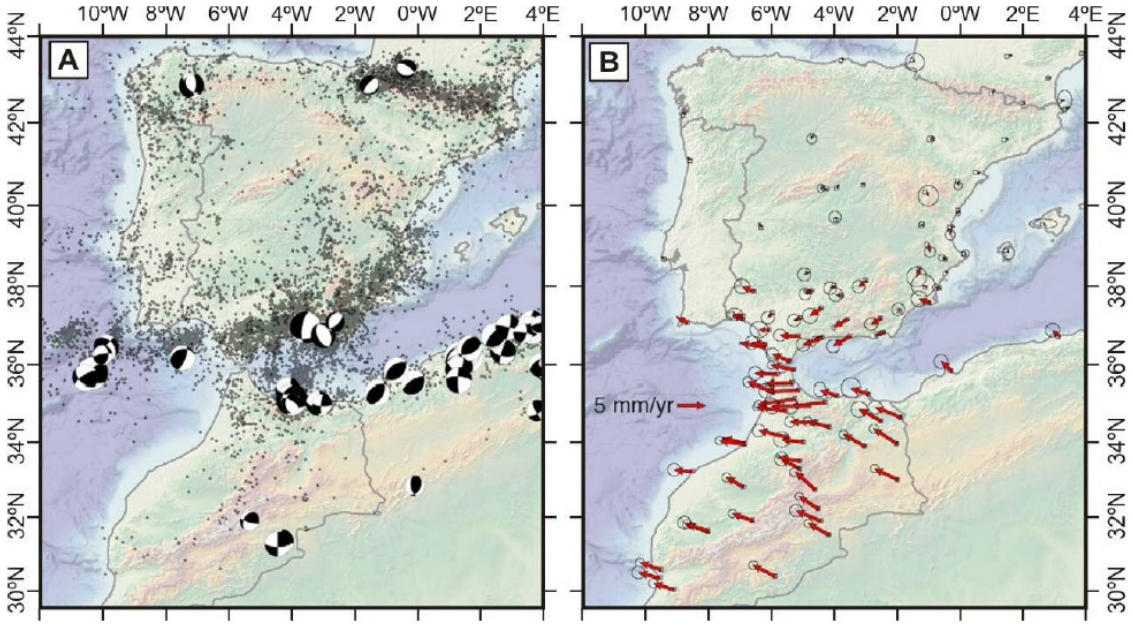


***Figure 2.20.*** *a) Seismicity distribution (NEIC catalogue, 1976–2010) and focal mechanisms between 1976–2011. b) Velocity distribution in a Eurasia fixed reference frame. Modified from Nocquet, (2012) in Martínez-Loriente, (2013).*

Seismicity is distributed in four main clusters (Custódio et al., 2015; Geissler et al., 2010; Silva et al., 2017) (Fig. 2.21): a) **The Gorringe Bank cluster**, elongated along a NE-SW direction and sub-parallel to the GBF. The focal mechanisms of this cluster are mainly strike-slip and reverse dip-slip with few normal events. b) **The São Vicente Canyon cluster**, which extends along the SVC between the NE tip of the HF and the NE tip of the SVF. This cluster is also parallel to the to the MPF. Focal mechanisms in this area show strike-slip and oblique-slip with reverse component, although few normal mechanisms are also identified. c) **The Horseshoe cluster** is elongated in a NW-SE direction along the HAP and across three different lithospheric domains (Martínez-Loriente et al., 2014). This cluster is partially associated to the HAT (Martínez-Loriente et al., 2014, 2018) and partially with the LSF (Bartolome et al., 2012). The focal mechanisms are mainly pure strike-slip, oblique-slip with reverse dip-slip component and few normal events. d) **The Guadalquivir Bank cluster** is located at the inner Gulf of Cadiz in the PB and GuB area and has an elongated NE-SW trend. This trend is related to the positive gravity anomaly corresponding to the basement highs with mainly strike-slip and reverse focal mechanisms (Buforn et al., 2004; Custódio et al., 2015). Regional micro-seismicity was recorded during 11 months by a temporal network of 24 ocean bottom seismometers. The results led Silva et al., (2017) to suggest that micro-seismicity is mostly located in the upper mantle (at 20-50 km depth) and it is associated with inverted rift structures, locally coincident with areas of fault- intersection (NE-SW thrusts and WSE-ESE strike-slip faults) as well as the transition between different rheological domains. The micro-seismicity depths suggest that the shallow crustal fabrics may be replicated in lithospheric mantle depths, while the crustal structures are aseismically moving and frictional slip only occurs in high-magnitude seismic events (Silva et al., 2017).

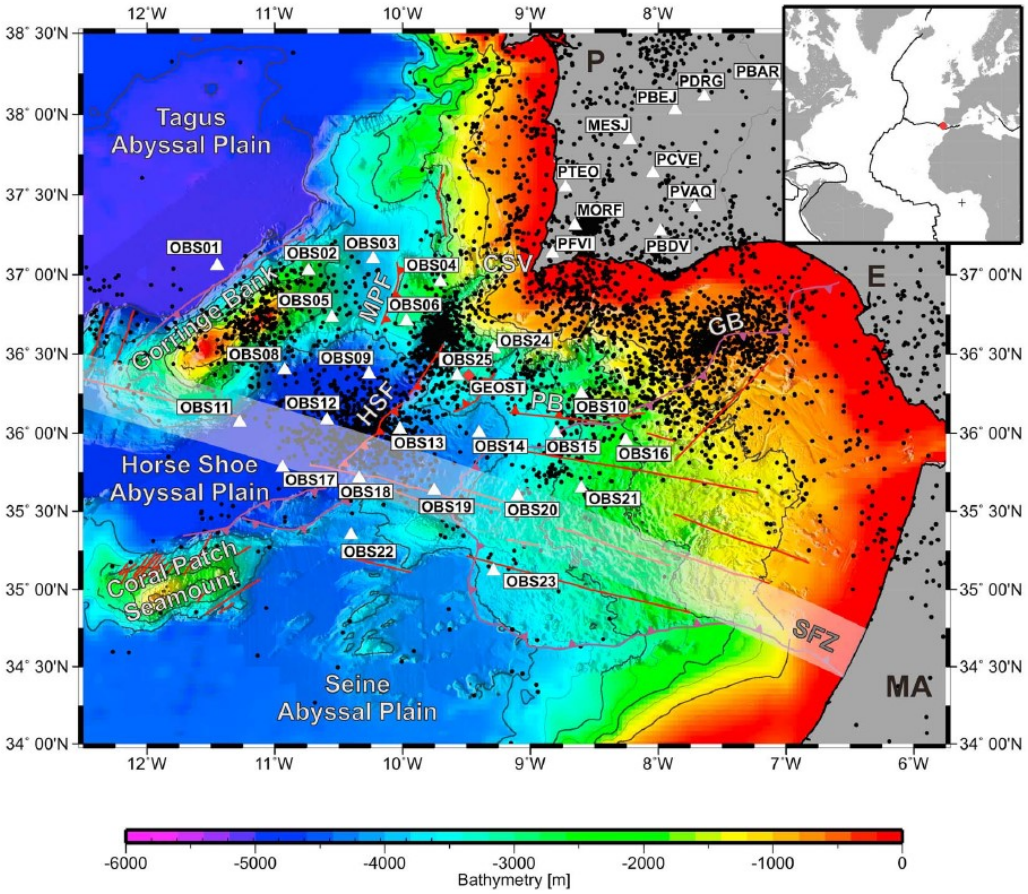


***Figure 2.21.*** *Bathymetric map of the SW Iberian margin with the main faults after Zitellini et al., (2009). Location of OBS and land stations are shown with white triangles. Seismicity from Bulletin of the Institute of Lisbon in black dots. GB, Guadalquivir Bank; CSV, Cape São Vincente; HSF, Horseshoe Fault; MPF, Marquês de Pombal Fault; PB, Portimão Bank; SFZ, SWIM Fault Zone. Modified from Geissler et al., (2010).*

Seismogenic and tsunamigenic events have affected the SW Iberian margin since ancient times. Historical chronicles make reference to 16 tsunamis in the Iberian and Moroccan Atlantic coasts, since 218 B.C. until 1848 (Campos, 1991). The most relevant events in this area include the 218-209 BC Lacus Lingustinus earthquake and tsunami (Vidal, 2016), the 382 Cape São Vicente earthquake ($M_w$ 7.5) and tsunami (Baptista & Miranda, 2009), the 27 December 1722 Tavira earthquake ($M_w$ 6.5) and tsunami (Baptista & Miranda, 2009), the 1 November 1755 Lisbon earthquake ($M_w \geq 8.5$) and tsunami (Martínez Solares & López Arroyo, 2004), the recent 28 February 1969 Horseshoe earthquake ($M_w$ 7.9-8.0) and tsunami and the 17 December 2009 earthquake ($M_w$ 5.5) (Lozano et al., 2019; Stich et al., 2006). Based on turbidite paleoseismology of the SW Iberian margin, Gràcia et al., (2010) determined a recurrence interval of about 1800 years for great earthquakes ($M_w \geq 8.5$) during the Holocene.

The most catastrophic event, which caused more than 60.000 causalities (Baptista et al., 1998) occurred on November 1st 1755, generating an earthquake and a destructive tsunami (Fig. 2.22) that hit the coasts of Portugal, Spain, Morocco and the North Atlantic (Baptista et al., 1998). The origin of this large event it is still a matter of debate. During last years, several authors proposed different sources for the earthquake and tsunami: the MPF, the HF and a combination of the two (Gràcia et al., 2003a; Zitellini et al., 2001, 2004), the MPF and the PSF (Terrinha et al., 2003), the MPF and the GuBF (Baptista et al., 1998) and the GCIW (Gutscher et al., 2002). However, none of these options or their combinations are consistent with the earthquake epicenter, located in the HAP, as it occurs with the 1969 Horseshoe earthquake (Fukao, 1973; Lozano et al., 2019; Stich et al., 2006) (Fig. 2.23). These results show that future investigations need to focus on the active seismogenic and tsunamigenic structures of the Gulf of Cadiz, in order to obtain highly accurate models referring to the large earthquakes and tsunamis that occurred in this area.

***Figure 2.22.*** *Photography of the damage caused by the 1755 Lisbon earthquake in the Convento do Carmo, Lisbon. From BonAppetour, (2020).*

***Figure 2.23.*** *Image of the destruction generated by the 1969 Horseshoe earthquake in the Lisbon region. From CERU, (2015).*

## 2.5. Stratigraphy of the SW Iberian margin

The stratigraphy of the SW Iberian margin is described based on the lithostratigraphic units identified in the DSDP (Deep Sea Drilling Project) and IODP (Integrated Ocean Drilling Program) well sites drilled in the SW Iberian margin (Fig. 2.4). In this work Site 135 in the Coral Patch area (Hayes et al., 1972), Site 120 (Ryan et al., 1973) in the Gorringe Bank area and the site U1391 drilled during IODP Expedition 339 (Hernández-Molina et al., 2015) in the Portuguese and Spanish continental margins, are particularly useful to characterize the stratigraphy. In addition, industry boreholes in the continental shelf (Lopes et al., 2006; Mulder et al., 2006) and seismic correlation carried out by different authors (Gràcia et al., 2003b; Lopes et al., 2006; Maldonado et al., 1999; Martínez-Loriente et al., 2013, 2014, 2018; Mencaroni et al., 2021; Serra et al., 2020; Toyos et al., 2016) have been taken into account. The most comprehensive seismo-stratigraphic interpretations in the entire SW Iberian margin were the works of (Martínez-Loriente et al., 2013, 2014, 2018). On the basis of these studies (Fig. 2.24) and previous ones, the following stratigraphic and seismo-stratigraphic units can be recognized:

- ***Paleozoic Basement**:* It has been only identified in the continental shelf. It is mainly composed by shales, coals and volcanic rocks. This unit is characterized by discontinuous, high-amplitude and low-frequency seismic facies (Gràcia et al., 2003; Lopes et al., 2006).
- ***Triassic**:* It is identified in the continental shelf and the slope and is composed by siliciclastic materials at the base and evaporates, mainly anhydrites and gypsum. Towards the distal continental shelf, the presence of gypsum decreases and anhydrites are dominant. These materials favour plastic deformation and diapiric structures. This unit presents seismic-facies with highly variable amplitude and frequency (Lopes et al., 2006; Pereira & Alves, 2013).
- ***Lower Jurassic**:* In the half-east HAP and SAP (Seine and Gulf of Cadiz Domains), Jurassic materials composed by oceanic crust conform the seismo-stratigraphic basement (Martínez-Loriente et al., 2014). The Jurassic materials in the continental-shelf are mainly composed by dolomites and limestones. The seismic facies are discontinuous with low-amplitude and high-reflectivity (Lopes et al., 2006).
- ***Upper Jurassic**:* Unit V in Fig. 2.24. In general terms this unit is made of dolomites, limestones, shale limestones and marls (Gràcia et al., 2003; Lopes et al., 2006; Maldonado et al., 1999; Pereira & Alves, 2013).
- ***Lower Cretaceous**:* Unit IV in Fig. 2.24. The Lower Cretaceous that constitutes the basement of the Gorringe Bank and the west-half of the HAP and TAP is made of exhumed mantle (Gorringe Bank Domain) (Martínez-Loriente et al., 2014; Sallarès et al., 2013). In the GB ridge, the Lower Cretaceous basement is constituted by ophiolitic breccias (Ryan et al., 1973; Zitellini et al., 2009), while the Barremian, Aptian and Albian are conformed by dark-shales. For the same period the Coral Patch area is constituted by black-marls of terrigenous material (Hayes et al., 1972). In the continental shelf, siliciclastic materials are predominate (Pereira & Alves, 2013).
- ***Cretaceous**:* Unit III in Fig. 2.24. In general terms, the Cretaceous is constituted by black-shales and green siliceous mudstones (Hayes et al., 1972; Pereira & Alves, 2013). This unit has semi-continuous and low-amplitude to transparent reflectors (Martínez-Loriente et al., 2013).
- ***Upper Cretaceous-Lower Eocene**:* Unit II in Fig. 2.24. This unit is composed by limestones and evaporites at the base, and limestone, marls and dolomites in the Lower Eocene (Hayes et al., 1972; Lopes et al., 2006; Maldonado et al., 1999; Pereira & Alves,

2013). The seismic facies are constituted by continuous and high-amplitude reflectors changing to discontinuous and lower amplitudes towards the top (Martínez-Loriente et al., 2013).

- ***Lower Eocene- Upper Oligocene****:* In general terms, this unit is made of shale limestones and brown-clays with coarse sand-layers in the Portuguese continental shelf (Pereira & Alves, 2013). In the distal SW Iberian margin, such as the Coral Patch area, this unit does not exist as there is an Hiatus (Fig. 2.24) (Hayes et al., 1972; Martínez-Loriente et al., 2013).
- ***Upper Oligocene-Middle Miocene****:* Unit Id in Fig. 2.24. This unit is mainly composed by shaly limestone and dolomites at the base and siliciclastic material in the upper part of the unit (Lopes et al., 2006; Pereira & Alves, 2013). This unit displays parallel and high-amplitude reflectors (Martínez-Loriente et al., 2013).
- ***Middle Miocene-Pliocene****:* Unit Ib-Ic in Fig. 2.24. In this period, the GCIW and the HGU were emplaced. This GCIW allochthonous mass is composed of a mixture of Triassic evaporites (i.e., salt, gypsum) and a succession of Jurassic to Middle Miocene sedimentary rocks, mainly clays (Gràcia et al., 2003b; Iribarren et al., 2007; Andrés Maldonado et al., 1999). The HGU materials are gravitational deposits originating from the GCIW and surrounding areas (Iribarren et al., 2007). In the rest of SW Iberia margin, this unit is composed by siliciclastic materials (Pereira & Alves, 2013). The seismic facies is characterized by highly variable reflectors and amplitudes (Martínez-Loriente et al., 2013).
- ***Plio-Quaternary****:* Unit Ia in the Fig. 2.24. The Plio-Quaternary is mainly composed of silty-clays and clays (Lopes et al., 2006) with conturites and turbidites deposits (Hernández-Molina et al., 2015). In the Gorringe Bank area, foraminifera oozes predominate (Ryan et al., 1973), while in the Coral Patch Ridge area this unit is constituted by chalk ooze (Hayes et al., 1972). The seismic facies are characterized by low-medium amplitude and continuous reflectors (Martínez-Loriente et al., 2013). Several authors, such as Hernández-Molina et al., (2003, 2014); Llave et al., (2007); Mencaroni et al., (2021); Mulder et al., (2003); Stow et al., (1986), showed the relationship between the Plio-Quaternary sedimentary unit in the Gulf of Cadiz and the hydrodynamic conditions of the MOW. Along its pathway, the MOW transports, deposits and reworks the sediments of the SW Iberian margin generating extensive contourite drifts on the middle slope (Hernández-Molina et al., 2003; Mencaroni et al.,

2021). There are two types of contourite deposits in the Plio-Quaternary unit, elongated and separated mounded drift and sheeted drift (Hernández-Molina et al., 2003).

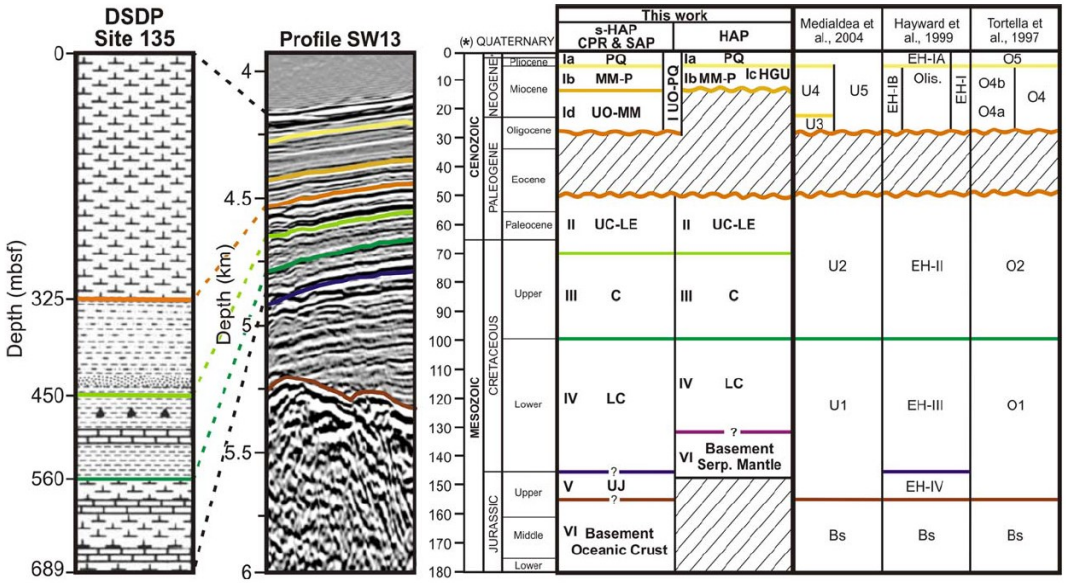


***Figure 2.24.*** *Seismo-stratigraphy from Martínez-Loriente et al., (2013) based on DSDP Site 135 (Hayes et al., 1972). Units previously defined by Hayward et al., (1999); Medialdea et al., (2004); Tortella et al., (1997) in the external part of the Gulf of Cadiz included as reference. mbsf: meters below the seafloor; CPR: Coral Patch Ridge; SAP: Seine AbyssalPlain; s-HAP: southern Horseshoe Abyssal Plain. I.UO-PQ: Upper Oligocene to Quaternary; Ia. PQ: Plio-Quaternary; Ib.MM-P: Middle Miocene-Pliocene; Ic.HGU: Horseshoe Gravitational Unit, Upper Miocene; Id.UO-MM: Upper Oligocene-Middle Miocene; II.UC-LE: Upper Cretaceous-Lower Eocene; III.C: Cretaceous; IV.LC: Lower Cretaceous; V.UJ: Upper Jurassic; VI and Bs: Basement; Serp.: Serpentinized. From Martínez-Loriente et al., (2013).*

## 2.6. Oceanography of the SW Iberian margin

The oceanographic context of the SW Iberian margin is quite complex. The aperture of the Straits of Gibraltar (5.3 Ma ago) and the increment in sediment contribution in the Pleistocene (García et al., 2009) changed the character of the sedimentary deposition and the oceanographic circulation of the area (Habgood et al., 2003). This sedimentary deposition and the present-day circulation are dominated by the seawater-exchange between the Atlantic and Mediterranean through the Straits of Gibraltar (Hernández-Molina et al., 2003, 2015). This bottom current, the so-called MOW, is a salty, warm and poorly oxygenated submarine current (~ 13 ºC of temperature and an average salinity of 36.5 ‰) that in the present-day configuration

flows from the Straits of Gibraltar towards the Atlantic, following the slope and the Portuguese continental shelf between 300 and 1400 m (Hernández-Molina et al., 2003) (Fig. 2.25). Along its pathway, the MOW loses velocity and increases in depth. The MOW accelerates through the Straits of Gibraltar (30 cm/s) and moves north-westward along the mid-continental slope of the Gulf of Cadiz, decreasing the velocity until 20 cm/s in the CSV area (Ambar & Howe, 1979; Hernández-Molina et al., 2003; Mulder et al., 2003). At the head of the SVC, the MOW generates sedimentary deposits such as contourites (Hernández-Molina et al., 2015; Hernández-Molina et al., 2003; Mencaroni et al., 2021). The MOW flows northward above the NADW (North Atlantic Deep Water) and below the AIW (Atlantic Inflow Water). The AIW is constituted by the North Atlantic Superficial Water (NASW) (surface to 100 m water depth) and the Eastern North Atlantic Central Water (ENACW) (100 m to 700 m) with an average temperature of 13-16ºC and 34.7-36.25‰ average salinity (Hernández-Molina et al., 2014, 2015). The underlying NADW is colder (3-8 ºC) and less saline (34.95-35.2 ‰), flowing below the 1500 m isobath from the Greenland-Norwegian Sea region towards the south (Baringer & Price, 1999; Hernández-Molina et al., 2015; Serra et al., 2005).

Due to the complex continental slope-morphology of the Gulf of Cadiz, the MOW splits in two main flow cores: the MOW Upper core (MU) and the MOW Lower core (ML) (Fig. 2.25). The ML follows a general north-western trend, between the 800 and 1400 m depth with a temperature of 10.5-11.5 ºC and 36.5-37.5 ‰ of salinity (Hernández-Molina et al., 2015; Llave et al., 2007). While the MU (13-14 ºC and 35.7-37 ‰) flows parallel to the SW Iberian slope, at depths of 500-800 m and is partially captured by the PC (Hernández-Molina et al., 2015; Marchès et al., 2007).

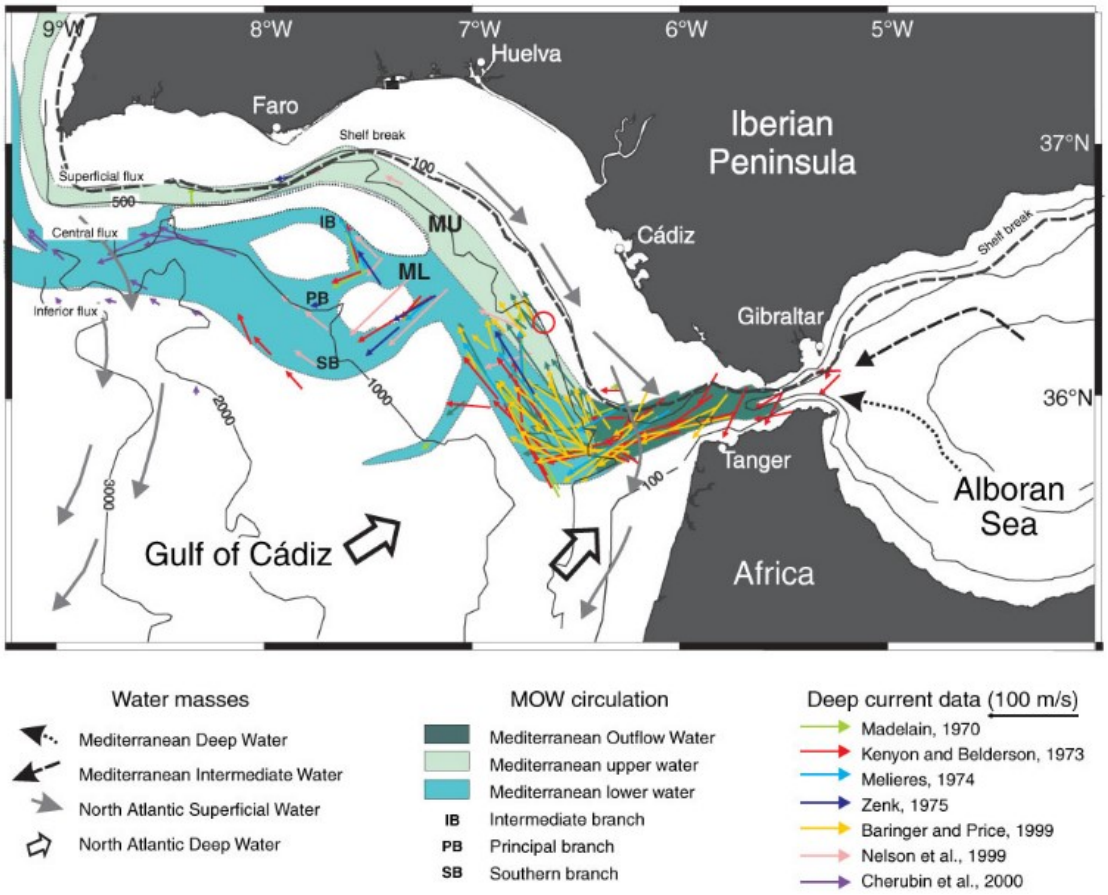


***Figures 2.25.*** *Oceanographic distribution of the MOW in the Gulf of Cadiz (SW Iberia) showing its main cores and branches. From García et al. 2009.*

The ML divides into three distinct branches with a general northwest direction: the southern branch (SB), the principal branch (PBr) and the intermediate branch (IB) (Hernández-Molina et al., 2015). The hydrodynamic conditions of the MOW are highly dependent on the climatic stage (glacial and interglacial cycles) (Bahr et al., 2015; Llave et al., 2006). On the one hand, during the glacial periods (colder) the freshwater input in the Mediterranea decrease, therefore, the resulting current from the Strait of Gibraltar increase its density enhancing the ML. The result is a strong interaction of the MOW with the seafloor (Bahr et al., 2015; Llave et al., 2006). On the other hand, during interglacial periods (warmer), the freshing of Atlantic surface waters due to the melting of the ice results in a high-density contrast between Atlantic and Mediterranean water masses and a stronger upper MU (Bahr et al., 2015; Llave et al., 2006).

# CHAPTER 3

# Data and methods

## 3.1. The INSIGHT project

The SW Iberian margin has been investigated in this PhD Thesis during the period 2017-2021 collecting new geophysical data on the main active structures of the area. Such data collection has taken place in the frame of the project INSIGHT -*"ImagiNg large SeismogenIc and tsunamiGenic structures of the Gulf of Cadiz with ultra-High resolution Technologies"*. During the INSIGHT project, two oceanographic surveys have been carried out: the INSIGHT-Leg1 and the INSIGHT-Leg2.

During the INSIGHT-Leg1 (PI. E. Gràcia), active fault structures, mud volcanoes, and a diapir were mapped, with unprecedented resolution, using the AUV "Abyss" from GEOMAR- Kiel (Germany). In addition, other marine technologies, such as the 2D-high-resolution seismic system, high-resolution swath-bathymetry, parametric sub-bottom profiler and sedimentary sampling (i.e. multicores, gravity cores and piston cores) (Fig. 3.1) were used to collected new data.

In the frame of the INSIGHT-Leg2 cruise (PI. R. Urgeles), the same active structures were revisited using new technologies, such as the Controlled Source ElectroMagnetic (CSEM) method, and the 2D-high-resolution seismic system, swath-bathymetry, parametric sub-bottom profiler and sediment sampling (gravity coring) (Fig. 3.1).

The geophysical data of INSIGHT surveys comprises five study areas: a) the Marquês de Pombal area, b) the Lineament South west section (LSW), c) the Lineament South east section (LSE), d) the Ginsburg mud-volcano area, and e) the Lolita salt-diapir area (Fig. 3.1).

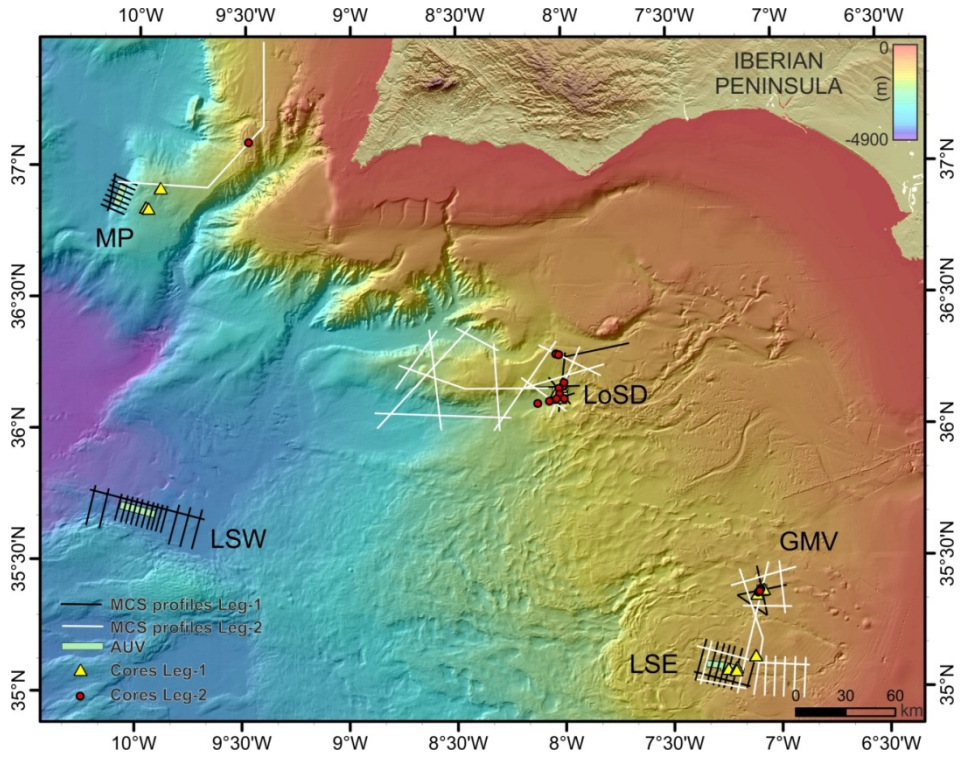


***Figure 3.1.*** *Bathymetric map of the SW Iberian margin with the location of the data acquired during the INSIGHT cruises (INSIGHT Leg-1 and Leg-2). AUV: Autonomous Underwater Vehicle; GMV: Ginsburg mud volcano area; LoSD: Lolita Salt Diapir area; LSE: Lineament South East area; LSW: Lineament South West area; MP: Marquês de Pombal area; MCS: Multi-channel seismic.*

## 3.2. The geophysical methods used

Despite this PhD thesis was developed in the framework of the project INSIGHT, it integrated and associated results from different geological and geophysical data acquired in several surveys (since mid-90s) and used different methods. The multi-scale dataset includes swath-bathymetry, high-resolution bathymetry from AUV, sidescan-sonar TOBI mosaics, parametric sub-bottom profiles and 2D MCS data. These methods will be described in the following pages.

Using this variety of multi-scale data, different assessments of the SW Iberian margin can be made. Bathymetry and 2D-multichannel seismic profiles of lower resolution can cover a large area. AUV maps, TOBI side-scan sonar images, TOPAS profiles and High-Resolution multi-channel seismic profiles allow us to obtain higher-resolution information although covering smaller areas (Table 3.1).

| *Method* | *Typical Resolution* | *Sub-bottom penetration* |
|---|---|---|
| ***Swath-bathymetry*** | 50 m | 0 m |
| ***2D MCS*** | 10 - 20 m | 9,000 m |
| ***TOBI*** | 2.5 - 6 m | 0 m |
| ***2D High-Resolution MCS*** | 2 m | 4,000 m |
| ***Sub-bottom profiler*** | 2 m | 80-150 m |
| ***AUV bathymetry*** | 1 m | 0 m |

***Table 3.1*** *Comparison of the different resolution and sub-bottom penetration values for each geophysical method used in this Thesis. Values extracted from Gràcia & INSIGHT Cruise Party, (2018).*

### *3.2.1. Swath-bathymetry and acoustic backscatter*

The multibeam-echosounder allows us to obtain an accurate cartographic seafloor-map, providing information on the water-depth, geomorphology, seismo-stratigraphy and tectonics. Multibeam-echosounders provide two types of data: the water-depth and backscatter of the seafloor. The multibeam echosounder measures the water-depth sending acoustic pulses (i.e., beams from the transmitter) and receiving the reflections or echoes from the seafloor. The seafloor depth is calculated using the arrival angle and arrival time of the acoustic signal in function of the acoustic velocity propagation through the water-column. The transmission and reception of the acoustic signal is done by a transducer. The transducers convert electrical pulses to acoustic signals. Later, they convert the pressure differences of the arrival of the reflected acoustic-waves in an electric signal that includes the depth information (Lurton, 2010).

The traducers emit a signal composed by numerous straight-beams generating a band perpendicular to the vessel axis (width swept) (Martínez-Loriente, 2013), hence while the vessel is sailing it records a continuous map of the seafloor (Lurton, 2010). In addition, multibeam echosounder equipment is composed by the following parts: 1) Transmission and reception arrays unit; 2) User interface (with system control options and real-time processing results); and 3) Ancillary systems, such as the positioning system, attitude sensor unit and sound velocity profiles (Díez & Gràcia, 2005). The horizontal (x, y) and vertical (z) position of each beam is determined by the GPS

position and the data of the vessel motion sensors, which are the pitch, roll and yaw (Fig. 3.2). Usually, the multibeam echo-sounder is fixed in the hull of the research vessel, with the beams bouncing off the seabed and returning to the ship with the echoes recorded from the system. The vessel usually sails at velocities between 6 and 10 knots.

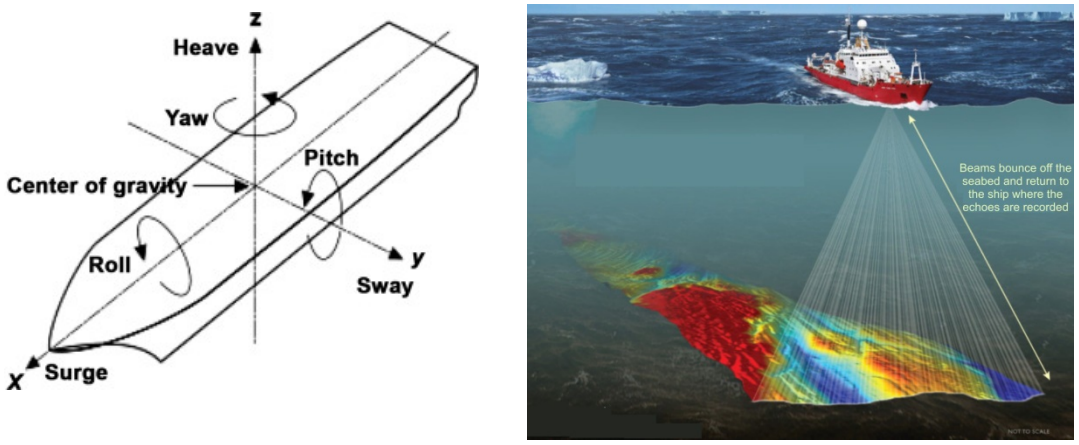


***Figure 3.2.*** *Left: Scheme portraying the six degrees of freedom of a vessel. Surge, Sway, and Heave are* linear movements *in the* x, y, z *directions, respectively, while Roll, Pitch, and Yaw are* rotary movements *about the* x, y, z *axes, respectively. From ScienceDirect, (2020). Right: Operation of a multibeam echosounder fixed in a vessel. Modified from British Antartic Survey, (2015).*

Depending on the application (i.e., water depth of the study area), multibeam echosounders use different frequency ranges. The system resolution increases with the frequency and it also does the water attenuation. High-frequency instrumentation will have a better resolution and accuracy than a low-frequency instrument for a certain water depth. Frequencies between 12 and 15.5 kHz are used to work in deep-waters until 11,000 m depth, while 95 kHz are typically used for waters less than 1,000 m depth (Bourillet et al., 1996). To obtain high-quality bathymetric data, an adequate correction of the tide and the acoustic velocity profile in the water-column are essential. The acoustic velocity changes depending on the temperature, salinity and pressure, therefore several profiles of the water column properties during the bathymetric acquisition are made. To describe the multibeam echosounder equipment's the acoustic frequency, the maximum angular aperture, number of beams, beam spacing, length of emission and cadence are the basic parameters (Díez & Gràcia, 2005). The frequency

determines the sub-bottom penetration into the sediment, the maximum angular aperture controls the swath-width (ranging between 90º and 150º) and the beam-spacing that can be equidistant or equiangular. The acoustic emissions are referred as "pings" and are portions of sinusoidal signals restricted to a length and the cadence is the length between two successive emissions (Martínez-loriente, 2013).

The processing of raw-data is essential to introduce the corrections and filtering of erroneous data. In general terms, the processing of bathymetric data implies the following steps: a) Filter of the vessel-position data (i.e., pitch, roll, yaw and heave), b) applying the acoustic velocity-profile of the water-column, c) clean navigation to avoid loops, d) automatic edition of the beams to remove the external beams noise and e) manual spike-cleaning. To process the raw bathymetric data software such as *Caraibes, Swathed* or *CARIS HIPS&SIPS* is used.

In this PhD Thesis, three sources of bathymetric data have been used: a) The EuroMargins "SWIM" multibeam compilation (Zitellini et al., 2009), the data collected during the "INSIGHT 2018-2019" cruises and the "SRTM-15" dataset. The SWIM compilation (Zitellini et al., 2009) refers to a total of 20 marine cruises that took place from year 2001 to year 2009 by 14 European research institutions (Fig. 3.3). During the INSIGHT cruises on board of the Research Vessel "Sarmiento de Gamboa", (Leg-1 and Leg-2), a total of 10,000 $km^2$ of swath-bathymetric data, was acquired with the ATLAS Hydrosweep DS multibeam echosounder. The ATLAS DS works at a frequency ranging between 14.5 and 16 kHz. It operates between 10 to 11,000 m depth, with a maximum vertical resolution of 6.1 cm, and 0.5 m of accuracy (ATLAS HYDROGRAPHIC, 2010). The maximum angular coverage is 5.5 times the water-depth (140º), with up to 141 hardware beams, 1ºx1º, corresponding to 345 beams with high order beam-forming. It includes the ATLAS Hydrosweep Control software, which incorporates controls for the acquisition and visualization settings. All beams are calibrated in real-time for the ship attitude (i.e., roll, pitch, yaw, heave) (Gràcia & INSIGHT Cruise Party, 2018). The average speed for the navigation acquisition was about 5 knots up to 6-7 knots. The data acquired was processed on board using the CARIS, HIPS&SIPS software. The DTM (i.e. digital terrain model) of 50m cell-size was finally achieved (Gràcia & INSIGHT Cruise Party, 2018).

Finally, the SRTM 15-bathymetry is an open access bathymetric database of a global-elevation at a spatial sampling interval of 15 arc sec (~500 × 500 m pixel size at

the Equator) (Olson et al., 2016; Tozer et al., 2019). The bathymetric data is constructed using a compilation of global shipboard soundings (~351 million sounding records from numerous marine research institutions) with global marine gravity-models and satellite-derived predicted depths (Olson et al., 2016). The predictions from the latest global gravity-models where obtained from the satellites CryoSat-2 and Jason-1, along with 494 million carefully edited depth-soundings at 15 arc-second resolution (Olson et al., 2016). This database is accessible through the following link: https://topex.ucsd.edu/index.html.

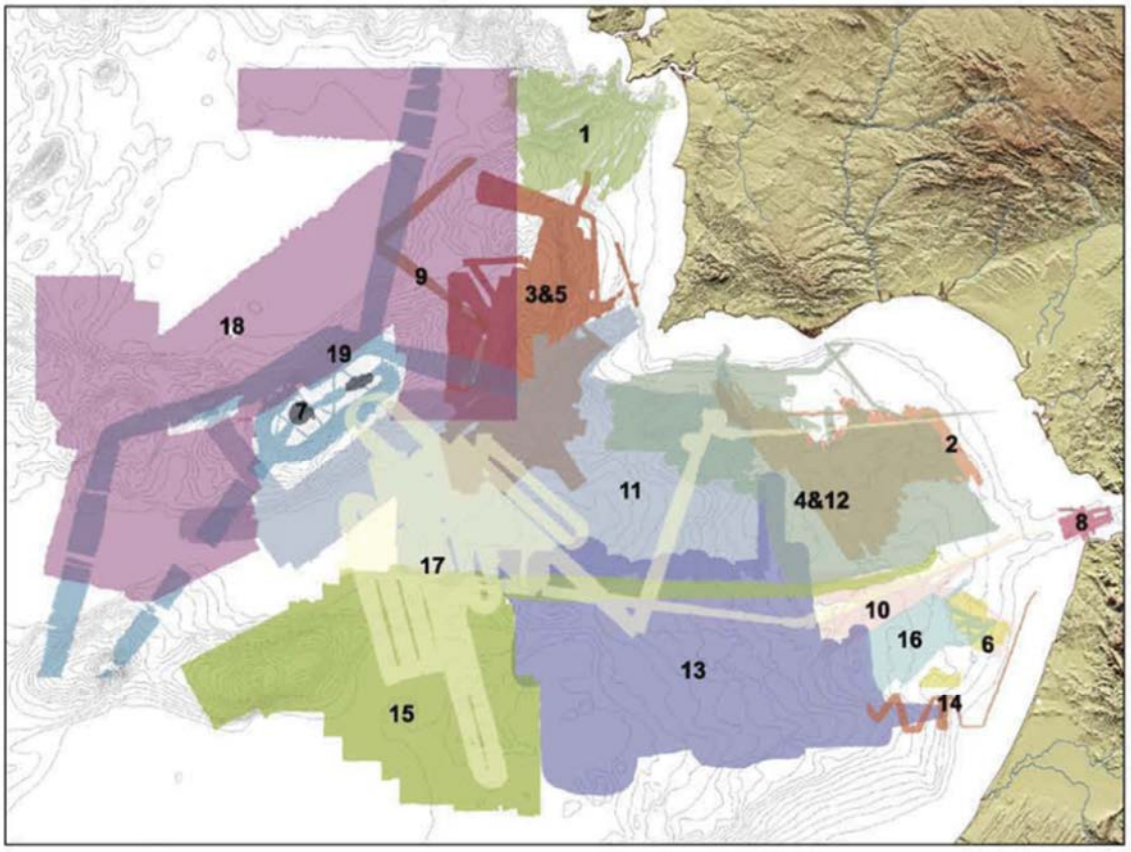


***Figure 3.3.*** *List of the marine surveys carried out in the Gulf of Cadiz, as well as its respective coverage used in the SWIM compilation. 1. ESPICHEL cruise, 1991 (Ifremer, France); 2. TASYO cruise, 2000 (IGME, Spain); 3. PARSIFAL cruise, 2000 (CSIC, Spain); 4. CADISAR-1 cruise, 2001 (Université Bordeaux, France); 5. HITS cruise, 2001 (CSIC, Spain); 6. CADIPOR cruise, 2002 (Ghent Uiversity, Belgium); 7. GORRINGE cruise, 2003 (IAMC-CNR, Italy); 8. TV-GIB cruise, 2003 (IUEM, France); 9. PICABIA cruise, 2003 (CSIC, Spain); 10. GAP cruise, 2003 (Universität Bremen, Germany); 11. MATESPRO cruise, 2004 (Universidade de Lisboa, Portugal); 12. CADISAR-2 cruise, 2004 (Université Bordeaux, France); 13. DELILA cruise, 2004 (IUEM, France); 14. DELSIS cruise, 2005 (IUEM, France); 15. SWIM-2 cruise, 2005 (ISMAR, Italy);16. HERMES cruise, 2006 (NOC, UK); 17. SWIM cruise, 2006 (CSIC,*

*Spain);18. Digital terrain model (EMPEC, Portugal); 19. Several transit data from SISMER database. Modified from Vizcaino,(2009) and Zitellini et al.,( 2009).*

In this Thesis, multibeam bathymetric data have been used to generate bathymetric maps and other derived data, such as shaded-relief maps, slope maps, 3D-view images and combinations of all of them. With the resulting information, it is possible to identify seafloor structures, such as escarpments, submarine landslides, and fault systems with their surface expression. All this dataset has been managed and interpreted using the free software *QGIS* and the commercial package *ArcGIS 10*. One of the main goals to use bathymetry and other derived products in this Thesis is to obtain the volume of erosional features. Using the software *Mirone*, the volume of eroded material by the Sao Vicente submarine canyon has been determined by calculating the difference in elevation between a spline-smoothed grid, where the canyon topography was removed (with the function Crop), therefore simulating the slope without canyon incision (filling the topography of the canyon) and the grid of the actual slope.

### *3.2.2. The Autonomous Underwater Vehicle "Abyss"*

An AUV is a self-propelled, unmanned, untethered underwater vehicle able to carry-out programmed missions with little and automatic supervision (Bellingham, 2009). These underwater vehicles allow us to obtain very high-resolution bathymetric maps, detailed sidescan sonar images and high-quality photographies to characterize the deep seafloor. There are a large variety of AUV models, which depend on the depth rating, autonomy and sensors used (e.g., multibeam echosounder, sidescan sonar, underwater camera, acoustic doppler current profiler, CTD (Conductivity, Temperature, Depth), magnetometer, etc). An AUV allows us to collect also chemical data, seawater column data and biological water properties (Bellingham, 2009). Depending of the type of AUV, it is possible to work at depths of up to 6,000 m.

The AUV equipment comprises the AUV itself (Fig. 3.4), a control and workshop container, transponders and a mobile Launch and Recovery System (LARS) with a deployment frame. To determine the position an AUV working in deep-waters uses the long-baseline (LBL) navigation technique. The LBL operates on the principle that the distance between an underwater vehicle and a fixed acoustic transponder can be precisely related to the time of flight of an acoustic signal, propagating between the vehicle and the transponder (Humphris, 2009). Two or more transponders will be

deployed in the seafloor of the study area at selected locations, to optimize the acoustic range and geometry of the seafloor work zone (Fig. 3.5). The position of the transponders is determined by using the GPS system on board of the research vessel, ranging to them acoustically while the ship circles the point where each transponder was dropped. The transponders clocks are synchronized with those on the AUV and on the research vessel (Humphris, 2009).

The AUV and the research vessel have a transceiver to receive and send communication signals to the transponders. The work frequency of the transponders is between 9 and 12 kHz. They listen and transmit the acoustic signals from the AUV to the research vessel or vice-versa. Each transponder works in a specific frequency, so the AUV and the ship can recognize which transponder is sending information. The flight time of the acoustic signals, gives a measure of distance to each transponder, and using a simple triangulation, the point in three-dimensional space where all distances measured from all the transponders and the ship intersect can be calculated (Humphris, 2009) (Fig. 3.5). The fundamental limitation of the AUV's is the energy efficiency. The AUV's are powered by rechargeable batteries with few hours of autonomy (about 10 hours depending on the model). After the dive, the AUV should be brought on-board to charge the batteries for the next dive and to download the recorded data (Bellingham, 2009). For recovering the AUV, the nose float of the AUV pops-off when an acoustic command is sent (Fig. 3.4). The float and the recovery-line drift away from the vehicle, so that a grapnel hook can snag the line. The line is then connected to the LARS winch, and the vehicle is pulled up (Gràcia & INSIGHT Cruise Party, 2018).

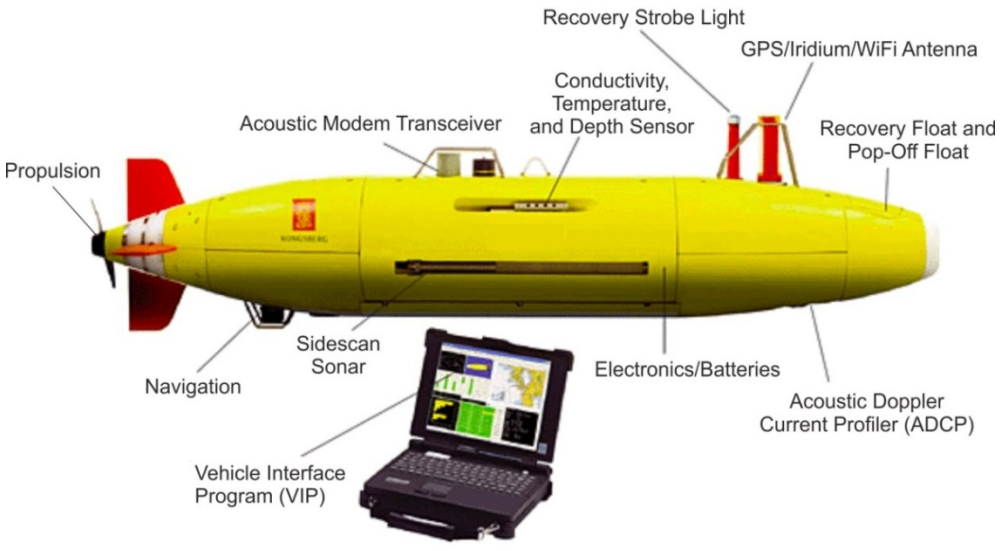

***Figure 3.4.*** *Enlarged view of the parts of the AUV REMUS 6000. Modified from La macchina del tempo, (2014).*

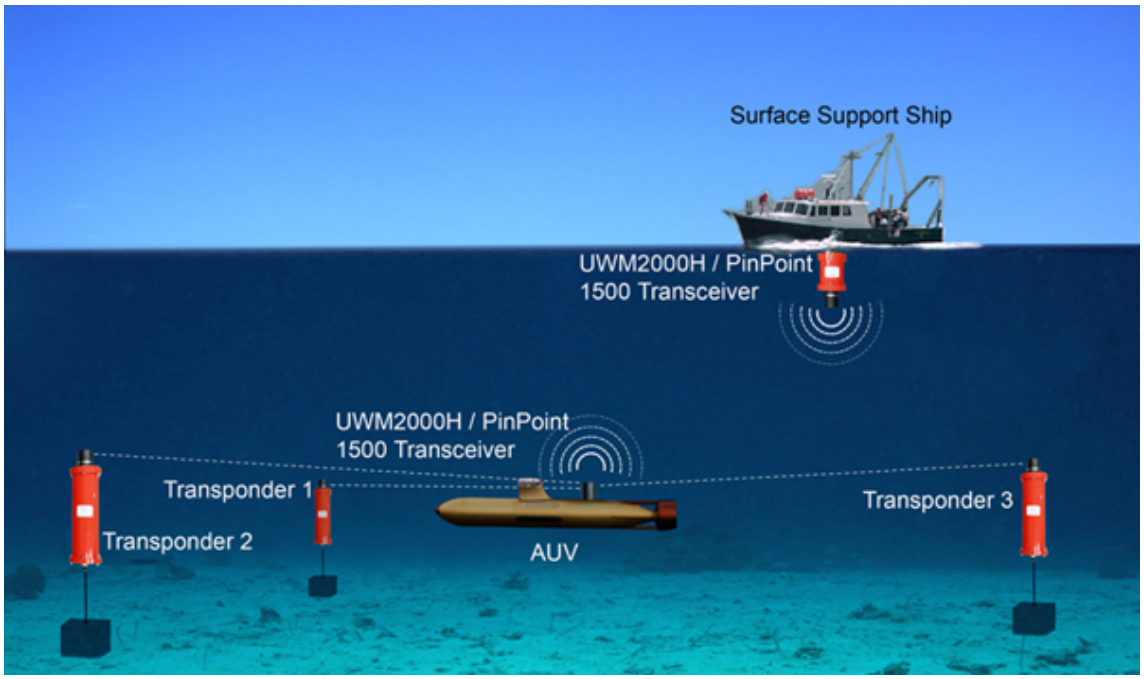


***Figure 3.5.*** *Scheme of operation of an AUV using long-baseline. From LinkQuest Inc., (2020).*

Five high-resolution AUV bathymetric maps (Marquês de Pombal area, the Portimão Bank, the Lineament South including the West end and the East end, the Lolita Salt Diapir and the Ginsburg Mud Volcano) were acquired during the INSIGHT Leg-1 cruise using the AUV "Abyss"; three of them (Marquês de Pombal area and Lineament South including the West end and the East end) have been analysed in this PhD Thesis. The AUV "Abyss" is a torpedo-shaped system developed in 2008 by the Forschungszentrums für Marine Geowissenschaften "GEOMAR". This AUV can collect data in deep water areas up to 6000 m depth. This AUV uses state-of-the-art technologies to map in detail the seafloor and investigate the overlying water column (Haase et al., 2009; Hensen et al., 2015; Speckbacher et al., 2012; Yeo et al., 2016). The AUV "Abyss" can be launched and recovered in weather conditions with a swell up to 2.5 m and wind speeds up to 6 Beaufort.

The AUV operational speed is of up to 4 knots and its lithium batteries have and autonomy of 16-20 hours, depending on the sensors used, and need approximately 12-14 hours to be recharged. The AUV descends with velocities about 1 m/s whereas the ascent velocity is about 0.7 m/s or 1m/s if the ascent weight is dropped (Gràcia & INSIGHT Cruise Party, 2018). The AUV Abyss incorporated the following standard

sensors: SBE 49 CTD, fluorometer and turbidity sensor, side scan sonar 120/410 kHz and RESON Seabat 7125 200 kHz multibeam echosounder (Gràcia & INSIGHT Cruise Party, 2018). The main objectives of the INSIGHT-Leg 1 cruise were the acquisition of high resolution bathymetry maps, therefore the main sensor used for the AUV was the 200 kHz multibeam echosounder (Table 3.2) and CTD to calibrate the bathymetry.

| | | |
|---|---|---|
| Vendor | Reson | |
| Typ | SeaBat 7125<br>Receiver EM7216 PN:85002184 SN:1713118<br>200kHz Projektor TC2163 PN: 85000327 SN: 3710027 | |
| Last calibration | September 2017 | |
| Exported data | S7k files | |
| Unit | - | |
| Notes | The following specifications are taken from the general datasheet | |
| Frequency | 200kHz (400kHz available on request) | |
| Along-track transmit beamwidth | 2.2° (± 0.5°) at 200 kHz / 1° (± 0.2°) at 400 kHz | |
| Across-track receive beamwidth | 1.1° (± 0.05°) at 200 kHz / 0.54° (± 0.03°) at 400 kHz | |
| Max ping rate | 50 Hz (± 1 Hz) | |
| 50 Hz (± 1 Hz) | 33 µsec to 300 µsec | |
| Number of beams | 256EA*/256ED* at 200kHz<br>256EA*, 512EA*, 512ED* at 400kHz | * EA= Equi-angle /<br>ED= Equi-distant |
| Max Swath angle | 128° | |
| Depth resolution | 6mm | |
| | Bathymetry, sidescan & snippets<br>7K data format<br>Gbit Ethernet | |

***Table 3.2.*** *Parameters of the multibeam echosounder Reson SeaBat 7125 integrated on the AUV "Abyss". From Gràcia & INSIGHT Cruise Party, (2018).*

The workflow processes for the AUV raw-bathymetric data includes the following steps: a) Loading the raw-data onto the AUV server; b) Use the Qinsy/Quimera software package to check the multi-beam parameters and verify that it was properly working. With the same software, the data is cleaned and a working map is generated. c) Calibration of the data is carried out using the software PDS2000. d) Once done the first steps, the data is transferred to the MB System software. With this software, the position of the multi-beam head transducer is referenced to the vehicle coordinates and the attitude biases are considered. e) The overlapping areas (i.e., from different dives in adjacent areas) are manually adjusted, using tie-points on both sections resulting in adjustment of the navigation; and f) manual data-cleaning is carried out (Gràcia & INSIGHT Cruise Party, 2018).

### *3.2.3. Sidescan sonar imagery (TOBI)*

A sidescan sonar is a system towed by a research vessel consisting of a set of transducers, which transmit acoustic wave-energy through the water-column to the seafloor and perpendicular to the sailing direction. Once this energy arrives at the seafloor it is specularly-scattered from the seafloor. A portion of this energy is scattered back to the sonar-system, amplified and recorded (Blondel & Murton, 1997). The distance travelled from the acoustic transducer to the seafloor is referred to as the "slant-range", while the horizontal distance between the sonar's nadir and the target is called "ground-range" (Fig. 3.6). The total horizontal distance insonified across the track is referred to as the "swath width" (Blondel & Murton, 1997).

The travel-time of the scattered-wave and its intensity is processed to obtain the acoustic-imaging of the topography, roughness and acoustic properties of the seafloor (Fig. 3.6). The work frequency of these systems is between 30 and 500 kHz, therefore the results of the data acquisition are of high-resolution images (Blondel & Murton, 1997).

The sidescan sonar data used in this Thesis were acquired on board the RV "*Hesperides"* during the "HITS" (*High Resolution Imagining of Tsunamigenic Structures of the Southern Iberian Margins*) survey (Gràcia et al., 2003a; Gràcia et al., 2006) by using the TOBI side-scan sonar vehicle (Flewellen et al., 1993), of the National Oceanography Centre in Southampton, United Kingdom (Fig. 3.7). The TOBI vehicle is 4.25 m long, 1.1 m wide and 1.45 m high and contains along both sides a towed side-scan transducer array pointing down at 20 degrees from the horizontal.

A magnetometer, thermistor and emergency acoustic location beacon complete the usual instrumentation, even though other sensors can also be added (Le Bas et al., 1995). To maintain the stability and buoyancy of TOBI at a constant depth, a 600 kg depressor-fish is connected several meters in front of the towed vehicle. The TOBI sidescan sonar system can work at water depths up to 6,000 m, with a 30 kHz sonar frequency. The vehicle is towed between 200 to 500 m above the seafloor to generate images with 6 m along-track resolution (Blondel & Murton, 1997). The velocity of acquisition during the HITS cruise was about 2.5 to 3 knots. The data acquired for this study consisted of four 6-km-wide parallel tracks covering the MPF area, PSF area, the CSV area and northern of the HF.

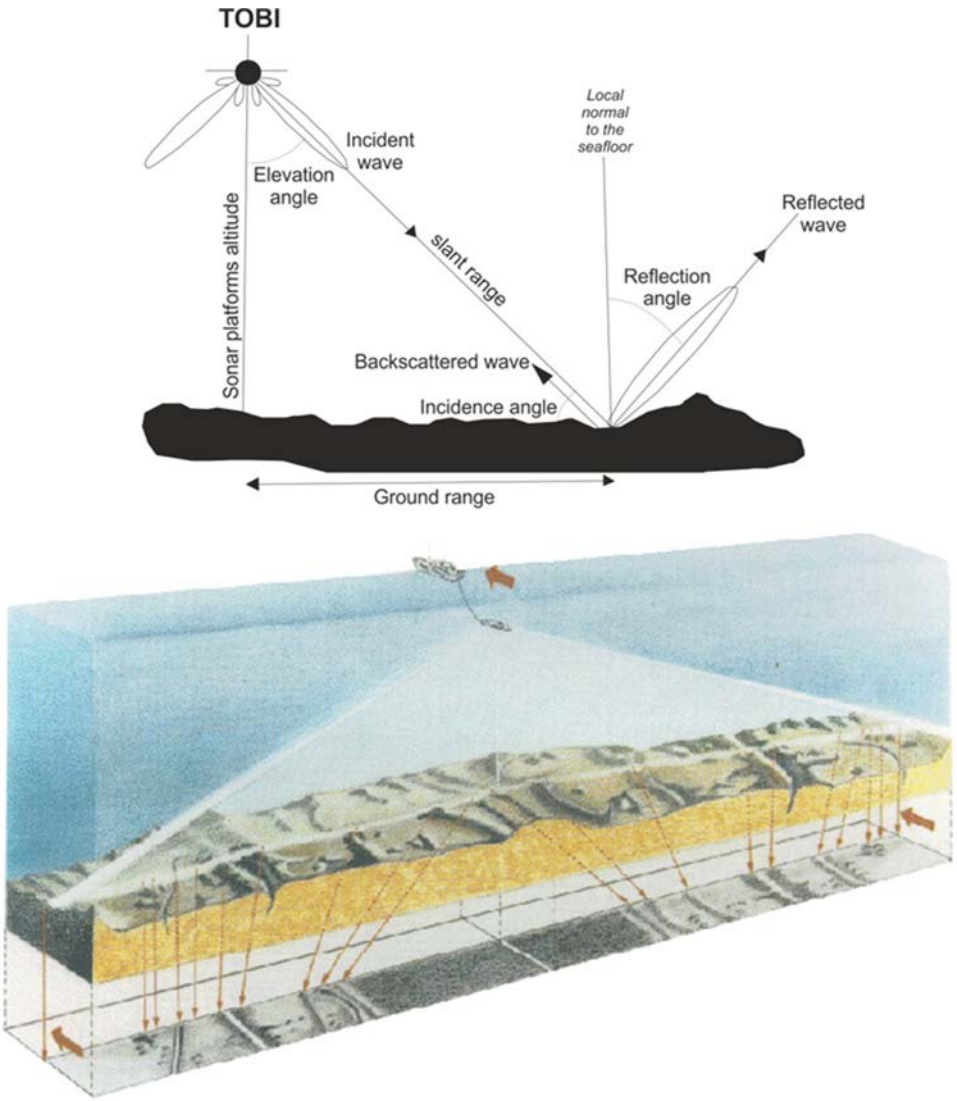


***Figure 3.6**. a) Interaction of the acoustic pulse with the seafloor and definition of parameters. Modified from Blondel & Murton, (1997). b) A side-scan sonar at work, and how the seafloor topography creates changes in the backscattered acoustic energy. From Somers et al., (1978) in USGS,(2020).*

The processing of TOBI data (Fig. 3.7) were done using the softwares *PRISM* and *ERDAS-Imagine.* It involves the following steps (Blondel & Murton, 1997): 1) Correction of the navigation data using the heading, speed, heave, roll, pitch and yaw; 2) Suppression of the sea surface reflections (very important for shallow-waters), which are manifested as bright-lines in the along-track direction. 3) Depending on the incidence angle, two close targets can be identically associated with the same slant-range; hence, slant-range correction to ground-range will be applied using the altitude of the vehicle. 4) During the data acquisition, there are small speed variations along the

transects so the inter-pixel spacing will be different. To correct this variable, the anamorphosis process (reversible deformation of an image) produces an image in which the inter-pixel spacing is the same across- and along-track. 5) A range-dependent illumination coefficient is used on the basis of the seafloor acoustic behaviour. 6) Finally, the correction, filtering and suppression of noise have been carried out. The four TOBI tracks used in this Thesis have been merged, managed and interpreted using the *ArcGIS 10 commercial package*. The TOBI images will be used to interpret small-scale topographic elements of the seafloor and the sedimentary processes of the study area.


***Figure 3.7.*** *The TOBI (Towed Ocean Bottom Instrument) underwater side-scan sonar was used to obtain seafloor images during the HITS-2001 survey on board the RV "Hesperides" (Gràcia et al., 2006; Vizcaino, 2009).*

### *3.2.4. The high-resolution sub-bottom profiler*

Most sub-bottom profiling systems are integrated into research vessels and are used to obtain very high-resolution seismic profiles of the uppermost layers below the seafloor, penetrating the sediments down to few hundred meters. The sub-bottom profiler technique consists of a sound source, the transducer, which generates a vertical acoustic signal through the water-column towards the seafloor. The signal penetrates the seabed and it is reflected when encounters a boundary between two layers with different acoustic impedance (related to the density and the sound-velocity propagation of a

sedimentary layer). The reflected sound signal returns to the vessel and the time that it takes is used to calculate the thickness and the position of the layers below the seafloor. The sub-bottom profiler systems used in this Thesis are based in the parametric effect, which generates a low-frequency signal by the non-linear interaction of two high-frequency signals (Fig. 3.8) providing a narrow beam and good sub-bottom penetration (Martínez-Loriente, 2013).

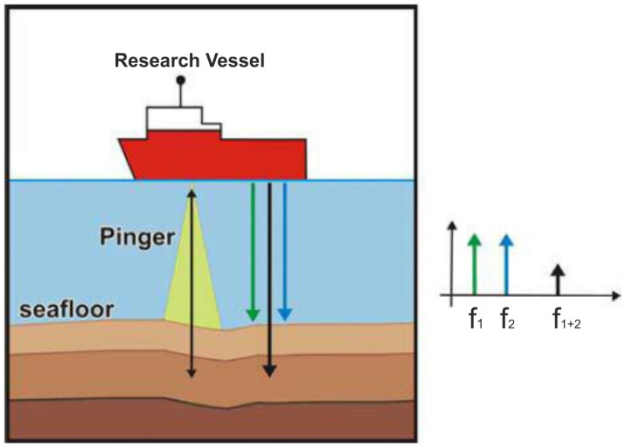


***Figure 3.8.*** *Scheme of the operation of a high-resolution parametric sub-bottom profiler. Modified from Martínez-Loriente, (2013).*

In this Doctoral Thesis, high-resolution sub-bottom profiles from three different surveys (i.e. *SWIM-2006, INSIGHT Leg1-2018 and INSIGHT Leg 2-2019*) have been used. During the SWIM survey (Gràcia et al., 2003a; Gràcia et al., 2006), the Simrad TOPAS PS18 was used. The primary frequency of the system is 15-21 kHz and the secondary frequency is 1 to 6 kHz. Data sampling frequency was 16 kHz. The TOPAS PS18 has a maximum penetration of 80-100 m assuming a sediment velocity of 1.5 km/s (Martínez-Loriente, 2013). During the SWIM 2006 survey, 16 high-resolution TOPAS profiles were acquired simultaneously with the MCS profiles at sailing velocities of 5 knots (Martínez-Loriente, 2013). During the INSIGHT 2018-2019 surveys (Leg1 and Leg2) on board of the RV "*Sarmiento de Gamboa*", the ATLAS Parasound P35 sub-bottom profiler was used. The Parasound uses a primary frequency of 18-39 kHz and a secondary frequency of 0.5 to 6 kHz. The maximum seafloor penetration is up to 150 m. During the INSIGHT cruises (Leg 1 & Leg 2), a Chirp pulse around a centre frequency of 4 kHz and a continuous pulse with a centre frequency of 3.5 kHz have been used. The pulse length was 0.57 ms. and the data was recorded at a sampling rate of 6.1 kHz (Gràcia & INSIGHT Cruise Party, 2018; Urgeles & INSIGHT Cruise Party, 2019).

During the INSIGHT cruises, a total of 71 high-resolution ATLAS Parasound sub-bottom profiles were acquired at sailing speeds between 3 and 8 knots. In general terms, most of the profiles in the three surveys are oriented perpendicular to the selected active faults in the SW Iberia margin. The quality of the sub-bottom profiles highly depends on the sea state, substrate type and morphology of the studied area. The best results are obtained in shallow and flat seafloor, mainly constituted by highly penetrative sediments. Penetration is very low in rock outcrops, while in deep waters the signal is usually weak. Also, in abrupt seafloor topographies with pronounced slopes and scars side echoes usually appear. To reduce noise from various sources as much as possible the recording parameters (i.e., amplitude scale, threshold and bottom TVG) were constantly updated during the two cruises (Urgeles & INSIGHT Cruise Party, 2019) (Fig. 3.9).

The *ATLAS PARASTORE* software was used during the INSIGHT surveys to record, process and visualize the acquired data. Re-processing the sub-bottom profiler data, if needed, can be done using the software *RadexPro.* However, in general, the only processing step recorded in the output SEG-Y files was the envelope generation (i.e., absolute value of the amplitudes contained in the match-filtered data) (Urgeles & INSIGHT Cruise Party, 2019).

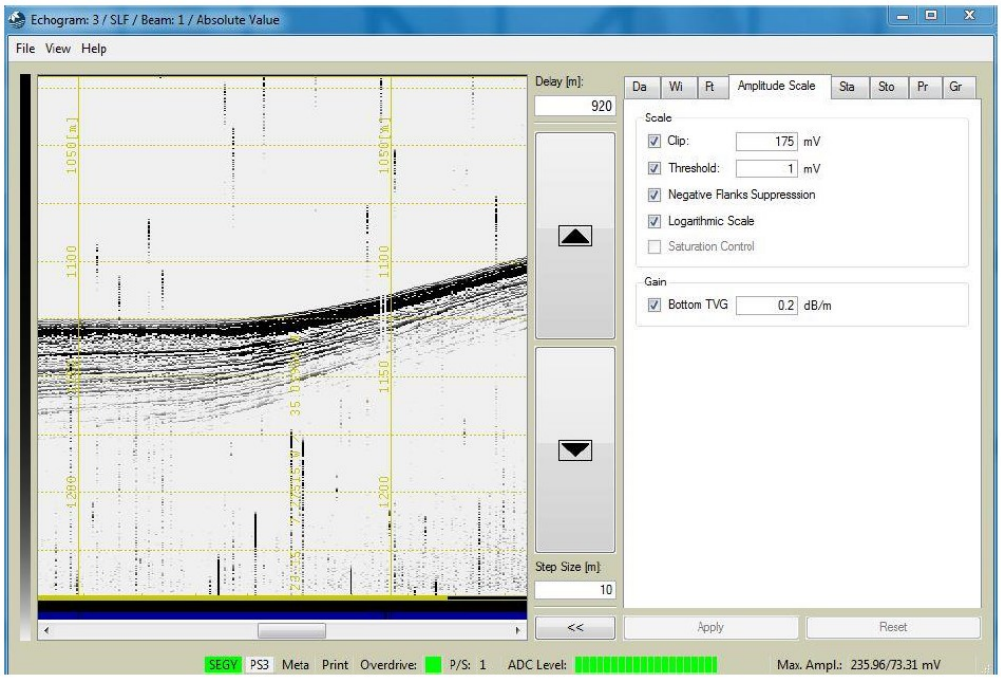


***Figure 3.9.*** *Example of ATLAS PARASTORE Echogram view from the INSIGHT Leg 2 survey. From Urgeles & INSIGHT Cruise Party, (2019).*

The analyses, management and interpretation of the parametric echosounder profiles have been done using the *IHS "Kingdom Suite"* seismic interpretation software. The high-resolution sub-bottom profiles of the first meters below the seafloor, give us important information about the Plio-Quaternary and Holocene active processes, such as active tectonic structures, mass-wasting processes, mud-volcanoes, fluid-flow and gas-escapes.

### *3.2.5. Multi-channel seismic reflection profiles*

The MCS reflection method is one of the most important techniques of geophysical prospecting in the field of marine geosciences. This methodology is often used to study the sub-surface through the artificial generation of a seismic-wave. The MCS reflection method is based on reflection of the sound, which is produced at the boundary of two layers with different acoustic impedance, defined as the product of the wave velocity within a layer and its density (Lowrie, 2007; Yilmaz, 2001). Therefore, physical properties of the sub-surface can be estimated. With this method, water-depth and seafloor and sub-seafloor images can be obtained.

The MCS reflection method works as follows: An artificial seismic signal is generated through an explosion (i.e., acoustic energy), and a shot produced in a point with known spatial coordinates and time. The sound-waves travel with spherical shape through the water-column and propagate in the sub-surface until they are partially reflected and refracted in the surface boundary, between two layers with a contrast of acoustic impedance (Lowrie, 2007). The time that a sound-wave spends from being emitted, reflected in a sub-surface layer and returned to the vessel is recorded by several receivers, as time series. Hence, for each shot several seismic traces are recorded (Yilmaz, 2001) (Figs. 3.10 and 3.11).

The instruments used on the marine MCS exploration are towed by the research vessel. The source of the artificial acoustic signal is, in the case of the seismic data used for this Thesis, the airgun array (Fig. 3.12a), which generates a burst of compressed air from the compressors. The airguns are towed a few meters in between the vessel and the receivers and submerged 1 to 6 m below sea surface. Each airgun generates a pulse of energy (i.e., pressure signature) which is composed by an initial burst and a secondary burst of lower energy that is produced by interaction between the air bubbles of the initial burst and the water (Parkes & Hatton, 1986). To disable as much as possible the bubble effect and to obtain a single spike signal, combinations of airguns with different

air-capacity chambers are simultaneously used. Synchronizing the energy of the first bubble as much as possible to destroy the rest of the signal. The time between two consecutive shots is referred as the shot-interval.

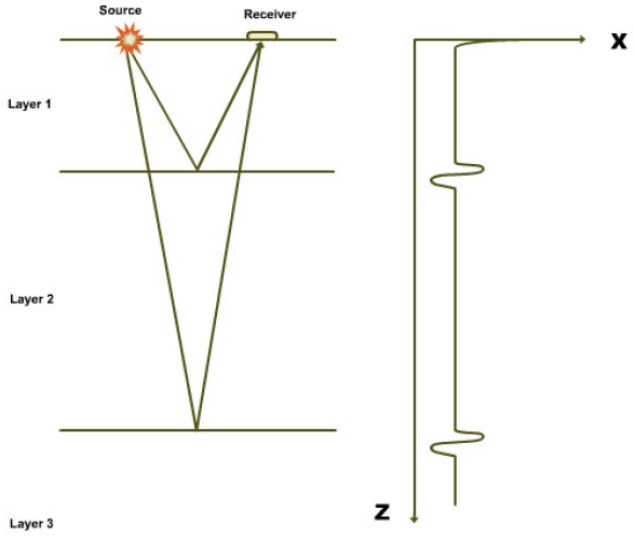


***Figure 3.10.*** *Example of recorded signal (seismic trace) using the reflection energy produced by the acoustic impedance contrast between two different layers. From Mjelde et al., (2013).*

The receivers or recording instruments are the hydrophones, which are periodically distributed (i.e., group interval), along a cable referred to as the streamer (Fig. 3.12b). The hydrophones are made of piezo-electric ceramics that deform due to the effect of the differential pressure produced when the reflected seafloor and sub-surface layers signal arrives at the surface and generate an electrical impulse (i.e., voltage difference) (National Ocean Service, 2020).

The group interval for deep MCS exploration is about 25 m to 15 m, while for high-resolution MCS exploration this distance is reduced to 3.125 m or 6.25 m (Martínez-Loriente et al., 2013). To maintain a constant buoyancy and control of the streamer depth, a series of instruments referred to as "birds" are systematically attached along a certain fixed distance of the streamer (Fig. 3.12c). These "birds" incorporate compasses to monitor the streamer position and control its course to avoid deviations. Finally, the last element of the streamer is the "tail buoy" that incorporates a GPS to record with precision the position of the end of the streamer.

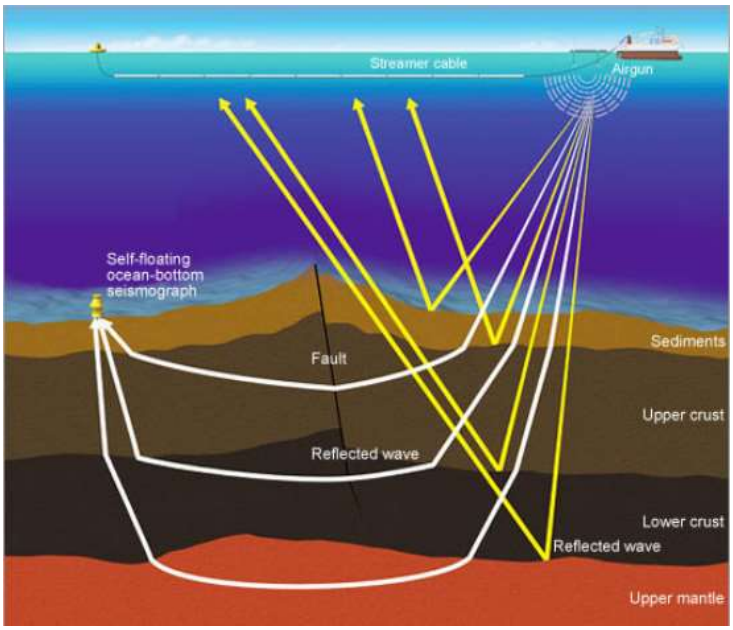


***Figure 3.11.*** *Scheme of the function of the MCS reflection methodology. The yellow lines represent the reflected wave and the white lines the refracted wave. From Japan Agency for Marine-Earth Science and Technology, (2020).*


***Figure 3.12.*** *MCS reflection elements used during the INSIGHT cruises. a) Airgun array 10 G-GUNII, b) GeoEel Geometrics streamer, c) Bird. From Gràcia & INSIGHT Cruise Party, (2018); Urgeles & INSIGHT Cruise Party, (2019)*

In the seismic traces, aside of the primary reflections of the sub-surface layers, coherent and incoherent noise, such as multiples, refracted wave, source bubbles etc is usually found. All these noise reduce the quality of the MCS profiles and should be corrected by processing of the seismic data. Depending on the MCS equipment used, the acquisition parameters and the studied area, different processing steps need to be applied. However, there are three basic steps that will be applied in all seismic data processing: a) Deconvolution, b) Common Mid-Point (CMP) stack and c) Migration (Yilmaz, 2001). The objective of the deconvolution step is to increase the vertical resolution of the data. To get it, the signal is compressed (wavelet) close to a spike and the reverberations are suppressed. The deconvolution tries to approximate the generated wavelet to the earth-impulse response. CMP stack will increase the signal-to-noise ratio. The migration step removes the diffractions and puts the reflections closer to their real position in the sub-surface, increasing horizontal resolution (Gómez de la Peña, 2017). An example of a complete processing for a specific case is the "INSIGHT-Leg2" processing-flow that is showed in the figure 3.13 (Urgeles & INSIGHT Cruise Party, 2019). The profiles are usually exported in "SEG-Y" format to easily import the resulting sections into the interpretation software.

In this Thesis, a total of 74 MCS reflection profiles has been used (Fig. 3.14). These profiles were collected in the frame of six marine cruises in the SW Iberian Margin: The ARRIFANO, IAM, BIGSETS, VOLTAIRE and INSIGHT Leg1 and Leg 2 surveys shown in Fig. 3.14. These profiles were interpreted from scratch, while the SWIM profiles and the three southernmost BIGSETS profiles had been corroborated or re-interpreted from previous interpretations carried out by Martínez-Loriente et al., (2013, 2018). The analyses and geological interpretation of the MCS profiles used in this study were carried out using the "IHS Kingdom Suite" seismic interpretation software. The physical parameters and main processing steps of the different surveys are here described and synthesized in the table 3.3.

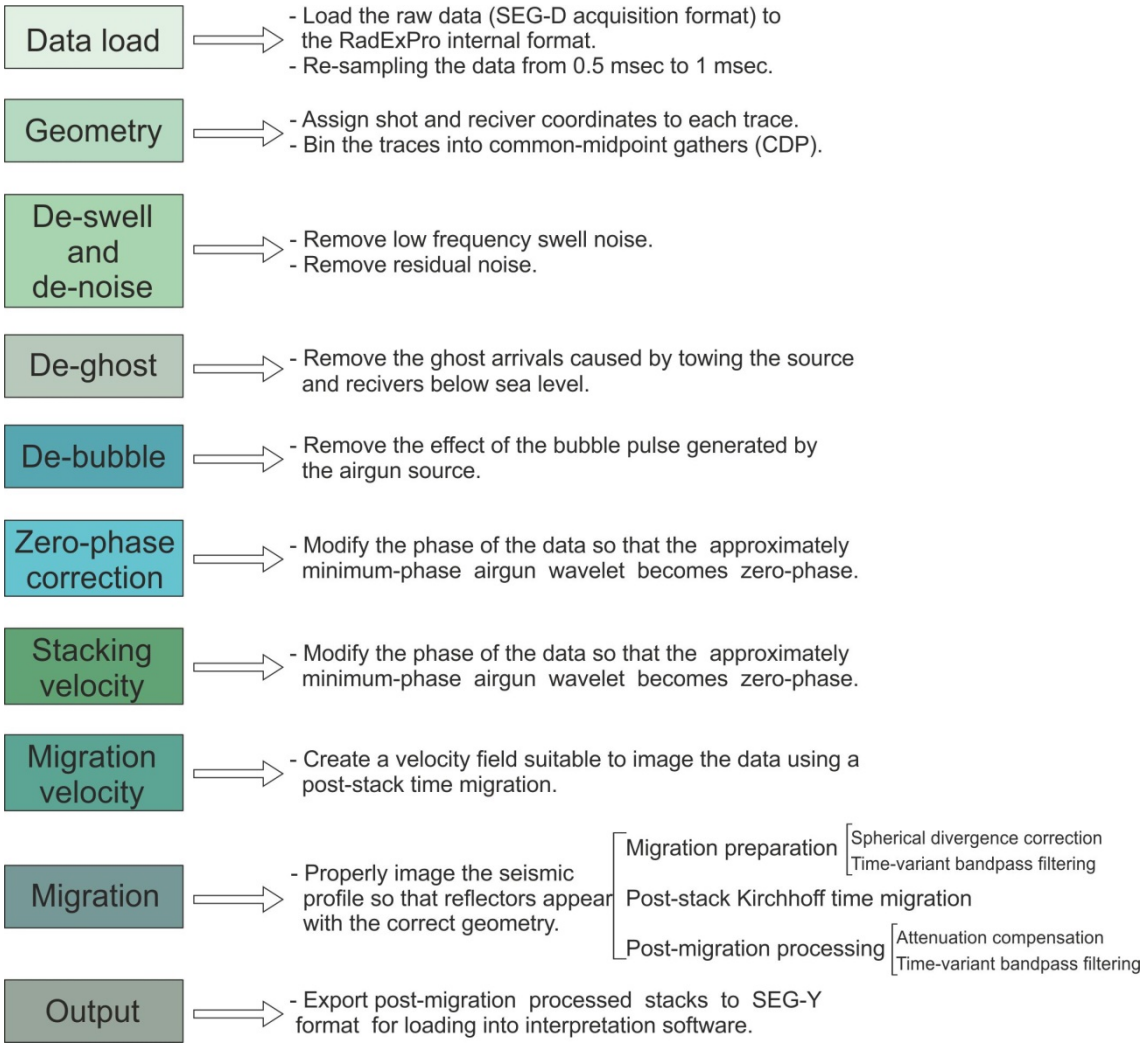


***Figure 3.13.*** *Example of a complete processing workflow for the MCS profiles acquired during the INSIGHT-Leg 2 survey. Information from Urgeles & INSIGHT Cruise Party, (2019).*

The "AR" profiles, belonging to the 1992 ARRIFANO cruise, were acquired with the RV OGS "Explora" (Zitellini et al., 1999). This survey used an airgun array of 32 guns with a total capacity of 4880 cubic inches (c.i.) and a 3-km-long streamer with 120 channels and 50 m shooting interval (Zitellini et al., 1999). The AR data was re-sampled to 8 ms and processed with spiking deconvolution, spherical divergence correction, NMO correction, finite-difference wave-equation migration and time variant band-pass frequency filter (Zitellini et al., 1999).

The IAM profiles, belonging to the 1994 IAM cruise were acquired on board the Geco Sigma vessel (Banda et al., 1995). In this survey, 30 airguns with a total volume capacity of 7524 c.i. and a 4.8 km-long streamer with 192 channels and 75 m shooting interval were used. The processing of IAM MCS profiles consisted in resampling to 8 ms, trace-editing, spherical divergence correction, deconvolution, FK de-multiple,

NMO correction, spherical divergence correction, noise attenuation FK filter as well as time and space variant band-pass frequency filter (Banda et al., 1995).

The "BS" profiles from the BIGSETS survey were acquired on board the RV "Urania" during November 1998 (Zitellini et al., 2001). The seismic source consisted of an array of two GI-guns with a total volume ranging from 150 to 465 c.i. The seismic signal was recorded with a 48 channels, 1.2 km-long streamer and 25, 37 and 50 m shooting interval (Zitellini et al., 2001, 2004). The processing of BIGSETS MCS data consisted in spiking deconvolution, velocity analyses every 2.5 km, NMO correction, spherical divergence correction and finite-difference wave-equation time-migration using stack velocities reduced by 10% (Zitellini et al., 2004).

The "VOL" profiles correspond to the 2002 VOLTAIRE survey that was carried out on board the RV "Urania". On this survey, 2 GI guns totalling 210 c.i. were shot every 50 m and a 600 m-long, 48 channel-streamer was used (Terrinha et al., 2009). The MCS VOLTAIRE dataset was re-sampled to 2 ms and processed with trace editing, shot delay removal, amplitude recovery, predictive deconvolution, velocity analysis every 200 CMPs, NMO correction, stack, bandpass-frequency filtering and time-migration using stack velocities reduced by 10%.

The "SW" profiles correspond to the SWIM survey that was carried out on board the RV "Hesperides" in 2006. During the survey, an array composed by 8 airguns with a total volume capacity of 1050 c.i. was shot every 37.5 m and a 2.4 km-long, 96 channels streamer was used. The SWIM data-processing includes data resampling to 4 ms, channel and shot-editing, top-mute in a shot gather domain, true amplitude recovery, FK and bandpass filters, deconvolution, NMO corrections and brut-stack, spiking deconvolution, Stolt FK migration and bandpass filter. After the normal processing, a pre-stack depth migration is applied to represent the MCS profiles in the depth domain (Martínez-Loriente et al., 2013) .

The "INS" profiles from the INSIGHT Leg-1 and Leg-2 cruises were acquired on board the RV "*Sarmiento de Gamboa*" during May 2018 and October 2019, respectively. The seismic source for both legs consisted of an array of 10 G-guns with a total volume capacity of 930 c.i., shot at intervals of 25 m. The seismic data were recorded with a 72 channels. 445 m-long streamer for Leg-1, and a 56 channels, 350 m-long streamer for Leg-2. The channel spacing in both cases was 6.25 m. The processing of the INSIGHT data included resampling to 1 ms, navigation and geometry

corrections, trace editing, swell noise-attenuation, de-ghost correction, de-bubble filter, zero-phase band-pass filtering, CMP binning and NMO correction, and final stacking.

| Survey | Year | Vessel | Seismic Source | Streamer length | Channels | Shooting interval |
|---|---|---|---|---|---|---|
| ARRIFANO | 1992 | Explora | 32 airguns (4880 c.i.) | 3 km | 120 | 50 m |
| IAM | 1994 | Geco Sigma | 30 airguns (7524 c.i.) | 4.8 km | 192 | 75 m |
| BIGSETS | 1998 | Urania | 2 GI-guns (465 c.i.) | 1.2 km | 48 | 25, 37 and 50 m |
| VOLTAIRE | 2002 | Urania | 2 GI-guns (210 c.i.) | 600 m | 48 | 50 m |
| SWIM | 2006 | Hesperides | 8 airguns (1050 c.i.) | 2.4 km | 96 | 37.5 m |
| INSIGHT-Leg1 | 2018 | Sarmeinto de Gamboa | 10 airguns (930 c.i.) | 445 m | 56 | 12.5, 18.5 and 25 m |
| INSIGHT-Leg2 | 2019 | Sarmeinto de Gamboa | 10 airguns (930 c.i.) | 350 m | 56 | 12.5 and 18.75 m |

***Table 3.3.*** *Summary of the acquisition parameters of the MCS profiles used in this PhD Thesis.*

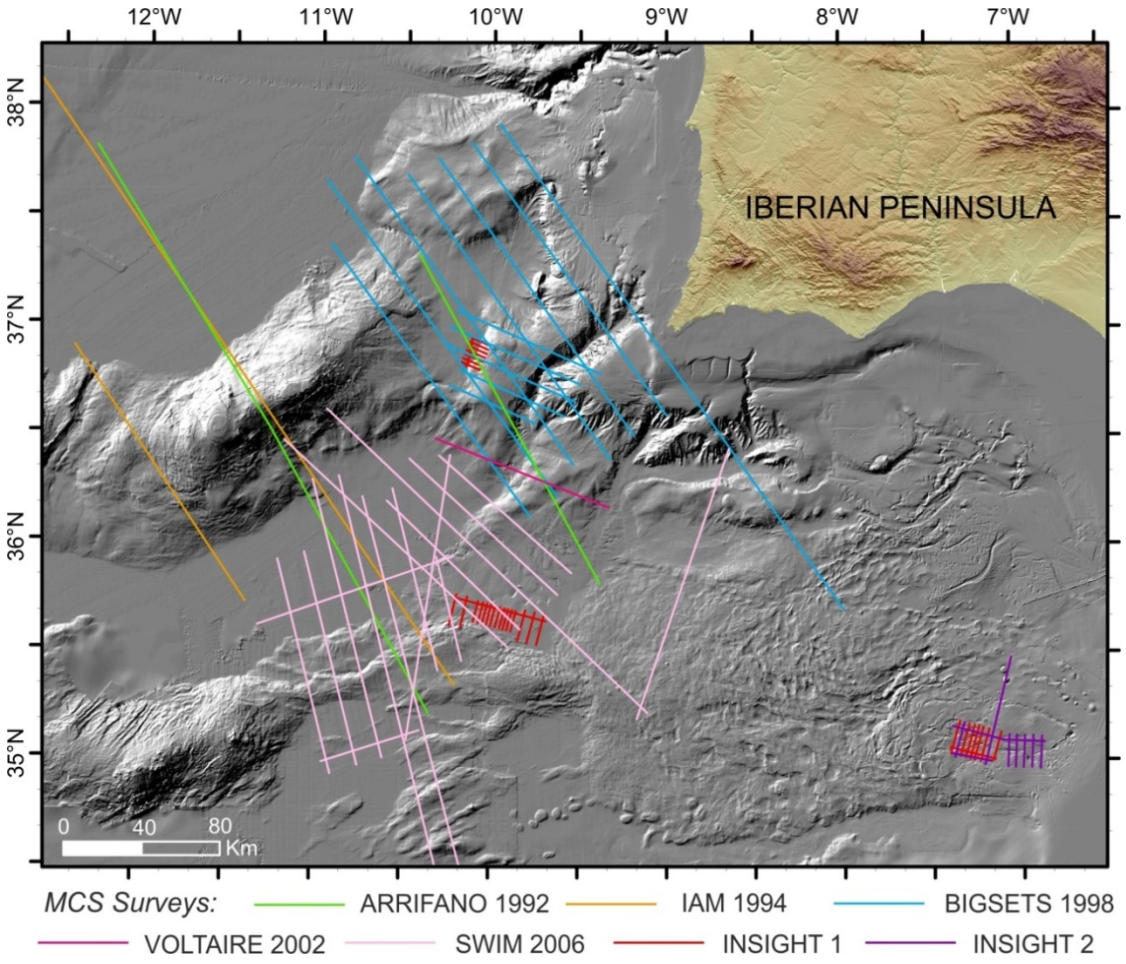

***Figure 3.14.*** *Geographical location of the MCS profiles used in this thesis. Shaded relief map of the external part of the SW Iberian Margin (Atlantic Ocean).*

## 3.3. Data interpretation criteria

Once the data is fully processed, it should be analysed and interpreted accurately and objectively using globally accepted distinct criteria for each type of data. The main interpretation criteria used in this PhD Thesis are explained below.

### *3.3.1. The TOBI interpretation criteria*

The TOBI sidescan sonar images are generated from seafloor backscattered sound, as explained above. The backscatter highly depends on geometry of the sensor-target system (i.e., angle of incidence of each beam and local slope), physical characteristics of the surface, and intrinsic nature of the surface (e.g., composition, density, etc.) (Blondel & Murton, 1997). In TOBI mosaics, different acoustic facies can be identified depending on seafloor composition and roughness. When the seafloor is hard (e.g., outcrops), a significant amount of backscattered energy is returned and the TOBI mosaic displays white and light-grey colours. For blocks and coarse-grained seafloor sediments, the backscatter is medium and the TOBI image mainly shows grey-colours. When the seafloor is constituted by fine-grained sediments (such as hemipelagic sediments), the backscatter is low and the TOBI mosaic displays dark-grey colours. When a completely black area appears in the TOBI mosaic (no backscatter), it is interpreted as an acoustic shadow due to an outstanding element in the terrain (i.e., resulting from an object with significant relief). In a similar way, the texture of the TOBI image, spatial organization of the grey levels (backscatter) within a neighborhood (Blondel et al., 1998) highly varies depending on the seafloor material. The textures can be described as smooth or rough, small-scale or large-scale, random or organised (Blondel et al., 1998).

On the basis of the characteristics explained above, the following TOBI acoustic facies can be distinguished (Fig. 3.15):

a) High backscatter area with high frequency linear to undulated fabric interpreted as rock outcrop with stratification (e.g. slightly dark lines).

b) High backscatter area with large-size grainy pattern interpreted as coarse grained sediment.

c) Medium and low backscatter area with small-scale grainy pattern interpreted as fine-grain sedimentary deposits.

d) Heterogeneous medium-backscatter area with a large-size grainy texture and a slightly dark lineal fabric that corresponds to channels in the canyon bed.

e) Low-backscatter area with rough texture and large acoustic shadows interpreted as gullies and scars.

f) Medium-backscatter image with a slightly bright backscatter and grainy pattern area in the center interpreted as homogenous landslide deposit.

g) Low-backscatter area with a rough and irregular semi-circular morphology associated with large acoustic shadows interpreted as a scar.

h) Medium and low backscatter area with a rough texture and small acoustic shadows interpreted as fossilized gullies by hemipelagic sedimentation.

i) Homogeneous low-backscatter area with small-scale grainy pattern interpreted as Very fine-grained sediment, probably hemipelagic sedimentation.

j) Heterogeneous backscatter image, with high backscatter area of large-size grainy pattern interpreted as coarse grained sediment; and homogenous low backscatter lineal fabric interpreted as ocean-floor ruptures.

k) Acoustic high-backscatter facies with high frequency linear to undulated fabric corresponding to a sedimentary outcrop.

l) Artifact located at the margins of the TOBI track.

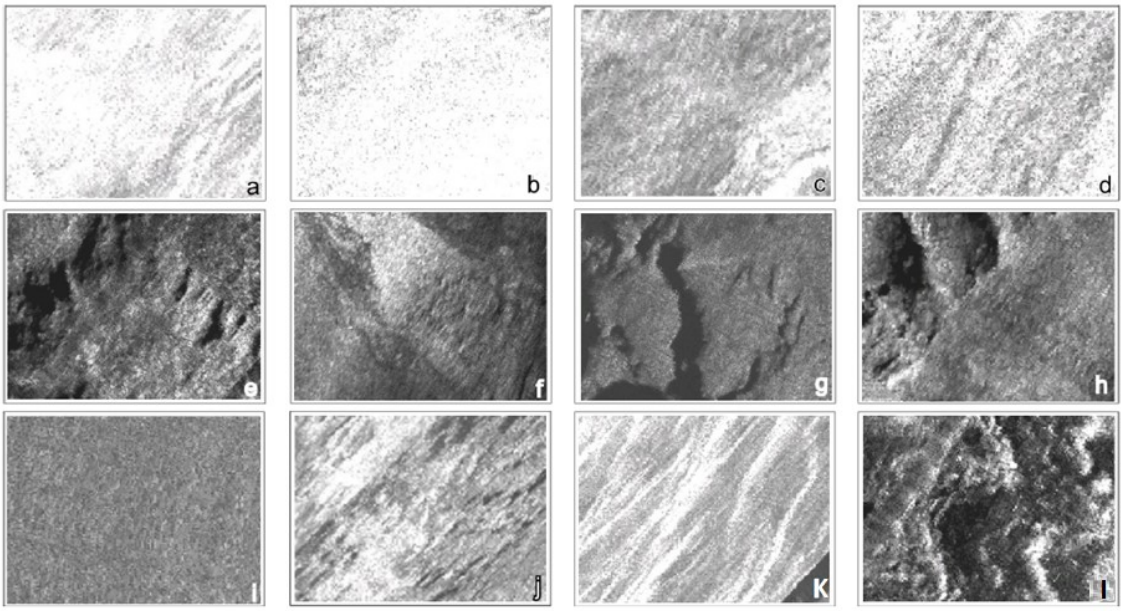


***Figure 3.15**. Selection of different TOBI acoustic facies in the study area. From Vizcaino, (2009).*

### *3.3.2. Interpretation criteria for high-resolution sub-bottom and MCS profiles*

The interpretation of the high-resolution sub-bottom profiles and MCS profiles is based on seismic facies (i.e., internal and external configuration/geometry, lateral continuity, amplitude and frequency). Although the same sedimentary package may display different seismic facies depending on the source and receiver characteristics (hence resolution and sub-bottom penetration), the same classification scheme can be used for data of different source-receiver characteristics.

To carry out an accurately seismic stratigraphic interpretation, first, the different seismic facies should be identified on the base of their acoustic characteristics. The main parameters to analyze are the follow (Brown Jr. & Fisher, 1980) (Fig. 3.16):

- Reflections configuration: Patterns of the seismic reflections (reflections geometry) than can be: Parallel, Subparallel, Divergent, Oblique parallel, Oblique trangential, Complex Sigmoid Oblique and Sigmoid. Geologically, the configuration of the reflectors can be interpreted as, bedding patterns related to the depositional processes, erosion or paleotopography or presence of fluids.
- Reflections continuity: Degree of uninterrupted reflectors. The continuity of a reflection depends on the continuity of the velocity contrast along the strata, therefore, continuous reflectors in geological terms represents depositional processes with strata lateral continuity.

- Amplitude: Degree of velocity-density contrast along stratal surface. Geologically depends on the material density contrast, bed spacing and fluid content.
- Frequency: Number of reflectors in a defined space. In geological terms the frequency depends on the bed thickness and the fluid content.

In general terms a seismic reflection represent an isochronous surface, except if the reflection surface is an unconformity. Unconformities are surface of erosion or non-deposition which represents gaps in the geological record (Brown Jr. & Fisher, 1980). Unconformities can be identified in the seismic profiles finding reflection terminations. Based on the position with respect the discontinuity the terminations can be classified in: Onlap and Downlap if the termination is above the discontinuity; or Truncation and Toplap if the termination point is located below a discontinuity (AAPG, 2015; Brown Jr. & Fisher, 1980) (Fig. 3.16).

High-resolution sub-bottom and MCS profiles usually display transparent, hyperbolic and chaotic seismic facies (Fig. 3.17). The transparent and chaotic facies are usually related to the presence of mass-wasting deposits, free gas and fluid escape features. The hyperbolic facies are common in high-resolution sub-bottom profiles, corresponding to unstable areas, rocky outcrops and high-slope areas.

Once the acoustic characteristics have been analyzed, and the seismic facies classified, the seismic units are described on the basis of the geometric relationship between reflectors (Fig. 3.16). In the case of this PhD thesis, the seismic units interpreted in the seismic profiles where previously defined by Martínez-Loriente et al., (2013) based on the DSDP Site 135 (Hayes et al., 1972) located in the study area.

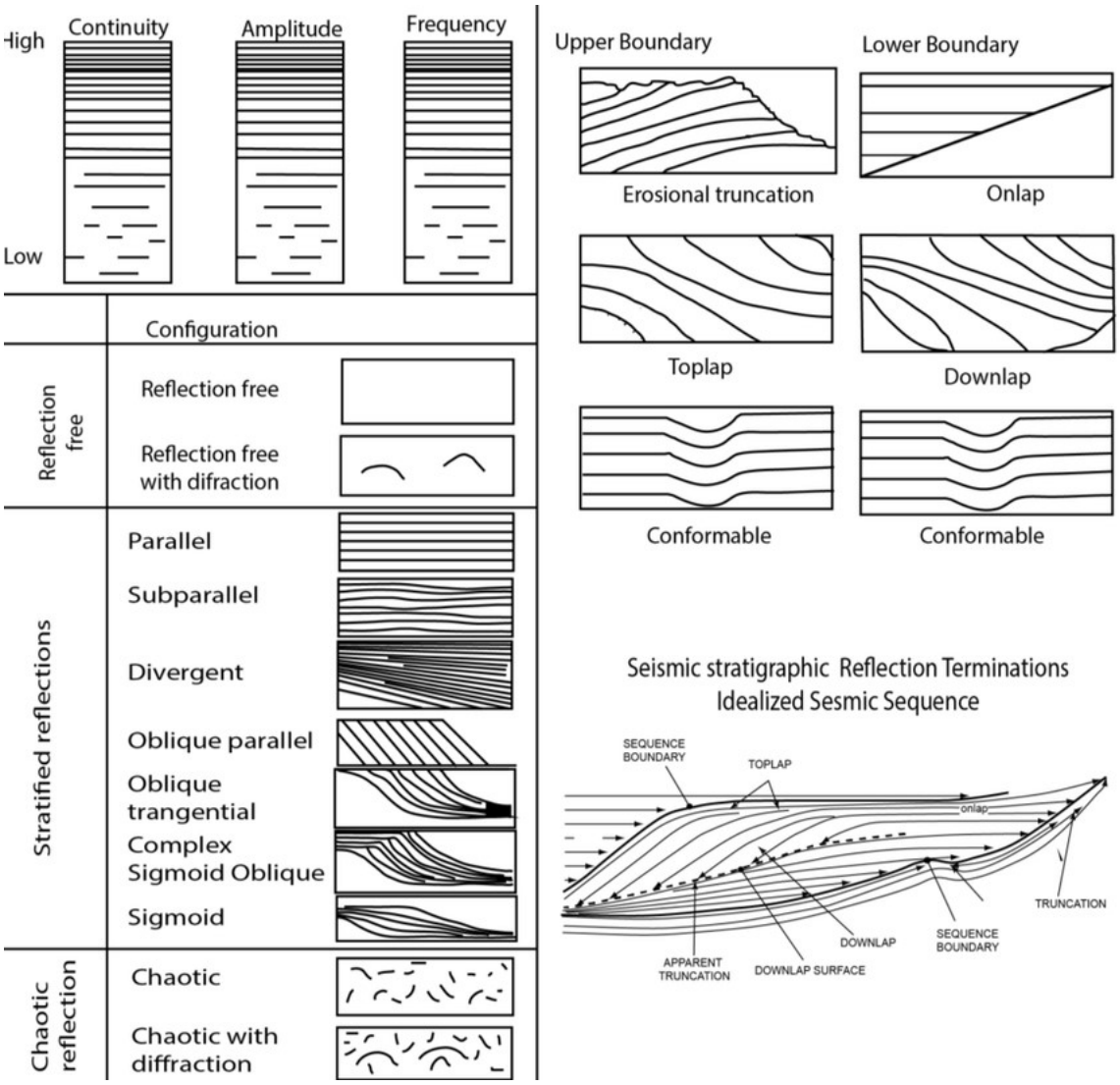


***Figure 3.16.*** *Different seismic configurations used to describe the acoustic properties and geometrical relationship between different seismic horizons. From Mitchum Jr. & Sangree, (1977).*

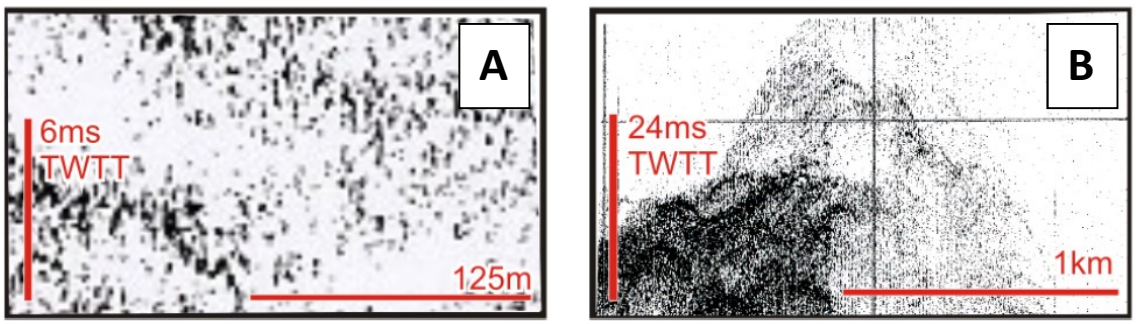


***Figure 3.17.*** *Transparent (a) and hyperbolic (b) seismic facies from a TOPAS profile. Modified from Vizcaino, (2009).*

Once the acoustic properties of the reflectors and their geometric relationships are described, the presence of fractures and their recent activity are described. The main fault indicators in seismic profiles are the following (Martínez-Loriente, 2013):

a) Abrupt terminations of reflectors towards the fault plane (cut-offs).

b) Abrupt termination of fold-limbs and kink-bands.

c) Fault-plane reflections generated by the change in velocity and density across or within the fault.

Finally, in this Thesis a tectonic structure is classified as active if the following elements are identified in high-resolution sub-bottom profiles and/or in the MCS profiles:

a) Fault planes that generate surface-ruptures

b) Presence of recent folding that is generated by a blind-thrust.

c) Presence of growth-strata generated by a blind-thrust.

## 3.4. The Tsunami modelling process

Taking into account all previous methodological information together with the data exposed above, the simulation of tsunamis that the largest faults in SW Iberia margin can generate is carried-out. The simulations carried out in this Thesis involve the worst-case tsunami scenario for the following faults:

- The GBF and the HF. They are the largest reverse-faults in the study area with a seismicity cluster associated. In addition, several authors propose that these faults may be a possible source of the 1755 Lisbon earthquake and tsunami.
- The MPF. It is a 50 km long active thrust and has been proposed by several authors as the source of the 1755 “Lisbon earthquake and tsunami”.
- The NCPF and the SCPF. They have been recently mapped in detail, and they are active thrusts. However, no previous study attempted to simulate a tsunami originating in these faults.
- The LSF. It is the largest strike-slip fault in the SW Iberian margin. The LSF is also the plate boundary between the Eurasian and African plates that goes from the HAP (West) to the to the accretionary wedge (East), where numerous mud-volcanoes, diapirs, giant-countourites and levees are located.

The dataset used in this Thesis for the tsunami simulations includes the existing swath-bathymetry (Fig. 3.1) as well as the collection and integration of TOPAS sub-bottom profiles and MCS data (Fig. 3.18 and section 3.2.5).

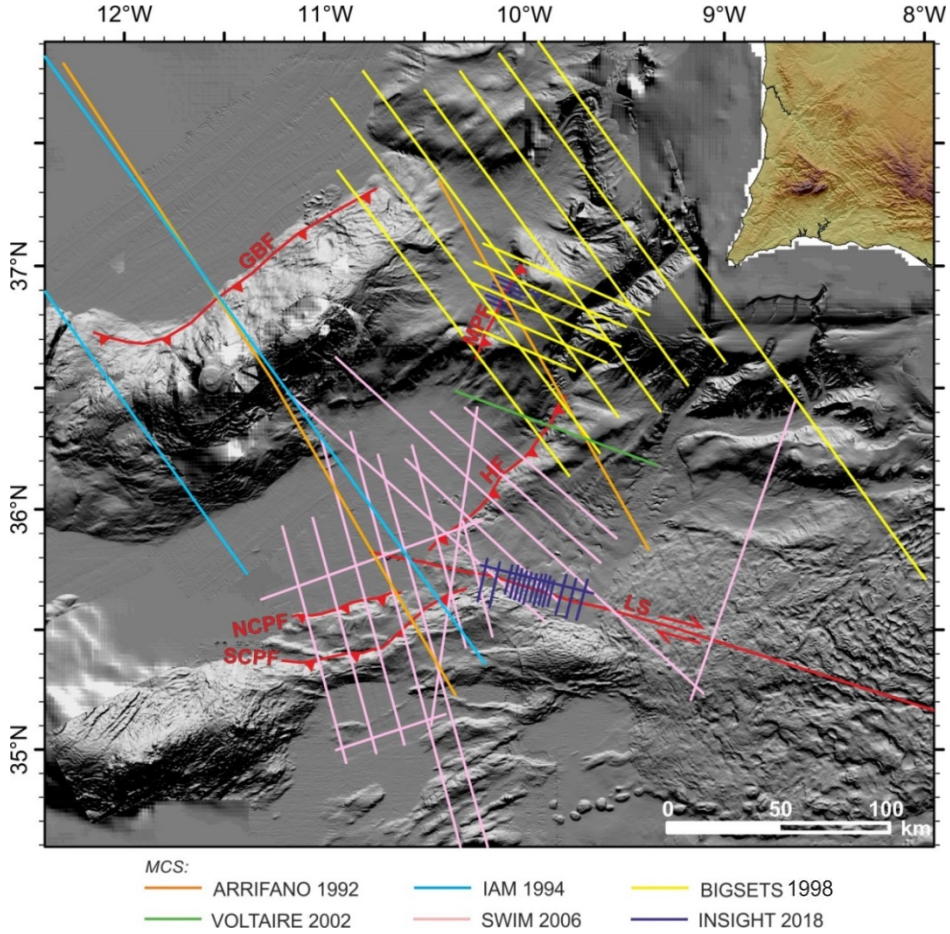


***Figure 3.18.*** *Relief map of the external part of the SW Iberian margin. Colour lines correspond to the TOPAS and MCS profiles used in this study and acquired during different marine surveys.*

### *3.4.1. The Workflow*

The basic workflow to obtain the tsunami scenarios here presented involves four major steps (Fig. 3.19). Note that not all of these steps, described below, apply to all considered cases, depending on whether simple or complex fault geometries and uniform or heterogeneous slip distributions are considered for each specific fault.

(1) The TOPAS and MCS profiles (TWTT- Two-Way Travel Time) are interpreted with the aid of the IHS Kingdom software, to define the sub-seafloor geometry of the main active faults. The fault-traces along the seafloor are mapped based on the TOPAS interpretation, MCS profiles and topographic fault expression. Based on the tectonic and stratigraphic interpretation of the 2D-MCS profiles, triangular 3D-meshes of selected

fault surfaces and adjacent stratigraphic horizons, are constructed using the Delaunay triangulation method within the MOVE software (Fig. 3.20). To convert the 3D-subsurface models from time (TWTT) to depth (km), velocity values are assigned to the main units: a) Basement: 3500 m/s, b) Jurassic: 2700 m/s, and c) Plio-Quaternary: 2000 m/s. The assigned velocity values are based on existing velocity models used to perform the PSDM (Pre-stack depth migration) for the SWIM profiles (Martínez-Loriente et al., 2013). To validate the time-to-depth conversion, the results are compared with the position of the horizons and the geometry of the faults in the PSDM SWIM profiles.

(2) The size of realistically large ruptures that can be hosted by the reconstructed faults is determined starting from a fault area covering almost the entire fault plane. It is first assumed that a fault may rupture entirely along one of its principal dimensions (either length or width), taking the first saturating value of length or width while honouring the empirical scaling relations proposed by Leonard, (2014) for crustal earthquakes in interplate regions. The earthquake moment magnitude ($M_w$) and average slip are both then derived from the relationships $M_w = a + b\ x\ log\ (X)$, where $a$ and $b$ are empirically derived constants that depend on the tectonic setting and the faulting style, and $X$ can be either length, width or average slip. Next, the average direction of fault movement (rake) is estimated from the direction of the maximum horizontal stress axes (Carafa & Barba, 2013). Only the expected values of the relationships are used in this work, disregarding the associated uncertainty.

(3) The heterogeneous slip-distribution is applied to both, the simple and the complex HF models. For a given magnitude, each rupture surface is built starting from a geometric centre (i.e., midpoint of the length and width of the fault plane) and then, iteratively adding neighbour mesh cells; the process arrests when the area exceeds the expected value for that magnitude (Scala et al., 2020). An asperity is defined according to a Gaussian-shaped Probability Density Function. A heterogeneous slip distribution can be superimposed using a stochastic composite "k-square" ($k^{-2}$) source model (Ruiz et al., 2011) based on random spatial distribution of overlapping circular dislocations (sub-asperities), optimized for non-regular surfaces (Herrero & Murphy, 2018).

(4) Finally, tsunami simulations are performed using the Tsunami-HySEA software, a finite-volume multi-GPU-optimised code that solves nonlinear shallow-water equations in spherical coordinates (de la Asunción et al., 2013) (Figs. 3.21, 3.22, and 3.23). The files to perform the tsunami simulations are available in Annex 1. The

initial seawater elevation is considered equal to the vertical displacement of the sea bottom, computed as a Volterra's formulation of the elastic dislocation theory applied to a source buried in an elastic half-space, using the Okada (1985) code for the uniform slip ruptures and the Meade (2007) code for the complex ruptures obtained as superposition of triangular patches. The rake angle is kept constant all over the fault in all cases. The rupture is considered instantaneous and the initial velocity field is zero. Tsunami simulations have been conducted on a regular grid (SRTM15+) with a spatial resolution of 15 arc seconds, considering open boundary conditions. Results of tsunami modelling are processed to obtain regional tsunami wave propagation patterns and maximum wave height (MWH) profiles at selected coastal points. MWHs are extracted at approximately 50 meters depth. They are subsequently extrapolated at the 1 m depth using the Green's law approximation for 1D shoaling as the 4th root of the 50 m, that is by applying a multiplicative amplification factor of ~ 2.66. For each modelled tsunami, arrival times at the coast are calculated with the TTT software (Geoware, 2015), using the 15 arc-sec digital bathymetry (SRTM15) Sandwell et al., (2020), 64 Huygens nodes, and a set of source points on a rectangle obtained from the projection of the fault on the Earth's surface. While it might be assumed that here in most of the cases the arrival times refer to the same portion of the wave train that includes the maximum wave height, this is not necessarily the case and late significant arrivals are always possible. In the chapter 6, we report both the MWH and the arrival times.

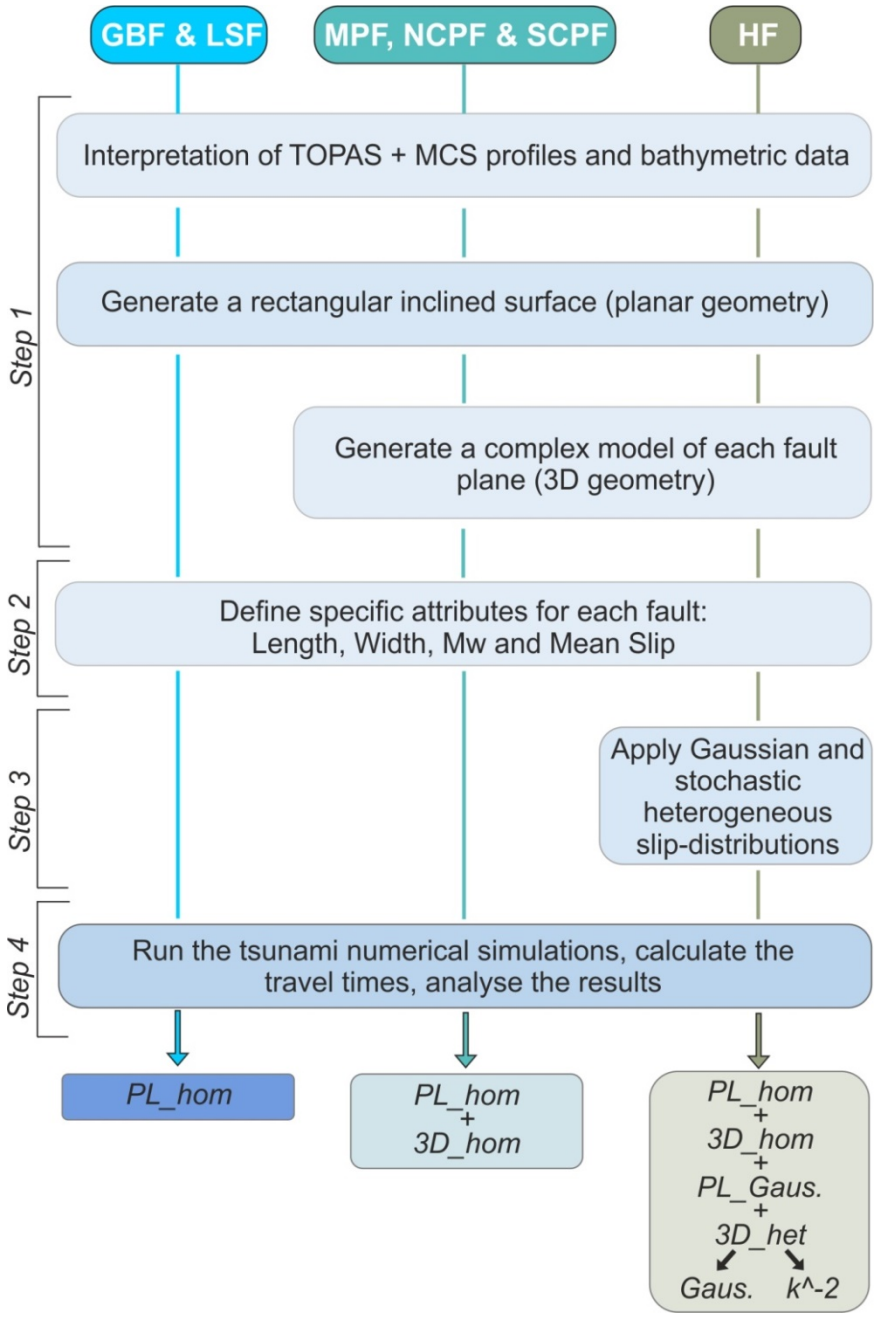


***Figure 3.19.*** *Workflow to obtain a tsunami scenario as realistic as possible based on the characteristics of the faults (GBF, LSF, MPF, NCPF, SCPF and HF) and available data. PL_hom: Tsunami scenario obtained using a planar fault geometry and homogeneous slip distribution; 3D_hom: Tsunami scenario obtained using a 3D fault geometry and homogeneous slip distribution; PL_Gaus: Tsunami scenario obtained using a planar fault geometry and Gaussian heterogeneous slip distribution; 3D_het: Tsunami scenario obtained using a 3D fault geometry and heterogeneous (Gaussian and k^-2) slip distribution.*

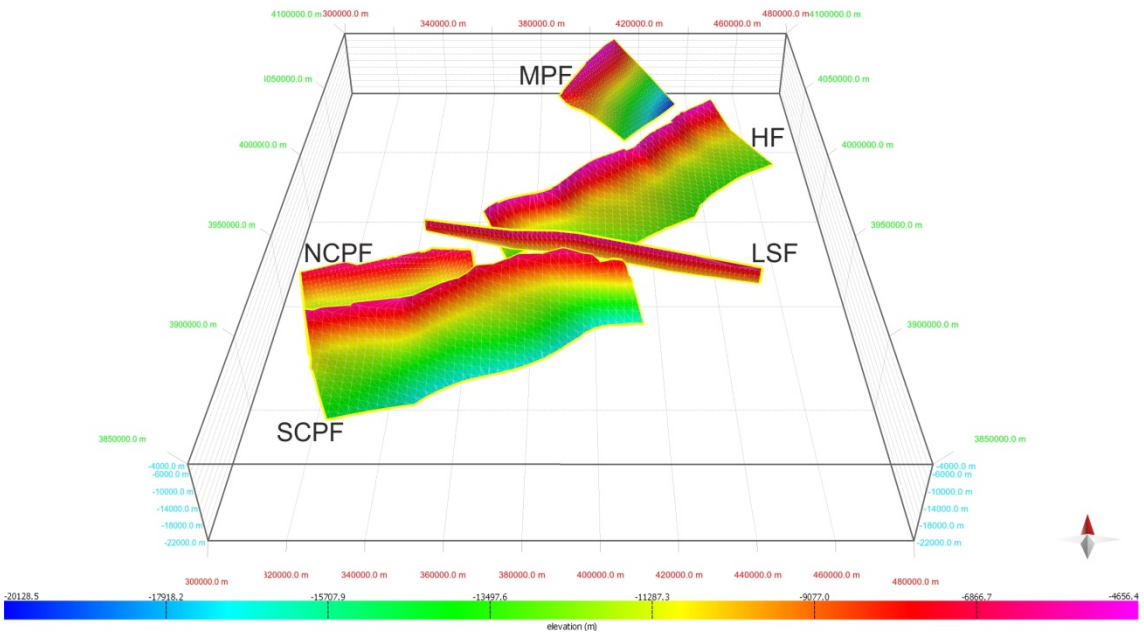


***Figure 3.20.*** *Complex triangular 3D meshes of the fault planes displayed in the software MOVE-view. HF: Horseshoe Fault; LSF: Lineament South Fault; MPF: Marquês de Pombal Fault; NCPF: North Coral Patch Fault; SCPF: South Coral Patch Fault.*

```
HF_mean_Def              # Title
Cadiz15.grd         # Bathymetry file for level 0
1                   # Initialization type (1: Standard Okada, 2: Triangular Okada, 3: Okada from file, 4:
Gaussian)
0               # Apply Kajiura filter to the Okada deformation (0: no, 1: yes)
1                   # Number of faults (>= 1)
0. -10.0485 36.1470 6.6 107 38.7 50 20 75 2.46    # Time(sec) Lon_epicenter Lat_epicenter Depth_hypocenter
(km) Fault_lenght(km) Fault_width(km) Strike Dip Rake Slip(m)
HF_mean_Def               # NetCDF file prefix for level 0
1 1 0 0 0 0       # Variables saved (eta, maximum eta, velocities, modulus of velocity, momentum flux,
maximum momentum flux) (1: save, 0: do not save)
1                   # Number of levels
1                   # Upper border condition (1: open, -1: wall)
1                   # Lower border condition
1                   # Left border condition
1                   # Right border condition
7202.0             # Simulation time (sec)
300                 # Saving time of NetCDF files (sec) (-1: do not save)
1                  # Read points from file (0: no, 1: yes). Used for time series
ts.dat              # File with locations
30                  # Saving time of time series (sec)
0.7                 # CFL
5e-3                # Epsilon h (m)
20                  # Threshold for the 2s+WAF scheme (m)
0.2                 # Stability coefficient
0.03                # Water-bottom friction (Manning coefficient)
100                 # Maximum allowed velocity of water
100000              # L (typical length)
1000                # H (typical height)
```

***Figure 3.21.*** *Example of the information introduced in the Tsunami-HySEA software to simulate a tsunami scenario with the simple fault plane for the Horseshoe Fault.*

```
HF_3d                        # Title
Cadiz15.grd             # Bathymetry file for level 0
2                            # Initialization type (1: Standard Okada, 2:Triangular Okada, 3: Okada from
file, 4: Gaussian)
0                            # Apply Kajiura filter to the Okada deformation (0: no, 1: yes)
1013                           # Number of faults (>= 1) for each triangle a line with: Time(sec) Lon_v1
Lat_v1 Depth_v1(km) Lon_v2 Lat_v2 Depth_v2(km) Lon_v3 Lat_v3 Depth_v3(km) Rake Slip(m)
0 -10.462103 35.798142 9.452635 -10.454115 35.818956 8.823854 -10.445762 35.798646 10.18174 75 3.24
0 -10.441136 35.777525 11.37048 -10.462103 35.798142 9.452635 -10.445762 35.798646 10.18174 75 3.24
0 -10.441136 35.777525 11.37048 -10.445762 35.798646 10.18174 -10.427638 35.80017 10.92647 75 3.24
0 -10.427638 35.80017 10.92647 -10.419276 35.776946 12.28259 -10.441136 35.777525 11.37048 75 3.24
0 -10.414586 35.751831 13.5 -10.441136 35.777525 11.37048 -10.419276 35.776946 12.28259 75 3.24
0 -10.414586 35.751831 13.5 -10.419276 35.776946 12.28259 -10.401516 35.765417 13.5 75 3.24
0 -10.419276 35.776946 12.28259 -10.403605 35.788048 12.4569 -10.401516 35.765417 13.5 75 3.24
0 -10.403605 35.788048 12.4569 -10.3752 35.78898 13.5 -10.401516 35.765417 13.5 75 3.24
0 -10.403385 35.807407 11.65758 -10.3752 35.78898 13.5 -10.403605 35.788048 12.4569 75 3.24
0 -10.403605 35.788048 12.4569 -10.427638 35.80017 10.92647 -10.403385 35.807407 11.65758 75 3.24
0 -10.429782 35.823819 9.808165 -10.403385 35.807407 11.65758 -10.427638 35.80017 10.92647 75 3.24
0 -10.454115 35.818956 8.823854 -10.429782 35.823819 9.808165 -10.427638 35.80017 10.92647 75 3.24
0 -10.455544 35.842271 7.686947 -10.429782 35.823819 9.808165 -10.454115 35.818956 8.823854 75 3.24
0 -10.455544 35.842271 7.686947 -10.454115 35.818956 8.823854 -10.476701 35.838217 6.779763 75 3.24
0 -10.484005 35.863306 5.0328 -10.454343 35.861443 6.722229 -10.455544 35.842271 7.686947 75 3.24
0 -10.484005 35.863306 5.0328 -10.455544 35.842271 7.686947 -10.476701 35.838217 6.779763 75 3.24
0 -10.484005 35.863306 5.0328 -10.476701 35.838217 6.779763 -10.502134 35.837694 5.25377 75 3.24
0 -10.502134 35.837694 5.25377 -10.476701 35.838217 6.779763 -10.480598 35.820039 7.43219 75 3.24
0 -10.484005 35.863306 5.0328 -10.461533 35.883839 5.0328 -10.454343 35.861443 6.722229 75 3.24
0 -10.461533 35.883839 5.0328 -10.431493 35.866811 7.626615 -10.454343 35.861443 6.722229 75 3.24
0 -10.461533 35.883839 5.0328 -10.427195 35.885064 6.659675 -10.431493 35.866811 7.626615 75 3.24
0 -10.461533 35.883839 5.0328 -10.42266 35.906132 5.0328 -10.427195 35.885064 6.659675 75 3.24
0 -10.431493 35.866811 7.626615 -10.427195 35.885064 6.659675 -10.405014 35.870486 8.819981 75 3.24
0 -10.405014 35.870486 8.819981 -10.405119 35.849759 9.871969 -10.431493 35.866811 7.626615 75 3.24
.................................


0 -10.430681 35.845815 8.906133 -10.455544 35.842271 7.686947 -10.454343 35.861443 6.722229 75 3.24
0 -10.476701 35.838217 6.779763 -10.454115 35.818956 8.823854 -10.480598 35.820039 7.43219 75 3.24
0 -10.430681 35.845815 8.906133 -10.429782 35.823819 9.808165 -10.455544 35.842271 7.686947 75 3.24
0 -10.429782 35.823819 9.808165 -10.404749 35.8291 10.82378 -10.403385 35.807407 11.65758 75 3.24
0 -10.3752 35.78898 13.5 -10.403385 35.807407 11.65758 -10.378795 35.812163 12.36799 75 3.24
0 -10.427638 35.80017 10.92647 -10.403605 35.788048 12.4569 -10.419276 35.776946 12.28259 75 3.24
0 -10.445762 35.798646 10.18174 -10.454115 35.818956 8.823854 -10.427638 35.80017 10.92647 75 3.24
0 -10.480598 35.820039 7.43219 -10.454115 35.818956 8.823854 -10.462103 35.798142 9.452635 75 3.24
0                    #Use Okada computation window (0: no, 1: yes)
HF_3d                # NetCDF file prefix for level 0
1 1 0 0 0 0          # Variables saved (eta, maximum eta, velocities, modulus of velocity, momentum flux,
maximum momentum flux) (1: save, 0: do not save)
1                            # Number of levels
1                            # Upper border condition (1: open, -1: wall)
1                            # Lower border condition
1                            # Left border condition
1                            # Right border condition
28802.0                       # Simulation time (sec)
60                          # Saving time of NetCDF files (sec) (-1: do not save)
1                             # Read points from file (0: no, 1: yes). Used for time series
ts.dat               # File with locations
30                         # Saving time of time series (sec)
0.7                          # CFL
5e-3                         # Epsilon h (m)
20                           # Threshold for the 2s+WAF scheme (m)
0.2                          # Stability coefficient
0.03                         # Water-bottom friction (Manning coefficient)
100                          # Maximum allowed velocity of water
100000                       # L (typical length)
1000                         # H (typical height)
```

***Figure 3.22.*** *Example of the information introduced in the Tsunami-HySEA software to simulate a tsunami scenario with the 3D complex fault plane for the Horseshoe Fault considering a homogeneous slip-distribution.*

```
HF_3d_smooth                        # Title
Cadiz15.grd             # Bathymetry file for level 0
2                           # Initialization type (1: Standard Okada, 2:Triangular Okada, 3: Okada from
file, 4: Gaussian)
0                           # Apply Kajiura filter to the Okada deformation (0: no, 1: yes)
#wdep                       # Reference depth for Kajiura filter (m)
1013                         # Number of faults (>= 1)
for each triangle a line with: Time(sec) Lon_v1 Lat_v1 Depth_v1(km) Lon_v2 Lat_v2 Depth_v2(km) Lon_v3
Lat_v3 Depth_v3(km) Rake Slip(m)
0 -10.462103 35.798142 9.452635 -10.454115 35.818956 8.823854 -10.445762 35.798646 10.18174 75 0.029777
0 -10.441136 35.777525 11.37048 -10.462103 35.798142 9.452635 -10.445762 35.798646 10.18174 75 0.027416
0 -10.441136 35.777525 11.37048 -10.445762 35.798646 10.18174 -10.427638 35.80017 10.92647 75 0.032544
0 -10.427638 35.80017 10.92647 -10.419276 35.776946 12.28259 -10.441136 35.777525 11.37048 75 0.03373
0 -10.414586 35.751831 13.5 -10.441136 35.777525 11.37048 -10.419276 35.776946 12.28259 75 0.02899
0 -10.414586 35.751831 13.5 -10.419276 35.776946 12.28259 -10.401516 35.765417 13.5 75 0.032252
0 -10.419276 35.776946 12.28259 -10.403605 35.788048 12.4569 -10.401516 35.765417 13.5 75 0.039479
0 -10.403605 35.788048 12.4569 -10.3752 35.78898 13.5 -10.401516 35.765417 13.5 75 0.049884
0 -10.403385 35.807407 11.65758 -10.3752 35.78898 13.5 -10.403605 35.788048 12.4569 75 0.057313
0 -10.403605 35.788048 12.4569 -10.427638 35.80017 10.92647 -10.403385 35.807407 11.65758 75 0.048728
0 -10.429782 35.823819 9.808165 -10.403385 35.807407 11.65758 -10.427638 35.80017 10.92647 75 0.049156
0 -10.454115 35.818956 8.823854 -10.429782 35.823819 9.808165 -10.427638 35.80017 10.92647 75 0.040826
0 -10.455544 35.842271 7.686947 -10.429782 35.823819 9.808165 -10.454115 35.818956 8.823854 75 0.040872
0 -10.455544 35.842271 7.686947 -10.454115 35.818956 8.823854 -10.476701 35.838217 6.779763 75 0.034151

0 -10.140343 36.070124 6.64147 -10.171751 36.074176 5.0328 -10.152492 36.094097 5.045673 75 2.439694
0 -10.091445 36.066982 8.468475 -10.113399 36.063111 7.996341 -10.119793 36.08165 6.831537 75 3.320311
0 -10.119793 36.08165 6.831537 -10.092585 36.087509 7.462598 -10.091445 36.066982 8.468475 75 3.467208
0 -10.123754 36.124318 5.0328 -10.110501 36.135053 5.0328 -10.093652 36.110966 6.447177 75 3.218686
0 -10.066605 36.0701 9.054565 -10.092585 36.087509 7.462598 -10.066597 36.091529 8.028581 75 3.996246
0 -10.066597 36.091529 8.028581 -10.063577 36.112463 7.252102 -10.039338 36.093302 8.650546 75 4.371561
0 -10.093652 36.110966 6.447177 -10.110501 36.135053 5.0328 -10.082833 36.130411 5.975142 75 3.476544
0 -10.063577 36.112463 7.252102 -10.060356 36.135679 6.397507 -10.037994 36.115338 7.913422 75 4.348326
0 -10.082833 36.130411 5.975142 -10.110501 36.135053 5.0328 -10.079867 36.154995 5.0328 75 3.474246
0 -10.060356 36.135679 6.397507 -10.037711 36.138086 6.986389 -10.037994 36.115338 7.913422 75 4.474429

0 -10.429782 35.823819 9.808165 -10.404749 35.8291 10.82378 -10.403385 35.807407 11.65758 75 0.059421
0 -10.3752 35.78898 13.5 -10.403385 35.807407 11.65758 -10.378795 35.812163 12.36799 75 0.06886
0 -10.427638 35.80017 10.92647 -10.403605 35.788048 12.4569 -10.419276 35.776946 12.28259 75 0.040757
0 -10.445762 35.798646 10.18174 -10.454115 35.818956 8.823854 -10.427638 35.80017 10.92647 75 0.034904
0 -10.480598 35.820039 7.43219 -10.454115 35.818956 8.823854 -10.462103 35.798142 9.452635 75 0.027143
HF_3d_smooth               # NetCDF file prefix for level 0
1 1 0 0 0 0         # Variables saved (eta, maximum eta, velocities, modulus of velocity, momentum flux,
maximum momentum flux) (1: save, 0: do not save)
1                           # Number of levels
1                           # Upper border condition (1: open, -1: wall)
1                           # Lower border condition
1                           # Left border condition
1                           # Right border condition
28802.0                      # Simulation time (sec)
60                        # Saving time of NetCDF files (sec) (-1: do not save)
0                           # Read points from file (0: no, 1: yes). Used for time series
#ts.dat              # File with locations
#30                        # Saving time of time series (sec)
0.7                         # CFL
5e-3                        # Epsilon h (m)
20                          # Threshold for the 2s+WAF scheme (m)
0.2                         # Stability coefficient
0.03                        # Water-bottom friction (Manning coefficient)
100                         # Maximum allowed velocity of water
100000                      # L (typical length)
1000                        # H (typical height)
```

***Figure 3.23.*** *Example of the information introduced in the Tsunami-HySEA software to simulate a tsunami scenario with the 3D complex fault plane for the Horseshoe Fault considering a stochastic heterogeneous slip-distribution.*

# PART II

# RESULTS

# CHAPTER 4

# Characterization of the Cape São Vicente area

The results exposed in this chapter have been published in the following research article: **Serra, C.S.,** Martínez-Loriente, S., Gràcia, E., Urgeles, R., Vizcaino, A., Perea, H., Bartolome, R., Pallàs, R., Lo Iacono, C., Diez, S., Dañobeitia, J., Terrinha, P., Zitellini, N. (2020): Tectonic evolution, geomorphology and influence of bottom currents along a large submarine canyon system: The São Vicente Canyon (SW Iberian margin). *Marine Geology,* 426: 106219. https://doi.org/10.1016/j.margeo.2020.106219 (Annex 2)

The CSV area is located in the external part of the Gulf of Cadiz (SW Portuguese margin) in a convergent boundary between the Eurasian and African plate. The SVC, which transports sediments from the shelf-break at 200 m water-depth, where its head is located, to the HAP (at 4900 m depth) is the largest submarine canyon in the area (Fig. 4.1). It is bounded by the Sagres Plateau and the HF to the east and the MPB to the west. In this area, there are no major rivers to feed sediments to the SVC head.

The SVC is located in a syncline-fold between two prominent anticlines (the MPF block and the Sagrês Plateau) (Pereira & Alves, 2013; Vizcaino et al., 2005; Zitellini et al., 2001), and it is mainly dominated by the NE-SW-trending reverse Horseshoe Fault (Martínez-Loriente et al., 2018) (Fig. 4.1). The sediment inputs to the SVC are mainly fed by along-shelf sediment-transport sources (i.e., the MOW) (Mastbergen & Van Den Berg, 2003). Most of the sediments travelling along the SVC are deposited in the HAP (Eulàlia Gràcia et al., 2010), but a significant portion of the finest sediment fraction is incorporated to the MOW current and deposited on the MPB (Mencaroni et al., 2021).

In this chapter, a multi-scale geophysical dataset is used to define the tectonic, sedimentary and erosional processes along the canyon. We also propose a conceptual model to discuss the emplacement, age and evolution of the SVC. The dataset used to analyse the area in this chapter includes high-resolution swath-bathymetry (SWIM), high-resoluion sidescan sonar (TOBI) mosaics, and 17 MCS profiles that have been acquired using different configurations for each specific marine survey (Fig. 4.2).

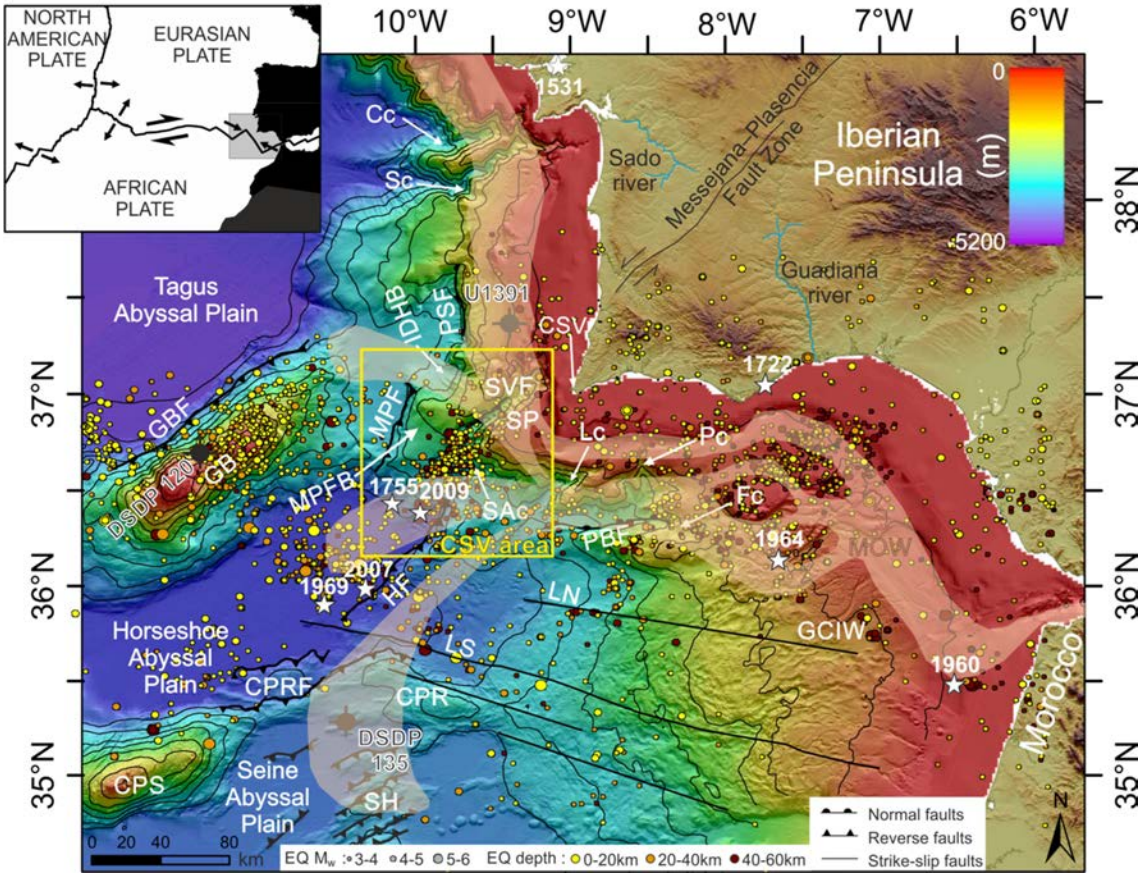


***Figure 4.1.*** *Bathymetric map of the Gulf of Cadiz with the location of the main fault systems after Martínez-Loriente et al., (2013, 2018). Yellow circles correspond to earthquake locations for the period 1400–2020 (Instituto Geográfico Nacional, 2020). Earthquake locations are according to Lozano et al., (2019) and Stich et al., (2006). Inset: Plate tectonic setting of the SW Iberian margin at the plate-boundary between the Eurasian, North-American and African Plates. The grey rectangle corresponds to the area depicted in Fig. 4.2. Cc: Cascais Canyon; CPR: Coral Patch Ridge; CPRF: Coral Patch Ridge Fault; CPS: Coral Patch Seamount; CSV: Cape Sao Vicente; Fc: Faro Canyon; GB: Gorringe Bank; GBF: Gorringe Bank Fault; GCIW: Gulf of Cadiz Imbricated Wedge; HF: Horseshoe Fault; IDHB: Infante Don Henrique Basin; LC: Lagos Canyon; LN: Lineament North; LS: Lineament South; MPF: Marquês de Pombal Fault; MPFB: Marquês de Pombal Fault Block; PBF: Portimão Bank Fault; PC: Portimão Canyon; PSF: Pereira de Sousa Fault; SC: Sagres Canyon; SC: Setubal Canyon; SH: Seine Hills; SP: Sagres Plateau; SVC: São Vicente Canyon; SVF: São Vicente Fault.*

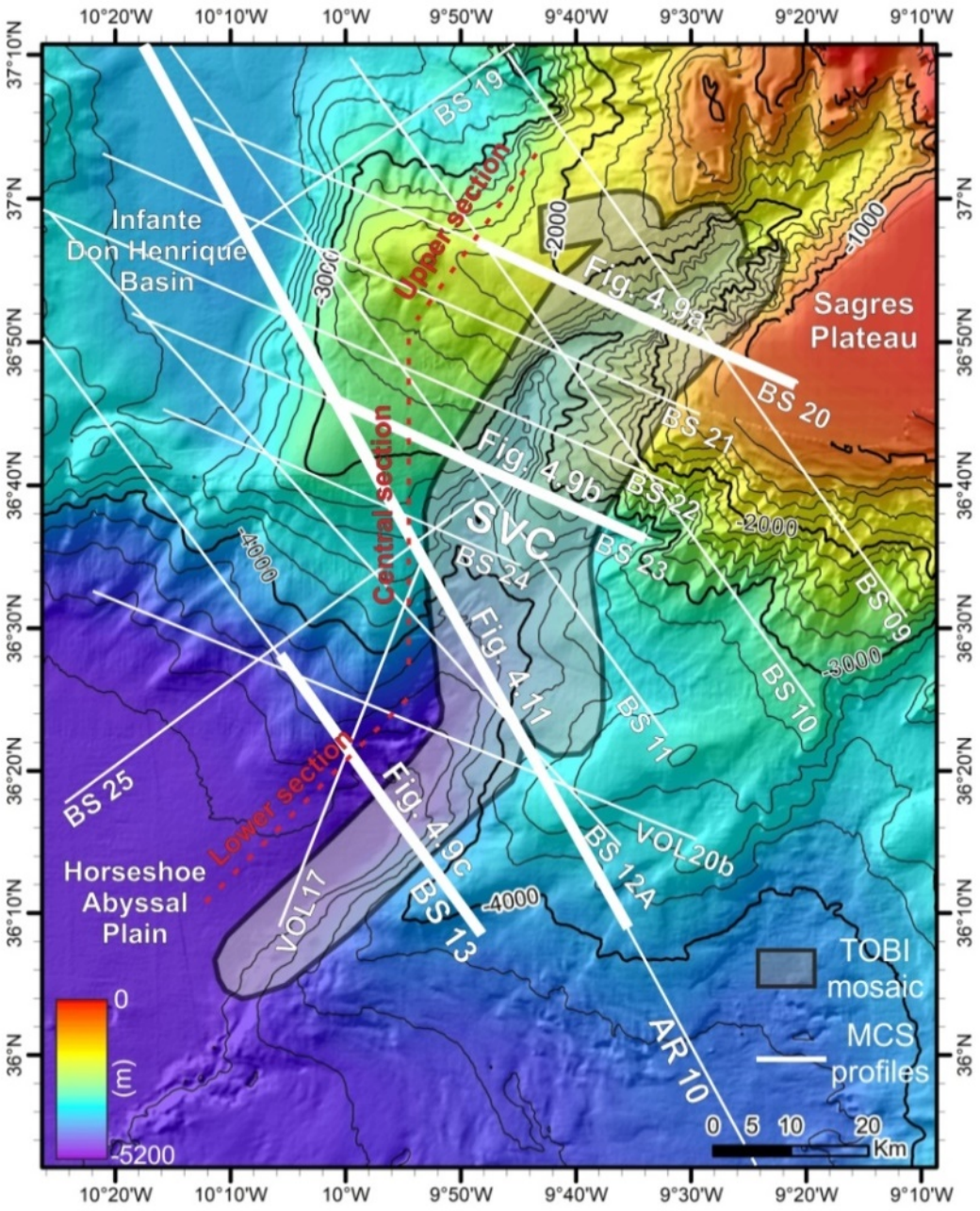


***Figure 4.2.*** *Bathymetric map of the study area in the SW Portuguese Margin. The grey area depicts the TOBI sidescan sonar mosaic of the São Vicente Canyon (SVC), acquired during the HITS-2001 survey (Gràcia et al., 2003a). White lines correspond to the multichannel seismic (MCS) profiles used in this study, which have been acquired during several cruises: BIGSETS-1998 (BS), ARRIFANO-1992 (AR) and VOLTAIRE-2004 (VOL) surveys (e.g. Terrinha et al., 2003; Zitellini et al., 2001, 2004). Thick white lines represent the seismic sections shown in Figs. 4.9 and 4.11.*

## 4.1. Geomorphology and acoustic character of the São Vicente Canyon

The SVC is a 157 km-long canyon that connects the continental shelf, at 200 m water-depth, to the HAP at 4900 m water-depth (Figs. 4.1 and 4.2). Its sinuosity (winding) is 1.12 and its average axial slope is 1.8º (Fig. 4.3). The path of the SVC is characterized by numerous changes in orientation and slope. The SVC can be divided in three main sections, from North to South: 1) The upper section (canyon head) is 60 km-long, trends N50, and extends from the continental-shelf at 200 m water-depth to 3200 m depth (Fig. 4.3a); 2) The central section is 54 km-long, it trends N20 in the northern part and N160 in the southern end, covering the area located between 3200 m and 4400 m water-depth (Fig. 4.3b); and 3) The lower section is 43 km-long, trends N30 (parallel to the Horseshoe Fault), and extends from 4400 m to 4900 m water-depth, towards the canyon mouth in the HAP (Fig. 4.3c). A significant characteristic of the SVC is that the longitudinal bathymetric profile of the canyon axis (Fig. 4.4) shows a rectilinear morphology with a rather constant slope and, therefore, it does not appear to be in equilibrium. In general, bathymetric profiles that are in equilibrium, such as rivers on-land, show a logarithmic longitudinal-profile (Amblas et al., 2012).

The flanks of the canyon are clearly asymmetric and their height and slope varies along the canyon (profiles across the canyon in Figs 4.4a-c) (Fig. 4.3). On the TOBI mosaic, the canyon floor and the lower part of the flanks display heterogeneous high-backscatter acoustic facies (i.e., shown as white and light-grey in Figs 4.5-4.7). In contrast, the canyon flanks and part of the hanging-wall blocks of the MPF, HF and SVF outside the canyon, are characterized by homogenous dark-grey to black colour (i.e., low acoustic backscatter). The uppermost head-scarps of the flanks in the upper and central sections are homogeneous, showing high-acoustic backscatter facies.

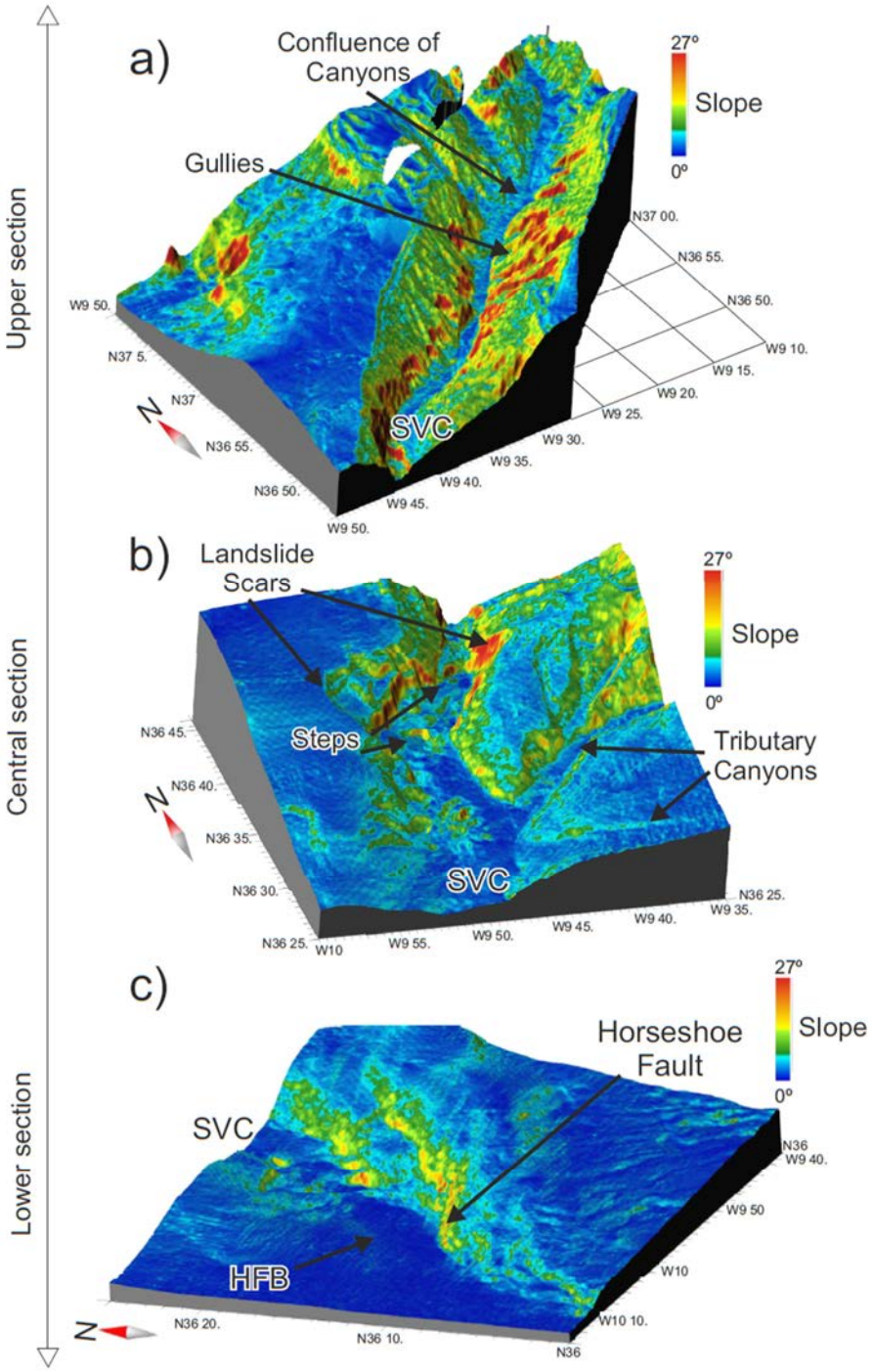


***Figure 4.3.*** *Slope maps superimposed on the 3D bathymetry of the Sao Vicente Canyon (SVC). The slope is represented as percentages in dark blue for the lowest slope (0%) and red for the highest slope (≥ 50%). a), b) and c) correspond to the Upper, Central and Lower sections of the canyon respectively. HFB: Horseshoe Fault Basin. Modified from Vizcaino, (2009).*

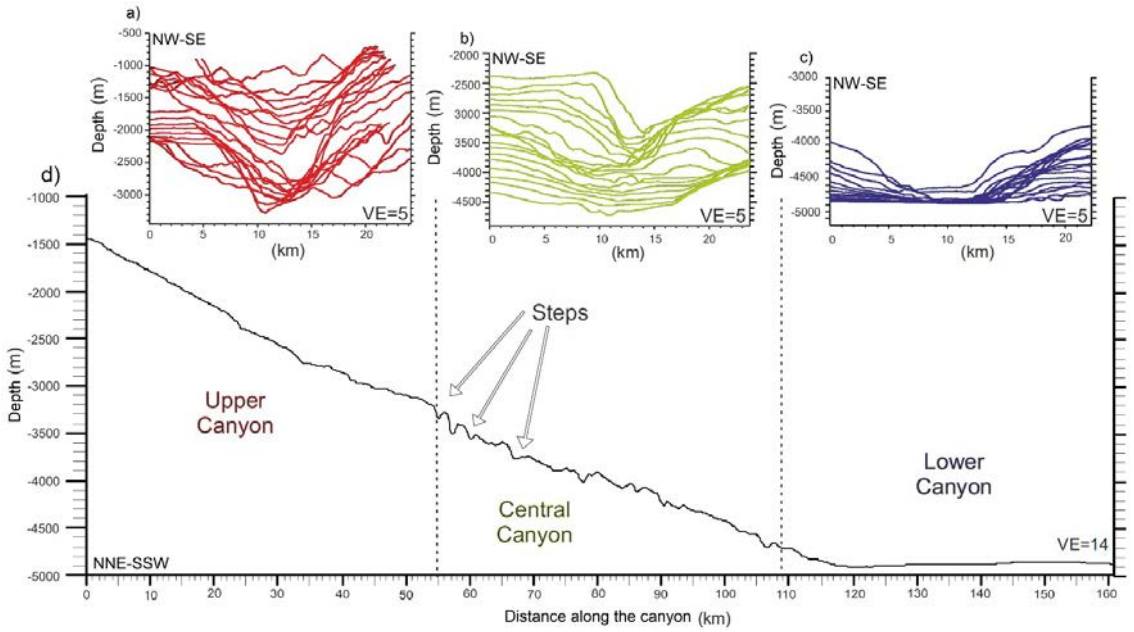


***Figure 4.4.*** *a,b,c) Northwest-southeast oriented bathymetric profiles across the São Vicente Canyon at the Upper, Central, and Lower sections (respectively); and d) Bathymetric longitudinal profile along the São Vicente Canyon axis. Modified from Vizcaino, (2009).*

### *4.1.1. The upper section of the São Vicente Canyon*

The head of the SVC shows a semi-circular shape, cut by three major tributary-canyons that converge on 36º59'N (at 2000 m water depth) (Figs 4.2 and 4.3a). At this location, the flanks are steep and the V-shaped thalweg becomes narrower (3 km) (Figs. 4.3a, 4.4a). Along the canyon, the slope is relatively constant around 1.02° (Fig. 4.3a). In this section of the canyon, the flanks are characterized by gradients that range from 9.7° to 26.6°, with rugged topography. The flanks show a network of rectilinear gullies, which are topped by semi-circular erosional scarps (from 1 to 10 km of diameter) and other minor sediment-pathways, oriented sub-parallel to the maximum slope direction with gradients reaching up to 24° (Fig. 4.3a). The slope gradients, the topographic profiles, and the backscatter signal (Figs. 4.3a, 4.4a, and 4.5) indicate that the NW flank of the canyon is rougher than the SE flank. Both flanks show gullies, as well as minor flow pathways, although they are more abundant on the NW flank.

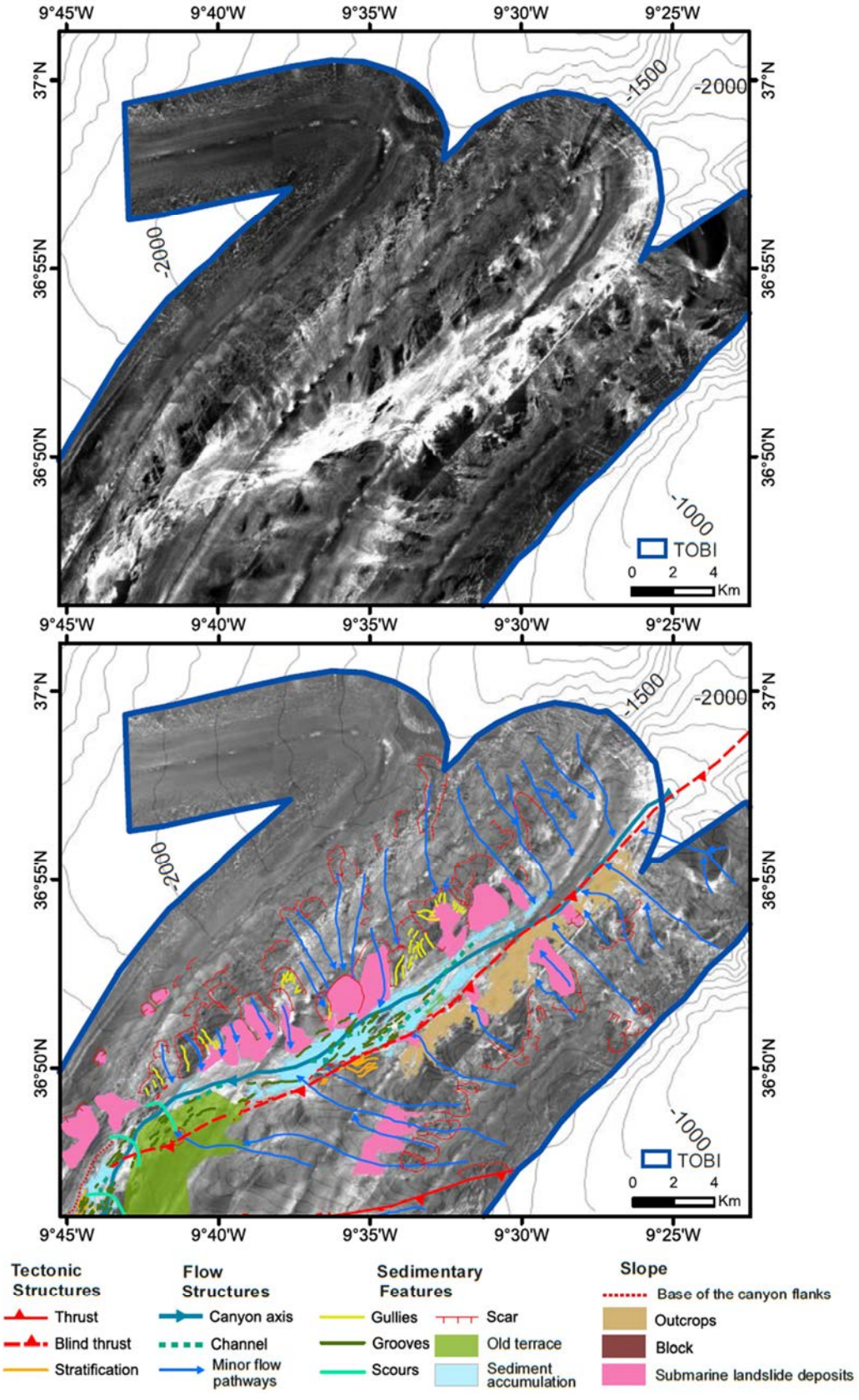


***Figure 4.5.*** *Upper: TOBI sidescan sonar image of the Upper section of the São Vicente Canyon. Lower: Interpreted TOBI mosaic of the same area identifying sedimentary and tectonic features.*

The gullies and minor sediment pathways (13–14 km-length) appear further incised in the SE flank compared to the NW one (Figs. 4.2, 4.3 and 4.4d), as the rocky substrate crops out in the lower part of the SE flank. The scars above the gullies are about 1-4 km-wide on both flanks. However, the SE flank shows a single generation of scars, whereas the NW flank displays evidence for at least two generations of scars. The first generation is located in the uppermost part of the NW flank, while the second generation is longer and develops at mid-elevation, disrupting the minor sediment-pathways that originate in the first generation of scars. The scars on both flanks, but particularly in the NW flank, are accompanied by submarine landslide deposits, which may reach up to 5 km-long and 4 km-wide (Fig. 4.5).

The most striking feature in the TOBI side-scan sonar mosaic is the ENE-WSW trending stripe of high-backscatter that corresponds to the canyon-floor (Fig. 4.5). The acoustic character of the canyon-floor is however relatively heterogeneous and shows the following features: a) Multiple channels along the axis; b) pervasive, >1 km-long lineaments of low-to-medium backscatter (grey to light-grey colour) that are parallel to the canyon-axis interpreted as grooves; c) Sediment accumulation areas along the canyon axis of very-high backscatter; d) Low-backscatter lineaments indicative of acoustic shadows at the lower part of the eastern flank interpreted as stratification; and e) A low-backscatter semi-circular area with gentle slope, located on the internal side of a meander on the canyon East flank (area in green in Fig. 5) interpreted as an old terrace.

### *4.1.2. The central section of the São Vicente Canyon*

Along this section, the canyon-axis shows an average slope of 1.02°, whereas its flanks show slopes steeper than 26.6° on the upper part that gradually decreases southward to 14° (Fig. 4.3b). On the upper part of this central section, the canyon is incised about 1000 m on the west-flank and 800 m on the eastern one (Fig. 4.4b). Moving south along the canyon, these values decrease to less than 500 m on the west-flank and 300 m at the east one. Halfway along this section, the canyon profile progressively changes from V-shaped to U-shaped (Figs. 4.3b and 4.4b). Three main tributary canyons converge towards the main canyon in its central portion. Those can be recognized in the eastern flank of the slope, by medium to high backscatter stripes on the TOBI mosaic (Figs. 4.3b and 4.6). The tributary canyon, located further north, is oriented E-W, whereas the two other are oriented NE-SW and NW-SE respectively,

being the three of them >15 km-long. In this section, both flanks show evidence of stratification (middle-to-low backscatter lineaments along the canyon), and large scars although less abundant than in the upper section. Some of these scars are associated to submarine landslide deposits in the TOBI mosaic.

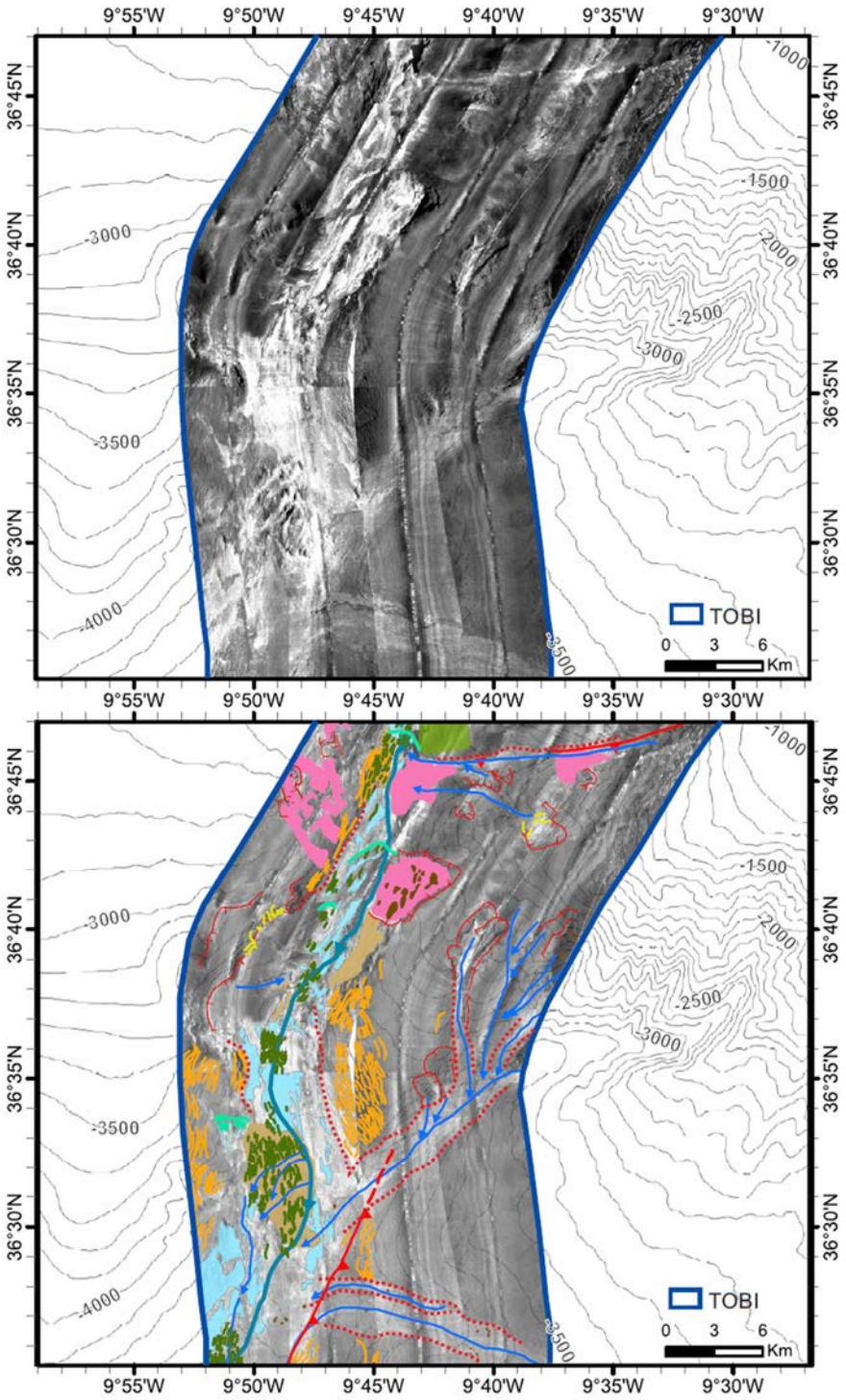


***Figure 4.6.*** *Upper: TOBI sidescan sonar image of the Central section of Sao Vicente Canyon. Lower: Interpreted TOBI mosaic of the same area labelling the main features of the area. See legend in Fig. 4.5.*

The largest submarine landslide deposit is located to the north of this section, associated to a semi-circular scar of ~3 km in diameter and characterized by > 0.5 km-long, high-backscatter patches. Long scars, such as the ones located in the central section of the NW flank are elongated (> 4 km-long) and characterized by low backscatter. The canyon floor in this section shows several features, similar to those described along the upper section of the canyon (Figs. 4.5 and 4.6), including: a) middle-grey backscatter signal corresponding to the tributary canyons; b) grooves (i.e., erosive structures) that particularly stand-out in areas of very high-backscatter within the canyon floor (i.e., rock outcrops); c) High-backscatter areas (light-blue areas in Fig. 4.6) along the canyon-axis and canyon west-flank, that correspond to sediment accumulations; and d) Scours (semi-circular negative relief features, perpendicular to the flow-direction), which may attain a diameter of ~ 2 km and an elevation of 200 m (i.e. namely "steps" in the longitudinal profile on Figs. 4.3b, 4.4d and "scours" in Fig. 4.6).

### *4.1.3. The lower section of the São Vicente Canyon*

In this area, the SVC displays a wide U-shaped valley with a 7-km wide flat canyon-floor, low axis slope of 0.9° (Fig. 4.3c) and low-angle flanks (with a mean slope less than 14°), in comparison to the Upper and Central canyon sections (Figs. 4.3 and 4.4). The western flank slope flattens to the south towards the HAP, whereas the slope of the eastern flank increases, reaching mean values of 16.7°, and locally up to 26.6° (Fig. 4.3c). In this lower section, both the SW flank and the HAP display a homogeneous low-backscatter facies, and the SW flank presents a large number of canyon-parallel lineaments (i.e., stratification). In the TOBI mosaic (Fig. 4.7), the canyon-floor shows high-backscatter, which progressively decreases towards the south (Martínez-Loriente et al., 2018). In this section, the canyon does not show a well-developed channel, and it rather fades into the HAP. The main features on this area includes: a) High-backscatter patches (probably outcrops), b) Canyon-parallel, pervasive grooving (0.5–1 km long) in the north-eastern part of the canyon-floor, and c) Low backscatter, 1 km long comet-like, irregular scours along the main channel.

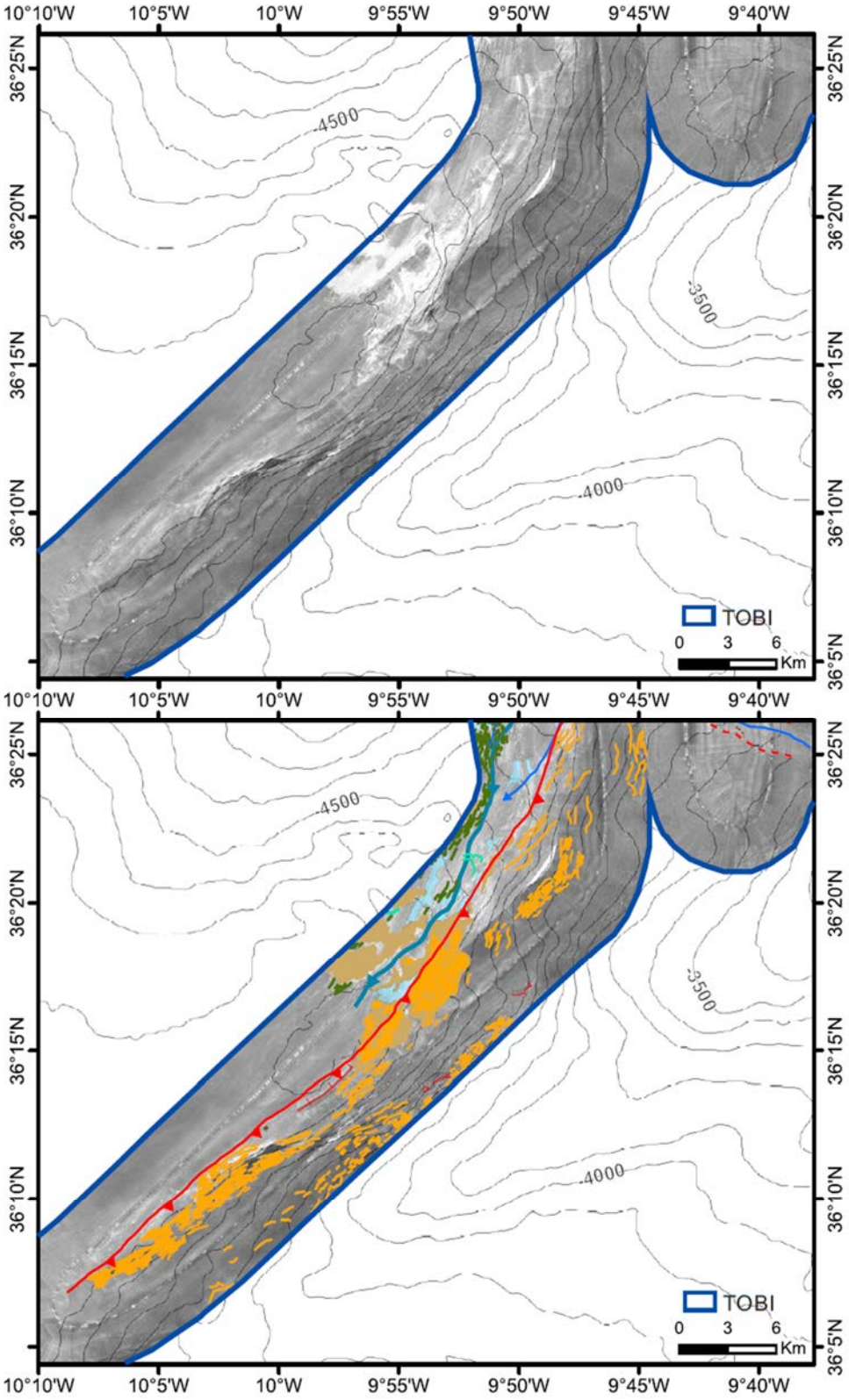


***Figure 4.7.*** *Upper: TOBI sidescan sonar image of the Lower section of Sao Vicente Canyon. Lower: Interpreted TOBI mosaic of the same area identifying the main elements of this sector. See legend in Fig. 4.5 (modified from Martínez-Loriente et al., 2018).*

## 4.2. Seismo-stratigraphy of the Cape São Vicente area

Seismic horizons have been interpreted on the basis of previous chronostratigraphic information (Fig. 4.8) *(*Hayes et al., 1972; Hernández-Molina et al., 2015; Martínez-Loriente et al., 2013, 2018*)*. They are correlated through the network of vintage and recent MCS profiles, and include the following seismo-stratigraphic units: Plio-Quaternary (Ia), Middle Miocene - Pliocene (Ib), Horseshoe gravitational unit (HGU-Ic), Upper Oligocene - Middle Miocene (Id), Upper Cretaceous - Early Eocene (II), Cretaceous (III), Lower Cretaceous (IV), Upper Jurassic (V) and basement (VI) (Figs. 4.9, 4.10 and 4.11).

### *4.2.1. The Pliocene-Quaternary (Ia)*

Unit Ia is characterized by middle-frequency and middle-amplitude continuous reflectors. This unit shows lateral continuity, except near the SVC, which completely erodes the Plio-Quaternary unit in the Upper and Central sections of the canyon axis (Fig. 4.9a, b). In the canyon flanks, gully incision and tributary canyons erode the uppermost part of this unit (Fig. 4.9a). The maximum thickness of unit Ia is 1.2 s (TWTT) in the upper section of the canyon, which progressively decrease to 0.1 s (TWTT) towards the lower section. In the upper section of the SVC, contourite geometries (low-aspect, lenticular sedimentary bodies) have been distinguished, (i.e. low-aspect, lenticular sedimentary bodies) both on the NW flank (Mencaroni et al., 2021) and SE flank. Within this unit, we identify four discontinuities that correspond to Late Quaternary (LQD), Mid Pleistocene (MPD), Early Quaternary (EQD) and Late Pliocene (LPD) discontinuities (Figs. 4.8 and 4.10), described by Hernández-Molina et al., (2014, 2015) on the basis of the IODP Site U1391 (Fig. 4.1).

### *4.2.2. The Middle Miocene-Pliocene (Ib)*

Unit Ib is characterized by middle-frequency, middle-amplitude and continuous reflectors. The thickness of this unit is variable along and across the SVC (Figs. 4.9 and 4.11) with a maximum thickness of 0.7 s (TWTT) below the lower section of the canyon-axis, which progressively thins towards the flanks. This unit shows onlaps toward the Marquês de Pombal anticline and also towards the hanging-wall block of the HF (Fig. 4.11), so it is possible to distinguish multiple, progressive unconformities in the central and lower sections (Figs. 4.9b and 4.10). The incision of the canyon causes total erosion of Unit Ib on the upper section of the SVC axis, whereas it is only partially eroded in the central section. Both, top and base of Unit Ib are unconformities.

### *4.2.3. The Horseshoe Gravitational Unit (HGU-Ic)*

The HGU-Ic is a wedge-shaped allochthonous body formed by stacked debris-flows, which originates from the westward migration of the GCIW and was emplaced during the Upper Miocene (Tortonian) (Gràcia et al., 2003b; Iribarren et al., 2007; Torelli et al., 1997) (Figs. 4.9c and 4.11). The HGU is characterized by high-amplitude, chaotic seismic-facies with numerous diffractions and hyperbolic reflections. Only few internal reflectors can be identified, and the top and bottom are defined as unconformities (Figs. 4.9c and 4.11). The HGU fills the Horseshoe Valley and the HAP, where it pinches-out towards the edge of the Horseshoe valley (Martínez-Loriente et al., 2013). Therefore, the HGU can only be identified in the lower-section of the canyon, where it reaches a maximum thickness of 1.3 s (TWTT- Two-Way Travel Time). In this section of the Canyon, the HGU is partially or totally eroded underlying Unit Id.

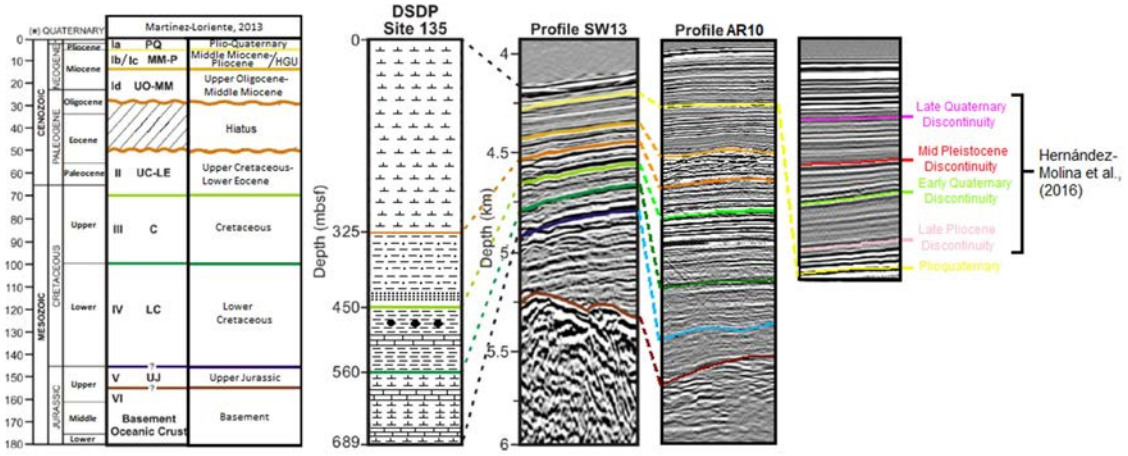


***Figure 4.8.*** *Seismostratigraphy based on DSDP Site 13 (Hayes et al., 1972; Martínez-Loriente et al., 2013) and IODP expedition 339* (F. J. Hernández-Molina et al., 2015)*. mbsf: meters below the seafloor. Modified from Martínez-Loriente et al., (2013).*

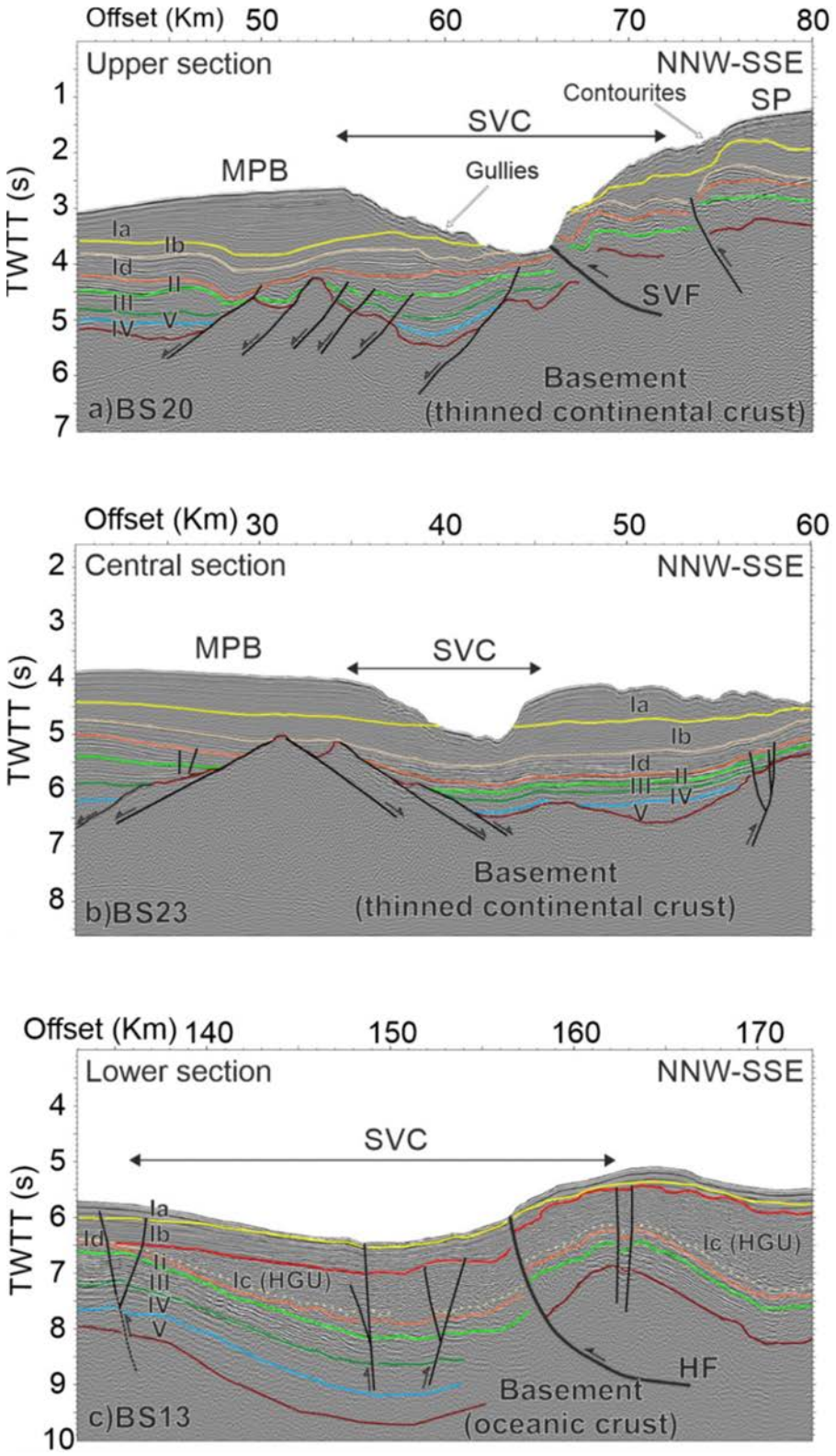


***Figure 4.9.*** *Interpreted sections of 3 multichannel seismic profiles in time across the three sections (upper, central, lower) of the São Vicente Canyon. See location in Fig. 4.2. Stratigraphy from Martinez-Loriente et al., 2013 (see Fig. 4.8). Ia = Plio-Quaternary; Ib = Middle Miocene - Pliocene; Ic-HGU = Horseshoe gravitational unit; Id = Upper Pliocene - Middle Miocene; II = Upper Cretaceous - Lower Eocene; III = Cretaceous; IV = Lower*

*Cretaceous; V = Upper Jurassic; VI = Basement; HF: Horseshoe Fault; MPB: Marquês de Pombal Fault Block; IDHB: Infante Don Henrique Basin; SP: Sagres Plateau; SVF: São Vicente Fault; SVC: São Vicente Canyon; TWTT: Two-way travel time. VE (vertical exaggeration) = 2. Uninterpreted seismic profiles in Annex 3.*

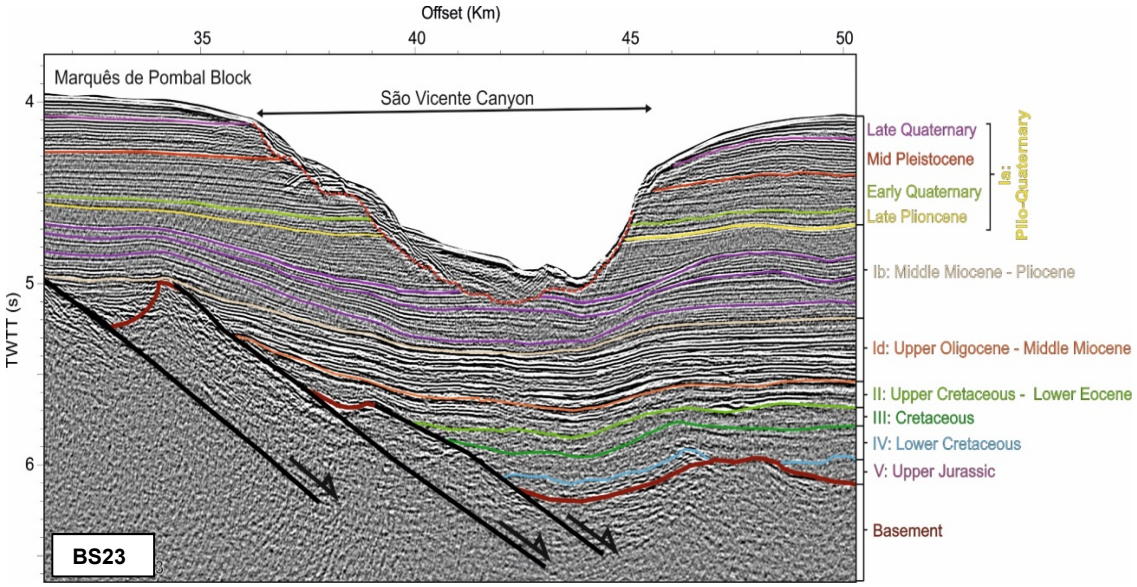


***Figure 4.10.*** *Close-up of profile BS23 showing the progressive unconformities within Unit Ib, likely related to contemporary active-folding with sediment deposition. The Plio-Quaternary sub-units described by Hernández-Molina et al., (2015) have been displayed as a reference. The discontinuous red-line depicts the erosion of the SVC. Uninterpreted seismic profile in Annex 3.*

### *4.2.4. The Upper Oligocene-Middle Miocene (Id)*

Unit Id is characterized by high-amplitude and low-frequency continuous reflectors. In the upper and central sections of the canyon, Unit Id lies directly below Unit Ib and reaches a maximum thickness of 0.5 s (TWTT) (Fig. 4.9a). In contrast, in the lower section of the SVC, Unit Id lies below the HGU, that is partially eroded at its top. In this section, the top corresponds to an erosive-surface, generated by excavation and erosion during the emplacement of the HGU.

### *4.2.5. The Upper Cretaceous-Lower Eocene (II) and Cretaceous (III)*

The seismic facies of Units II and III show similar characteristics (Fig. 4.9). Both show low-frequency and high-amplitude continuous reflectors. The contacts between both units as well as that with the underlying unit (IV) are concordant. The top of Unit II is composed by a prominent unconformity marked by a high-amplitude reflector corresponding to a regional sedimentary-hiatus from the Lower Eocene to the Upper Oligocene (Hayes et al., 1972; Martínez-Loriente et al., 2013). Both units onlap the top

of the basement (Figs. 4.9a and b). Their thickness is relatively uniform with a maximum value for Unit II of 0.45 s (TWTT) and 0.4 s (TWTT) for Unit III. The minimum thickness for Unit II is 0.1 s (TWTT) below the HGU in the lower section of the canyon (Figs. 4.9c and 4.11), and of 0.2 s (TWTT) for Unit III below the central section of the SVC (Fig. 4.9b). These units infill graben structures of the basement, mainly generated as a result of the Mesozoic rifting (Martínez-Loriente et al., 2013).

### *4.2.6. The Lower Cretaceous (IV) and Upper Jurassic (V)*

The Lower Cretaceous Unit IV and Upper Jurassic Unit V show semi-transparent and transparent seismic-facies, with low-frequency and low-amplitude reflectors (Fig. 4.9). The contact between these units is concordant and can be identified by parallel reflectors onlapping the top of the basement highs (Figs. 4.9a, b and 4.11). Unit IV reaches a maximum thickness of 0.5 s (TWTT) at the hanging-wall of the MPF. Unit V overlies the basement (i.e., discordant contact) and fills pre-existent half-graben depressions, where onlap geometries characterize the reflections above the basement (Fig. 4.11). Accordingly, the thickness of Unit V is highly variable, reaching a maximum value of 0.7 s (TWTT) in the lower section of the canyon (Figs. 4.9c and 4.11).

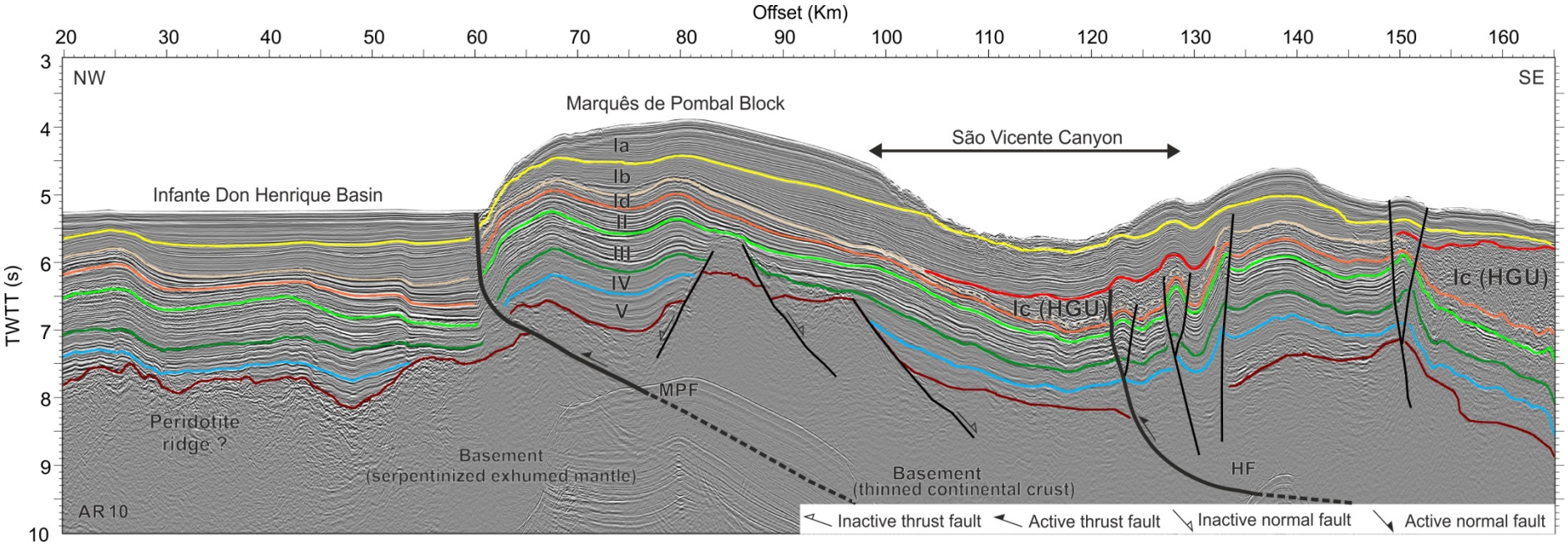


***Figure 4.11.*** *Interpreted section of the AR10 multichannel seismic profile in time across the Cape São Vicente area. See location in Fig. 4.2. Stratigraphy from Martínez-Loriente et al., (2013) (see Fig. 4.8). VE (vertical exaggeration) = 2. See legend in Fig. 4.9. Uninterpreted seismic profile in Annex 3.*

### *4.2.7. The Basement (VI)*

The Basement (Unit VI) is interpreted to be composed by: a) Thinned continental crust in the area of the SVC, Sagres Plateau and hanging-wall of the MPB; b) Oceanic-crust at the southern half of the lower section of the SVC; and c) Serpentinized exhumed mantle at the footwall of the MPB (Martínez-Loriente et al., 2014). This heterogeneous composition results in differences on the tectonic architecture of the basement. In the upper and central sections of the SVC, as well as in the MPB, the MCS profiles reveal tilted basement-blocks bounded by large, old normal faults (Figs. 4.9a, b, and 4.11). In contrast, in the IDHB, the basement structure is completely different, and peridotite ridges have also been identified (Martínez-Loriente et al., 2013) (Fig. 4.11).

## 4.3. Tectonic structures of the Cape São Vicente area

The strata across the SVC are folded by two anticlines bounding a synclinal (Figs. 4.9c and 4.11), partially eroded by the incision of the SVC. The synclinal and anticlinal folds are more pronounced and well-defined in the lower-section of the canyon, whereas their morphology is attenuated towards the upper section (Fig. 4.9). The anticline, located in the western flank of the canyon, is controlled by the west-verging monocline thrust MPF (Fig. 4.11) and corresponds to the hanging-wall of this active reverse fault (Gràcia et al., 2003a; Gràcia et al., 2010).

The MCS profiles (Figs. 4.9 and 4.11) show that the sedimentary sequence rises and tilts towards the SVC axis. The eastern flank of the upper-section of the SVC seems to be controlled by the SVF. The west-verging SVF is an NNE-SSW trending thrust-fault, that affects all the seismo-stratigraphic units from the basement to the seafloor (Ia) (Fig. 4.9a). Towards the SSW, the SVF becomes a blind-thrust along the canyon axis, which progressively attenuates and disappears (Fig. 4.9b).

The lower section of the SVC (Figs. 4.9c and 4.11) is dominated by the presence of the west-verging HF, which is also oriented parallel to the canyon axis, trending NE-SW. In this section, the southeastern flank of the canyon corresponds to the hanging-wall block of the HF, whereas the canyon-floor corresponds to the footwall block. Minor folds are observed in the hanging-wall block near the HF as a propagation-fold (Figs. 4.9c and 4.11). Flexure at the frontal part of the HF thrust generates accommodation space in the footwall, which is progressively filled by sediments transported downstream along the canyon.

The HF can be easily identified in the MCS profiles (Figs. 4.9c and 4.11), as well as in the TOBI mosaic (Fig. 4.7). In the lower section of the canyon, the HF cuts and displaces the entire seismo-stratigraphic sequence (Fig. 4.9c) (Martínez-Loriente et al., 2018). However, in the lower part of the SVC central section, the HF cuts only the sedimentary cover until the HGU (Tortonian age) folding the uppermost units, and acting as an active blind-thrust (Fig. 4.11). In the middle part of the central section of the SVC, the HF cannot be identified neither in the MCS profiles nor in the TOBI mosaic (Figs. 4.7 and 4.9b) (Martínez-Loriente et al., 2018).

# CHAPTER 5

# The Lineament South and the Marquês de Pombal faults: high-resolution data

As previously explained, a series of WNW-ESE trending lineaments are identified in the topography of the Gulf of Cadiz. Zitellini et al., (2009) and Terrinha et al., (2009) defined the origin of these lineaments as tectonic. Bartolome et al., (2012) focused on the two most prominent lineaments in the area: LNF and the LSF and identified them as currently active dextral strike-slip faults. Zitellini et al., (2009) hypothesized that these lineaments constituted a 600 km-long wide-deformation zone, extending from the GB to the Moroccan shelf, constituting a precursor to the formation of a new transcurrent plate-boundary between Africa and Eurasia. This hypothesis is strengthened by the fact that these lineaments are reactivating old-structures inherited from the Jurassic Transfer zone (Martínez-Loriente et al., 2014) and likely not older than 2 Ma (Rosas et al., 2009). The lineaments cut-off the active NW-SE thrust faults.

Finally, on the basis of the WAS profiles, Martínez-Loriente et al., (2014) identified that the LSF constitutes the plate-boundary between two types of Jurassic oceanic crust: a) The central Atlantic crust, and b) The western Thetys crust. This fact leads to thinking that, at Present, the main deformation associated to the Eurasian-African plate-boundary transcurrent zone, occurs along the LSF. Therefore, in this chapter, the two tips of the LSF have been investigated in detail using bathymetry from the AUV "Abyss", to identify the signs and characteristics of present-day activity. Moreover, we also mapped with high-resolution AUV bathymetry the MPF. The MPF has been selected for detailed study because is one of most evident thrust-faults in the area and its activity is evidenced by the large number of landslides (see also Ford et al., 2021) originitaing in the hanging-wall block (MPB) and deposited at the footwall-block (IDHB) together with the turbidite record. Besides, several authors also hypothesize that this fault is the source of the Lisbon earthquake and tsunami event of year 1755.

In this chapter, AUV bathymetries, MCS data and TOPAS and Parasound sub-bottom profiles will be used to describe the topographic expression and the tectonic-activity of the two end segments of the LSF as well as the central part of the MPF. The dataset used in this chapter includes: The existing "SWIM" swath-bathymetry, the AUV "Abyss" high-resolution bathymetry and the MCS profiles that have been acquired with different configurations during the INSIGHT Leg-1 and Leg-2 marine surveys (See Chapter 3).

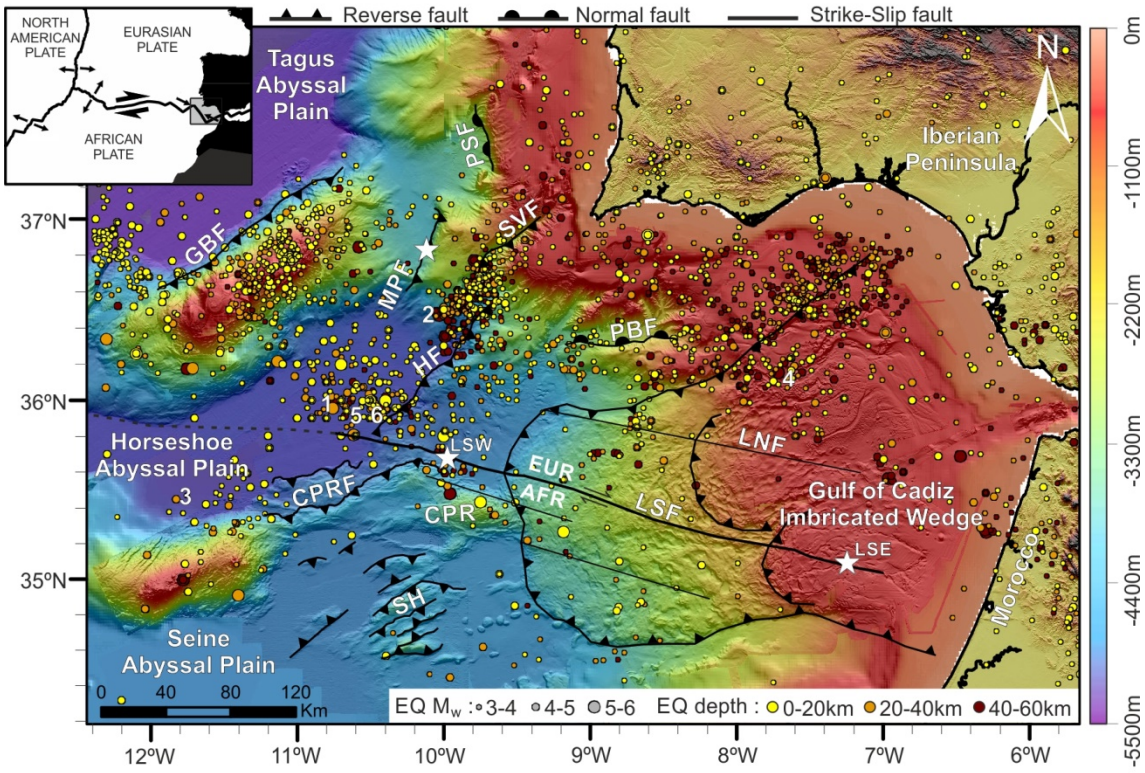


***Figure 5.1.*** *Bathymetric map of the Gulf of Cadiz with the location of the main faults. Yellow, brown and orange circles correspond to the epicenter locations for the period 1400–2020 (Instituto Geográfico Nacional, 2020). Earthquake locations according to Lozano et al., (2019). The numbers correspond to epicentres of large events:* ***1.*** *12 September 1320, intensity I = X;* ***2.*** *11 January 1755, estimated Mw 8.5;* ***3.*** *07 November 1915, Mw 6.2;* ***4.*** *15 March 1964, Mw 6.6;* ***5.*** *28 February 1969, Mw 8.0; 2 December 2007, Mw 6.0 (after Bartolome et al., 2012). White stars represents the AUV dives location. Inset: Plate tectonic setting of the SW Iberian margin at the boundary between the Eurasian and African Plates. AFR: African Plate; CPR: Coral Patch Ridge; CPRF: Coral Patch Ridge Fault; EUR: Eurasian Plate; GBF: Gorringe Bank Fault; HF: Horseshoe Fault; LSF: Lineament South Fault; MPF: Marquês de Pombal Fault; PBF: Portimão Bank Fault; PSF: Pereira de Sousa Fault; SH: Seine Hills; SVF: São Vicente Fault.*

## 5.1. High-resolution imaging using the AUV

Three high-resolution bathymetries were collected using the AUV "Abyss" (Fig. 5.1). The first one corresponds to the west-end of the LSF, which extends from the outer-edge of the GCIW to the HAP. It comprises an area of 42 $km^2$ (14 x 3). The second one is located at the eastern end of the LSF on the Moroccan slope, with an area of 48 $km^2$ (16 x 3). The last high-resolution bathymetry is located at the centre of the MPF, with an area of 30 $km^2$ (10 x 3) (Fig. 5.1).

### 5.1.1. The Lineament South Fault, West section (LSW)

The high-resolution AUV bathymetry of the LSW section (Fig. 5.1), referred to as "LSW AUV image", presents seafloor morphologies indicative of multiple geological processes and the trace of the dextral strike-slip LSF can be easily identified (Figs. 5.2 and 5.3). Physiographically, the LSW AUV image is located in the deepest area, with the western end of the AUV image of the LSW located close to the HAP and extending in water-depths down to 4580 m. The shallower part of the LSW AUV image, on the south-eastern corner, has a water depth of 4336 m (Fig. 5.2). Along the LSW, the 14 km-long AUV image presents a maximum relief variation of 244 m.

The slope-map shows that the southern area of the LSW AUV image, around the fault-trace of the LSF, is rougher than the northern area (Fig. 5.3). The slope remains more or less constant, between 1º and 2.5º, mainly at the northern part of the "LSW AUV image". The steepest slopes are between 8º and 19º and are located following longitudinal alignments with ENE-WSW trend, in the centre and the SE part of the image (Fig. 5.3). The variations in the slope can be correlated with the different morphological structures that can be distinguished in the LSW AUV image. Three types of structures are considered of sedimentary origin and two types structures of tectonic origin.

Amongst the features of sedimentary origin, the following are identified:

1) A series of ENE-WSW trending undulated ridges with mega-herringbone structures and asymmetric flanks, are located across the area, especially to the north of the LSF (Figs. 5.2 and 5.3). The flank facing SE is steeper than the one facing NW. These structures are interpreted as submarine dunes. In the NW part of the LSW AUV image, the submarine dunes are continuous and they form a ridge of more than 6 km-long, crossing the AUV image in a WSW-ENE direction (Figs. 5.2 and 5.3). In the rest

of the AUV image, it is possible to recognize individual submarine crescent-shaped dune-structures, not longer than 200 m. The smallest dunes show a wavelength of 50 m and a height of 2 m, while the largest ones have a wavelength of 170 m and a height of 5 m (Figs. 5.2 and 5.3).

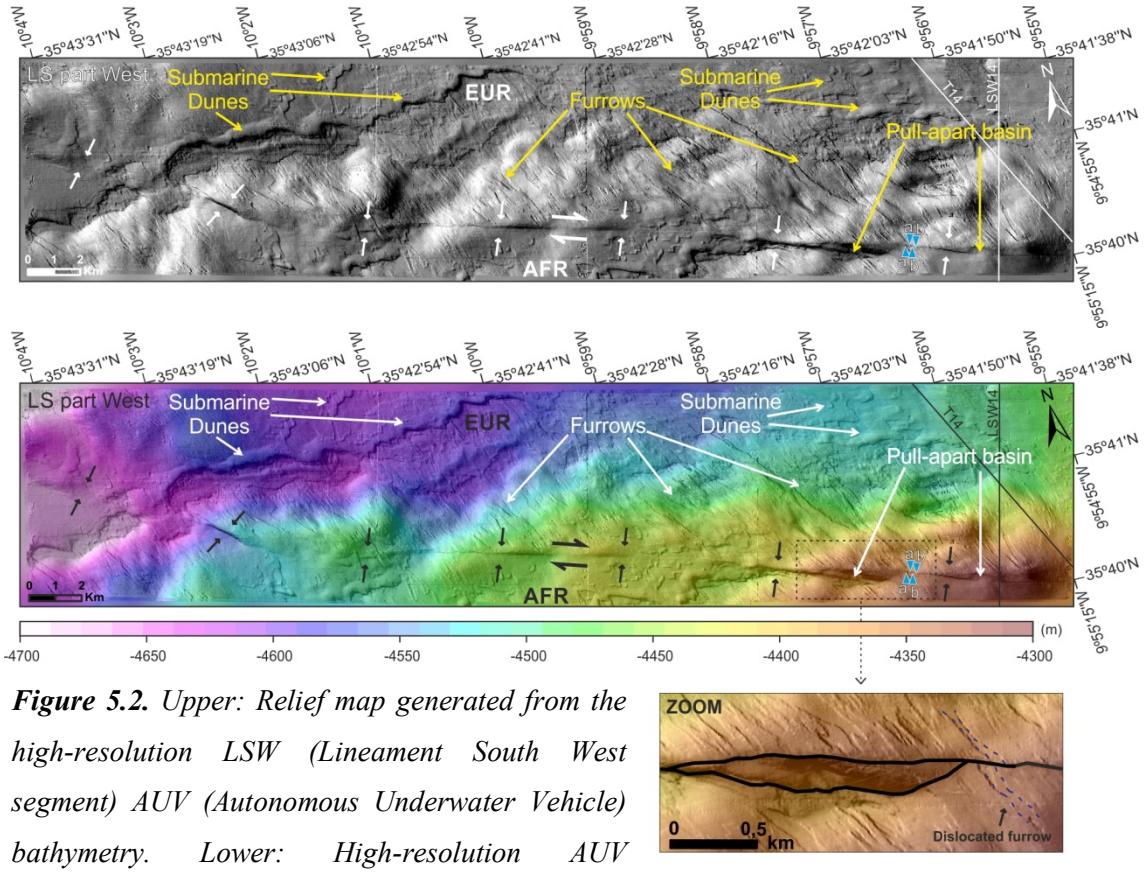


***Figure 5.2.*** *Upper: Relief map generated from the high-resolution LSW (Lineament South West segment) AUV (Autonomous Underwater Vehicle) bathymetry. Lower: High-resolution AUV bathymetry of the LSW. AFR: African Plate; EUR: Eurasian Plate*

2) NNW-SSE trending, large longitudinal erosional bed-forms interpreted as furrows (Allen, 1971, 1983; Peakall et al., 2020). These furrows are long, relatively narrow and show comet-shaped depressions at the seafloor (Figs. 5.2 and 5.3). The whole field of furrows extends for about 14 km around the LSF trace. The spacing between individual furrows (edge to edge) is ~20 to 215 meters; they range from 20 to 260 m in width, are 1 to 3 m deep, and 60 to 2400 m long. In general terms, the furrows field is dissected by the LSF trace, however, due to a large number of furrows, their similar morphology and the irregularities of the seafloor, it is not possible to determine the correspondence between the different furrows on both side of the fault trace. Even so, at the SE margin of the LSW, the AUV image shows a longitudinal current-mark

corresponding to a furrow, which is sectioned and dislocated by 60 m to the right by the LSF trace (Figs. 5.2 and 5.3).

3) The last sedimentary structure in the LSW AUV image is a semi-circular negative relief, which attains a diameter of ~650 m and a depth of 50 m that is located at the NE part of the AUV image, above the trace of the LSF (Fig. 5.3), interpreted as a mass movement scar.

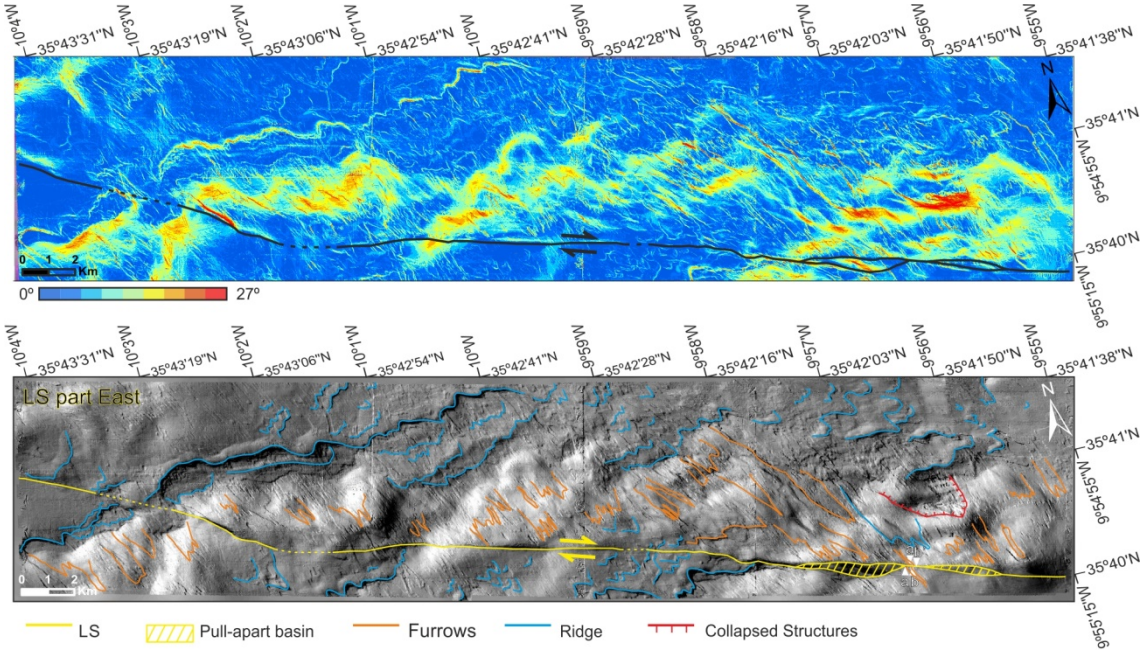


***Figure 5.3.*** *Upper: Slope map of the high-resolution LSW (Lineament South West segment) AUV colored bathymetry. Lower: Background grey-colored relief of the LSW high-resolution AUV bathymetry and interpretation.*

In terms of tectonic structures, the following are identified:

1) In this area, the LSF trace displays an E-W trending across the whole LSW AUV mosaic. The mapped fault trace is 14.7 km-long, it is relatively continuous and it is possible to identify at least four different segments that slightly change in trend. The two westernmost segments are shorter, with a WNW-ESE orientation, while the two easternmost segments are W-E oriented (Figs. 5.2 and 5.3).

2) Two W-E elongated tectonic depressions are bounded on their sides by the surface expresion of the LS strike-slip fault. They are found along the easternmost segment of the fault and have been interpreted as pull-apart basins. The largest basin has a length of 1.5 km, a width of 200 m, and a depth of 10 m. The smallest basin has a length of 1 km, a width of 110 m and a depth of 6 m (Figs. 5.2 and 5.3).

### *5.1.2. The Lineament South Fault, East section (LSE)*

In the high-resolution AUV bathymetry of the LSE section (Fig. 5.4), referred to as "LSE AUV image" is located at the eastern end of GCIW, in front of the continental shelf of the Moroccan Atlantic margin, in water depths between 1.285 m and 958 m (Fig. 5.4).

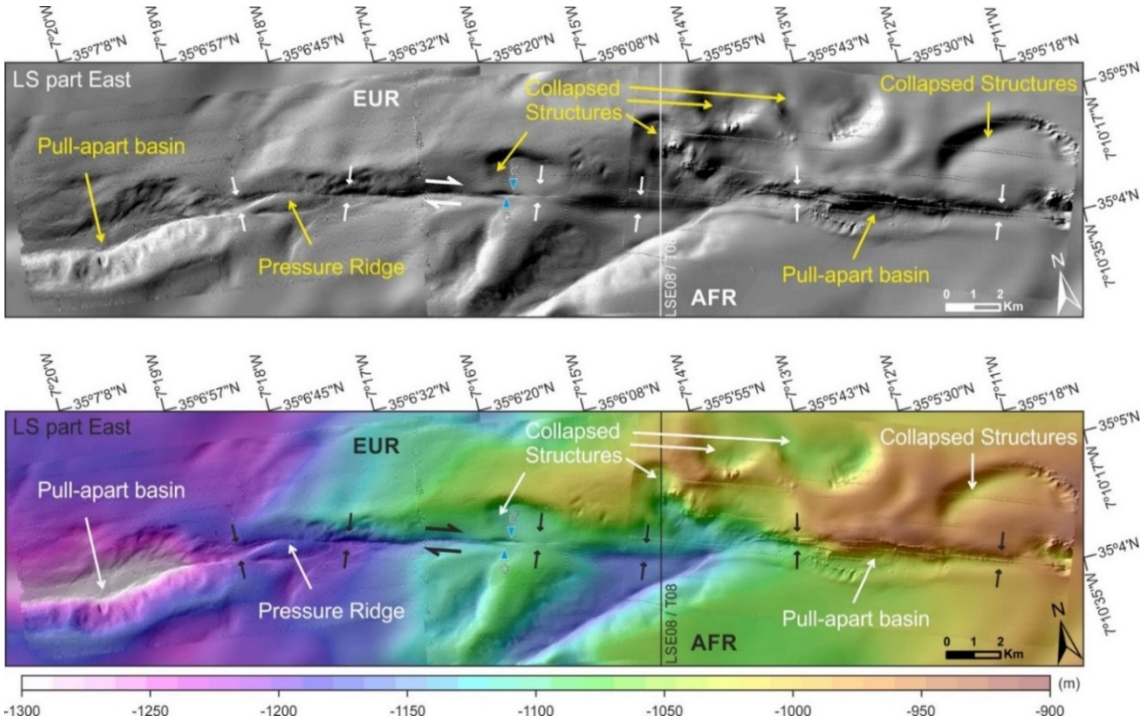


***Figure 5.4.*** *Upper: Relief map generated from the high-resolution LSE (Lineament South West segment) AUV (Autonomous Underwater Vehicle) bathymetry. Lower: High-resolution AUV bathymetry of the LSE. AFR: African Plate; EUR: Eurasian Plate.*

Along the 16 km of the LSE AUV image, the slope map indicates that the area around the trace of the LSF is rougher than the area without the influence of the fault. The slope of the area remains more or less constant, between 1º and 2.5º. The most prominent and penetrative morphology of the seafloor, in addition to the fault and its associated structures, are semi-circular escarpments (with a slope between 10º and 20º) that delimit depressions (Fig. 5.5). These negative reliefs may attain a diameter of up to 2 km and a depth between 30 and 85 m. These scarps mostly located in the NE of the LSE AUV image, just above the fault trace, and oriented in all directions have been interpreted as collapsed structures (Figs. 5.4 and 5.5).

In this case, the LSF trace has a general W-E trend and is continuous. Throughout its 16 km of seafloor expression, different tectonic structures such as pull-apart basins,

pressure ridges and dislocated ridges can be identified (Figs. 5.4 and 5.5). The two pull-apart basins located in this area are larger and better developed than those in the LSW (Figs. 5.2 and 5.3). Both are 2.5 km long, the westernmost one has a width of 300 m and a depth of 100 m, while the easternmost one has a width of 670 m and a depth of 65 m (Figs. 5.4 and 5.5).

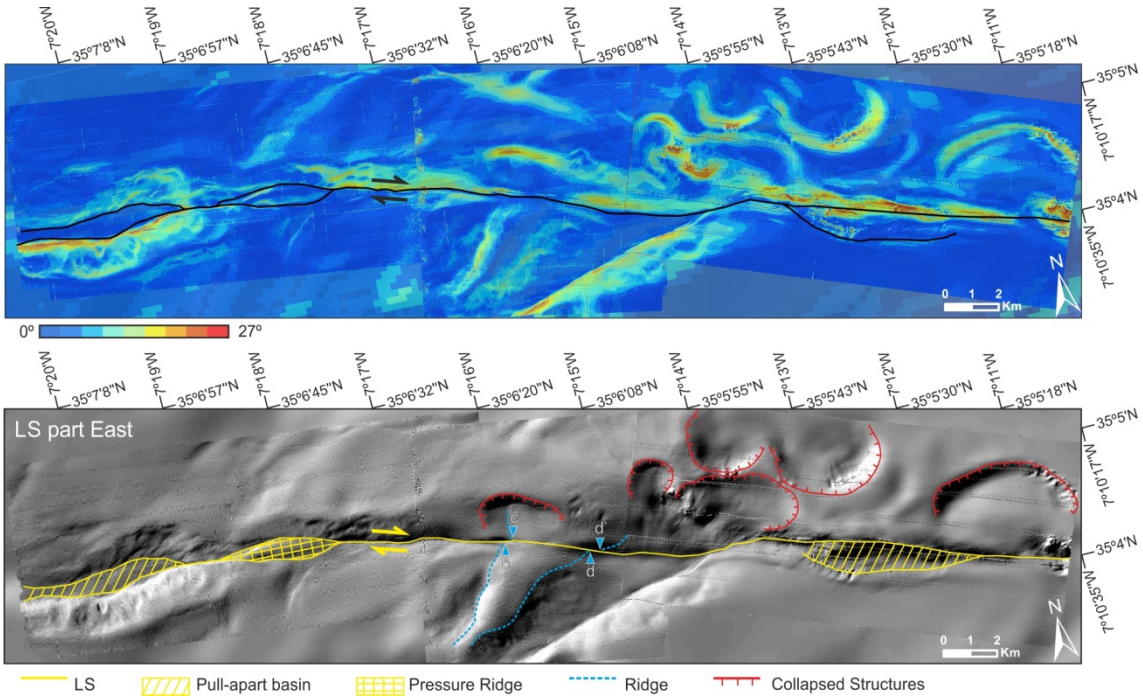


***Figure 5.5.*** *Upper: Slope map of the LSE (Lineament South East segment) high-resolution AUV bathymetry. Lower: Background grey-colored relief of the LSE high-resolution AUV bathymetry and interpretation.*

The escarpments along the margins of the pull-apart basins present some of the steepest slopes in the area of about 30º (Fig. 5.5). Adjacent to the western pull-apart basin, a longitudinal ridge is bordered by two narrow and longitudinal depressions lines corresponding to the fault trace. This ridge oriented parallel to the fault, like the pull-apart basins, has a length of 1.8 km and a width of 300 m. In the centre of the LSE AUV image, a NE-SW trending ridge can be distinguished. This ridge is dissected and dislocated about 150 m to the right by the LSF trace (Figs. 5.4 and 5.5; blue triangles).

### *5.1.3. The Marqûes de Pombal Fault*

Finally, the high-resolution AUV bathymetry of the Marquês de Pombal fault (Fig. 5.6), from now on refered as the "MPF AUV image", is located about 100 km to the west of the CSV, in the central part of the fault. The thrust fault separates the IDHB, corresponding to the foot-wall block of the fault, from the MPB, which corresponds to

the hanging-wall block. The deepest part of the bathymetry, at 3920 m water-depth, is located in the IDHB, south of the MPF AUV image. The shallowest part, at 3700 m water-depth, is placed in the SE margin of the MPF AUV image, right at the centre of the upper block. The total difference in water-depth of the MPF AUV image is about 220 m (Fig. 5.6).

While the IDHB is almost flat with a slope less than 1º, the hanging-wall block of the MPF is steep and rough, due to the presence of a number of submarine mass-movements (some of which are referred to in Gràcia et al., 2003a). The slopes of the hanging-wall block are about 16º at the top of the image (ENE), and around 25º near the base of the slope, where mass-wasting processes are commonplace (Fig. 5.6).

Along the MPF trace two segments, with a different trend, which changes at the centre of the image can be distinguished: The northern and the southern. The southern segment is 5.5 km-long and shows a general NE-SW trend, while the northern segment of the fault is 5 km-long and is oriented NNE-SSW. Parallel to the fault-trace, few meters to the west, in the footwall, is possible to identify a not continuous elongated ridge with an elevation of ~20 m over the surrounding seafloor. The ridge shows two main branches, which separate at the point of a small-bend in the hanging-wall block (centre of the figure 5.6). At this point of the image, the ridge trace is not recognizable for about 1 km, the hanging-wall block shows a steeper slope and roughness, and the largest mass movements occur. This ridge is more developed in the southern branch, where it is divided into two more branches: the most meridional branch is closest to the fault-trace and the most central branch is further away from the fault-trace. In the northern branch, the ridge is poor-developed and it is only distinguishable in the meridional extreme. Due to its proximity to the MPF trace, its parallel orientation, and its absence in the centre of the AUV image where the MPF change its trend, leads to thinking that this ridge could be of tectonic origin. It could be the morphological expression of a poor-developed complementary fault to MPF. Even so, there is no evidence of this structure in the MCS profiles.

Unlike the LSW, the MPF AUV image does not show penetrative current-marks or sedimentary structures at the seafloor. However, at the footwall close to the MPB, it is possible to identify asymmetric elongated mounds, identified as mass-transport deposits (MTD) generated by the mass-wasting processes of the hanging wall (Fig. 5.6).

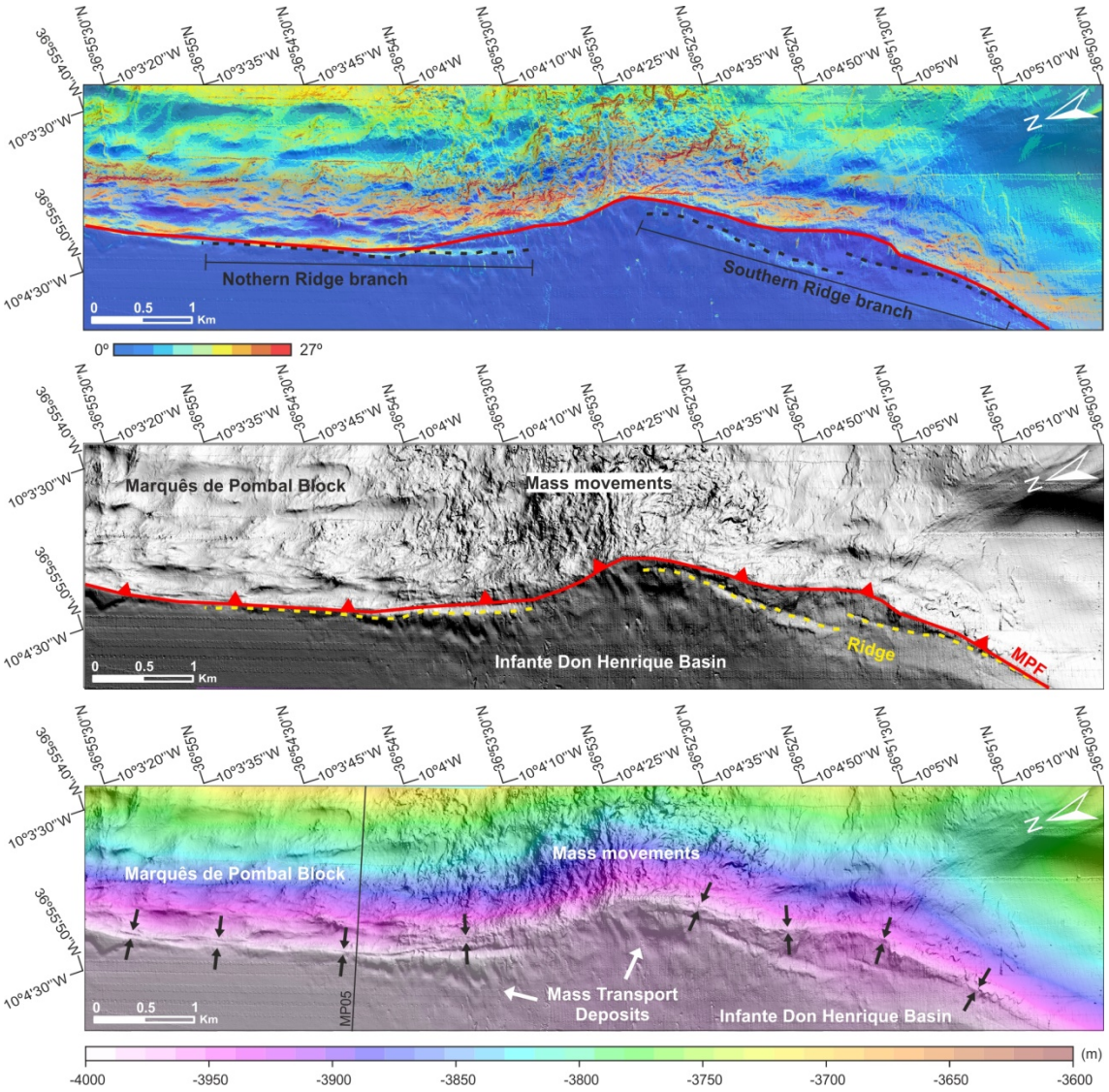


***Figure 5.6.*** *Upper: Slope map of the MPF (Marquês de Pombal Fault) high-resolution AUV (Autonomous Underwater Vehicle) bathymetry. Middle: Relief of the MPF from the High-resolution AUV bathymetry. Lower: MPF high-resolution AUV bathymetry.*

## *5.2. The high-resolution seismic imaging*

The seismo-stratigraphic units described for the MPF area (Fig. 5.7) are based on those proposed by Martínez-Loriente et al., (2013), as can be seen in Chapter 4, section 4.2 and will not be presented further in this section. In contrast, for the LSF (both in the LSE and LSW AUV image areas) we use the seismo-stratigraphy proposed by Toyos et al., (2016), as there are no crossing lines with the study of Martínez-Loriente et al., (2013). The seismic line "Mound-22" (Toyos et al., 2016), which crosses the Ginsburg

and Yuma mud volcanoes, also intersects the INSIGHT-Leg2 MCS lines on the LSE area. The MCS profiles that we use to illustrate the stratigraphy of the LSF area (LSW14 and LSE08) are both from cruises INSIGHT-Leg1 and Leg2. The vertical penetration of these profiles is limited to a maximum of about 2 s (TWTT) (Fig. 5.8).

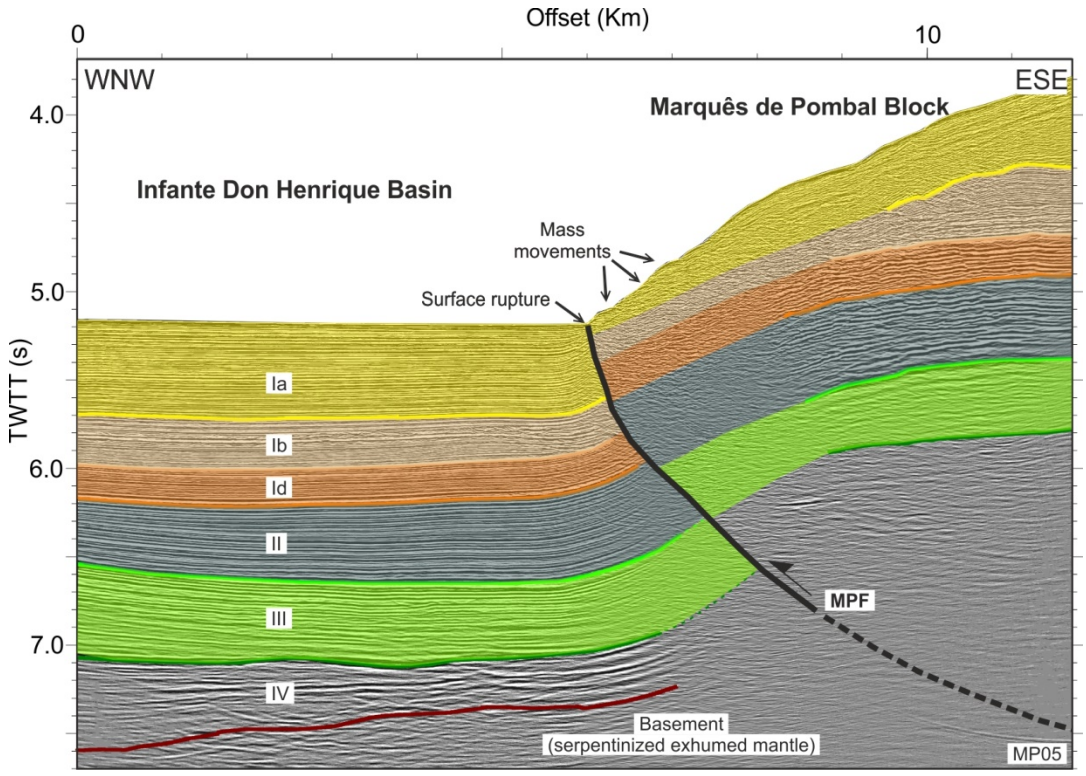


***Figure 5.7.*** *Interpreted sections of multichannel seismic profile MP05 in two way travel time (TWTT) from Martinez-Loriente et al. (2013) (see Chapter 4, Fig. 4.8). Ia = Plio-Quaternary; Ib = Middle Miocene - Pliocene; Id = Upper Pliocene -Middle Miocene; II = Upper Cretaceous - Lower Eocene; III = Cretaceous; IV = Lower Cretaceous; MPF: Marquês de Pombal Fault TWTT: Two-way travel time. VE (vertical exaggeration) = 1.5. Uninterpreted seismic profile in Annex 3.*

### *5.2.1. Stratigraphy of the area surrounding the Lineament South (LSW and LSE)*

Along the LSF, the following horizons have been identified, correlated and tracked from Toyos et al., (2016): The top of the GCIW; BQD (Base of Quaternary Discontinuity); MPD (Mid-Pleistocene Discontinuity) and TM (Top of Miocene Discontinuity) (Fig. 5.8).

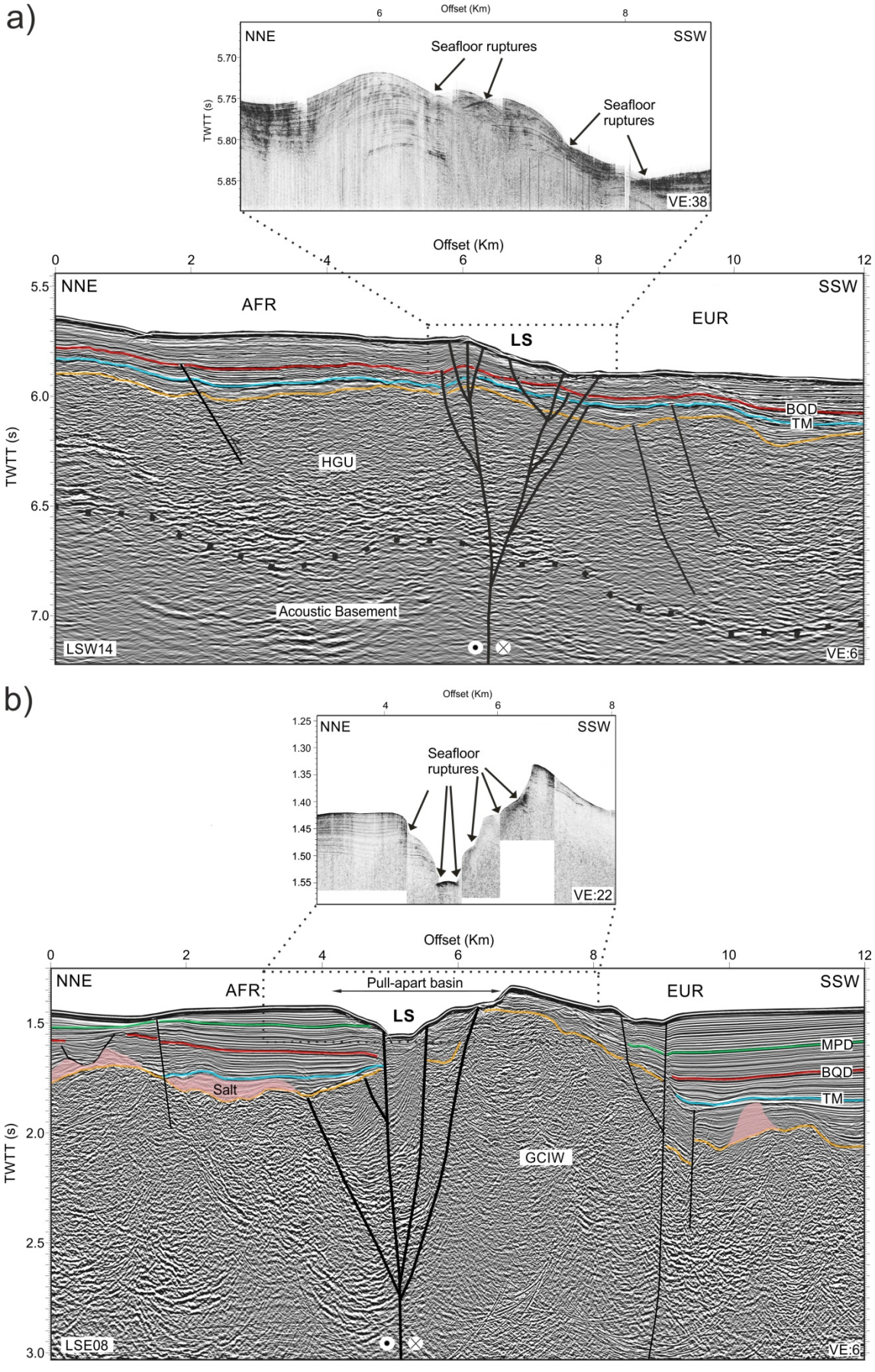
a)
Offset (Km)
NNE
SSW
Seafloor ruptures
Seafloor ruptures
TWTT (s)
VE:38
Offset (Km)
NNE
SSW
AFR
EUR
LS
BQD
TM
HGU
Acoustic Basement
TWTT (s)
LSW14
VE:6
b)
Offset (Km)
NNE
SSW
Seafloor ruptures
VE:22
Offset (Km)
NNE
AFR
Pull-apart basin
EUR
SSW
LS
MPD
BQD
TM
Salt
GCIW
TWTT (s)
LSE08
VE:6

***Figure 5.8.*** *Interpreted sections of multichannel seismic and Parasound profiles in two-way-time across the two end segments of the Lineament South fault. Stratigraphy from Toyos et al., (2016). a) Interpreted section of the Parasound profile T14 and MCS profile LSW14 across the LS west segment. b) Interpreted section of the Parasound profile T08 and the MCS profile LSE08 across the LS east segment. AFR: African plate; BQD: Base of Quaternary Discontinuity; EUR: Eurasian Plate; GCIW: Gulf of Cadiz Imbricated Wedge; HGU: Horseshoe Gravitational Unit; MPD: Mid-Pleistocene Discontinuity; TM: Top of Miocene Discontinuity; TWTT: Two-way travel time. Uninterpreted seismic profiles in Annex 3.*

The unit comprised between the seafloor and the MPD is only present in the LSE segment (LSE08 MCS profile), since it corresponds to an area of important sediment accumulation. This unit is characterized by high-frequency and middle-amplitude continuous reflectors. The unit shows high lateral continuity and it is only interrupted by a high originated at the GCIW along MCS profile LSE08. The maximum thickness of the unit (0.17s TWTT) is located to the SSW of this MCS profile, and progressively decreases to 0.05 s (TWTT) towards the NNE. The bottom of this unit is defined by the Mid-Pleistocene Discontinuity, which is considered and important change in the climatic trend occurred 900-920 ka (Llave et al., 2007) (Fig. 5.8b).

The unit comprised between the Mid-Pleistocene Discontinuity (MPD) and the Base of the Quaternary Discontinuity (BQD) in profile LSE08, is characterized by middle-frequency, middle-amplitude and continuous reflectors. The unit in the LSE segment is also interrupted by the same high originated from the GCIW, where the unit internal refectors onlap, and it is possible to distinguish multiple unconformities. The maximum thickness of this unit in the LSE segment is about 0.1 s (TWTT) (Fig. 5.8b). In contrast, this unit in the LSW14 MCS profile comprises the sequence between the seafloor and the BQD. In the LSW section, the unit is characterized by high-frequency, middle-amplitude and discontinuous reflectors, and presents different internal discontinuities (Fig. 5.8a). The bottom of the unit is defined by an unconformity, which corresponds to the basal Quaternary Discontinuity.

The Pliocene unit is comprised by the sedimentary sequence between the BQD and the TM. This unit is characterized by middle-frequency, middle-amplitude and continuous reflectors. In the LSW14 MCS profile and in the SSW part of the LSE08 MCS profile, the unit lies directly above the TM, and reaches a maximum thickness of 0.15 s (TWTT) in the LSE08 and 0.08 s (TWTT) in the LSW14. In contrast, in the NNE

part of the MCS profile LSE08, the unit lies above the top of the GCIW, where salt deformation structures can be identified. Both, top and base of this unit are unconformities. Several other minor discontinuities occur within this unit (Fig. 5.8).

The Messinian unit is made by the sedimentary package comprised between the TM and the top of the GCIW in the case of the LSE. In the LSW segment this unit is comprised between the top of the HGU and the TM. Both, the GCIW and the HGU are of Tortonian age. The Messinian unit is characterized by middle-frequency, low-amplitude and discontinuous reflectors. In the LSE segment, the unit is interrupted by protrusions from the GCIW, where the unit shows onlaps towards these highs. There, it is possible to distinguish multiple progressive unconformities indicating synchronous deformation while deposition. In the LSE segment, one of the main characteristics of the Messinian unit, is the presence of salt masses at its base, which deform and fracture it. The top and the base of this unit are unconformities. The maximum thickness of the unit is 0.22 s (TWTT) in the LSE08 MCS profile and 0.07 s (TWTT) in the LSW14 MCS profile (Fig. 5.8).

The HGU is a wedge-shaped allochthonous body, as explained in Chapter 4, section 4.2.3. This unit was emplaced during the Tortonian by stacking of debris-flows that originated from the westward migration of the GCIW (Gràcia et al., 2003b; Iribarren et al., 2007; Torelli et al., 1997). The HGU fills the Horseshoe Valley and the HAP and for this reason it is only present in the LSW area, close to the HAP (Fig. 5.8a). In the LSE, this unit is replaced by the GCIW (Fig. 5.8b). The HGU is characterized by high-frequency, high to medium-amplitude and chaotic seismic facies. It is difficult to identify internal reflectors. The top and bottom are defined by unconformities. The HGU is thicker (0.87 s TWTT) to the SSW, as it is closer to the source, the GCIW, and progressively thins towards the NNE, where the thickness reduces to 0.64 s (TWTT) in the multichannel seismic profile (Fig. 5.8b). The top and bottom of this unit are defined by unconformities (Fig. 5.8). The GCIW is a Tortonian unit with a clear wedge geometry that this away from the Gulf of Cadiz coast towards the HAP. The GCIW appears highly deformed and is characterized by high-amplitude, chaotic seismic facies with numerous diffractions and hyperbolic reflections (Fig. 5.8b). The acoustic basement present in the MCS profile LSW14 is composed by Early Eocene to Mesozoic material (Bartolome et al., 2012). This unit is characterized by middle-amplitude and middle-frequency seismic facies with hyperbolic reflections (Fig. 5.8a).

### *5.2.2. Lineament South Fault characteristics from MCS profiles and high-resolution sub-bottom profiles data*

The LSF is a dextral strike-slip fault (Bartolome et al., 2012; Terrinha et al., 2009; Zitellini et al., 2009) that extends from the HAP to the Moroccan continental shelf across the Horseshoe Valley and the GCIW for 377 km. The wide deformation area of the LSF is about 2.5 km perpendicular to the fault trace (Fig. 5.1). The LSF is a sub-vertical fault that according to the studies by several authors (Bartolome et al., 2012; Martínez-Loriente et al., 2014; Terrinha et al., 2009) roots at great depths (40 to 60 km depth) in the oceanic crust. Along the fault trace, several ridges and basins that deform the seafloor appear (Figs. 5.2, 5.3, 5.4 and 5.5), mainly due to the changes in strike and dip of the fault-plane, as (Sylvester, 1988) described for the strike-slip faults on land. Along the LSF trace, several crests and troughs corresponding to a seafloor rupture appear (Figs. 5.2, 5.3, 5.4 and 5.5). On certain segments, the fault shows positive and negative flower-like structures. These structures can be clearly identified in the high-resolution MCS and sub-bottom profiles (Fig. 5.8).

In the high-resolution MCS profile LSW14, the LSF shows a flower-like structure, which generates a positive relief at the seafloor. This positive flower-like structure shows two main branches, as well as several smaller branches that raise to the seafloor generating, at least, four surface ruptures that are clearly distinguished in the sub-bottom profiles (Fig. 5.8a). In the high-resolution MCS profile LSE08, it is possible to identify a flower-like structure that generates a negative relief on the seafloor. This flower structure shows four main branches of which three of them reach the surface and generate, at least, 6 surface ruptures from further subbranches (Fig. 5.8a). Some of these ruptures are directly related to the escarpments corresponding to the collapse-structures identified in the LSE AUV image (Figs. 5.4 and 5.5).

The LSF is a sub-vertical fault that cuts and displaces the entire seismo-stratigraphic sequence, breaching the seafloor, on both segments (LSW and LSE) indicating present-day activity (Fig. 5.8). Furthermore, a small vertical offset and stratigraphic mismatch indicates not only a transcurrent displacement, but also a vertical component. On the base of the AUV image of the fault trace, the average strike of the LSF is 107º and the current rake is ~160º, therefore, the LSF is a right-lateral fault with a small reverse component. This reverse component is also evidence by a vertical displacement between the reflectors on both sides of the fault. In the LSW (Fig. 5.8a)

the base of the HGU shows a vertical slip of ~0.1s (TWTT); while in the LSE (Fig. 5.8b) the vertical slip is constant for all horizons (MPD, BQD and TM) with an average of ~0.15s (TWTT).

### *5.2.3. Marquês de Pombal Fault characteristics from MCS profiles*

As explained in Chapter 4, section 4.3, the seismic profile of Fig. 5.7, the MPF fault, is a west-verging monocline-thrust that cuts the whole seismo-stratigrapic sequence at least, several seconds (3s TWTT) below the seafloor. The hanging-wall of the MPF is controlled by an anticline structure and has an irregular surface due to the numerous submarine landslides and mass-movements that have been identified (Fig. 5.7). The vertical slip of the MPF show some differences, measured at the base-horizons of the seismo-stratigraphic units. The units III and II, in the hanging wall (MPB), show a relatively constant thickness towards the fault and their base horizons show a constant vertical slip of ~0.3s (TWTT), while the base of the unit Id shows a slightly large vertical slip of ~0.35s (TWTT). In contrast, the units Ib and Ia, in the hanging wall (MPB), are clearly thinned towards the fault and the base horizons of these units show a higher vertical slip of ~0.4s (TWTT) (Fig. 5.7), indicating synchronous deposition to the MPF activity. The dip angle of the MPF is higher the first kilometres below the seafloor and decrease progressively toward the basement. On the base of the AUV image of the fault trace, the average strike of the MPF is 22º and the current rake is ~50º, therefore, MPF is a left-lateral reverse fault.

# CHAPTER 6

# Seismogenic and tsunamigenic potential of the active faults of the SW Iberian margin

The SW Iberian margin is one of the most seismically active areas in Western Europe (See Chapter 2). The convergence between the Eurasian and African plates is the responsible of the destructive earthquakes and tsunamis that occurred in the region (e.g. Martínez-Loriente et al., 2014; Zitellini et al., 2009).

For instance, in 1755 a magnitude ($M_w$) > 8.5 earthquake caused a tsunami that hit several coastal areas and cities along the North-Africa and South-West Iberia, destroying the city of Lisbon, causing an extensive damage in Cadiz, Huelva, Tangier and Casablanca. These cities are nowadays large urban areas, where more than 7 million people lives. Moreover, this area receives more than 40 million tourists annually (INE, 2019), hosting critical infrastructures, such as commercial harbours, nuclear power-plants, etc.. Therefore, this is a highly vulnerable area.

This chapter focus on tsunamis generated by earthquakes, when the seafloor abruptly deforms and vertically displaces the overlying water, losing its equilibrium status (Satake, 2015). The intensity of the tsunami that affects a given coastal locality, strongly depends on the source parameters (i.e. location and geometry, focal depth, slip-distribution and kinematics; e.g. (Geist, 1998)). The importance of using a detailed fault-geometry in tsunami numerical simulations defines hazard scenarios that sometimes are overlooked (Tonini et al., 2020). Conversely, using a heterogeneous slip, even on planar faults, is a common established practice (Geist et al., 2019). More in general, analysing the adopted source model complexity versus the sensitivity of the resulting tsunamigenic potential of the faults is a first important step before conducting a full probabilistic tsunami hazard analysis (PTHA). PTHA in fact typically requires the numerical modelling of a very large number of sources (Selva et al., 2016), involving the use of massive HPC (High Performance Computing) resources (Gibbons et al., 2020). Hence, relative source and source parameter importance needs to be carefully evaluated carefully, possibly in combination with other strategies, such as the

computational time (Lorito et al., 2015; Volpe et al., 2019; Williamson et al., 2020). Simplifying the source treatment introduces first-order uncertainties that affect, for example, the extent of the coastal inundation (Tonini et al., 2020).

Previous studies carried-out tsunami simulations to understand tsunami-hazard offshore the SW Iberia. According to the NEAMTHM18 (Basili et al., 2021), this is the area with the highest tsunami hazard in the Atlantic side of the NEAM region (i.e., the North-eastern Atlantic, the Mediterranean, and connected seas as per the UNESCO/IOC subdivision of the World's oceans). Thus, it is worth investigating if and how most of this hazard assessment may be sensitive to adopt non-planar geometries and heterogeneous slip-distributions for local crustal faults, which have not been considered in previous works.

In this chapter, as a first step in this direction, we consider that the 3D-geometrical complexities of the different fault-systems, are addressed through numerical-simulations with a detailed reconstruction of the source-geometry may directly influence the tsunami impact. A large geophysical dataset acquired offshore the SW Iberia (Fig. 6.1) is employed to characterize the main potential tsunamigenic structures and model several tsunami scenarios, generated by large earthquakes on these structures (Fig. 6.2). First, rectangular rupture-planes are used. Then, more realistic 3D-faults are adopted, considering their geometry significantly non-planar and sufficiently well-constrained by the available data. Finally, the influence on the modelled tsunami of heterogeneous slip-distributions is analysed by a selected fault. For all tsunami scenarios, a rough estimate of the expected arrival time is reported. It is relevant to analyse together the tsunami-waves and their arrival-times, since the latter affects the evacuation potential. Indeed, composite wave-height/arrival time probabilistic hazard assessments have been recently developed (Wood et al., 2020; Zamora et al., 2021).

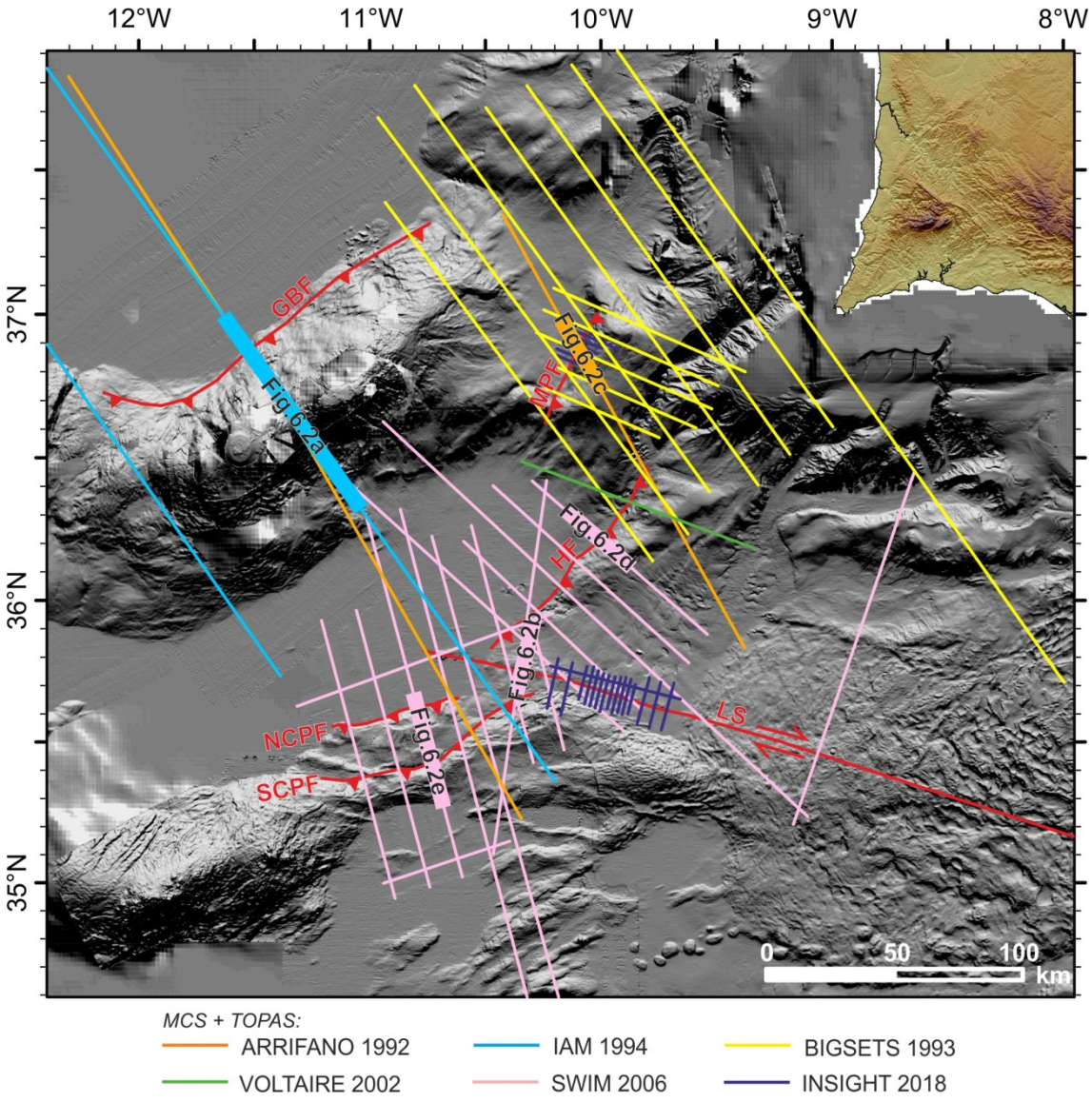


***Figure 6.1.*** *High-resolution relief map of the SW Iberian margin. Thin coloured lines correspond to the available TOPAS and MCS profiles used in this study and acquired during ARRIFANO 1992 (Sartori et al., 1994), IAM 1994 (Banda et al., 1995), BIGSETS* (Zitellini et al., 2001)*, VOLTAIRE 2002 (Terrinha et al., 2003), SWIM 2006 (Martínez-Loriente et al., 2013) and INSIGHT 2018-2019 cruises (Gràcia & INSIGHT Cruise Party, 2018; Urgeles & INSIGHT Cruise Party, 2019). Thick coloured lines label the multichannel seismic profiles (Fig. 6.2).*

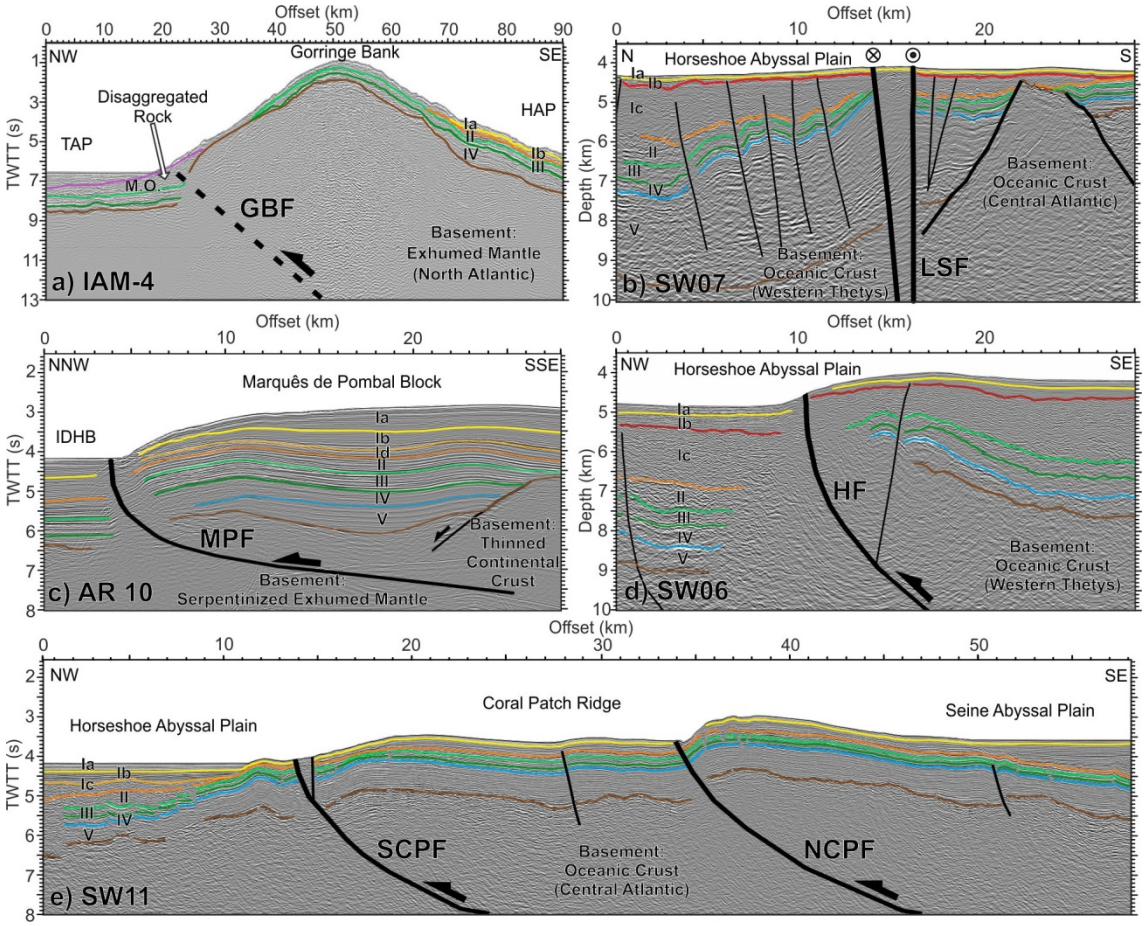


***Figure 6.2.*** *Five MCS profiles corresponding to: a) Interpreted time-section of profile IAM-4 across the GBF (after Zitellini et al., 2009); b) Interpreted depth-section of profile SW07 across the LSF (after Hensen et al., 2015); c) Interpreted time-section of profile AR10 across the MPF (after Serra et al., 2020); d) Interpreted depth-section of profile SW06 across the HF (after Martínez-Loriente et al., 2018); and e) Interpreted depth-section of profile SW11 across the NCPF and SCPF (after Martínez-Loriente et al., 2013). See location of MCS profiles in Fig. 6.1. Stratigraphy from Martínez-Loriente et al., 2013: Ia = Plio-Quaternary; Ib = Middle Miocene - Pliocene; Id = Upper Pligocene -Middle Miocene; II = Upper Cretaceous - Lower Eocene; III = Cretaceous; IV = Lower Cretaceous; V = Upper Jurassic; VI = Basement; M.O.: Miocene Olistostrome; TWTT: Two-way travel time; VE (vertical exaggeration) = 1.5. Uninterpreted seismic profiles in Annex 3.*

## 6.1. Fault parameters for tsunami simulation

The fault plane geometries used in this Thesis are shown in figure 6.3 and their parameters, including earthquake scenario parameters, are reported in Table 6.1. In the case of the GBF, the fault plane is not distinguishable in MCS profiles and,

consequently, its geometry is poorly constrained. Therefore, it did not make sense to construct a complex mesh. The LSF, is a sub-vertical and rather planar fault, and the data coverage was limited to the western portion of the fault (Fig. 6.1). Also in this case, we preferred not to construct a 3D geometry. The fault parameters in these two cases were fixed according to the available knowledge (Bartolome et al., 2012; Martínez-Loriente et al., 2013). In the simulated scenarios, the entire fault length was assumed to rupture and the rupture width, slip and magnitude were consistently derived using the scaling relationship of Leonard, (2014). For all other faults (HF, MPF, NCPF, and SCPF), the 3D geometries (Fig. 6.3) have been reconstructed using the workflow described in Chapter 3, section 3.4. The planar fault orientation was obtained by fitting an inclined plane through the 3D mesh; the rectangle dimensions were constrained to preserve the seismic moment (and moment magnitude) and the fault centroid location of the 3D rupture consistent with those on the corresponding planar fault, while keeping to a minimum the unavoidable differences with the fault scaling relationships.

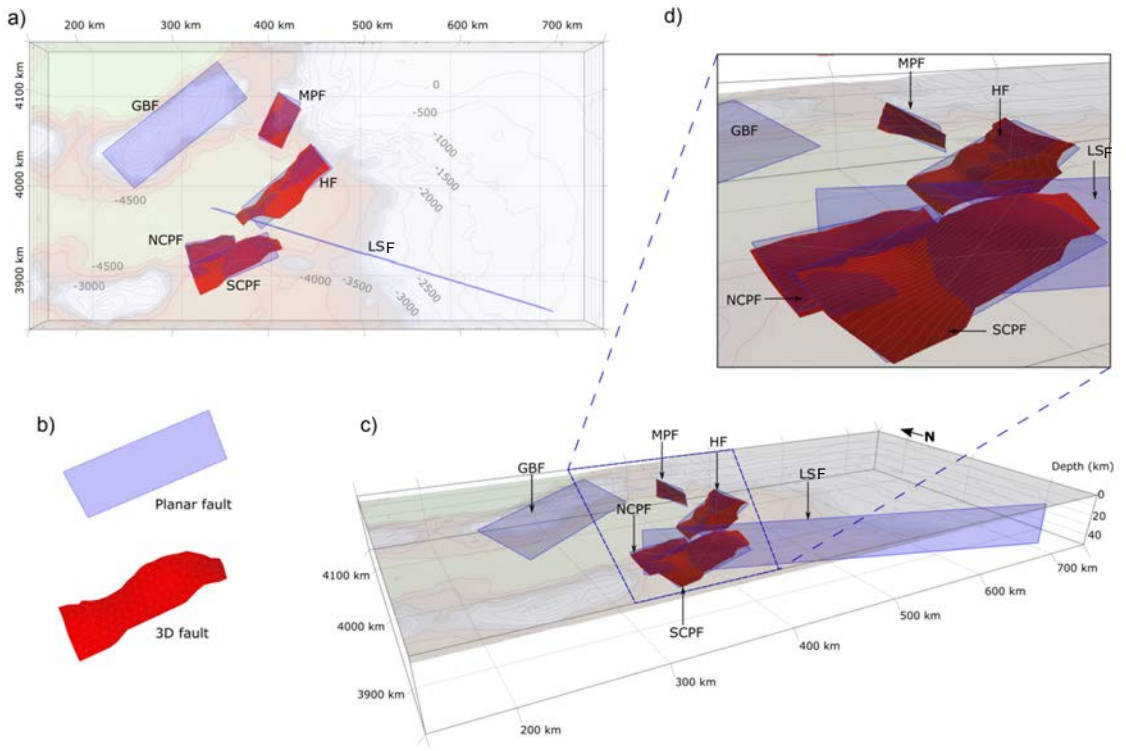


***Figure 6.3.*** *a) Map view of the active faults modelled in this study: Gorringe Bank fault (GBF), Marquês de Pombal fault (MPF), North Coral Patch fault (NCPF), South Coral Patch fault (SCPF), Horseshoe fault (HF) and Lineament South fault (LSF); b) The type of source fault planes used for tsunami simulations. In purple: simple rectangular fault planes. In red: Complex 3D fault planes; c) 3D view of the fault planes used in this study; and d) Close-up of*

*fault planes showing the different geometry of both surfaces (i.e., rectangular-planar vs complex 3D).*

| Fault Type | Parameter | HF | MPF | NCPF | SCPF | GBF | LSF |
|---|---|---|---|---|---|---|---|
| **Planar** | **Latitude** | 36.224 | 36.809 | 35.619 | 35.534 | 36.861 | 35.424 |
| | **Longitude** | -10.010 | -10.126 | -10.794 | -10.585 | -11.411 | -8.790 |
| | **Depth (km)** | 5.7 | 6.6 | 5.4 | 6.6 | 9.5 | 20.3 |
| | **Strike** | 49 | 22 | 80 | 66 | 50 | 107 |
| | **Dip** | 17 | 24 | 20 | 21 | 20 | 88 |
| | **Rake** | 65 | 50 | 88 | 82 | 85 | 160 |
| | **Length (km)** | 100 | 53 | 52 | 90 | 155 | 377 |
| | **Width (km)** | 32 | 28 | 26 | 32 | 50 | 39 |
| | **Area ($km^2$)** | 3200 | 1484 | 1352 | 2880 | 7735 | 14590 |
| | **Slip (m)** | 3.00 | 1.35 | 1.34 | 2.13 | 3.38 | 3.16 |
| | **Moment (Nm)** | 3.17E+20 | 6.61E+19 | 5.98E+19 | 2.02E+20 | 8.63E+20 | 1.52E+21 |
| | **Mw** | 7.60 | 7.14 | 7.11 | 7.47 | 7.89 | 8.05 |
| **3D** | **Latitude** | 36.122 | 36.765 | 35.514 | 35.410 | - | - |
| | **Longitude** | -9.899 | -9.995 | -10.768 | -10.518 | - | - |

| | | | | | | | |
|---|---|---|---|---|---|---|---|
| | **Depth (km)** | 6.2 | 7.2 | 5.7 | 6.2 | - | - |
| | **Strike** | 49 | 22 | 81 | 64 | - | - |
| | **Dip** | 18 | 24 | 21 | 21 | - | - |
| | **Rake** | 65 | 50 | 88 | 82 | - | - |
| | **Area ($km^2$)** | 3197 | 1528 | 1391 | 2784 | - | - |
| | **Slip (m)** | 3.00 | 1.35 | 1.34 | 2.13 | - | - |
| | **Moment (Nm)** | 3.16E+20 | 6.81E+19 | 6.15E+19 | 1.96E+20 | - | - |
| | **Mw** | 7.60 | 7.15 | 7.12 | 7.46 | - | - |

***Table 6.1.*** *Parameters of the modeled faults. Geometric fault reconstructions based on previous works (Bartolome et al., 2012; Gràcia et al., 2003; Martínez-Loriente et al., 2013, 2018; Sallarès et al., 2013). Seismic parameters determined according to scaling relationships (Leonard, 2014). Latitude, longitude, and depth (below seafloor) refer to the fault centroid. For the calculation of seismic moment, the rigidity was fixed at 33 GPa, as in the scaling relationships.*

Note that the fault rake values, based on the regional tectonic average trend in the study area, resulted in ranges from pure and oblique thrusting (50°-88°) to strike-slip (160°) kinematics (Table 6.1). The rake was retained uniform in both planar and 3D complex fault geometries. The earthquake moment magnitude obtained for these structures is in the range $7.1 \leq Mw \leq 8.1$. The LSF, HF and GBF are the faults that can host the largest ruptures. With our choices and with respect to the average values from the scaling relationships, the faults of the Gulf of Cadiz can rupture their entire length, but not their entire width, we thus constrained the earthquake rupture in the upper part of the fault to explore the maximum efficiency in deforming the seafloor. The calculated average slip ranges from ~1.3 m (MPF and NCPF cases) to ~2.1 m (SCPF) and over 3.0 m (HF, GBF, and LSF).

To explore the variability of the tsunami simulations based on different geometric reconstructions of the fault geometries, two earthquake scenarios were defined for each fault, one considering the inclined planar surface, the other considering the complex 3D surface. For all faults, homogeneous slip was used in both cases. For the HF only, we also explored different alternative heterogeneous slip distributions with the same average slip value. We first considered a Gaussian-shaped asperity, then five different stochastic slip distributions superimposed on the Gaussian. The values of the wave height in the different coastal points for all the tsunami simulations, before and after applying Green's law, are available in Annex 4.

## 6.2. Tsunami simulations with planar faults and homogeneous slip

All the tsunami scenarios described below concern the planar faults with homogeneous slip distribution, which is the simplest scenario configuration commonly adopted in preliminary studies, or when data are poor, or when performing studies over very wide regions.

The GBF tsunami scenario obtained with a planar fault approximation (Fig. 6.4a) shows that the most affected coastal areas are in SW Portugal, where the MWH is almost 1 m in a sustained way from Lisbon to Portimão (points 3-6, Fig. 6.4b); and in western Morocco, where 1 m MWH is exceeded in the stretch between Rabat and Safi (points 11-13, Fig. 6.4b). The tsunami waves take 30-40 min to reach the SW Portuguese coasts, and 60-70 min to reach the Moroccan coasts. Most of the tsunami energy generated by the GBF is directed to the northwest in the North Atlantic Ocean (Fig. 6.4a).

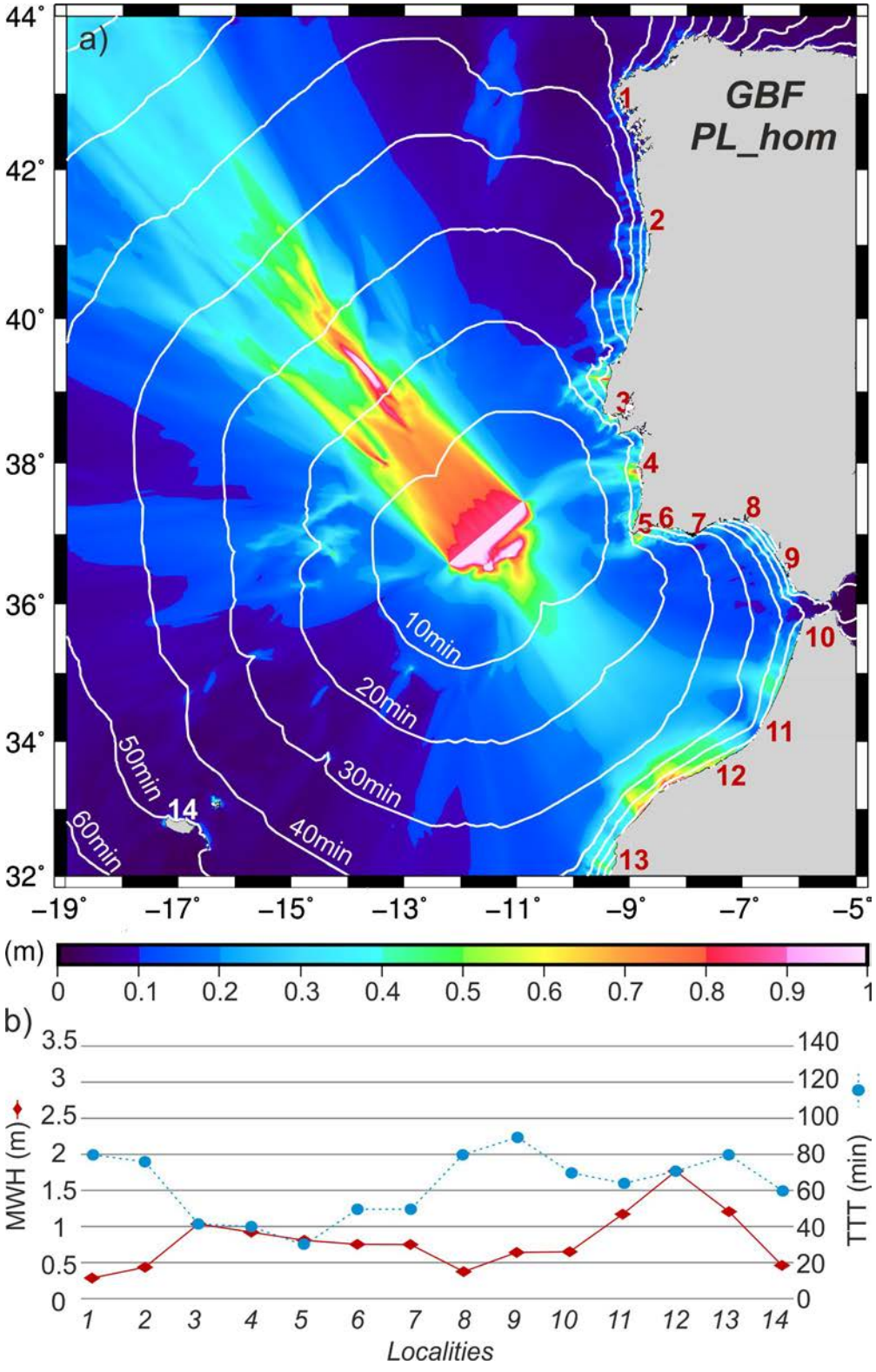


***Figure 6.4.*** *Tsunami simulation results for the Gorringe Bank fault (GBF). a) Map showing maximum wave heights and tsunami travel time (10 min contour intervals) for the GBF considering a simple (rectangular-planar) fault plane and homogeneous slip distribution (PL_hom). b) Maximum GBF tsunami wave height (MWH) and arrival travel times (TTT) at different locations just before reaching the coast. Points 1-14 are coastal localities where*

*maximum tsunami wave height and arrival times have been extracted (1: Fisterra, 2: Porto; 3: Lisbon; 4: Sines; 5: Sagres, 6: Portimão, 7: Faro; 8: Punta Umbria; 9: Cadiz; 10: Tangier; 11: Rabbat, 12: Casablanca; 13: Safi; 14: Madeira).*

The LSF is a planar fault, which generates a tsunami propagation pattern that scatters over an extensive area of the SW Iberian coasts (Fig. 6.5a). The propagation pattern over the Iberian shelf, which is reached only after ~10 min, shows that the tsunami energy is channelled in several northward-directed beams, with the Algarve coast being reached in ~30 min (points 5-7, Fig. 6.5b) and the Spanish coast in ~70 min (points 8 and 9, Fig. 6.5b) with a wave-height peaking at over 3 m in Sagres (point 5, Fig. 6.5b) and ~1 m at all other locations from Sines to Cadiz (points 4, and 6-9, Fig. 6.5b). The NW coast of Morocco is also affected by waves exceeding 0.5 m, with an average arrival time of ~50 min (points 10-13, Fig. 6.5b).

The MPF planar fault scenario (Fig. 6.6a), despite involving a dip-slip component, produces an overall smaller tsunami than the LSF. The tsunami is also smaller than that of the GBF, mostly because the fault dimensions are smaller and, accordingly, we modelled an earthquake of smaller magnitude and slip value. The tsunami propagation for the MPF planar-fault scenario (Fig. 6.6a) is highly controlled by the seafloor relief (Fig. 6.1), which guides the tsunami energy distribution. The GB to the northwest dampens tsunami propagation, while the SVC and the Sagres Plateau, to the southeast, guide tsunami energy towards CSV (nearby Sagres, point 5, Fig. 6.6a-b), and the Portimão and Sines coasts (points 4 and 6, Fig. 6.6a-b). In these localities, the MWH reaches ~0.3 m and the arrival time ranges between 20 and 40 min (points 5 and 6, Fig. 6.6c). A similar MWH affects the Madeira Island to the southwest 1 hour after tsunami initiation (point 14, Fig. 6.6c). The Spanish and Moroccan coasts are not significantly affected by the MPF generated tsunami (points 8-13, MWH < 0.2 m).

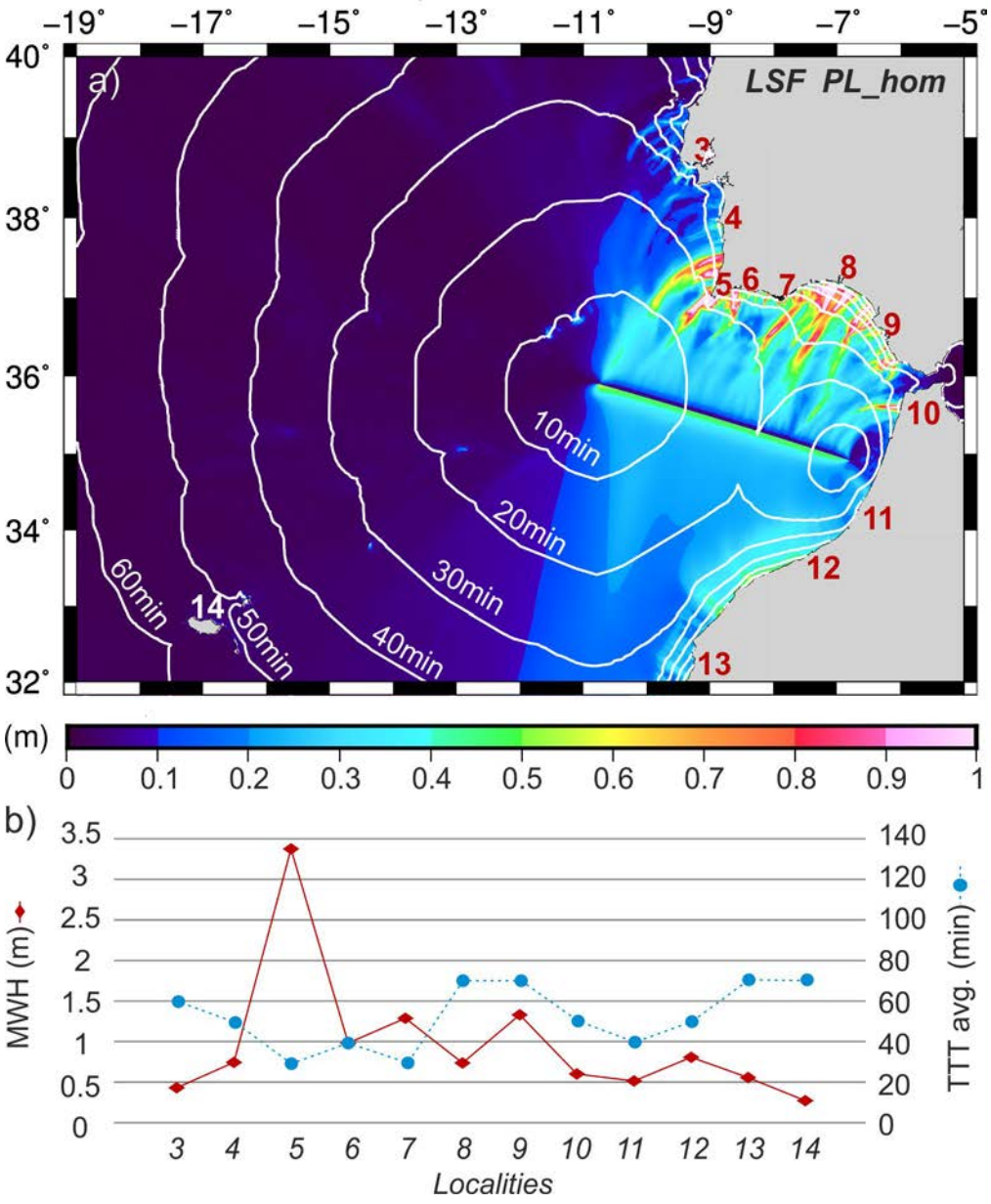


***Figure 6.5.*** *Tsunami simulation results for the Lineament South fault (LSF). a) Map showing maximum wave heights and tsunami travel time (10 min contour intervals) for the LSF considering a simple (rectangular-planar) fault plane and homogeneous slip distribution (PL_hom). b) Maximum LSF tsunami wave height (MWH) and arrival travel times (TTT) at different locations just before reaching the coast. For key to localities 1-14 see Fig. 6.4.*

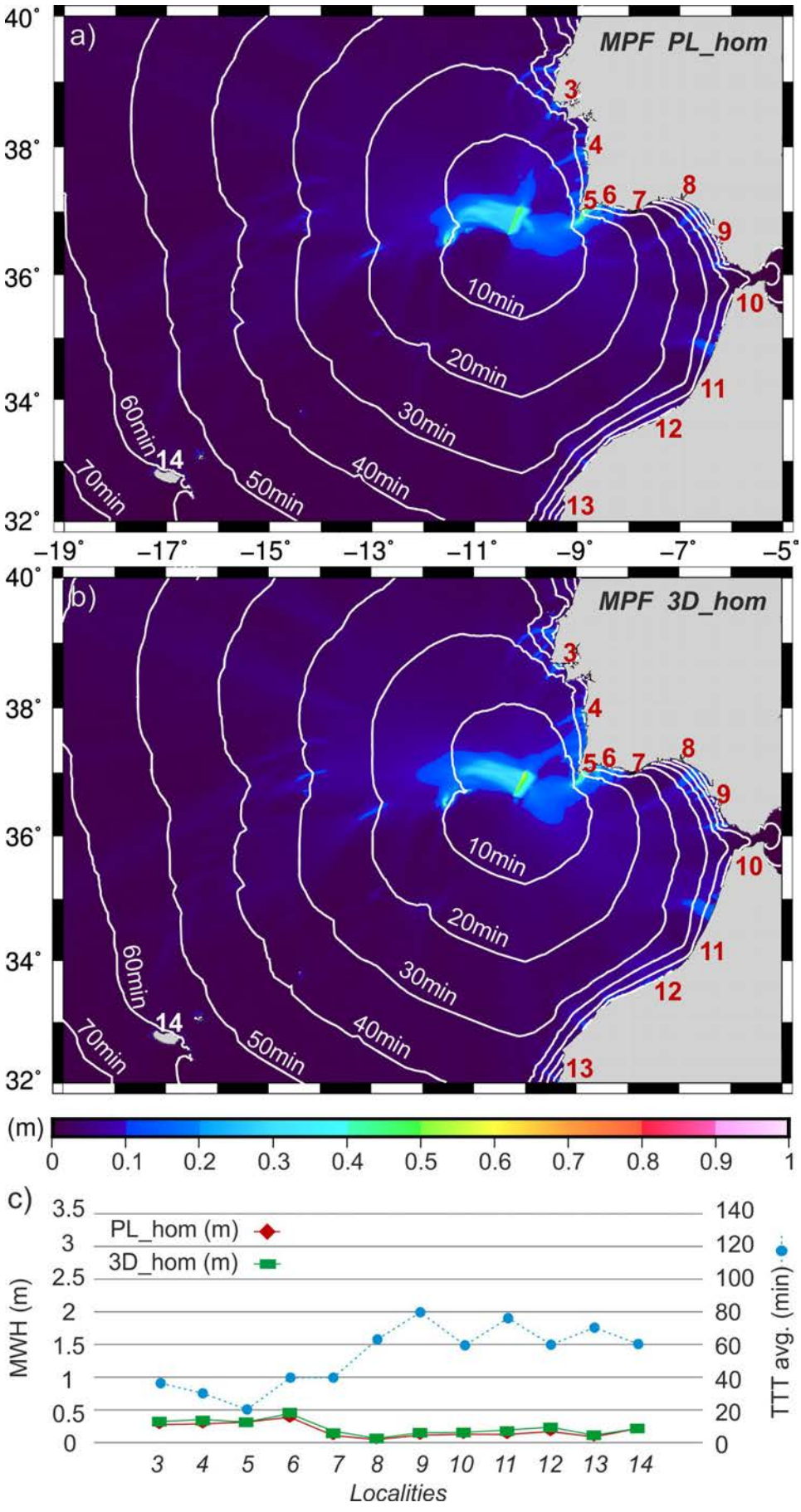
a)
MPF PL_hom
b)
MPF 3D_hom
10min
20min
30min
40min
50min
60min
70min
3
4
5
6
7
8
9
10
11
12
13
14
40°
38°
36°
34°
32°
−19°
−17°
−15°
−13°
−11°
−9°
−7°
−5°
(m)
0
0.1
0.2
0.3
0.4
0.5
0.6
0.7
0.8
0.9
1
c)
PL_hom (m)
3D_hom (m)
MWH (m)
TTT avg. (min)
Localities

***Figure 6.6.*** *Tsunami simulation results for the Marquês de Pombal fault (MPF). Map showing maximum wave heights and tsunami travel time (10 min contour intervals) for the MPF considering a simple (rectangular-planar) fault plane and homogeneous slip distribution (PL_hom) (a) and considering a 3D geometry and homogeneous slip distribution (3D_hom) (b); c) Maximum MPF tsunami wave height (MWH) and average of the arrival travel times (TTT avg.) at different locations just before reaching the coast for both tsunami simulations. For key to localities 1-14 see Fig. 6.4.*

The tsunami scenarios for the NCPF and SCPF using planar fault geometries yield roughly similar patterns (Figs. 6.7a and 6.7d, respectively), but differ in amplitude and, slightly, in orientation of the tsunami propagation due to different fault position, orientation, shape and earthquake size (Figs. 6.1, 6.3 and Table 6.1). In the NCPF case, MWH ranges from 0.2 to 0.3 m from Lisbon to Portimão (points 3-6, Fig. 6.7c) and from Tangier to Madeira (points 10-14, Fig. 6.7c). In the SCPF tsunami simulation, the same localities are affected by higher waves peaking at over 0.6 m in Sagres (point 5, Fig. 6.7f). Similarly to the MPF scenario, the tsunami propagation for the NCPF and SCPF scenarios is dampened to the northwest by the GB. The arrival times to the coast of both tsunami scenarios are similar, since they involve relatively close sub-parallel structures. The tsunami waves take ~30 min to reach the coast of SW Portugal and ~50 min to reach the Moroccan coast (Figs. 6.7c and 6.7f).

The HF scenario mostly affects the Moroccan and Portuguese coasts (Fig. 6.8a). Tsunami MWHs exceed 1 m in Rabat, Casablanca, and Sagres (points 5, 11 and 12 Fig. 6.8j). The tsunami arrival times for the Moroccan coast are ~50 min, 20-30 min for the SW Portuguese coast and 60-70 min for the Spanish coast where the MWH is ~0.50 m in Cadiz. Similarly to the other cases, the GB dampens tsunami propagation to the north.

Overall, for all the scenarios with planar fault and homogeneous slip the most affected localities are Sagres and Casablanca (points 5 and 12, Figs. 6.4-6.8).

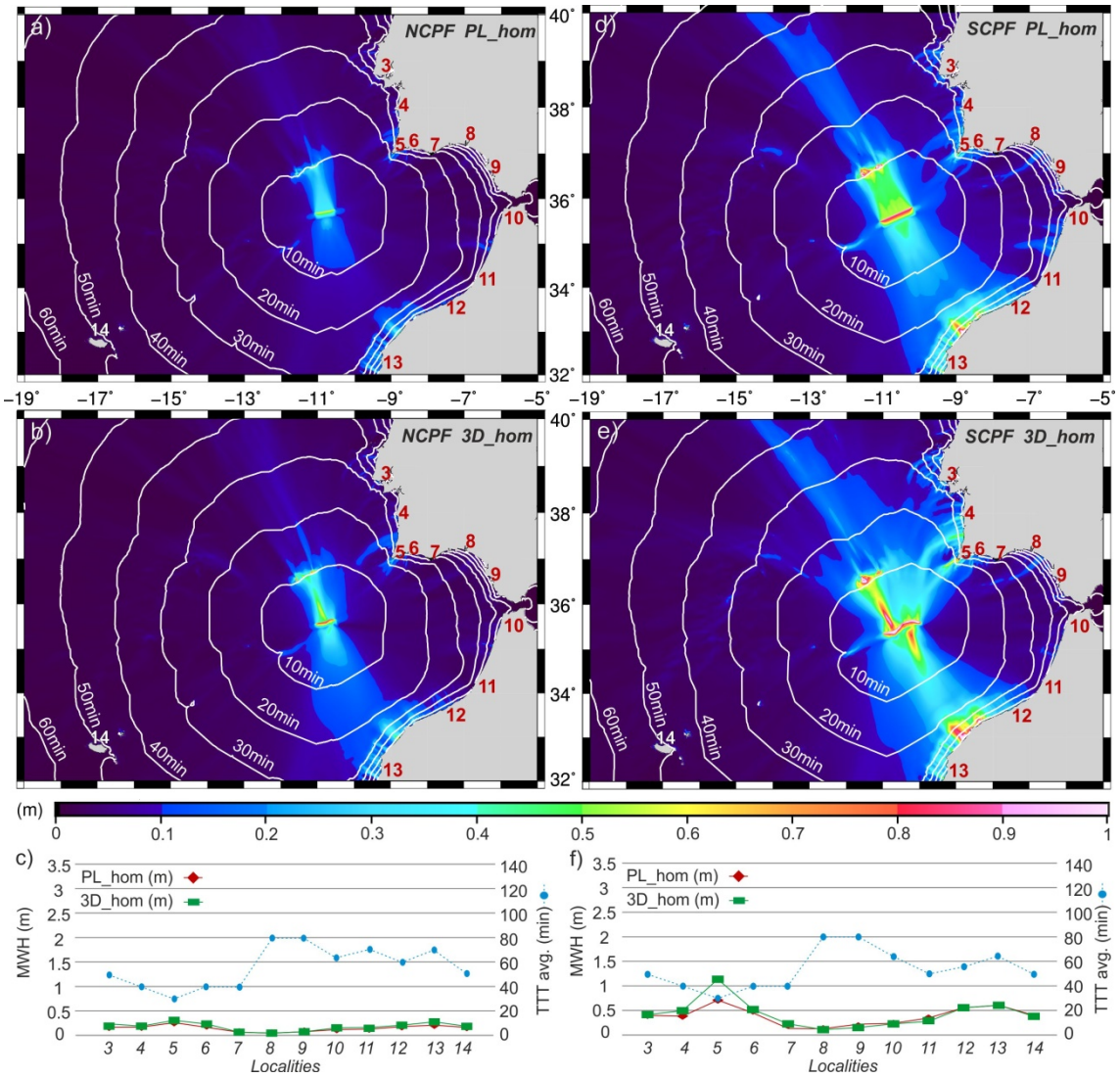


***Figure 6.7.*** *Tsunami simulation results for the North Coral Patch fault (NCPF) and the South Coral Patch fault (SCPF). Map showing maximum wave heights and tsunami travel time (10 min contour intervals) for the NCPF considering a simple (rectangular-planar) fault plane and homogeneous slip distribution (PL_hom) (a) and considering a 3D geometry and homogeneous slip (3D_hom) (b); c) Maximum NCPF tsunami wave height (MWH) and the average of the arrival travel times (TTT avg.) at different locations just before reaching the coast for both tsunami simulations. Map showing maximum wave heights and tsunami travel time (10 min contour intervals) for the SCPF considering a simple (rectangular-planar) fault plane and homogeneous slip (PL_hom) (d) and considering a 3D geometry and homogeneous slip (3D_hom) (e); f) Maximum SCPF tsunami wave height (MWH) and the average of the arrival travel times (TTT avg.) at different locations just before reaching the coast for both tsunami simulations. For key to localities 1-14 see Fig. 6.4.*

## 6.3. Tsunami simulations with 3D and homogeneous slip

To explore the influence of rupture geometry in crustal faults, the tsunami simulations carried out with the simplified planar fault models (described in the previous section) are compared with a new set of simulations. These new simulations are carried out for the MPF, NCPF, SCPF and HF with the corresponding complex 3D geometry using homogeneous slip distributions (Figs. 6.6b, 6.6c, 6.7b, 6.7c, 6.7e, 6.7f, 6.8b and 6.8j). For all these scenarios, the most affected localities are again Sagres and Casablanca (points 5 and 12). Comparing the results of the tsunami simulations for each rupture pair (i.e., simple fault plane vs. complex fault plane), it is observed that the overall MWH pattern is quite similar for all scenarios. However, the MWH absolute value generally increases by about 20% on average when a 3D geometry is used in the simulation (Fig. 6.9a). We also observe MWH peak values up to ~80% higher than the value for the corresponding planar faults. In particular, the highest increments occur for the HF (from 0.5 to 1.5 m, Fig. 6.8j) and for the SCPF (from 0.7 to 1.1 m, Fig. 6.7f), whereas the MWH increments for the MPF and NCPF tsunami scenarios are generally smaller but steadier at all studied localities (Figs. 6.6c, 6.7c). A 3D geometry may focus/defocus the tsunami energy due to fault curvature and introduce shorter wavelengths in the displacement distribution of the tsunami initial condition. As a consequence, a locally larger tsunami in the nearer-field coasts can be observed. The effect is more pronounced for larger, more complex faults, close to the affected coast (e.g. Geist, 2009, and references therein). This effect was also observed in the Ionian Sea from simulations of tsunamigenic earthquakes generated by the Calabrian Arc subduction zone; the convex shape of the rupture causes the tsunami waves to take different paths with respect to the planar rupture, in some cases locally enhancing the resulting impact (Tonini et al., 2020).

## 6.4. Tsunami simulations with planar and 3D faults and heterogenous slip

To explore the influence of spatial earthquake rupture heterogeneities in the resulting tsunami characteristics, we applied heterogeneous slip distributions to the planar and complex 3D models for the HF (Figs. 6.8c-6.8j).

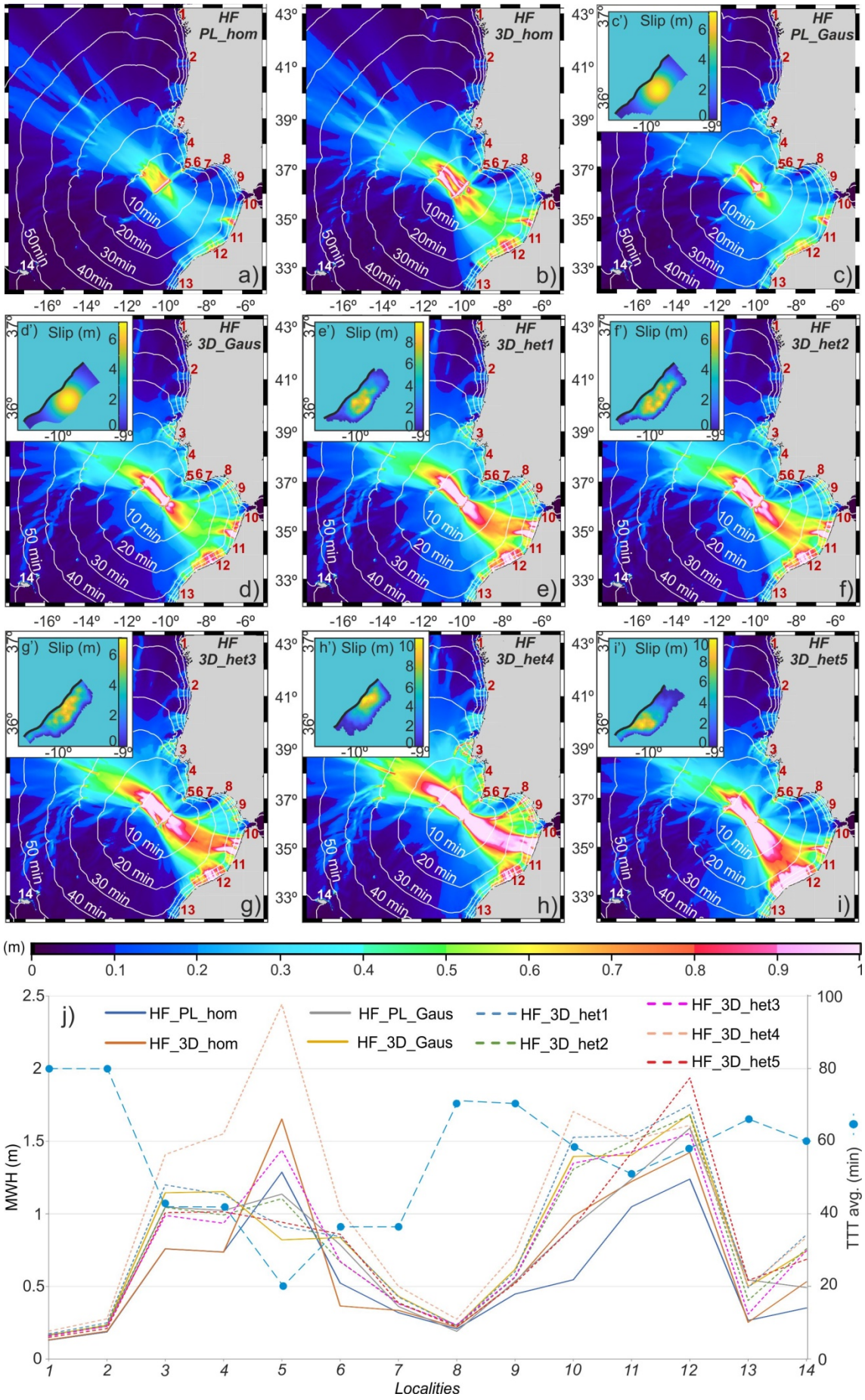
HF PL_hom
HF 3D_hom
HF PL_Gaus
HF 3D_Gaus
HF 3D_het1
HF 3D_het2
HF 3D_het3
HF 3D_het4
HF 3D_het5
Slip (m)
10min
20min
30min
40min
50min
(m)
j)
HF_PL_hom
HF_3D_hom
HF_PL_Gaus
HF_3D_Gaus
HF_3D_het1
HF_3D_het2
HF_3D_het3
HF_3D_het4
HF_3D_het5
MWH (m)
TTT avg. (min)
Localities

***Figure 6.8.*** *Tsunami simulation results for the Horseshoe fault (HF). a) Map showing maximum wave heights and tsunami travel time (10 min contour intervals) for the HF considering a simple (rectangular-planar) fault plane and homogeneous slip distribution (PL_hom). b) Same as panel a) but considering a 3D fault plane and homogeneous slip distribution (3D_hom). c) Same as panel a) but considering a simple rectangular-planar fault plane and gaussian heterogeneous slip distribution (PL_Gaus). d) Same as panel a) but considering a 3D fault plane and gaussian heterogeneous slip (3D_Gaus). e-i) same as panel a) but considering a 3D fault plane and five different stochastic heterogeneous slip distributions (3D_het1-2-3-4-5). j) Maximum tsunami wave heights (MWH) for all HF scenarios at different locations just before reaching the coast and the average of the arrival travel times (TTT avg.) for each location. For key to localities 1-14 see Fig. 6.4. Enlarged tsunami simulations in Annex 5.*

To perform this comparison, we tessellated with a triangular mesh the planar fault using a similar number of elements and average element size as for the complex 3D fault mesh. The slip model in the case of the planar fault is a Gaussian modulation of the uniform slip (Fig. 6.8c), whereas for the 3D fault we used one Gaussian slip model (Fig. 6.8d) and five different realizations of a more realistic stochastic distribution (Figs. 6.8e-i; see Chapter 3, section 3.4). These progressively more complex fault geometry and slip distribution combinations are aimed at representing a progressively increasing degree of similarity to possibly more realistic earthquake scenarios.

The overall pattern of tsunami energy distribution resulting from the scenarios with higher level of complexity remains generally similar to those using the planar fault and homogenous slip (Fig. 6.8). However, in the case of the planar fault, the Gaussian slip distribution determines generally higher MWHs at most locations with respect to the homogeneous slip distribution (Fig. 6.9b). The MWH increment is often higher than the increment obtained with the 3D fault and homogeneous slip (Fig. 6.9b).

For example, off the coast of Casablanca (point 12, Fig. 6.8j), located along the main direction of propagation, there is an increase in MWH from 1.2 m to 1.6 m when using a Gaussian slip on the planar fault, whereas the MWH due to the 3D geometry with homogeneous slip is 1.4 m and with Gaussian slip is 1.7 m. Looking at Sagres (point 5, Fig. 6.8j), located almost orthogonally to the main direction of propagation, the 3D geometry with homogeneous slip yields the second largest MWH value (1.6 m).

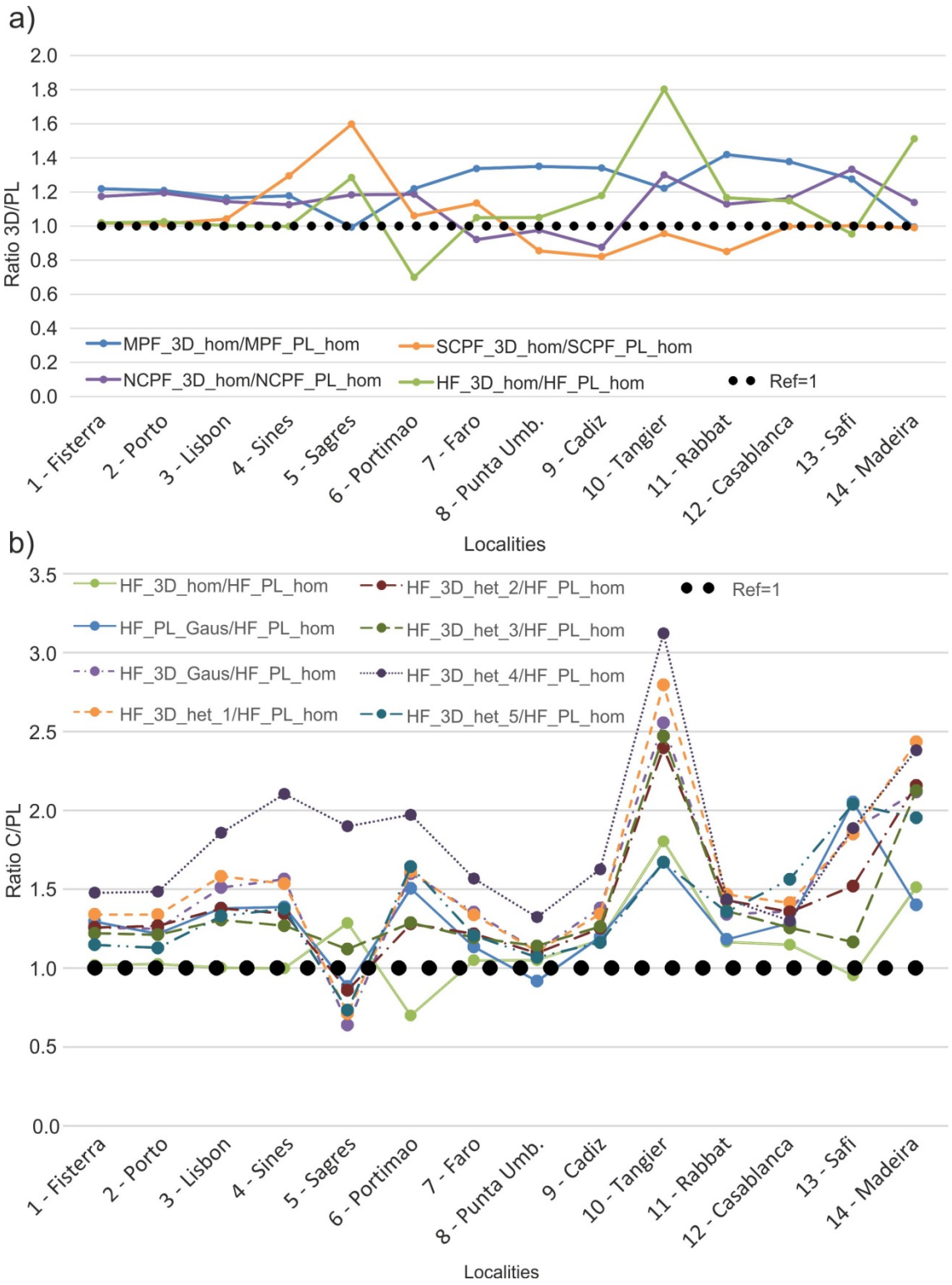


***Figure 6.9.*** *a) Ratio between maximum tsunami wave heights obtained for the 3D fault and homogeneous slip distribution tsunami scenarios (3D: 3D geometry with homogeneous slip) vs. the correlative simple realization (PL; planar fault, homogeneous slip) at the various localities. b) Ratio between the tsunami maximum wave heights obtained for the complex scenarios (C; combination of either planar or 3D geometry with homogeneous, Gaussian, and heterogeneous*

*slip) vs. the correlative simple realization (PL; planar fault, homogeneous slip) at the various localities.*

However, the 3D geometry with Gaussian slip yields the smallest (0.8 m) MWH. The reduction in MWH at Sagres can be counter-intuitive, but it is likely due to the fault orientation, perpendicular to the coast, and slip being concentrated towards the centre of the fault, which makes it more distant from the coast. Irrespective of the specific reason, the overall sensitivity of the phenomenon to the source details induces differences that have in turn a direct implication on tsunami hazard in areas such as the SW Iberian margin, where the fault is very close to the coast and the tsunami has a short travel-time to the impact area (less than 30 min).

When using different realizations of stochastic composite slip (Figs. 6.8e-6.8i), which are more heterogeneous and richer in spatial high-frequency slip than the Gaussian-shaped distributions (Figs. 6.8c-6.8d), the differences are generally more pronounced. For example, heterogeneous slip model h' (Fig. 6.8h), which slip concentrates towards the northeastern edge of the fault, determines an important MWH increase in Sagres (point 5, Figs. 6.8h-j), while heterogeneous slip model i' (Fig. 6.8i), which slip concentrates towards the southwestern edge of the fault, determines a significant MWH increase in Casablanca (point 12, Figs. 6.8i-j). There is also one scenario, heterogeneous slip model 1 (Fig. 6.8e), where the two closely adjacent asperities in the middle of the fault determine enhanced MWH peaks both in Portugal and in Morocco (Fig. 6.8j). These observations suggest a strong MWH dependence on the slip concentration, which in turn depends on the fault geometry. The well-known sensitivity of, at least, local tsunamis to the slip distribution effect, is further enhanced when both the 3D fault and the heterogeneous slip are used.

# PART III

# DISCUSSION

# CHAPTER 7

# Discussion

## 7.1. The tectono-sedimentary evolution of the Cape São Vicente area

### *7.1.1. Sedimentary processes along the São Vicente Canyon*

The highly variable TOBI backscatter evidences Present activity of the canyon. If the identified sedimentary morphologies were relict structures, a thin layer of hemipelagic sediment would homogenize the backscatter while preserving the morphology. Therefore, the TOBI mosaics show that the SVC is a significantly active pathway for sediment transport. Combining the TOBI mosaic and the morphological characteristics of the SVC, reveals a predominance of submarine mass-wasting and erosive processes can be envisaged (Chapter 4, Figs. 4.3, 4.5, 4.6 and 4.7). These processes are widespread along the canyon-flanks characterized by homogenous light-grey colours, characteristic of high-backscatter (corresponding to remobilized sediments), to dark-grey acoustic facies, characteristic of low-backscatter (corresponding to hemipelagic sediments).

Retrogressive erosion is prevalent on the upper-section of the canyon, with steep slopes favouring the incision of gullies along the canyon walls. These gullies often are topped by circular head-scarps, characteristic of retrogressive erosion occurs. Landslide scars are often coalescent and form a sinuous array of unstable features following the main canyon path. Erosion is practically non-existent in the lower section of the SVC (Chapter 4, Figs. 4.3 and 4.7). Of relevance is the NW flank of the SVC, characterized by a large number of submarine landslide deposits and two generations of landslide scars (Chapter 4, Figs. 4.5 and 4.6). The topographically lower landslide scars postdates the upper landslide scars, in contrast with the overall retrogressive and erosional setting of the SVC. The lower set of landslide scars (i.e., the second generation) suggest recent re-arrangement of the NW flank. Such re-arrangement, may result from changes in the base level of the SVC, which tries to come closer to a new equilibrium. In support of this hypothesis, most of the associated deposits with the upper landslide-scars, cannot be recognized as they have been likely eroded. In contrast, the deposits associated with the lower landslide scars can be identified and have not yet been remobilized. The NW

flank is located at the hanging-wall of the MPF (Chapter 4, Fig. 4.9a), that acts as a barrier and hinders the progression of the axial canyon incision. Mass-wasting processes seem to be particularly active in the NW flank of the canyon, although the length of the flank is shorter and slope gradients are gentler than those in the SE flank.

The SVC (Chapter 4, Fig. 4.1), where the so-called São Vicente earthquake cluster nucleates (Geissler et al., 2010; Grevemeyer et al., 2017; Stich et al., 2005) is one of the most seismically active areas of the SW Iberian margin. Several authors suggested that the MPF is the tectonic source of the SVC cluster, which nucleates along the canyon at 20 to 40 km depth (Geissler et al., 2010; Grevemeyer et al., 2017; Martínez-Loriente et al., 2018; Silva et al., 2017). In consequence, seismicity is of great relevance to the occurrence of submarine mass-movements in the SVC. The slope of the canyon-axis significantly decreases in the lower section of the canyon, where submarine mass-movements and turbidity currents also reduce velocity and erosional capacity (Chapter 4, Figs. 4.3 and 4.4). In this section, erosive structures are almost non-existent and the canyon shows a broad U-shaped profile, also suggesting that there is a change in the dynamics of the canyon and a reduction in erosive capacity. The high-backscatter values in the TOBI mosaic along the canyon thalweg indicate the sediment accumulation of gravel and sand (i.e., coarse-grained deposits) (Blondel & Murton, 1997), which provide evidence of the high-energy sediment transport activity along the canyon floor (Chapter 4, Figs. 4.5, 4.6 and 4.7). The accumulation of gravel and sand is, however, scarce and discontinuous, and can probably attest to the presence of lag-deposits from sediment gravity-flows, periodically funnelled along the canyon. The medium-high backscatter values of the three main tributary canyons may suggest turbidity current activity. If the tributary canyons were inactive, they would be covered by a thin layer of hemipelagic sediments, and their backscatter would be rather low. Finally, we also recognize erosive bedforms (i.e., grooves and scours) along the central section of the canyon thalweg. Scours form semi-circular steps (stepped scours or cyclic steps that can be erosive, depositional or mixed) perpendicular to the canyon axis (Chapter 4, Fig. 4.4d) and partially filled by coarse-grained sediment, as inferred from the high-backscatter areas in the TOBI sidescan-sonar mosaic (Chapter 4, Fig. 4.6). Stepped scours (i.e., upstream-migrating bedforms), have been interpreted to result from supercritical turbidity currents (Covault et al., 2017) (Chapter 4, Fig. 4.6).

Migration and growth of these cyclic-steps takes place when the high density basal layer of the hyperpycnal flow, interacts with the seabed triggering a hydraulic-jump downstream at the base of the step (Clarke et al., 2016). Masson et al., (2004) suggested that this type of scour formation requires a minimum current speed between 1.0 and 2.5 m/s.

### *7.1.2. Sediment sources of the São Vicente Canyon*

One of the main characteristics of the SVC is that there is not a significant fluvial system onshore that feeds sediments to the canyon-head (Chapter 4, Fig. 4.1). The main rivers close to the SVC are the Sado River (located 140 km to the north) and the Guadiana River (located 170 km to the east). Both rivers have an adjacent submarine canyon-system that trap and distribute their sediments. Therefore, the direct contribution of sediments from the continent to the SVC is relatively low. Thus, the question is, being the canyon disconnected from the onshore fluvial sources, which are the mechanisms that provide sediments to maintain it active and growing?

Isochore maps show that sediments are mainly accumulated in the central and lower sections of the SVC, since the Middle Miocene (Fig. 7.1c), apparently related to the uplift of the HF hanging-wall block, and the generation of depositional space in the subsiding footwall-block. It seems plausible to consider that the main sediment sources along the SVC, are the materials provided by the erosion of the canyon-flanks through gullies, tributary-canyons and submarine mass-movements that generate submarine landslide deposits, which are abundant in the upper and central sections of the canyon. Arzola et al., (2008) proposed a similar process of flank dismantling in other canyon systems along the Portuguese coast, such as the Nazaré and Setúbal canyons. The total volume eroded from the SVC is estimated at 1219 $km^3$ (Fig. 7.2).

Nevertheless, there are also secondary sediment-sources feeding both, the main SVC and three tributary canyons. The submarine canyons developed along the Portuguese coast incising the continental shelf (e.g., the SVC at the shelf-break), and work as traps for sediments that are transported by bottom-currents along the shelf and upper slope. This is particularly significant in the oceanographic framework of the Gulf of Cadiz, with a complex environment dominated by the MOW (Chapter 2, Fig. 2.25; Chapter 4, Fig. 4.1). Along the pathway from the Straits of Gibraltar towards the West Iberian Margin, the MOW decreases in velocity, temperature and salinity (Hernández-Molina et al., 2015). This favours the formation of sedimentary deposits (i.e.,

contourites) located at the head and flanks of the canyons, such as the SVC (Hernández-Molina et al., 2015; Mencaroni et al., 2021) (Chapter 4, Figs. 4.1 and 4.9a).

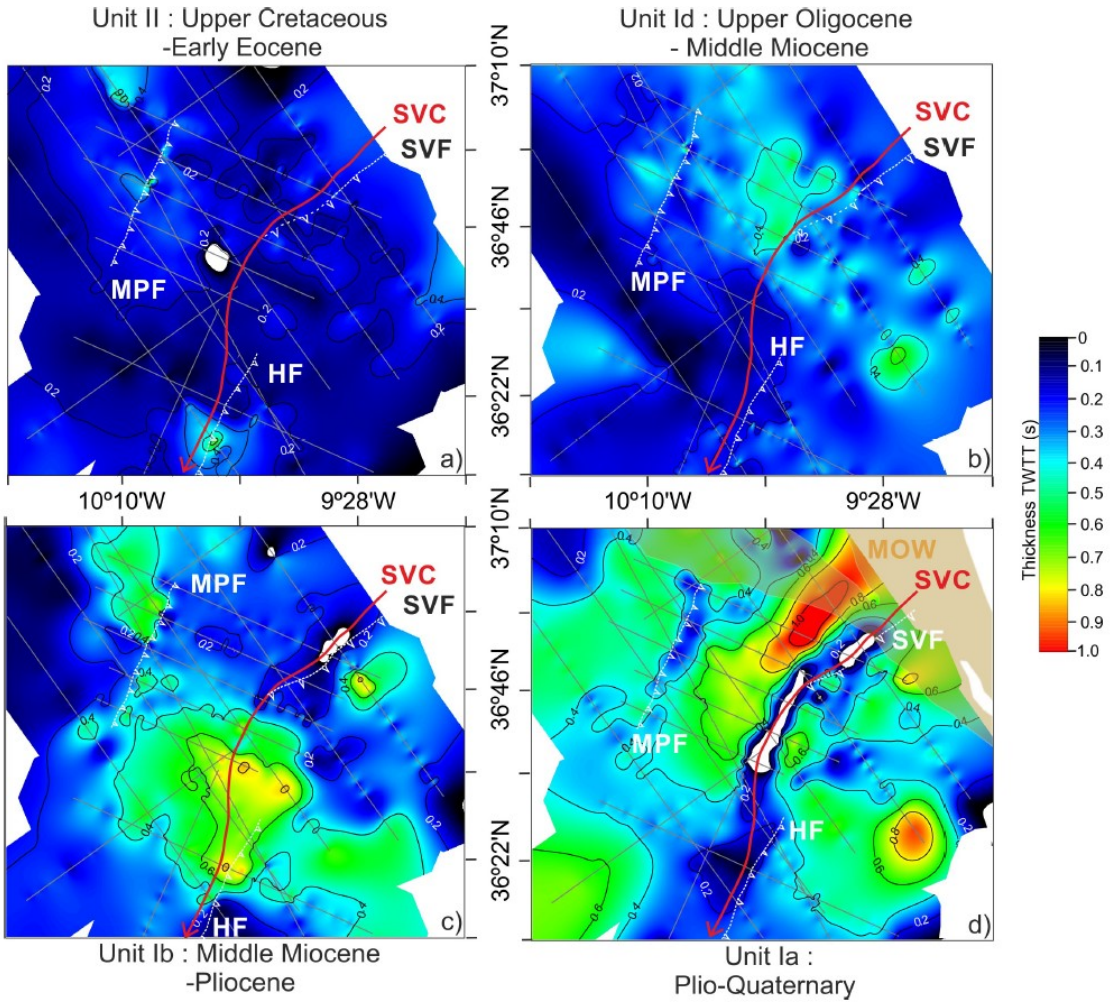


***Figure. 7.1.*** *Isochore maps that illustrate the variation in thickness of the different stratigraphic units through time: a) Upper Cretaceous – Early Eocene (Unit II); b) Upper Oligocene – Middle Miocene (Unit Id); c) Middle Miocene – Pliocene (Unit Ib); and d) Plio-Quaternary (Unit Ia). HF: Horseshoe Fault; MOW: Mediterranean Outflow Water; MPF: Marquês de Pombal Fault; SVC: São Vicente Canyon; SVF: São Vicente Fault; TWTT: Two-way travel time, in seconds.*

The contourites located in the upper section of the SVC, are deposited in water-depths up to 1400 m at Present. At this depth, the sediment transported by the MOW is sand-rich (Hernández-Molina et al., 2015). The TOBI sidescan-sonar images show coarse-grained sedimentary deposits in the upper and central sections of the SVC, that may have been partially deposited by the MOW. Thus, the SVC likely acts as a sediment trap. The coarse-grained and dense sediment of the MOW is trapped at the head of the canyon, which, eventually, could evolve into a hyperpycnal-flow that would

travel down the canyon and form the cyclic-steps in the canyon bed. Also, the relatively high-seismicity of the area (Chapter 2, Section 2.4) likely triggers periodic failure of sediments accumulated at the edge or at the flanks of the canyon, which are subsequently transported along the SVC to the HAP, as previously described.

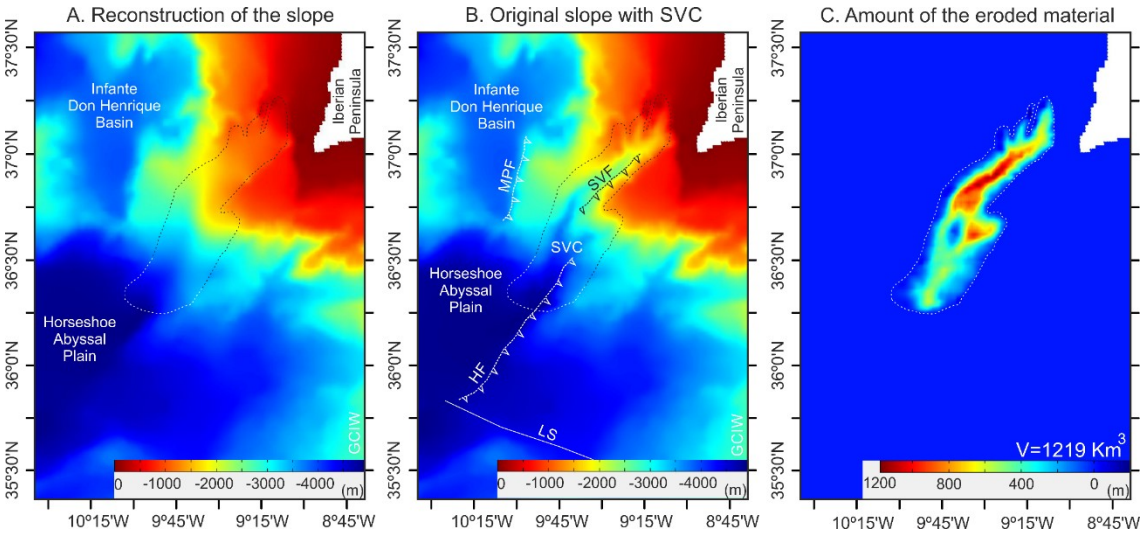


***Figure. 7.2.*** *Volume calculation of the eroded material (C) at the SVC. The volume is calculated from the difference in elevation between a reconstructed spline-smoothed grid in the area of the canyon where the topography has been removed, simulating the original slope (i.e., without the SVC; (A)), and a grid with the actual slope of the SVC (B) (i.e., C=A-B) is calculated.*

### *7.1.3. The formation of the São Vicente Canyon, timing and evolution of the active faults of the Cape São Vicente area*

The SVC is located in a syncline between two reverse fault-controlled anticlines related to the SVF, HF and MPF thrust-faults, suggesting a strong structural control on its development (Chapter 4, Figs. 4.1, 4.9 and 4.11; this Chapter, Figs. 7.2 and 7.3). Their trend (NE-SW) is compatible with the present-day African-Eurasian plate convergence (NW-SE) (Martínez-Loriente et al., 2013, 2018). Our multi-disciplinary dataset give us insights about the timing of formation and evolution of these reverse faults and neighbouring areas. The Upper Cretaceous to Early Eocene period (Unit II) was a tectonic quiescence phase in the SVC area and the low sedimentation rate along the area neighboring the canyon was rather uniform, with the exception of the current mouth of the canyon (Chapter 4, Figs. 4.9, 4.11; this Chapter, Figs. 7.1a and 7.3a). The isochore map (Fig 7.1a) reveal a small depocenter that can be related to the uplift of the HF or the filling of an older rifting structure.

In the lower section of the SVC, the sedimentary record of Unit Id (Upper Oligocene to Middle Miocene) is eroded in the Tortonian due to the emplacement of the allochthonous HGU (Unit Ic,). Therefore, the related isochore map (Fig. 7.1b) does not provide relevant information about the tectonic-activity and sedimentation in this sector of the study area. However, the AR10 seismic profile (Chapter 4, Fig. 4.11) shows that the HGU is not present in the hanging-wall of the HF at the intersection between the central and lower sections of the SVC. This evidence suggests that the lowermost section of the canyon is controlled by the HF and that activity of the fault started before emplacement of the HGU. Thus, this is the oldest section of the SVC of Middle or Late Miocene age (Fig. 7.3b). The isochore map of Unit Id shows a relatively small depocenter at the footwall of the current MPF, and in the southern segment of the SVF (i.e., upper section of the SVC) (Figs. 7.1a and b). According to the seismic reflection data, these depocenters would correspond to the filling of pre-existing rifting structures (Chapter 4, Figs. 4.9a and b).

The MCS profiles show that within Unit Ib (Middle Miocene to Pliocene) there are various unconformities, onlapping reflectors, and thin chaotic units in the central and lower sections of the SVC (Chapter 4, Figs. 4.9 and 4.11). In addition, the isochore map (Fig. 7.1c) reveals a clear depocenter located in the same area. These evidences suggest a contemporaneous sedimentation and progressive folding and uplift of the HF and MPF, which generate accommodation space in the central segment of the canyon, during the Pliocene age (Fig. 7.3c). Unit Ib is locally eroded in the upper section (Fig. 7.1c), but there is no clear evidence that the unit has been eroded by the SVC (Chapter 4, Fig. 4.9a).

The isochore map also shows a depocenter in the footwall of the northern segment of the MPF (Fig. 7.1c). The growth-strata configuration identified in the seismic data (Chapter 4, Fig. 4.11; Chapter 5, Fig. 5.7) suggests synchronous sedimentation with the uplift of the fault. This tectonic activity may have generated accommodation space in the footwall-block that would have been filled by sediments coming from the surrounding morphostructural highs (e.g., Marquês de Pombal Block and Gorringe Bank). In the MPF AUV image (Chapter 5, Fig.5.6), is evidence that this process is still active nowadays since it is possible to recognize the dismantling of the MPB by mass-wasting processes, which generate MTD in the footwall block of the MPF.

The Quaternary deposits are slightly folded, both in the hanging-wall block of the MPF and in the upper and lower sections of the canyon (Chapter 4, Figs. 4.9a, 4.9c and 4.11). This evidence suggests that the Pliocene folding is currently active. This is not the case for the central section of the canyon, where seismic data shows an unfolded Plio-Quaternary Unit (Unit Ia) and no other major tectonic structure could be identified (i.e., the lateral prolongation of the SVF or the HF) (Chapter 4, Fig. 4.9b). The isochore map shows Unit Ia fully eroded along the canyon axis in the upper and central sections, and a highly diminished thickness in the lower section (Fig. 7.1d). The fairly rectilinear profile along the canyon axis (Chapter 4, Fig. 4.4d) suggests that it has not yet reached its long-term equilibrium profile (e.g. Amblas et al., 2011).

Evidence for significant erosion has been observed in the upper and central sections of the canyon (Fig. 7.1) that most likely indicate that the canyon is trying to reach equilibrium. This observation provides further evidence about the relatively young age of the SVC. The isochore map shows three main depocentres, one of them associated with the footwall-block of the MPF (Fig. 7.1d). This observation indicates that during this period, the maximum activity or development of the MPF took place. Therefore, the incision of the SVC may have started during the Pliocene being maximum at the same time that the maximum development of the MPF (Fig. 7.3d). In consequence, this may suggest that the MPF plays an important role in the depositional dynamics of the SVC.

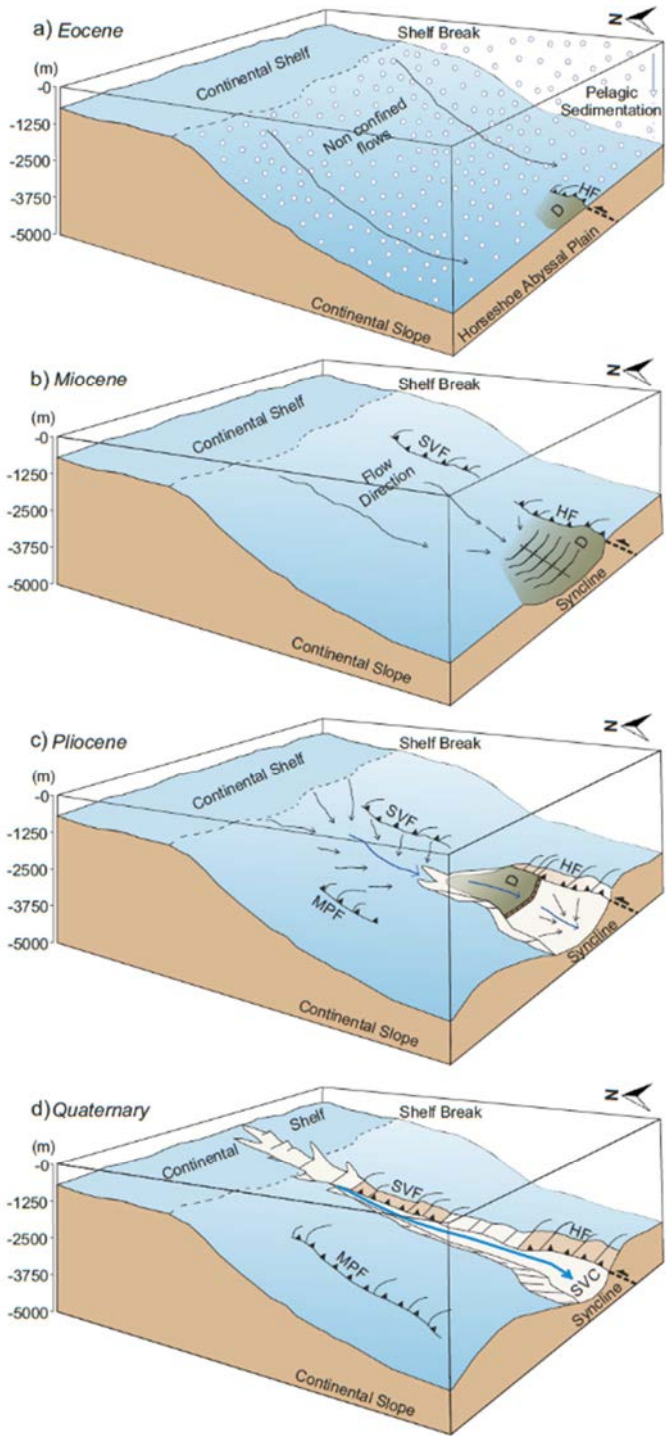


***Figure 7.3.*** *Formation and evolution model of the Sao Vicente area from the Upper Cretaceous to the Plio-Quaternary, including the São Vicente Fault (SVF), the Horseshoe Fault (HF) and Marquès de Pombal Fault (MPF). D: Depocentre; M.M.-P.: Middle Miocene-Pliocene; P-Q: Plio-Quaternary; U.C.-E.E.: Upper Cretaceous-Early Eocene; U.O.-M.M.: Upper Oligocene-Middle Miocene; SVC: São Vicente Canyon.*

All these observations indicate that the canyon, likely developed in the late Quaternary from the central section, where erosion is largest and retrograded via mass-movements on their flanks to the upper section and outer continental shelf (Figs. 7.3c and d). The incision along the SVC axis makes the flanks unstable, which enhances retrogression and canyon widening (Baztan et al., 2005). Mass-movements triggered by turbidity currents may have favoured the incision of the canyon and their progression towards the HAP.

The isochore map of Unit Ia, also shows two depocentres located on both sides of the SVC, in the MPB and the Sagres Plateau (Fig. 7.1d). These depocentres result from sediment contribution by geostrophic currents, which favour sediment accumulation at the head and flanks of the SVC (Hernández-Molina et al., 2003). In summary, the growth of the three main fault systems (MPF, HF and SVF) conditioned the entire existence of the canyon, from its orientation to the incision and width. The initial uplift of the HF generated a depocenter, which became an embryonic canyon with the subsequent evolution of the SVF and the MPF (Fig. 7.3). These structures are currently active, and their uplift constrains the incision and activity of the canyon (permanently in disequilibrium).

### *7.1.4 Local and global relevance of the SVC*

Comparing the morphometric parameters (i.e., length, head-depth, mouth-depth, width, S index and incision) of the SVC with the average in the global inventory of large submarine canyons (Harris & Whiteway, 2011), it turns out that the SVC parameters are significantly larger (at least in terms of length and depth range) (Fig. 7.4, Tables 7.1 and 7.2). A similar relationship can be found when we compare with the average of the parameters in submarine canyons of Western Europe (Fig 7.4, Table 7.1 and Table 7.2). According to the submarine canyon classification by Harris & Whiteway, (2011), three different submarine canyons typologies are distinguished:

- **Type 1**, shelf-incision with connection to a major river-system;
- **Type 2**, shelf-incision without a connection to a major river-system; and
- **Type 3**, blind-canyons.

The SVC belongs to the Type 2 by definition, even though the morphometric parameters are closer to Type 1 (Fig. 7.4). Table 7.2 shows the comparison between the morphometric parameters of different canyon-systems of the West Iberian margin (i.e.,

Cascais, Setubal-Lisbon canyons), as well as the canyons systems of the Southwest Iberian margin (i.e., São Vicente, Sagrês, Lagos, Portimão and Faro canyons). The São Vicente, Setubal-Lisbon and Portimão canyons, the three are controlled by faults and are the longest in a straight line from head to mouth. Together with the Cascais Canyon, they have the greatest depth-range. In addition, their depth at the canyon head is shallower and they all incise the continental-shelf. In contrast, the Sagrês and Faro canyons are shorter, less-incised and their head is located in the upper slope. Among the compared canyons, the only canyon with a clear river-connection is the Setúbal-Lisbon Canyon, which belongs to type 1 and it is the widest canyon.

However, the São Vicente and Portimão canyons also show morphometric parameters, such as length, incision, head and mouth-depth, typical of submarine canyons fed by a large river, despite they have no clear connection to a fluvial system. Finally, when we observe the trace of the MOW (Chapter 2, Fig. 2.25; Chapter 4, Fig. 4.1), it is evident that the heads of the submarine canyons in south and west Iberia, coincides with the trace of the MOW, which may interact with other submarine canyons as it does with the SVC. The SVC has an important sedimentary contribution from the MOW current; therefore it can be classified as a new type of canyon, which is strongly influenced by bottom-currents and also by active tectonic-structures (faults). Despite some authors classify the Gulf of Cadiz and SW Iberia as a passive margin (Harris & Whiteway, 2011), it has been demonstrated that this area is an active margin that hosts the Present-day Eurasia-Africa plate boundary (Bartolome et al., 2012; Gràcia et al., 2003a; Gràcia et al., 2010; Martínez-Loriente et al., 2013, 2014, 2018; Sallarès et al., 2013; Terrinha et al., 2003; Zitellini et al., 2004, 2009).

Some of the world's largest submarine canyons do not have a river connection, and are associated to active margins with subduction zones. On this context, the base-level of these canyons is constantly changing. Therefore, the submarine canyons are not in equilibrium and are constantly incising and growing due to retrogressive erosion. Some examples are the submarine canyons located on the Pacific plate subduction margin, such as the Bering canyon, 400 km-long (Harris & Whiteway, 2011); the Navarin canyon, 250 km-long (Carlson & Karl, 1988); the Zhemchug canyon, 196 km-long (Carlson & Karl, 1988); the Pribilof canyon, 145 km-long (Normark & Carlson, 2003); and the Monterey canyon, 111 km-long (Carlson & Karl, 1988). Other examples, are the submarine canyons that are associated to the subduction-system of the Caribbean

plate, such as the Great Bahama canyon, 175 km-long (Andrews et al., 1970). Thus, the SVC is a clear example of how a large submarine canyon may develop within an active and long-recurrence seismogenic margin.

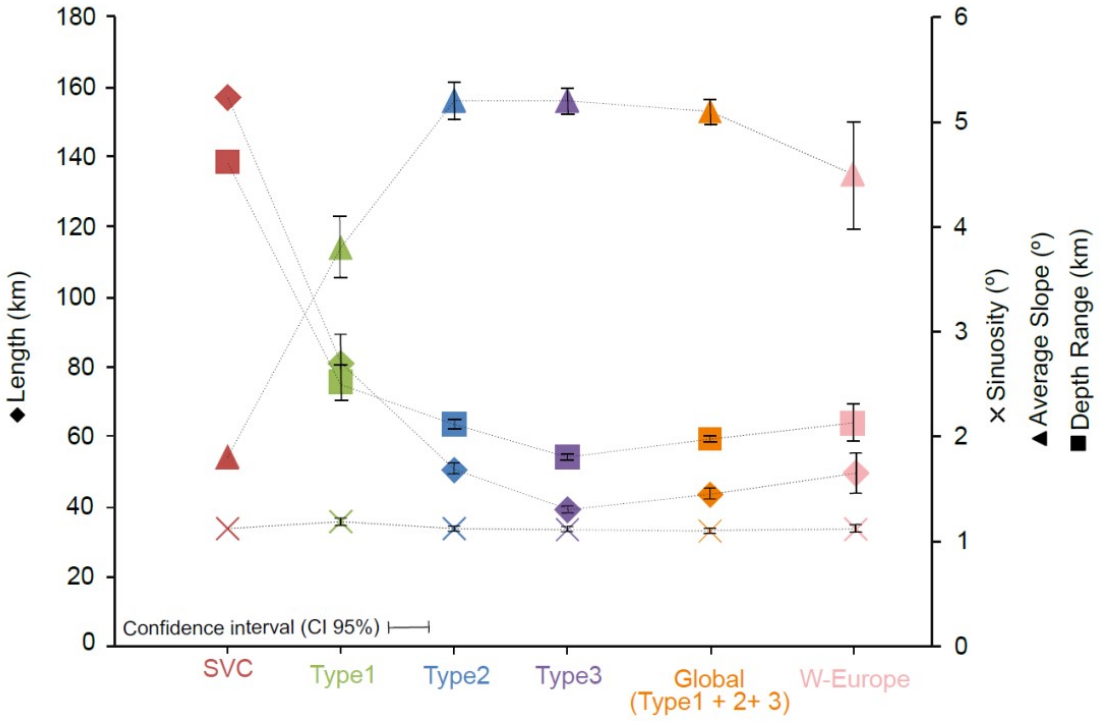


***Figure 7.4.*** *Plot of the mean statistics of the submarine canyons arranged in order of decreasing 959 percentages. Classification of canyons according to Harris et al. (2011): Type 1: Connected to a 960 major river system; Type 2: without connection to a major river system; Type 3: blind canyon. 961 Parameter averages of the submarine canyons in W-Europe and global average of canyon types 962 from Harris et al. (2011). Statistics in table 7.1.*

| | N. | *Length (km)* | | Sinuosity (º) | | Average Slope (º) | | Depth Range (km) | |
|---|---|---|---|---|---|---|---|---|---|
| | | ***SD*** | ***Mean ± CI*** | ***SD*** | ***Mean ± CI*** | ***SD*** | ***Mean ± CI*** | ***SD*** | ***Mean ± CI*** |
| **Type 1** | 153 | 50.9 | 80.9 ± 8.1 | 0.199 | 1.187 ± 0.032 | 1.7 | 3.8 ± 0.3 | 1.080 | 2.767 ± 0.171 |
| **Type 2** | 1671 | 42.4 | 50.4 ± 2 | 0.162 | 1.121 ± 0.008 | 4.2 | 5.2 ± 0.2 | 0.920 | 2.265 ± 0.044 |
| **Type 3** | 4025 | 31.2 | 39.1 ± 1 | 0.154 | 1.111 ± 0.005 | 3.8 | 5.2 ± 0.1 | 0.754 | 1.849 ± 0.023 |
| **Global** | 5849 | 41.5 | 56.8 ± 1 | 0.172 | 1.139 ± 0.004 | 3.2 | 4.7 ± 0.1 | 0.918 | 2.293 ± 0.023 |
| **W-Europe** | 139 | 37.5 | 49.6 ± 6 | 0.118 | 1.120 ± 0.020 | 2.7 | 4.5 ± 0.5 | 1.101 | 2.326 ± 0.183 |

***Table 7.1.*** *Submarine canyons statistics for geomorphic parameters: Length, Sinuosity, Average Slope and Depth Range. Confidence Interval (CI 95%) calculation based on Standard Deviation (SD) from Harris and Whiteway, (2011). N= number of canyons.*

| **Canyon name** | **Straight length (km)** | **Depth at the head (mbsl)** | **Mouth depth (mbsl)** | **Width (km)** | **Sinuosity Index** | **Tectonic control** | **Max. Incision (m)** | **River connection** | **Information Source** | **Canyon type [(1)].** |
|---|---|---|---|---|---|---|---|---|---|---|
| **Cascais** | 61.5 | 175 | 4600 | 4.2-28 | 1.44 | Unknown | 1800 | No | Lastras et al., 2009 | Type 2 |
| **Setúbal-Lisbon** | 145.8 | 150 | 4800 | 7.8-40 | 1.2 | Lower Tagus fault zone and Grãndola fault | 2200 | Tagus and Sado rivers | Lastras et al., 2009 | Type 1 |
| ***São Vicente*** | ***157*** | ***200*** | ***4900*** | ***1.5-3.5*** | ***1.12*** | ***MPF, SVF, HF*** | ***2000*** | ***No*** | ***This study*** | ***Type 2*** |
| **Sagres** | 41.7 | 1300 | 4200 | 1.26-2.89 | 1.06 | Unknown | 300 | No | This study | Type 3 |
| **Lagos** | 56 | 760 | 3600 | 2.46-12.4 | 1.16 | Unknown | 1500 | No | (Marchès et al., 2007) & this study | Type 3 |
| **Portimão** | 134.7 | 100 | 4000 | 2.3-5.7 | 1.125 | Portimão Fault | 1600 | Unknown | (Marchès et al., 2007) & this study | Type 2 |
| **Faro** | 48 | 1300 | 2700 | 4.9-11.8 | 1.16 | Unknown | 700 | No | This study | Type 3 |

***Table 7.2.*** *Morphometric parameters of the canyons in the west and southwest Iberian margins.*

## 7.2. The Lineament South Fault: How active it is?

Until now, evidence for recent activity of the LSF had only been found close to the HAP, where several authors (Bartolome et al., 2012; Terrinha et al., 2009; Zitellini et al., 2009) analysed MCS profiles. Fault activity has been corroborated by the location of few seismic epicentres close to the fault trace (Silva et al., 2017). The total length of the LSF and the maximum extension that may break in a single seismic-event, have been assumed for years on the basis of its topographic expression. However, the fault-trace is not easy to follow and it is not clear at all, in the central part of the GCIW, where the roughness of the seafloor prevents to accurately determine the continuation of the fault-system. In this study, both extremes of the fault have been analysed, the LSW close to the HAP and the LSE close to the Moroccan continental shelf. On both segments, there is clear evidence of present-day activity, which has been revealed throughout the topographic expression of the fault: presence of pressure-ridges, pull-apart basins and a series or crest and troughs, as well as the seismic profiles where the fault system affects the entire sedimentary sequence, and clearly reaches the seafloor surface (Chapter 5, Figs. 5.2, 5.4, 5.6, 5.7 and 5.8).

The AUV bathymetry and the MCS profiles demonstrate that both ends of the fault, which acts throughout its length as a boundary between two-types of oceanic crust (Martínez-Loriente et al., 2014), are active at present-day. In this thesis, we have considered that the entire extent from the active Lineament South West (LSW) segment to the active Lineament South East (LSE) segment constitutes the maximum fault-length that can break, which in total it means a total length of 377 km. The LSF is a deep fault (i.e., reaching down to about 50 km) and, therefore, mechanically it may break along the entire length of the fault. Thus eventually, it may cause one of the most powerful earthquakes in the SW Iberian margin, reaching up to $M_w$ 8.05 (calculated with Leonard, 2014).

The LSW AUV image shows seafloor sedimentary structures, such as submarine dunes and furrows. These sedimentary structures occur directly over the fault and therefore, their understanding may provide additional clues on the fault activity. These sedimentary structures show a perpendicular geometric relationship in between them (Chapter 5, Figs. 5.2 and 5.3). The asymmetry of the dunes is a reliable indicator of their direction of motion and, indirectly, as an indicator of the direction of the flow that generated them (Perillo, 2001). The submarine dunes are generated perpendicular to the

flow-direction, from the trough of the dunes to the slip-face (Dalrymple & Rhodes, 1995). On the basis of this postulation, it can be inferred that the submarine flows that generate and move the submarine dunes in the LSW segment comes from the NNW and travels towards the SSE. The furrows are one of a series of longitudinal bed-forms, which are aligned with the net direction of the water flows and are typically attributed to the development of secondary helicodal circulation-cells, that occur above the sediment/water interface (Allen, 1971; Viekman et al., 1989). The massive number of furrows and their orientation suggests that the furrows have been produced by NNW-SSE currents of strong deep-water flows (Cuevas, 2013).

Since the submarine dunes are perpendicular to the flow and the furrows are parallel, it seems logical that both bed-forms were produced by the same submarine current. Taking into account that the LSW segment is located in water-depths greater than 4000 m (Chapter 5, Fig.5.2), the bottom current that flow to these great depths in the Gulf of Cadiz is the NADW (North Atlantic Deep Water) (Baringer & Price, 1999; Hernández-Molina et al., 2015; Llave et al., 2006; Ochoa & Bray, 1991; Thorpe, 1975; Zenk, 1975). The NADW is a cold (3-8 ºC) and less saline (34.95-35.2 ‰) water-mass that flows from the Greenland-Norwegian Sea region to the Atlantic-Mediterranean at water-depths greater than 1500 m (Hernández-Molina et al., 2015; Llave et al., 2006). The NADW current acquired its present configuration at the end of the glacial-age, therefore, the current pathway of the NADW is about 10,000-11,000 years old (Elliot et al., 2002). As seen on the AUV image of the LSW there is a furrow structure, which is sectioned and dislocated 60 m to the right by the LSF trace (Chapter 5, Fig. 5.2 and 5.3). As it is proposed that the furrows were formed by the NADW, which is about 10,000 years old it has been inferred that the LSW segment has moved in a transcurrent-way, at least 60 m, during the Holocene period. Probably, along the LSF trace, there are more displaced furrows and dunes. However, due to the large number of bed-forms, their similar morphology and the irregularities of the seafloor around the fault, it is not possible to determine the correspondence between the other bed-forms on both sides of the fault trace. Despite the NADW seems to be the most plausible origin of the bed-forms, some authors (e.g. Beal et al., 2006; Mencaroni et al., 2021; Talley et al., 2011) propose that in this area the velocity of the NADW is close to zero. In this case, the NADW would not have enough energy to generate these bed-forms, and the only possible submarine currents that can generate it would be the turbidity currents (Tinterri

et al., 2020) from the submarine canyons of the SW Iberian margin. If the origin of the bed-forms is from the turbidity currents of the submarine canyons, with the data of this PhD Thesis is not possible to infer the date of the furrow dislocation.

In the LSE AUV image we reveal a ridge-structure that is sectioned and dislocated 150 m to the right, in comparison with the displaced furrows, however, the age of this ridge cannot be constrained with the available data (Chapter 5, Figs. 5.4 and 5.5). Despite the lack of time constraints for the displacements, the different right-lateral and vertical slip displacement on both ends of the LSF (Chapter 5, Fig. 5.8), might imply different slip/seismogenic behaviour along the fault-system.

Although, the main component of the LSF movement is right-lateral (evidence by the dislocated structures and the rake), a vertical component is evidence in the seismic profiles (Chapter 5, Fig. 5.8).

## 7.3. Relevance of complex models to obtain realistic tsunami

We analysed the tsunami MWH at 14 locations along the coasts of SW Iberia and NW Morocco produced by earthquake scenarios with different levels of complexity, from planar fault geometries with homogeneous slip distribution to the complex 3D fault geometries with highly heterogeneous slip distributions. The higher level of complexity tends to represent a more realistic earthquake scenario. Although the fault geometry characterization can be improved by acquiring more data, the slip distribution remains a random variable. The different cases analysed have shown that a higher level of complexity most often leads to higher MWH at coastal locations and only occasionally to lower MWH (Chapter 6, Figs. 6.6-6.9). Whether the MWH absolute values increase or decrease depends on the relative position of the coastal location with respect to the fault position and orientation, and ultimately on the position of the slip heterogeneity on the fault. The combination with local bathymetric features enhances the effect in several cases. In relative terms, these variations can be as high as three times as much as the simplest scenarios (planar fault and homogeneous slip) (Chapter 6, Fig. 6.9). This difference in wave-height between the two models has direct implications on the resulting run-up and the consequent inland flooding. Therefore, complex tsunami source models for crustal faults must be considered in future tsunami hazard assessment.

## 7.4. Bathymetric effects

In all simulated scenarios, spatial variations in the propagation of the tsunami (i.e., channelling of the tsunami energy) are observed. This effect is much more noticeable in the LSF scenario, which significantly affects the SW Iberian coast (Fig. 7.5). In this case, neighbouring locations have a very different tsunami impact. For instance, 42 km separate Sagres from Portimão, but there is a difference in wave-height of 250% (i.e., from 3.5 m to 1 m, respectively) (points 5 and 6 in Chapter 6, Fig. 6.5b; this Chapter Fig. 7.5).

Comparing the areas where the LSF tsunami energy focusses with the bathymetry of the area, a clear relationship can be established with the presence of submarine canyons and topographic reliefs. When tsunami waves travel through submarine canyons, such as the SVC, LC and PC, they do not lose as much velocity or increase as much wave height as when they pass above the high reliefs surrounding the canyon (Fig. 7.5). Consequently, the wave height and tsunami energy off locations facing the canyons is lower than in the absence of canyons, as observed in previous works (Aranguiz & Shibayama, 2013; Iglesias et al., 2014). In contrast, outside submarine canyons such as the SVC with topographic reliefs of 1500 m (MPB and Sagres Plateau; Chapter 6, Fig. 6.1; this Chapter Fig. 7.5), there is a velocity decrease and wave-height amplification by the shoaling effect (Iglesias et al., 2014).

The effect of canyons on velocity is highly dependent on the canyon's morphology. In the SW Iberian margin, the submarine canyon that can produce the least MWH increase is the SVC (Serra et al., 2020). In the case of the LSF tsunami scenario (Chapter 6, Fig. 6.5; this Chapter Fig. 7.5), the presence of the SVC prevents wave build-up and decreases the tsunami energy in the coastal area north of CSV, while the Sagres Plateau causes an increase of the wave-height in the Sagres area (point 5, Fig. 7.5).

In a similar way, the presence of the LC and PC induce a decrease in wave-height east of Sagres and in the coastal area between Portimão and Faro (points 6 and 7, Fig. 7.5). Similar effects have been verified in other geographic areas. For example, during the 2010 Mw 8.8 Maule earthquake and tsunami that hit Chile, the flooding reached 6-8 m high, while in areas in front of submarine canyons the inundation did not exceed 2 m-height (Aranguiz & Shibayama, 2013).

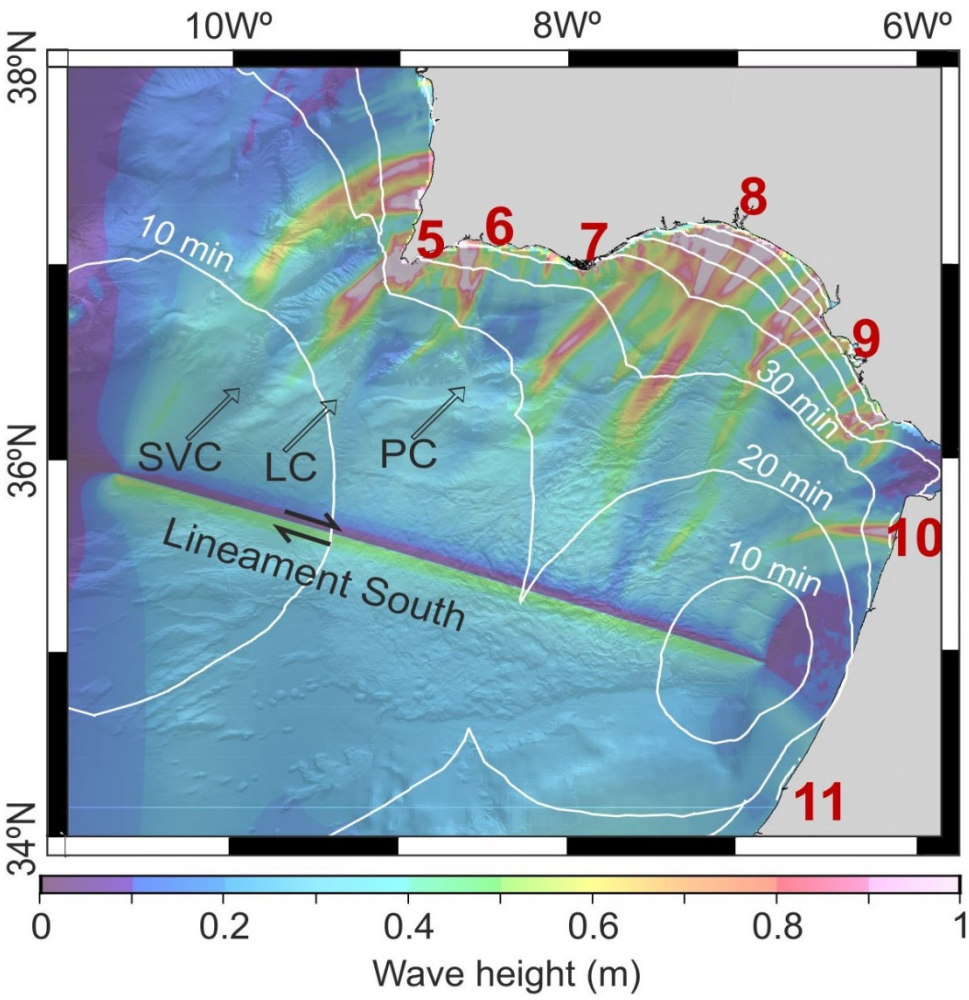


***Figure 7.5.*** *Lineament South fault dislocation simulated tsunami wave height distribution along the SW Iberian margin with shaded bathymetry (Zitellini et al., 2009) displaying the position of submarine canyons.*

There are other morphological features in the Gulf of Cadiz that control the propagation pattern of tsunami energy, such as the lobes of GCIW or the channel incised through the Straits of Gibraltar (Chapter 6, Fig. 6.1). In the LSF tsunami scenario, it can be observed how the presence of lobes focusses the tsunami energy, and hence increases the wave-height (Fig. 7.5). The channel crossing the Straits of Gibraltar, on the other hand, prevents the build-up of tsunami waves and diverts energy propagation. As a result of such energy diversion, the coastal area of Tangier is severely affected by the tsunami, with waves exceeding 1 m-high (Fig. 7.5). As explained above, due to the strong shoaling effect, the GB also has a great influence on propagation of tsunami energy, dissipating or scattering it (Chapter 6, Figs. 6.4-6.8). The Murray Ridge

in the Arabian Sea has a similar effect on the directivity of tsunamis originating from the Makran subduction zone (Swapna & Srivastava, 2014).

## 7.5. Impact of tsunami scenarios on the coasts of SW Iberia and NW Morocco

Tsunami simulation results indicate that the NW Moroccan coast is the most affected area if a tsunami originates on a thrust fault (Chapter 6, Figs. 6.4-6.8). The effects are notorious in the case of tsunamis generated by the GBF, HF, and SCPF. Most of the tsunami energy from these faults radiates perpendicular to the Moroccan coast, which has a wide, shallow continental shelf. Therefore, the shoaling effect is expected to cause a significant increase in the wave height. Although we did not investigate the inundation properties of the simulated scenarios, it should be considered that the Moroccan coastline is mainly composed by massive sand dune beaches and estuarine environments, which can be easily flooded (Lobo et al., 2014). Altogether, with the poor coverage of sea-barriers and coastal sea-defence structures in different areas of Morocco (Omira et al., 2011) make these coasts prone to enhanced tsunami effects.

The major thrust faults, the GBF (Chapter 6, Fig. 6.4) and the HF (Chapter 6, Fig. 6.8), radiate part of their energy to the Spanish and SW Portuguese coasts. The wide and shallow SW Iberian shelf induces an increase in wave-height, especially in the HF tsunami scenario, which has a significant impact on the Spanish coastal area. In the Algarve area, the presence of submarine canyons prevents the wave-height to increase along most of the coastline, except in the CSV and Sagres areas, where the Sagres Plateau acts as a guide for tsunami energy towards the coast and increases the wave-height (Chapter 6, Fig. 6.8). In the case of the GBF, most of the tsunami energy is radiated towards the North-Atlantic Ocean and the impact on the Peninsula is restricted to the W-Portuguese coast, between Sagres and Lisbon (Chapter 6, Fig. 6.4).

The LSF tsunami scenario generates the highest waves in the SW Iberian margin (Chapter 6, Fig. 6.5; this Chapter Fig. 7.5). Despite its sense of movement is not very efficient in deforming the seafloor, the significantly larger earthquake magnitude together with the rupture orientation determines that most of the tsunami energy is radiated towards the northeast. Its proximity to a large, wide and shallow shelf causes a

drastic increase in wave height on the Algarve and Spanish coasts (Fig. 7.5). However, a large coastal stretch of the Algarve is dominated by rocky cliffs (Lobo et al., 2014) and protected by the presence of submarine canyons, which prevent a significant increase of the tsunami wave height at its shores. In contrast, the Spanish coast is mainly made-up of estuaries, marshes and sandy beaches (Benavente et al., 2015) that could be easily flooded. Hence, the Spanish coasts are more prone to inundation than those of the Algarve.

Previous tsunami models in the SW Iberian margin (Baptista et al., 2011; Matias et al., 2013; Omira et al., 2011), substantiate the significant impact that tsunamis originating on the HF and GBF can have on the coasts of Morocco, Portugal and Spain. However, these works cannot be directly compared with our results because of the different approaches followed and the newly considered structures, such as the SCPF and, especially, the LSF.

Finally, other active faults in this area, such as the LNF, PSF and PBF faults (Chapter 6, Fig. 6.1), have not been analysed in this study due to the lack of relevant MCS data. However, considering their orientation (parallel to the coast) and proximity to the shore, these faults deserve to be considered in local tsunami hazard assessments. The difficulties posed by their lower level of knowledge (higher epistemic uncertainty) can be treated by including these faults into a category of potential seismic sources characterized by larger aleatory variability of their parameters adopting, for example, the method for probabilistic tsunami hazard analysis developed by Selva et al., (2016) and already applied at the regional scale by Basili et al., (2021). In this way, the hazard analysis can benefit from implementing an input dataset as complete as possible while treating and controlling the major uncertainty sources.

# PART IV

# CONCLUSIONS

# AND

# FORWARD LOOK

# CHAPTER 8

# Conclusions

In this thesis, new insights about the interaction between active tectonics, and the dynamics of submarine canyons are provided; the seismogenic and tsunamigenic potential of the main active-faults of the Gulf of Cadiz is evaluated; and the sensitivity of tsunami impact on the coastal areas, to the fault-geometry and slip-distribution is assessed. The most relevant findings of this research are:

*1st Hypothesis: The Marquês de Pombal fault plays a key role in the evolution of the Cape São Vicente area. Furthermore, the main active faults in this zone (i.e., Marquês de Pombal Fault, São Vicente Fault and Horseshoe Fault) controlled the development of one of the largest submarine canyon, in the Atlantic continental margins: São Vicente Canyon*.

A multiscale view of the SVC region includes the use of a multibeam echo-sounder data, 2D multi-channel seismic profiles and high-resolution TOBI sidescan sonar data, which allow us to carry-out an accurate morpho-sedimentary and tectonic study of the processes occurring in this area. The upper and the central sections of the SVC are deeply entrenched (2000 m incision) in the continental slope. The upper section shows a V-shape that progressively changes to a U-shape at the central section, whereas the lower section directly connects to the HAP. On the basis of its physiography (bathymetric profile with a rectilinear morphology and constant slope), at the present, the SVC is not in equilibrium and shows erosive dynamics. In the upper and central sections of the canyon, retrogressive erosion and dismantling of the flanks predominate, indicating that the canyon evolves from bottom-up. The submarine landslide deposits and landslide-scars are the main processes that allow bottom-up evolution of the SVC. The material resulting from the dismantling of the flanks and the contourites related to the MOW are the main sedimentary source, as the canyon is not fed by any river. The MOW contributes with material through two different processes: a) It deposits contourites on the flanks and head of the upper-section of the canyon, that periodically fail into the canyon; and b) The coarser-grained and denser sediment of the MOW might be trapped at the head of the canyon and be able to generate hyperpycnal flows. Erosion

by the hyperpycnal and other sediment gravity-flows, forms steps at the canyon bed on their way to the canyon mouth. Most of the sediment gravity-flows are likely triggered by frequent seismic events in this area. The origin of the canyon is fully tectonic and actively deforming at present as shown by the long-profile and active sedimentary dynamics. The canyon is mostly Quaternary in age, although related to initial uplift of the HF, which developed a synclinal fold at the base of the continental slope, during a NNW-SSE trending compressive stage (late Miocene). The topographic relief, latter enhanced by the evolution of the SVF and MPF, favoured the development of an embryonic canyon. During the Pliocene, the embryonic canyon develop towards the continental-shelf by means of retrogressive mass-failures induced by the tectonic uplift and steep slope gradient. Full development of the canyon took place coinciding with the period of maximum activity of the MPF, in the Quaternary, evidenced by the isochore maps and the vertical slip distribution of the fault. Therefore, the SVC is a diachronous and segmented canyon. Currently, the SVC shows a strong structural control and it is conditioned by three main active faults (i.e., the MPF, the SVF and the HF).

*2nd Hypothesis: The accuracy of the fault models has a considerable influence on the resulting tsunami-propagation pattern and the wave-height and improves significantly the simulation of the worst-case tsunami scenarios. Therefore, accurate parameters, realistic fault-planes and heterogeneous slip-distributions need to be taken into account during the tsunami hazard assessment process.*

A large dataset allowed us to determine and model the relatively detailed fault-geometries of the main active structures in the SW Iberian margin. While the 2D MCS profiles provided information to re-defining or corroborating previously determined parameters for each fault, AUV images allowed verifying the present-day activity of some of them. An example is the case of the LSF, where two AUV images demonstrated the activity of the fault at both ends of its trace; or the case of the MPF where the current trace of the fault and the mass-wasting processes, consequence of its activity, are evidence in the AUV image. By modelling and comparing tsunami scenarios for each fault using simple and complex fault-plane geometries and different slip-distributions (i.e. homogeneous and heterogeneous), it can be observed that the coastal zones affected by the tsunamis are quite similar for all scenarios. However, there is up to 50% variation in wave-height, in most of the coastal locations, when using complex fault-plane models. Adding a stochastic slip-distribution to the complex fault-

planes, the wave distribution of the tsunami models is relatively poorly affected, but the wave-height increases dramatically (up to 300%) at some points along the coastline, in comparison to the simple fault-plane with homogeneous slip-distribution. Therefore, considering a realistic fault-plane and a heterogeneous slip-distribution, it is highly relevant for tsunami hazard assessment. Submarine canyons strongly interact with tsunami features induced by fault and slip complexity, and play a major role in controlling regional tsunami hazard. It is then very important to accurately characterize the local bathymetry. On the basis of the tsunami simulations carried out in this study, the HF, GBF and SCPF are the faults that may pose the highest threat to the Moroccan coast, where the low topography along the coastline could also be easily flooded. In the case of the Iberian Peninsula, the LS seems to be the most threatening fault for the Spanish and Algarve coasts. The rocky cliffs of the Algarve coast are not easily flooded and the presence of the SVC, LC and PC attenuates the wave-height that reaches the coastline, decreasing the potential tsunami effects in this area. In contrast, the southern Spanish coast is dominated by plains and marshes that can easily be flooded. For the west coast of Portugal, the most threatening fault is the GBF, mainly because of the proximity of source and impact areas.

# CHAPTER 9

# Forward look

This PhD Thesis provides new insights that concern the development of the CSV area and the large SVC. A conceptual model to discuss the emplacement, age and evolution of the canyon system, which shows a strong structural-control, is proposed. This study also provides accurate analyses of the fault-plane geometries and fault-source parameters of the most relevant fault systems in the SW Iberian margin. Using this data, realistic 3D-fault planes and heterogeneous slip-distributions are used for tsunami modelling. Further to this work carried, we have several ideas to solve questions that raised as a result of the work presented in this PhD Thesis.

## 9.1. Installation of two moorings stations along the São Vicente Canyon

In this study, we do not use sedimentological information from gravity-cores, piston-cores or mooring stations along the SVC. Therefore, we cannot demonstrate the relationship between the MOW and hyperpycnal flows. We link these two processes as a potential hypothesis. To clarify if the sediments of the SVC are directly fed by the MOW and then trapped in the canyon or mobilized from periodic failures of sediment drifts at the edge of the canyon or both processes, I propose: The installation of two deep mooring-stations with sediment traps, current-meters, CTD, turbidimeters and profilers of the water column to measure the flow-water rate, its periodicity and characteristics and to mesure the transported sediment grain size.

## 9.2. Improving the tsunami models in the SW Iberian margin

### *9.2.1 The seismic imaging of the São Vicente, Lineament South, Lineament North and Pereira de Souza faults.*

In the framework of this PhD, the fault parameters are based on different datasets. However, despite the MPF, HF, SCPF and the NCPF appear to be well-constrained, the

LSF and other faults, such as the SVF, LNF and PSF need more information from MCS data to be properly constrained as explained below.

The SVF has been recognized in this PhD Thesis using a succession of high-resolution MCS profiles. Specifically, by means of 6 seismic-profiles acquired from November of year 1998 during the BIGSETS cruise. These seismic profiles are not of very high-qualit. However, despite the relatively low quality, they allow us to see how the SVF raise the seafloor and become a blind-thrust, which gradually attenuates until it disappears in the southern end. However, we miss several high-quality profiles at the northern end of the fault, to see its geometry appropriately. New MCS data would provide better high-quality data to constrain accurately the 3D geometry of the fault-plane.

In the case of the LSF, we have good constraints at the fault terminations, however, there is a lack of seismic data in the central part of the lineament. In this area, new MCS profiles would provide information to construct the 3D fault-plane geometry of the entire LSF. Finally, we recognize that we do not have enough good-quality and appropriately-oriented MCS profiles to constrain the fault-plane geometry of the LNF and PSF. Therefore, new MCS and several sub-bottom profiler profiles are needed. For all this reasons, I propose the accomplishment of a new geophysical survey to record 17 new seismic profiles in the SW Iberian margin (Fig. 9.1).

### *9.2.2. Tsunami modelling of other active structures in the area*

Due to the lack of relevant MCS data, the SVF, LNF, PBF and PSF systems in the SW Iberian margin, have not yet been carefully analysed. However, considering the orientation (i.e., parallel to the coast) of the LNF, PBF and PSF, and the proximity of the SVF to the Iberian Coast, I consider that it would be necessary to carry-out new tsunami models, considering the 3D fault-plane for each active structure to constrain geohazard properly. Before this is accomplished, a geophysical survey needs to be carried out to cover the requirements of section 9.2.1. Therefore, the new MCS data for the SVF, LNF and PSF to determine the 3D-fault-planes for the new tsunami simulations will be adequate (Fig. 9.1). The MCS data to generate the PBF 3D fault plane can be obtained from the dataset of the INSIGHT-Leg2 survey.

### *9.2.3. Tsunami scenarios for the LSF considering a complex fault-geometry and heterogeneous slip-distribution.*

Since the LSF is the largest and most threatening fault in the SW Iberian margin, I consider that is necessary to assess the tsunami threat to the SW Iberian Peninsula. Modelling the potential tsunami of the LSF with the 3D fault-plane geometry could also incorporate several stochastic slip-distributions. The 3D fault-plane could be generated with the MCS profiles acquired according to section 9.2.1.

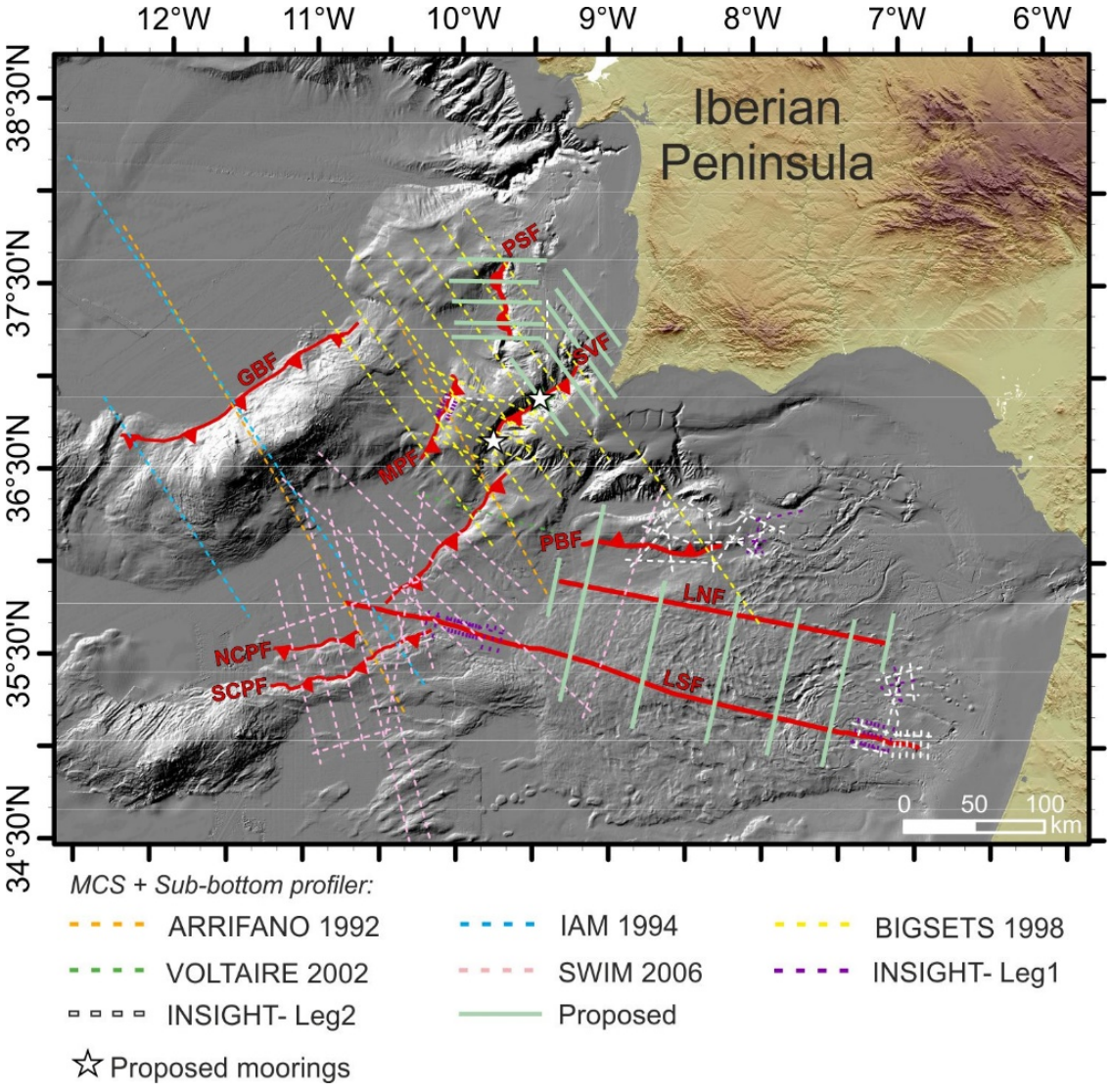


***Figure 9.1.*** *Relief map of the SW Iberian margin. Discontinuous coloured lines correspond to the available TOPAS and MCS profiles used in this study and acquired during different surveys (See Chapter 3). Continuous light green lines correspond to the new geophysical transects proposed in this Forward look. White stars, located in the upper and middle part of the SVC correspond to the location of the proposed moorings within the SVC.*

# PART V

# REFERENCES

# List of acronyms used in the Thesis text

AGFZ: Azores Gibraltar Fault Zone

AUV: Autonomous Underwater Vehicle

BQD: Base of Quaternary Discontinuity

CAO: Central Atlantic Ocean

CC: Cascais Canyon

c.i.: cubic inches

CMP: Common Mid-Point

COT: Continent-Ocean Transition

CPR: Coral Patch Ridge

CSV: Cape of São Vicente

CTD: Conductivity, Temperature, Depth

DSDP: Deep Sea Drilling Project

FC: Faro Canyon

GB: Gorringe Bank

GBF: Gorringe Bank Fault

GCIW: Gulf of Cadiz Imbricated Wedge

GiF: Gibraltar Fault

GuB: Guadalquivir Bank

GuBF: Guadalquivir Bank Fault

HAP: Horseshoe Abyssal Plain

HAT: Horseshoe Abyssal Plain Thrust

HF: Horseshoe Fault

HGU: Horseshoe Gravitational Unit

HPC: High Performance Computing

IB: MOW lower core, intermediate branch

IDHB: Infante Don Henrique Basin

IODP: Integrated Ocean Drilling Program

LARS: Launch and Recovery System

LBL: Long-baseline

LC: Lagos Canyon

LNF: Lineament North Fault

LSE: Lineament South, East section

LSF: Lineament South Fault

LSW: Lineament South, west section

m.b.s.l.: meters below sea level

MCS: Multi-channel seismic

ML: MOW lower core

MOW: Mediterranean Outflow Water

MPB: Marquês de Pombal fault Block

MPD: Mid-Pleistocene Discontinuity

MPF: Marquês de Pombal Fault

MTD: Mass-Transport Deposits

MU: MOW Upper core

MWH: Maximum Wave Height

NCPF: North Coral Patch Fault

PB: Portimão Bank

PBF: Portimão Bank Fault

PBr: MOW lower core, principal branch

PC: Portimão Canyon

PSDM: Pre-Stack Depth Migration

PSF: Pereira da Sousa Fault

PTHA: Probabilistic Tsunami Hazard Analysis

ROV: Remotely Operated Vehicle

SAC: Sagres Canyon

SAP: Seine Abyssal Plain

SB: MOW lower core, southern branch

SC: Setúbal Canyon

SCPF: South Coral Patch Fault

SH: Seine Hills

SHF: Seine Hills Faults

SVC: São Vicente Canyon

SVF: São Vicente Fault

SFZ: SWIM Fault Zone

TAP: Tagus Abyssal Plain

TM: Top of Miocene Discontinuity

TOBI: Towed Ocean Bottom Instrument

TOPAS: Topographic Parametric Sounder

TWTT: Two-way travel time

WAS: Wide-Angle Seismic

Ia: Plio-Quaternary

Ib: Middle Miocene – Pliocene

Id: Upper Pliocene -Middle Miocene

II: Upper Cretaceous - Lower Eocene

III: Cretaceous

IV: Lower Cretaceous

V: Upper Jurassic

VI: Basement

# REFERENCES

AAPG. (2015). Seismic sequence analysis. Retrieved 20 March 2021, from https://wiki.aapg.org/Seismic_sequence_analysis

Allen, J. R. L. (1971). A Theoretical and Experimental Study of Climbing-Ripple Cross-Lamination, with a Field Application to the Uppsala Esker. *Geografiska Annaler: Series A, Physical Geography*, *53*(3–4), 157–187. doi:10.1080/04353676.1971.11879843

Allen, J. R. L. (1983). Studies in fluviatile sedimentation: Bars, bar-complexes and sandstone sheets (low-sinuosity braided streams) in the brownstones (L. Devonian), welsh borders. *Sedimentary Geology*, *33*(4), 237–293. doi:https://doi.org/10.1016/0037-0738(83)90076-3

Alves, T. M., Gawthorpe, R. L., Hunt, D. W., & Monteiro, J. H. (2003). Cenozoic tectono-sedimentary evolution of the western Iberian margin. *Marine Geology*, *195*(1–4), 75–108. doi:10.1016/S0025-3227(02)00683-7

Ambar, I., & Howe, M. R. (1979). Observations of the Mediterranean outflow—I mixing in the Mediterranean outflow. *Deep Sea Research Part A. Oceanographic Research Papers*, *26*(5), 535–554. doi:https://doi.org/10.1016/0198-0149(79)90095-5

Amblas, D., Gerber, T. P., Canals, M., Pratson, L. F., Urgeles, R., Lastras, G., & Calafat, A. M. (2011). Transient erosion in the Valencia Trough turbidite systems, NW Mediterranean Basin. *Geomorphology*, *130*(3–4), 173–184. doi:10.1016/j.geomorph.2011.03.013

Amblas, D., Gerber, T. P., De Mol, B., Urgeles, R., Garcia-Castellanos, D., Canals, M., … Canning, J. (2012). Survival of a submarine canyon during long-term outbuilding of a continental margin. *Geology*, *40*(6), 543–546. doi:10.1130/G33178.1

Andrews, J., Shepard, F., & Hurley, R. (1970). Great Bahama Canyon. *Geological Society of American Bulletin*, *81*, 1061–1078.

Aranguiz, R., & Shibayama, T. (2013). Effect of submarine canyons on tsunami

propagation: A case study of the biobio canyon, Chile. *Coastal Engineering Journal*, *55*(4). doi:10.1142/S0578563413500162

Arboleya, M. L. (2018). De la tectónica de placa a la cordillera del Atlas. Retrieved 29 September 2020, from https://ddd.uab.cat/pub/llibres/2018/199432/tecplacor_a2018_p1.pdf

Arzola, R. G., Wynn, R. B., Lastras, G., Masson, D. G., & Weaver, P. P. E. (2008). Sedimentary features and processes in the Nazaré and Setúbal submarine canyons, west Iberian margin. *Marine Geology*, *250*(1–2), 64–88. doi:10.1016/j.margeo.2007.12.006

ATLAS HYDROGRAPHIC. (2010). Atlas Hydrosweep Ds. Deep-Sea Multibeam Echosounder. Retrieved 10 November 2020, from http://209.240.133.120/media/pdf/product_resources/75.pdf

Auzende, J. M., Olivet, J. M., Charvet, J., Le Lann, A., Le Pichon, X., Monteiro, J. H., … Ribeiro, A. (1978). Sampling and observation of mantle and crust on Gorringe Bank. *Nature*, *273*, 45–49.

Bahr, A., Kaboth, S., Jiménez-Espejo, F. J., Sierro, F. J., Voelker, A. H. L., Lourens, L., … Friedrich, O. (2015). Persistent monsoonal forcing of Mediterranean Outflow Water dynamics during the late Pleistocene. *Geology*, *43*(11), 951–954. doi:10.1130/G37013.1

Banda, E., Torne, M., & Investigation Group. (1995). Iberian Atlantic margins group investigates deep structure of ocean margins, a multichannel seismic survey. *EOS*, *76(3)*, 25–29.

Baptista, M. A., Heitor, S., Miranda, J. M., Miranda, P., & Mendes Victor, L. (1998). The 1755 Lisbon tsunami; Evaluation of the tsunami parameters. *Journal of Geodynamics*, *25*(1–2), 143–157. doi:10.1016/s0264-3707(97)00019-7

Baptista, M. A., & Miranda, J. M. (2009). Revision of the portuguese catalog of tsunamis. *Natural Hazards and Earth System Science*, *9*(1), 25–42. doi:10.5194/nhess-9-25-2009

Baptista, M. A., Miranda, J. M., Omira, R., & Antunes, C. (2011). Potential inundation

of Lisbon downtown by a 1755-like tsunami. *Natural Hazards and Earth System Science*, *11*(12), 3319–3326. doi:10.5194/nhess-11-3319-2011

Baringer, M.O., & Price, J. F. (1999). A review of the physical oceanography of the Mediterranean Outflow. *Marine Geology*, *155*, 63–82.

Baringer, M.O., & Price, J. F. (1999). A review of the physical oceanography of the Mediterranean outflow. *Marine Geology*, *155*(1), 63–82. doi:https://doi.org/10.1016/S0025-3227(98)00141-8

Bartolome, R., Gràcia, E., Stich, D., Martínez-Loriente, S., Klaeschen, D., de Lis Mancilla, F., Zitellini, N. (2012). Evidence for active strike-slip faulting along the Eurasia-Africa convergence zone: Implications for seismic hazard in the southwest Iberian margin. *Geology*, *40*(6), 495–498. doi:10.1130/G33107.1

Basili, R., Brizuela, B., Herrero, A., Iqbal, S., Lorito, S., Maesano, F. E., … Zaytsev, A. (2021). The Making of the NEAM Tsunami Hazard Model 2018 (NEAMTHM18). *Frontiers in Earth Science.* Retrieved from https://www.frontiersin.org/article/ 10.3389/feart.2020.616594

Baztan, J., Berné, S., Olivet, J.L., Rabineau, M., Aslanian, D., Gaudin, M., … Canals, M. (2005). Axial incision: The key to understand submarine canyon evolution (in the western Gulf of Lion). *Marine and Petroleum Geology*, *22*(6), 805–826. doi:https://doi.org/10.1016/j.marpetgeo.2005.03.011

Beal, L. M., Chereskin, T. K., Lenn, Y. D., & Elipot, S. (2006). The sources and mixing characteristics of the Agulhas Current. *Journal of Physical Oceanography*, *36*(11), 2060–2074. doi:10.1175/JPO2964.1

Beauchamp, W., Allmendinger, R. W., Barazangi, M., Demnati, A., El Alji, M., & Dahmani, M. (1999). Inversion tectonics and the evolution of the High Atlas Mountains, Morocco, based on a geological-geophysical transect. *Tectonics*, *18*(2), 163–184. doi:https://doi.org/10.1029/1998TC900015

Bellingham, J. (2009). Platforms: Autonomous Underwater Vehicles. In *Encyclopedia of Ocean Sciences* (pp. 473–484). doi:10.1016/B978-012374473-9.00730-X

Benavente, J., Gracia, F. J., Del Río, L., Anfuso, G., & Rodríguez-Ramírez, A. (2015).

Caracterización morfodinámica de las playas españolas del Golfo de Cádiz. *Boletin Geologico y Minero*, *126*(2–3), 409–426.

Betancourt, A. C., Ranero, C. R., & Gràcia, E. (2015). Structure and activity of the imbricated wedge of the Gulf of Cadiz from MCS images, *EGU. Geophysical Research Abstracts 17*, 8941.

Biscaye, P. E., & Eittreim, S. L. (1977). Suspended particulate loads and transports in the nepheloid layer of the abyssal Atlantic ocean. *Marine Geology*, *23*, 155–172.

Blondel, P., & Murton, B. (1997). *Handbook of the seafloor sonar imagery*. Published by Jhon Wiley & Sons and Praxis Publishing. West Sussex, England.

Blondel, P., Parson, L. M., & Robigou, V. (1998). *TexAn: Textural Analysis oft Sidescan sonar imagery and generic seafloor characterisation*. In *IEEE Oceanic Engineering Society. OCEANS'98* (p. 6). Nice: IEEE. doi:10.1109/OCEANS.1998.725780

BonAppetour. (2020). Must see attractions in Lisbon. Retrieved 30 October 2020, from https://www.bonappetour.com/blog/things-to-do-in-lisbon/

Booth-Rea, G., Ranero, C. R., Martínez-Martínez, J. M., & Grevemeyer, I. (2007). Crustal types and Tertiary tectonic evolution of the Alborán sea, western Mediterranean. *Geochemistry, Geophysics, Geosystems*, *8*(10). doi:https://doi.org/10.1029/2007GC001639

Borrero, J. C. (2005). Field Survey of Northern Sumatra and Banda Aceh, Indonesia after the Tsunami and Earthquake of 26 December 2004. *Seismological Research Letters*, *76*(3), 312–320. doi:10.1785/gssrl.76.3.312

Bourillet, J. F., Edy, C., Rambert, F., Satra, C., & Loubrieu, B. (1996). Swath mapping system processing: Bathymetry and cartography. *Marine Geophysical Researches*, *18*(2), 487–506. doi:10.1007/BF00286091

British Antartic Survey. (2015). Multibeam echosounder. Retrieved 10 November 2020, from https://www.bas.ac.uk/polar-operations/sites-and-facilities/facility/rrs-james-clark-ross/multibeam-echosounder-2/

Brown Jr., L. F., & Fisher, W. L. (1980). Seismic Stratigraphy Interpretation and

Petroleum Exploration. American Association of Petroleum Geologists. doi:10.1306/CE16409

Bryant, E. (2008). *Tsunami. The Underrated Hazard* (2nd ed.). Jointly published with Praxis Publishing, UK. Originally published by Cambridge University Press: Springer-Verlag Berlin Heidelberg. doi:10.1007/978-3-540-74274-6

Buforn, E., Bezzeghoud, M., Udías, A., & Pro, C. (2004). Seismic sources on the Iberia-African plate boundary and their tectonic implications. *Pure and Applied Geophysics*, *161*(3), 623–646. doi:10.1007/s00024-003-2466-1

Buforn, E., Sanz de Galdeano, C., & Udías, A. (1995). Seismotectonics of the Ibero-Maghrebian region. *Tectonophysics*, *248*(3–4), 247–261. doi:10.1016/0040-1951(94)00276-F

Campos, M. L. (1991). Tsunami hazard on the Spanish coasts of the Iberian Peninsula. *Science of Tsunami Hazards*, *9*, 83–90.

Canals, M., Puig, P., De Madron, X. D., Heussner, S., Palanques, A., & Fabres, J. (2006). Flushing submarine canyons. *Nature*, *444*(7117), 354–357. doi:10.1038/nature05271

Carafa, M. M. C., & Barba, S. (2013). The stress field in Europe: Optimal orientations with confidence limits. *Geophysical Journal International*, *193*(2), 531–548. doi:10.1093/gji/ggt024

Carlson, P. R., & Karl, H. A. (1988). Development of large submarine canyons in the Bering Sea, indicated by morphologic, seismic, and sedimentologic characteristics. *Bulletin of the Geological Society of America*, *100*(10), 1594–1615. doi:10.1130/0016-7606(1988)100<1594:DOLSCI>2.3.CO;2

CERU. (2015). O último grande sismo. Retrieved 2 November 2020, from http://www.ceru-europa.pt/en/galeria.php?page_foto=2

Chester, F. M., Mori, J., Eguchi, N., Toczko, S., & Scientists group. (2012). Japan Trench Fast Drilling Project (JFAST). *Proceedings of the Integrated Ocean Drilling Program*, *343/343T*, 1930–1014.

Clarke, H. J. E., Talling, P. J., Cartigny, M. J. B., & Pratomo, D. G. (2016).

Preconditioning and triggering of offshore slope failures and turbidity currents revealed by most detailed monitoring yet at a fjord-head delta. *Earth and Planetary Science Letters*, *450*, 208–220. doi:10.1016/j.epsl.2016.06.021

Covault, J. A., Kostic, S., Paull, C. K., Sylvester, Z., & Fildani, A. (2017). Cyclic steps and related supercritical bedforms: Building blocks of deep-water depositional systems, western North America. *Marine Geology*, *393*, 4–20. doi:10.1016/j.margeo.2016.12.009

Cox, A., & Hart, R. B. (1986). *Plate tectonics: How it works*. Blackwell Scientific Publications.

Cuevas, E. (2013). Morphological and sedimentological assessment of submarine dune fields on the coast of Yucatan, Mexico. *Ciencias Marinas*, *39*(1), 83–99. doi:10.7773/cm.v39i1.2152

Cunha, D., Roque, C., Silva, F., Silva, E. A., Lourenço, N., & de Abreu, M. P. (2009). Morphostructure of the S. Vicente Canyon, Marquês de Pombal Fault and Pereira de Sousa Fault (SW Iberia margin), *5*, 211–215.

Custódio, S., Dias, N. A., Carrilho, F., Góngora, E., Rio, I., Marreiros, C., Matias, L. (2015). Earthquakes in western Iberia: improving the understanding of lithospheric deformation in a slowly deforming region. *Geophysical Journal International*, *203*(1), 127–145. doi:10.1093/gji/ggv285

Dalrymple, R. W., & Rhodes, R. N. (1995). Estuarine dunes and bars. *Developments in Sedimentology*, *53*, 359–422. doi:10.1016/S0070-4571(05)80033-0

de la Asunción, M., Castro, M. J., Fernández-Nieto, E. D., Mantas, J. M., Acosta, S. O., & González-Vida, J. M. (2013). Efficient GPU implementation of a two waves TVD-WAF method for the two-dimensional one layer shallow water system on structured meshes. *Computers and Fluids*, *80*(1), 441–452. doi:10.1016/j.compfluid.2012.01.012

DeMets, C., Gordon, R. G., & Argus, D. F. (2010). Geologically current plate motions. *Geophysical Journal International*, *181*(1), 1–80. doi:10.1111/j.1365-246X.2009.04491.x

Díez, S., & Gràcia, E. (2005). Submarine Mapping using Multibeam Bathymetry and and Acoustic Backscatter: Illuminating the Seafloor. *Instrumentation Viewpoint*, *3*, 10–14.

Duarte, J. C., Rosas, F. M., Terrinha, P., Gutscher, M. A., Malavieille, J., Silva, S., & Matias, L. (2011). Thrust-wrench interference tectonics in the Gulf of Cadiz (Africa-Iberia plate boundary in the North-East Atlantic): Insights from analog models. *Marine Geology*, *289*(1–4), 135–149. doi:10.1016/j.margeo.2011.09.014

Earle, S. (2015). Physical Geology. The Geology of the Oceanic Crust. Retrieved 29 September 2020, from https://ecampusontario.pressbooks.pub/geology/chapter/18-2-the-geology-of-the-oceanic-crust/

Elliot, M., Labeyrie, L., & Duplessy, J. C. (2002). Changes in North Atlantic deep-water formation associated with the Dansgaard - Oeschger temperature oscillations (60-10 ka). *Quaternary Science Reviews*, *21*(10), 1153–1165. doi:10.1016/S0277-3791(01)00137-8

Encyclopaedia Britannica. (2015). Crustal Generation and Destruction. Retrieved 28 October 2020, from https://www.britannica.com/science/plate-tectonics/Earths-layers

Engdahl, E. R., & Villasenor, A. (2002). *Global Seismicity: 1900-1999*. Academic Press.

ESA. (2019). Sediment plume at sea. Retrieved 30 October 2020, from https://www.esa.int/ESA_Multimedia/Images/2019/02/Sediment_plume_at_sea

Escorza, M. (2007). Iconografía histórica de los terremotos hasta el de Lisboa en 1755. *Boletín de La Comisión de Historia de La Geología de España*, *29*, 225–247.

Flewellen, C., Millard, N., & Rouse, I. (1993). TOBI, a vehicle for deep ocean survey. *Electronics and Communication Engineering Journal*, *5*(2), 85–93. doi:10.1049/ecej:19930015

Ford, J., Urgeles, R., Camerlenghi, A., & Gràcia, E. (2021). Seismic diffraction imaging to characterise mass-transport complexes: examples from the Gulf of Cadiz, south west Iberian Margin. *Journal of Geophysical Research: Solid Earth*, 1–25.

doi:10.1029/2020jb021474

Fowler, C. M. R. (2005). *The Solid Earth: An Introduction to Global Geophysics*. Cambridge University Press.

Fukao, Y. (1973). Thrust faulting at a lithospheric plate boundary, the Portugal earthquake of 1969. *Earth and Planetary Science Letters*, *18*, 205–216.

García-Lafuente, J., Delgado, J., Criado-Aldeanueva, F., Bruno, M., del Rio, J., & Miguel Vargas, J. (2006). Water mass circulation on the continental shelf of the Gulf of Cadiz. In J. Ruiz & J. García-Lafuente (Eds.), *The Gulf of Cadiz Oceanography: A Multidisciplinary View. Deep Sea Research Part II: Topical Studies in Oceanography* (pp. 1182–1197).

García, M., Hernández-Molina, F. J., Llave, E., Stow, D. A. V, León, R., Fernández-Puga, M. C., & Somoza, L. (2009). Contourite erosive features caused by the Mediterranean Outflow Water in the Gulf of Cadiz: Quaternary tectonic and oceanographic implications. *Marine Geology*, *257*(1), 24–40. doi:https://doi.org/10.1016/j.margeo.2008.10.009

Gaudin, M., Berné, S., Jouanneau, J. M., Palanques, A., Puig, P., Mulder, T., & Imbert, P. (2006). Massive sand beds attributed to deposition by dense water cascades in the Bourcart canyon head, Gulf of Lions (northwestern Mediterranean Sea). *Marine Geology*, *234*(1–4), 111–128. doi:10.1016/j.margeo.2006.09.020

Geissler, W. H., Matias, L., Stich, D., Carrilho, F., Jokat, W., Monna, S., & Zitellini, N. (2010). Focal mechanisms for sub-crustal earthquakes in the Gulf of Cadiz from a dense OBS deployment. *Geophysical Research Letters*, *37*(18), 7–12. doi:10.1029/2010GL044289

Geist, E. L. (1998). Local Tsunamis and Earthquake Source Parameters. In R. Dmowska & B. B. T.-A. in G. Saltzman (Eds.), *Tsunamigenic Earthquakes and Their Consequences. Elsevier, pp. 117–209.* Elsevier. doi:https://doi.org/10.1016/S0065-2687(08)60276-9

Geoware. (2015). Geoware Tsunami Product List. Retrieved 12 November 2020, from http://www.geoware-online.com/tsunami.html

Gibbons, S. J., Lorito, S., Macías, J., Løvholt, F., Selva, J., Volpe, M., … Vöge, M. (2020). Probabilistic Tsunami Hazard Analysis: High Performance Computing for Massive Scale Inundation Simulations. *Frontiers in Earth Science*. Retrieved from https://www.frontiersin.org/article/10.3389/feart.2020.591549

Girardeau, J., Cornen, G., Agrinier, P., Beslier, M. O., Dubuisson, G., Le Gall, B., … Whitechurch, H. (1998). Premiers résultats des plong6es du Nautile sur le banc de Gorringe (Ouest Portugal). *CR Acad Sci Paris*, *326*, 247–254.

Gjevik, B., Pedersen, G., Dybesland, E., Harbitz, C. B., Miranda, P. M. A., Baptista, M. A., & Guesmia, M. (1997). Modeling tsunamis from earthquake sources near Gorringe Bank southwest of Portugal. *Journal of Geophysical Research*, *102*(13), 931–949. doi:10.1029/97JC02179

Gómez de la Peña, L. (2017). *The origin and tectono-sedimentary structure of the Alboran Basin*. Universitat de Barcelona. PhD Thesis. Retrieved from http://diposit.ub.edu/dspace/handle/2445/116802

Gómez de la Peña, L., Grevemeyer, I., Kopp, H., Díaz, J., Gallart, J., Booth-Rea, G., & Ranero, C.R. (2020). The Lithospheric Structure of the Gibraltar Arc System From Wide-Angle Seismic Data. *Journal of Geophysical Research: Solid Earth*, *125*(9), e2020JB019854. doi:https://doi.org/10.1029/2020JB019854

González, F. I., Bernard, E. N., Meinig, C., Eble, M. C., Mofjeld, H. O., & Stalin, S. (2005). The NTHMP Tsunameter Network. *Natural Hazards*, *35*, 25–39.

Gràcia, E., Dañobeitia, J., Vergés, J., & Team, P. (2003a). Mapping active faults offshore Portugal (36°N–38°N): Implications for seismic hazard assessment along the southwest Iberian margin. *Geology*, *31*(1), 83–86. doi:10.1130/0091-7613(2003)031<0083:MAFOPN>2.0.CO;2

Gràcia, E., & INSIGHT Cruise Party. (2018). *ImagiNg large SeismogenIc and tsunamiGenic structures of the Gulf of Cadiz with ultra-High resolution Technologies (INSIGHT-Leg1)*. Barcelona.

Gràcia, E., Dañobeitia, J., Vergés, J., Bartolomé, R., & Córdoba, D. (2003b). Crustal architecture and tectonic evolution of the Gulf of Cadiz (SW Iberian margin) at the convergence of the Eurasian and African plates. *Tectonics*, *22*(4), n/a-n/a.

doi:10.1029/2001tc901045

Gràcia, E., Grevemeyer, I., Bartolomé, R., Perea, H., Martínez-Loriente, S., Gómez de la Peña, L., & Ranero, C. R. (2019). Earthquake crisis unveils the growth of an incipient continental fault system. *Nature Communications*, *10*(1), 1–12. doi:10.1038/s41467-019-11064-5

Gràcia, E., Pallàs, R., Soto, J. I., Comas, M., Moreno, X., Masana, E., … Roque, C. (2006). Active faulting offshore SE Spain (Alboran Sea): Implications for earthquake hazard assessment in the Southern Iberian Margin. *Earth and Planetary Science Letters*, *241*(3–4), 734–749. doi:10.1016/j.epsl.2005.11.009

Gràcia, E., Vizcaino, A., Escutia, C., Asioli, A., Rodés, Á., Pallàs, R., … Goldfinger, C. (2010). Holocene earthquake record offshore Portugal (SW Iberia): testing turbidite paleoseismology in a slow-convergence margin. *Quaternary Science Reviews*, *29*(9–10), 1156–1172. doi:10.1016/j.quascirev.2010.01.010

Grevemeyer, I., Lange, D., Villinger, H., Custódio, S., & Matias, L. (2017). Seismotectonics of the Horseshoe Abyssal Plain and Gorringe Bank, eastern Atlantic Ocean: Constraints from ocean bottom seismometer data. *Journal of Geophysical Research: Solid Earth*, *122*(1), 63–78. doi:10.1002/2016JB013586

Gutscher, M.A., Malod, J., Rehault, J.P., Contrucci, I., Klingelhoefer, F., Mendes-Victor, L., & Spakman, W. (2002). Evidence for active subduction beneath Gibraltar. *Geology*, *30*(12), 1071–1074. doi:10.1130/0091-7613(2002)030<1071:EFASBG>2.0.CO;2

Haase, K. M., Koschinsky, A., Petersen, S., Devey, C. W., German, C., Lackschewitz, K. S., & Paulick, H. (2009). Diking, young volcanism and diffuse hydrothermal activity on the southern Mid-Atlantic Ridge: The Lilliput field at 9°33′S. *Marine Geology*, *266*(1), 52–64. doi:https://doi.org/10.1016/j.margeo.2009.07.012

Habgood, E. L., Kenyon, N. H., Masson, D. G., Akhmetzhanov, A., Weaver, P. P. E., Gardner, J., & Mulder, T. (2003). Deep-water sediment wave fields, bottom current sand channels and gravity flow channel-lobe systems: Gulf of Cadiz, NE Atlantic. *Sedimentology*, *50*(3), 483–510. doi:https://doi.org/10.1046/j.1365-3091.2003.00561.x

Hamblin, W. K., & Christiansen, E. H. (2003). *Earth's Dynamic Systems*. Pearson College Div.

Harris, P. T., & Whiteway, T. (2011). Global distribution of large submarine canyons: Geomorphic differences between active and passive continental margins. *Marine Geology*, *285*(1–4), 69–86. doi:10.1016/j.margeo.2011.05.008

Hayes, E., Pimm, A. C., Beckmann, P., Benson, W., Berger, W., Roth, P., & Supko, P. (1972). *Initial Reports of the Deep Sea Drilling Project*. Washington D.C.: Government Printing Office.

Hayward, N., Watts, A. B., Westbrook, G. K., & Collier, J. (1999). A seismic reflection and GLORIA study of compressional deformation in the Gorringe Bank, eastern North Atlantic. *Geological Journal International*, *138*, 831–850.

Hensen, C., Scholz, F., Nuzzo, M., Valadares, V., Gràcia, E., Terrinha, P., … Lackschewitz, K. (2015). Strike-slip faults mediate the rise of crustal-derived fluids and mud volcanism in the deep sea. *Geology*, *43*(4), 339–342. doi:10.1130/G36359.1

Hernández-Molina, F. J., Llave, E., Preu, B., Ercilla, G., Fontan, A., Bruno, M., … Arnaiz, A. (2014). Contourite processes associated with the Mediterranean Outfl ow Water after its exit from the Strait of Gibraltar: Global and conceptual implications. *Geology*, *42*(3), 227–230. doi:10.1130/G35083.1

Hernández-Molina, F. J., Sierro, F. J., Llave, E., Roque, C., Stow, D. A. V., Williams, T., … Brackenridge, R. E. (2015). Evolution of the gulf of Cadiz margin and southwest Portugal contourite depositional system: Tectonic, sedimentary and paleoceanographic implications from IODP expedition 339. *Marine Geology*, *377*, 7–39. doi:10.1016/j.margeo.2015.09.013

Hernández-Molina, J., Llave, E., Somoza, L., Fernández-Puga, M. C., Maestro, A., León, R., … Gardner, J. (2003). Looking for clues to paleoceanographic imprints: A diagnosis of the Gulf of Cadiz contourite depositional systems. *Geology*, *31*(1), 19–22. doi:10.1130/0091-7613(2003)031<0019:LFCTPI>2.0.CO;2

Herrero, A., & Murphy, S. (2018). Self-similar slip distributions on irregular shaped faults. *Geophysical Journal International*, *213*(3), 2060–2070.

doi:10.1093/gji/ggy104

Higgins Art Gallery and Museum (2020). Exibitions. Retrieved 30 October 2020, from https://www.thehigginsbedford.org.uk/Search_Page.aspx?search_keywords=tsunami%20Lisbon

Hildenbrand, A., Weis, D., Madureira, P., & Marques, F. O. (2014). Recent plate re-organization at the Azores Triple Junction: Evidence from combined geochemical and geochronological data on Faial, S. Jorge and Terceira volcanic islands. *Lithos*, *210*(2014), 27–39. doi:10.1016/j.lithos.2014.09.009

Hirono, T., Tsuda, K., Tanikawa, W., Ampuero, J. P., Shibazaki, B., Kinoshita, M., & Mori, J. J. (2016). Near-trench slip potential of megaquakes evaluated from fault properties and conditions. *Scientific Reports*, *6*, 1–13. doi:10.1038/srep28184

Humphris, S. E. (2009). Vehicles for Deep Sea Exploration. *Encyclopedia of Ocean Sciences* (pp. 255–266). Oxford: Academic Press. doi:https://doi.org/10.1016/B978-012374473-9.00734-7

ICGC. (2008). Basic knowledge. Concepts. Retrieved 30 October 2020, from https://www.icgc.cat/en/Public-Administration-and-Enterprises/Services/Geological-risks/General-information-on-geological-risks/Basic-knowledge.-Concepts

Iglesias, O., Lastras, G., Souto, C., Costa, S., & Canals, M. (2014). Effects of coastal submarine canyons on tsunami propagation and impact. *Marine Geology*, *350*, 39–51. doi:10.1016/j.margeo.2014.01.013

IGME. (2015). Quaternary Active Faults Database of Iberia. Retrieved 29 September 2020, from http://info.igme.es/qafi/

INE. (2019). España en cifras 2019. Retrieved 12 December 2020, from https://www.ine.es/prodyser/espa_cifras/2019/

Instituto Geográfico Nacional. (2020). Catálogo de terremotos. Retrieved 13 November 2020, from https://www.ign.es/web/sis-area-sismicidad

International Tsunami Information Center. (2020). General Info. Retrieved 30 October 2020, from http://itic.ioc-unesco.org/index.php

Iribarren, L., Vergés, J., Camurri, F., Fullea, J., & Fernàndez, M. (2007). The structure of the Atlantic-Mediterranean transition zone from the Alboran Sea to the Horseshoe Abyssal Plain (Iberia-Africa plate boundary). *Marine Geology*, *243*(1–4), 97–119. doi:10.1016/j.margeo.2007.05.011

Japan Agency for Marine-Earth Science and Technology. (2020). Investigating the Seafloor. Retrieved 12 November 2020, from https://www.jamstec.go.jp/e/about/equipment/observe/seabed.html

Jiménez-Munt, I., Fernàndez, M., Vergés, J., Afonso, J. C., Garcia-Castellanos, D., & Fullea, J. (2010). Lithospheric structure of the Gorringe Bank: Insights into its origin and tectonic evolution. *Tectonics*, *29*(5), 1–16. doi:10.1029/2009TC002458

Kanamori, H. (1977). The energy release in great earthquakes. *Journal of Geophysical Research (1896-1977)*, *82*(20), 2981–2987. doi:https://doi.org/10.1029/JB082i020p02981

Kearey, P. (1994). The Encyclopedia of the Solid Earth Sciences. On *Wiley Online Books*. Wiley. doi:https://doi.org/10.1002/9781444313895.fmatter

Keating, B. H., & McGuire, W. J. (2000). Island Edifice Failures and Associated Tsunami Hazards. *Pure and Applied Geophysics*, *157*(6), 899–955. doi:10.1007/s000240050011

Keller, E. A., & Pinter, N. (2002). *Active Tectonics, Earthquakes, Uplift and Landscape*. Prentice Hall.

Keller, E., & DeVecchio, D. (2015). *Natural Hazards: Earth's Processes as Hazards, Disasters, and Catastrophes (4th Edition)*. Pearson Australia. Retrieved from https://books.google.es/books?id=gf1HDgAAQBAJ

Kenyon, N. H. (1982). *The ocean floor (Bruce Heezen Commemorative Volume)*. (A. Scrutton and M. Talwani, Ed.), *Geological Journal* (Vol. 19). John Wiley & Sons, Ltd. doi:https://doi.org/10.1002/gj.3350190113

Khripounoff, A., Vangriesheim, A., Crassous, P., & Etoubleau, J. (2009). High frequency of sediment gravity flow events in the Var submarine canyon (Mediterranean Sea). *Marine Geology*, *263*(1–4), 1–6.

doi:10.1016/j.margeo.2009.03.014

Koshimura, S., & Shuto, N. (2015). Response to the 2011 Great East Japan Earthquake and Tsunami disaster. *Philosophical Transactions of the Royal Society A: Mathematical, Physical and Engineering Sciences*, *373*(2053). doi:10.1098/rsta.2014.0373

La macchina del tempo. (2014). REMUS 6000. Retrieved 12 November 2020, from https://gaetaniumberto.files.wordpress.com/2014/11/1416932528.gif

Labails, C., Olivet, J. L., Aslanian, D., & Roest, W. R. (2010). An alternative early open-ing scenario for the Central Atlantic Ocean. *Earth and Planetary Science Letters*, *297*(3–4), 355–368.

Lastras, G., Arzola, R. G., Masson, D. G., Wynn, R. B., Huvenne, V. A. I., Hühnerbach, V., & Canals, M. (2009). Geomorphology and sedimentary features in the Central Portuguese submarine canyons, Western Iberian margin. *Geomorphology*, *103*(3), 310–329. doi:10.1016/j.geomorph.2008.06.013

Latter, J. H. (1981). Tsunamis of volcanic origin: Summary of causes, with particular reference to Krakatoa, 1883. *Bulletin Volcanologique*, *44*(3), 467–490. doi:10.1007/BF02600578

Lay, T., Kanamori, H., Ammon, C. J., Nettles, M., Ward, S. N., Aster, R. C., … Sipkin, S. (2005). The Great Sumatra-Andaman Earthquake of 26 December 2004. *Science*, *308*(5725), 1127 LP – 1133. doi:10.1126/science.1112250

Le Bas, T. P., Mason, D. C., & Millard, N. C. (1995). TOBI image processing-the state of the art. *IEEE Journal of Oceanic Engineering*, *20*(1), 85–93. doi:10.1109/48.380242

Le Pichon, X. (1968). Sea-floor spreading and continental drift. *Journal of Geophysical Research (1896-1977)*, *73*(12), 3661–3697. doi:https://doi.org/10.1029/JB073i012p03661

Le Roy, P., & Piqué, A. (2001). Triassic–Liassic western Moroccan synrift basins in relation to the central Atlantic opening. *Marine Geology*, *172*, 359–381. doi:10.1016/S0025-3227(00)00130-4

Lebreiro, S. M., McCave, I. N., & Weaver, P.. E. (1997). Late quaternary turbidite emplacement on the Horseshoe abyssal plain (Iberian margin). *Journal of Sedimentary Research*, *67*(5), 856–870. doi:10.1306/d4268658-2b26-11d7-8648000102c1865d

Leonard, M. (2014). Self-consistent earthquake fault-scaling relations: Update and extension to stable continental strike-slip faults. *Bulletin of the Seismological Society of America*, *104*(6), 2953–2965. doi:10.1785/0120140087

Levin, B. W., & Nosov, M. (2015). *Physics of Tsunamis*. Springer International Publishing. Retrieved from https://books.google.es/books?id=sykdswEACAAJ

Lewis, K. B., & Barnes, P. M. (1999). Kaikoura Canyon, New Zealand: Active conduit from near-shore sediment zones to trench-axis channel. *Marine Geology*, *162*(1), 39–69. doi:10.1016/S0025-3227(99)00075-4

Lima, V. V., Miranda, J. M., Baptista, M. A., Catalão, J., Gonzalez, M., Otero, L., & Carreño, E. (2010). Impact of a 1755-like tsunami in Huelva, Spain. *Natural Hazards and Earth System Science*, *10*(1), 139–148. doi:10.5194/nhess-10-139-2010

LinkQuest Inc. (2020). Applications. Retrieved 11 November 2020, from https://www.link-quest.com/html/lbl_applications.htm

Llave, E., Hernández-Molina, F. J., Somoza, L., Stow, D. A. V., & Díaz del Río, V. (2007). Quaternary evolution of the contourite depositional system in the gulf of Cadiz. *Geological Society Special Publication*, *276*, 49–79. doi:10.1144/GSL.SP.2007.276.01.03

Llave, E., Schönfeld, J., Hernández-Molina, F. J., Mulder, T., Somoza, L., Díaz Del Río, V., & Sánchez-Almazo, I. (2006). High-resolution stratigraphy of the Mediterranean outflow contourite system in the Gulf of Cadiz during the late Pleistocene: The impact of Heinrich events. *Marine Geology*, *227*(3–4), 241–262. doi:10.1016/j.margeo.2005.11.015

Lobo, F. J., Le Roy, P., Mendes, I., & Sahabi, M. (2014). The gulf of Cádiz continental shelves. *Geological Society Memoir*, *41*(1), 109–130. doi:10.1144/M41.9

Lonergan, L., & White, N. (1997). Origin of the Betic-Rift mountain belt. *Tectonics*, *16*(3), 504–522. doi:10.1029/96TC03937

Lopes, F. C., Cunha, P. P., & Le Gall, B. (2006). Cenozoic seismic stratigraphy and tectonic evolution of the Algarve margin (offshore Portugal, southwestern Iberian Peninsula). *Marine Geology*, *231*(1–4), 1–36. doi:10.1016/j.margeo.2006.05.007

Lorito, S., Selva, J., Basili, R., Romano, F., Tiberti, M. M., & Piatanesi, A. (2015). Probabilistic hazard for seismically induced tsunamis: accuracy and feasibility of inundation maps . *Geophysical Journal International*, *200*(1), 574–588. doi:10.1093/gji/ggu408

Lowrie, W. (2007). *Fundamentals of Geophysics*. Cambridge University Press. Retrieved from https://books.google.es/books?id=h2-NjUg4RtEC

Lozano, L., Cantavella, J. J., & Barco, J. (2019). A new 3-D P-wave velocity model for the Gulf of Cadiz and adjacent areas derived from controlled-source seismic data: application to non-linear probabilistic relocation of moderate earthquakes. *Geophysical Journal International*, *ggz562*, 1–57. doi:10.1093/gji/ggz562

Lurton, X. (2010). *An Introduction to Underwater Acoustics. Principles and Applications* (2nd ed.). Springer-Verlag Berlin Heidelberg.

Maad, N., Le Roy, P., Sahabi, M., Gutscher, M. A. Babonneau, N., Rabineau, M., & Van Vliet Lanoe. (2010). The seismic stratigraphy of the NW Moroccan Atlantic continental shelf and Quaternary deformations at the offshore termination of the Southern Rif front. *Comptes Rendus Geoscience*, *342*, 731–740.

Machette, M. N. (2000). Active, capable, and potentially active faults - a paleoseismic perspective. *Journal of Geodynamics*, *29*(3–5), 387–392. doi:10.1016/S0264-3707(99)00060-5

Maldonado, A., Rodero, J., Pallarés, L., Pérez, L., & Somoza, L. (2003). Mapa Geológico de la Plataforma Continental Española y Zonas Adyacentes. Escala 1:200.000. Hojas 886-86S-87S (Cádiz). Madrid: IGME. Retrieved from http://info.igme.es/cartografiadigital/datos/Fomar200/mapas/jpgs/Mapa_textural_FM200_86.jpg

Maldonado, A., Somoza, L., & Pallarés, L. (1999). The Betic orogen and the Iberian-African boundary in the Gulf of Cadiz: Geological evolution (central North Atlantic). *Marine Geology*, *155*(1–2), 9–43. doi:10.1016/S0025-3227(98)00139-X

Malod, J. A., & Mauffret, A. (1990). Iberian plate motions during the Mesozoic. *Tectonophysics*, *184*(3–4), 261–278. doi:10.1016/0040-1951(90)90443-C

Marchès, E., Mulder, T., Cremer, M., Bonnel, C., Hanquiez, V., Gonthier, E., & Lecroart, P. (2007). Contourite drift construction influenced by capture of Mediterranean Outflow Water deep-sea current by the Portimão submarine canyon (Gulf of Cadiz, South Portugal). *Marine Geology*, *242*(4), 247–260. doi:10.1016/j.margeo.2007.03.013

Marques, F. O., Catalão, J. C., Demets, C., Costa, A. C. G., & Hildenbrand, A. (2013). GPS and tectonic evidence for a diffuse plate boundary at the Azores Triple Junction. *Earth and Planetary Science Letters*, *381*, 177–187. doi:10.1016/j.epsl.2013.08.051

Martin-Rojas, I., Somma, R., Delgado, F., Estévez, A., Iannace, A., Perrone, V., & Zamparelli, V. (2009). Triassic continental rifting of Pangaea: Direct evidence from the Alpujarride carbonates, Betic Cordillera, SE Spain. *Geological Society London*, *166*(3), 447–458. doi:10.1144/0016-76492008-091

Martínez-Loriente, S. (2013). *Geophysical and geological characterization of the active structures and of the nature of the basement in the Eurasia-Africa plate boundary ( SW Iberian Margin ): Implications for regional geodynamics and seismic hazard assessment*. Universitat de Barcelona. PhD Thesis.

Martínez-Loriente, S., Gràcia, E., Bartolome, R., Perea, H., Klaeschen, D., Dañobeitia, J. J., … Masson, D. G. (2018). Morphostructure, tectono-sedimentary evolution and seismic potential of the Horseshoe Fault, SW Iberian Margin. *Basin Research*, *30*, 382–400. doi:10.1111/bre.12225

Martínez-Loriente, S., Gràcia, E., Bartolome, R., Sallarès, V., Connors, C., Perea, H., … Zitellini, N. (2013). Active deformation in old oceanic lithosphere and significance for earthquake hazard: Seismic imaging of the Coral Patch Ridge area and neighboring abyssal plains (SW Iberian Margin). *Geochemistry, Geophysics,*

*Geosystems*, *14*(7), 2206–2231. doi:10.1002/ggge.20173

Martínez-Loriente, S., Sallarès, V., Gràcia, E., Bartolome, R., Dañobeitia, J. J., & Zitellini, N. (2014). Seismic and gravity constraints on the nature of the basement in the Africa-Eurasia plate boundary: New insights for the geodynamic evolution of the SW Iberian margin. *Journal of Geophysical Research: Solid Earth*, *119*(1), 127–149. doi:10.1002/2013JB010476

Martínez Solares, J. M., & López Arroyo, A. (2004). The great historical 1755 earthquake . Effects and damage in Spain. *Journal of Seismology*, *8*(1991), 275–294.

Masana, E., Martínez-Díaz, J. J., Hernández-Enrile, J. L., & Santanach, P. (2004). The Alhama de Murcia fault (SE Spain), a seismogenic fault in a diffuse plate boundary: Seismotectonic implications for the Ibero-Magrebian region. *Journal of Geophysical Research: Solid Earth*, *109*(B1), 1–17. doi:10.1029/2002jb002359

Masson, D. G., Wynn, R. B., & Bett, B. (2004). Sedimentary environment of the Faroe-Shetland and Faroe Bank Channels, north-east Atlantic, and the use of bedforms as indicators of bottom current velocity in the deep ocean. *Sedimentology*, *51*, 1207–1241. doi:10.1111/j.1365-3091.2004.00668.x

Mastbergen, D. R., & Van Den Berg, J. H. (2003). Breaching in fine sands and the generation of sustained turbidity currents in submarine canyons. *Sedimentology*, *50*(4), 625–637. doi:10.1046/j.1365-3091.2003.00554.x

Matias, L. M., Cunha, T., Annunziato, A., Baptista, M. A., & Carrilho, F. (2013). Tsunamigenic earthquakes in the Gulf of Cadiz: Fault model and recurrence. *Natural Hazards and Earth System Science*, *13*(1), 1–13. doi:10.5194/nhess-13-1-2013

Mauffrey, M. A., Urgeles, R., Berné, S., & Canning, J. (2017). Development of submarine canyons after the Mid-Pleistocene Transition on the Ebro margin, NW Mediterranean: The role of fluvial connections. *Quaternary Science Reviews*, *158*, 77–93. doi:10.1016/j.quascirev.2017.01.006

Meade, B. J. (2007). Algorithms for the calculation of exact displacements , strains , and stresses for triangular dislocation elements in a uniform elastic half space, *33*,

1064–1075. doi:10.1016/j.cageo.2006.12.003

Medialdea, T., Somoza, L., Pinheiro, L. M., Fernández-Puga, M. C., Vázquez, J. T., León, R., … Vegas, R. (2009). Tectonics and mud volcano development in the Gulf of Cádiz. *Marine Geology*, *261*(1–4), 48–63. doi:10.1016/j.margeo.2008.10.007

Medialdea, T., Vegas, R., Somoza, L., Vázquez, J. T., Maldonado, A., Díaz-Del-Río, V., … Fernández-Puga, M. C. (2004). Structure and evolution of the 'Olistostrome' complex of the Gibraltar Arc in the Gulf of Cádiz (eastern Central Atlantic): Evidence from two long seismic cross-sections. *Marine Geology*, *209*(1–4), 173–198. doi:10.1016/j.margeo.2004.05.029

Mencaroni, D., Urgeles, R., Camerlenghi, A., Llopart, J., Ford, J., Serra, C.S., … Zitellini, N. (2021). A mixed turbidite – contourite system related to a major submarine canyon: The Marquês de Pombal Drift (south-west Iberian margin). *Sedimentology*, 1–28. doi:https://doi.org/10.1111/sed.12844

Micallef, A., Ribó, M., Canals, M., Puig, P., Lastras, G., & Tubau, X. (2014). Space-for-time substitution and the evolution of a submarine canyon-channel system in a passive progradational margin. *Geomorphology*, *221*, 34–50. doi:10.1016/j.geomorph.2014.06.008

Mitchum Jr., R. M., Vail, P. R., & Sangree, J. B. (1977). Seismic Stratigraphy and Global Changes of Sea Level, Part 6: Stratigraphic Interpretation of Seismic Reflection Patterns in Depositional Sequences1. (C. E. Payton, Ed.), *Seismic Stratigraphy - Applications to Hydrocarbon Exploration*. American Association of Petroleum Geologists. doi:10.1306/M26490C8

Mjelde, R., Goncharov, A., & Müller, R. D. (2013). The Moho: Boundary above upper mantle peridotites or lower crustal eclogites? A global review and new interpretations for passive margins. *Tectonophysics*, *609*, 636–650. doi:https://doi.org/10.1016/j.tecto.2012.03.001

Morgan, J. K., Silver, E., Camerlenghi, A., Dugan, B., Kirby, S., Shipp, C., & Suyehiro, K. (2009). Addressing geohazards through ocean drilling. *Scientific Drilling*, (7), 15–30. doi:10.2204/iodp.sd.7.01.2009

Mori, N., Takahashi, T., Yasuda, T., & Yanagisawa, H. (2011). Survey of 2011 Tohoku earthquake tsunami inundation and run-up. *Geophysical Research Letters*, *38*(18). doi:10.1029/2011GL049210

Mulder, T., Lecroart, P., Hanquiez, V., Marches, E., Gonthier, E., Guedes, J. C., … Bujan, S. (2006). The western part of the Gulf of Cadiz: Contour currents and turbidity currents interactions. *Geo-Marine Letters*, *26*(1), 31–41. doi:10.1007/s00367-005-0013-z

Mulder, T, Voisset, M., Lecroart, P., Le Drezen, E., Gonthier, E., Hanquiez, V., … Morel, J. (2003). The Gulf of Cadiz: an unstable giant contouritic levee. *Geo-Marine Letters*, *23*(1), 7–18. doi:10.1007/s00367-003-0119-0

Mulder, T., & Cochonat, P. (1996). Classification of offshore mass movements. *Journal of Sedimentary Research*, *66*(1), 43–57.

National Ocean Service. (2020). What is a hydrophone? Retrieved 12 November 2020, from https://oceanservice.noaa.gov/facts/hydrophone.html

Neres, M., Carafa, M. M. C., Fernandes, R. M. S., Matias, L., Duarte, J. C., Barba, S., & Terrinha, P. (2016). Lithospheric deformation in the Africa-Iberia plate boundary: Improved neotectonic modeling testing a basal-driven Alboran plate. *Journal of Geophysical Research: Solid Earth*, *121*(9), 6566–6596. doi:10.1002/2016JB013012

Nocquet, J. (2012). Tectonophysics Present-day kinematics of the Mediterranean : A comprehensive overview of GPS results. *Tectonophysics*, *579*, 220–242. doi:10.1016/j.tecto.2012.03.037

Nocquet, J. M., & Calais, E. (2004). Geodetic measurements of crustal deformation in the Western Mediterranean and Europe. *Pure and Applied Geophysics*, *161*(3), 661–681. doi:10.1007/s00024-003-2468-z

Normark, W. R., & Carlson, P. R. (2003). Giant submarine canyons: Is size any clue to their importance in the rock record? *Special Paper of the Geological Society of America*, *370*, 175–190. doi:10.1130/0-8137-2370-1.175

Ochoa, J., & Bray, N. A. (1991). Water mass exchange in the Gulf of Cadiz. *Deep-Sea*

*Research*, *38*(1), 465–503.

Okada, Y. (1985). Surface deformation due to shear and tensile faults in a half-space. *Bulletin of the Seismological Society of America*, *75*(4), 1135–1154.

Okal, E. A., Fritz, H. M., Hamzeh, M. A., & Ghasemzadeh, J. (2015). Field Survey of the 1945 Makran and 2004 Indian Ocean Tsunamis in Baluchistan , Iran. *Pure and Applied Geophysics*, *172*, 3343–3356. doi:10.1007/s00024-015-1157-z

Olivet, J. L. (1996). Kinematics of the Iberian Plate. *Bulletin Des Centres De RecherchesExploration-Production Elf Aquitaine*, *20*(1), 131–195.

Olson, C., Becker, J., & Sandwell, D. (2016). SRTM15_PLUS: Data fusion of Shuttle Radar Topography Mission (SRTM) land topographywith measured and estimated seafloor topography (NCEI Accession 0150537). Retrieved 12 November 2020, from https://data.amerigeoss.org/it/dataset/srtm15-plus-data-fusion-of-shuttle-radar-topography-mission-srtm-land-topography-with-measured-

Omira, R., Baptista, M. A., Leone, F., Matias, L., Mellas, S., Zourarah, B., … Cherel, J. P. (2013). Performance of coastal sea-defense infrastructure at El Jadida (Morocco) against tsunami threat: Lessons learned from the Japanese 11 March 2011 tsunami. *Natural Hazards and Earth System Sciences*, *13*(7), 1779–1794. doi:10.5194/nhess-13-1779-2013

Omira, R., Baptista, M. A., Mellas, S., Leone, F., de Richemond, N. M., Zourarah, B., & Cherel, J.P. (2012). The November, 1st, 1755 Tsunami in Morocco: Can Numerical Modeling Clarify the Uncertainties of Historical Reports? *Tsunami - Analysis of a Hazard - From Physical Interpretation to Human Impact*, 1–16. doi:10.5772/51864

Omira, R., Baptista, M. A., & Miranda, J. M. (2011). Evaluating Tsunami impact on the Gulf of Cadiz Coast (Northeast Atlantic). *Pure and Applied Geophysics*, *168*(6–7), 1033–1043. doi:10.1007/s00024-010-0217-7

Omira, Rachid, Neres, M., & Batista, L. (2019). The Gloria Transform Fault—NE Atlantic: Seismogenic and Tsunamigenic Potential. In J. C. B. T.-T. P. B. and F. Z. Duarte (Ed.), *Transform Plate Boundaries and Fracture Zones* (pp. 157–167). Elsevier. doi:https://doi.org/10.1016/B978-0-12-812064-4.00008-6

Palanques, A., Durrieu de Madron, X., Puig, P., Fabres, J., Guillén, J., Calafat, A., … Bonnin, J. (2006). Suspended sediment fluxes and transport processes in the Gulf of Lions submarine canyons. The role of storms and dense water cascading. *Marine Geology*, *234*(1–4), 43–61. doi:10.1016/j.margeo.2006.09.002

Parkes, G. E., & Hatton, L. (1986). *The Marine Seismic Source*. Springer Netherlands. doi:10.1007/978-94-017-3385-4

Parsons, J. D., Whipple, K. X., & Simoni, A. (2001). Experimental Study of the Grain - Flow , Fluid - Mud Transition in Debris Flows Experimental Study of the Grain-Flow , Fluid-Mud Transition in Debris Flows. *The Journal of Geology*, *109*, 427–447. doi:10.1086/320798

Peakall, J., Best, J., Baas, J. H., Hodgson, D. M., Clare, M. A., Talling, P. J., … Lee, D. R. (2020). An integrated process-based model of flutes and tool marks in deep-water environments: Implications for palaeohydraulics, the Bouma sequence and hybrid event beds. *Sedimentology*, *67*(4), 1601–1666. doi:10.1111/sed.12727

Pereira, R., & Alves, T. M. (2011). Post-rift compression on the Southwest Iberian margin ( Eastern North Atlantic ): A case of prolonged inversion in the Ocean-Continent Transition Post-rift compression on the SW Iberian margin ( eastern North Atlantic ): a case for prolonged inversion in. *Journal of the Geological Society*, *168*(October), 1249–1263. doi:10.1144/0016-76492010-151

Pereira, R., & Alves, T. M. (2013). Crustal deformation and submarine canyon incision in a Meso-Cenozoic first-order transfer zone (SW Iberia, North Atlantic Ocean). *Tectonophysics*, *601*, 148–162. doi:10.1016/j.tecto.2013.05.007

Perillo, G. M. E. (2001). Hacia una nomenclatura y clasificación deformas de fondo transversales generadas por flujos de agua. *Rev. Asoc. Arg. Sedimentol.*, *8*, 37–56.

Pinheiro, L. M., Ivanov, M. K., Sautkin, A., Akhmanov, G., Magalhães, V. H., Volkonskaya, A., … Cunha, M. R. (2003). Mud volcanism in the Gulf of Cadiz: results from the TTR-10 cruise. *Marine Geology*, *195*(1), 131–151. doi:https://doi.org/10.1016/S0025-3227(02)00685-0

Piper, D. J. W., & Normark, W. R. (2009). Processes That Initiate Turbidity Currents and Their Influence on Turbidites: A Marine Geology Perspective Title. *Journal of*

*Sedimentary Research*, *79*, 347–362.

Piqué, A., Tricart, P., Guiraud, R., Laville, E., Bouaziz, S., Amrhar, M., & Ait Ouali, R. (2002). The Mesozoic–Cenozoic Atlas belt (North Africa): an overview. *Geodinamica Acta*, *15*(3), 185–208. doi:https://doi.org/10.1016/S0985-3111(02)01088-4

Pratson, L. F., Nittrouer, C. A., Wiberg, P. L., Steckler, M. S., Swenson, J. B., Cacchione, D. A., … Fedele, J. J. (2007). Seascape Evolution on Clastic Continental Shelves and Slopes. On *Wiley Online Books*. (A. N. Charles, J. A. Austin, M. E. Field, J. H. Kravitz, J. P. M. Syvitski, & P. L. Wiberg, Eds.), *Continental Margin Sedimentation*. Wiley. doi:https://doi.org/10.1002/9781444304398.ch7

Press, F., Siever, R., Siever, U. E. R., & Company, W. H. F. and. (1986). Earth: Fourth Edition. On *A series of books in Geology*. W. H. Freeman. Retrieved from https://books.google.es/books?id=CeJlaU-XiE4C

Puig, P., Palanques, A., & Martín, J. (2014). Contemporary Sediment-Transport Processes in Submarine Canyons. *Annual Review of Marine Science*, *6*(1), 53–77. doi:10.1146/annurev-marine-010213-135037

Ramos-Pereira, A., Trindade, J., & Neves, M. (2005). *Portugal: Coastal Dynamics*. *Sixth International Conference on Geomorphology*.

Roest, W. R., & Srivastava, S. P. (1991). Kinematics of the plate boundaries between Eurasia, Iberia, and Africa in the North Atlantic from the Late Cretaceous to the present. *Geology*, *19*(6), 613–616. doi:10.1130/0091-7613(1991)019<0613:KOTPBB>2.3.CO;2

Roque, C. (1998). *Análise Morfosedimentar da sequência deposicional do Quaternário Superior da Plataforma Continental Algarvia entre Faro e a foz do Guadiana*. Universidade de Lisboa. PhD Thesis.

Rosas, F. M., Duarte, J. C., Neves, M. C., Terrinha, P., Silva, S., Matias, L., … Bartolome, R. (2012). Thrust-wrench interference between major active faults in the Gulf of Cadiz (Africa-Eurasia plate boundary, offshore SW Iberia): Tectonic implications from coupled analog and numerical modeling. *Tectonophysics*, *548–*

*549*, 1–21. doi:10.1016/j.tecto.2012.04.013

Rosas, F. M., Duarte, J. C., Terrinha, P., Valadares, V., & Matias, L. (2009). Morphotectonic characterization of major bathymetric lineaments in Gulf of Cadiz (Africa-Iberia plate boundary): Insights from analogue modelling experiments. *Marine Geology*, *261*(1–4), 33–47. doi:10.1016/j.margeo.2008.08.002

Rovere, M., Ranero, C. R., Sartori, R., Torelli, L., & Zitellini, N. (2004). Seismic imagesand magnetic signature of the late Jurassic to early Cretaceous Africa–Eurasiaplate boundary off SW Iberia. *Geophysical Journal International*, *158*(2), 554–568.

Royden, L. H. (1993). The tectonic expression slab pull at continental convergent boundaries. *Tectonics*, *12*(2), 303–325. doi:https://doi.org/10.1029/92TC02248

Ruellan, E. (1985). *Géologie des marges continentales passives. Evolution de la marge atlantique du Maroc (Mazagan); étude par submersible, Seabeam et sismique-réflexion. Comparaison avec la marge N. W africaine et la marge homologue E. américane*. University of Bretagne Occidentale. PhD Thesis.

Ruiz, J. A., Baumont, D., & Bernard, P. (2011). Modelling directivity of strong ground motion with a fractal, k−2, kinematic source model. *Geophysical Journal International*, *186*, 226–244. doi:10.1111/j.1365-246X.2011.05000.x

Ryan, W. B. F., Hsü, K. J., Cita, M. B., Dumitrica, P., Llort, J., Maync, W., … Wezel, F. C. (1973). Annotated record of the detailed examination of Mn deposits from DSDP Site 126, Leg 13 (Core 126-2). *Supplement to: Ryan, WBF et Al. (1973): Site 126. In: Ryan, W.B.F.; Hsu, K.J.; et Al., Initial Reports of the Deep Sea Drilling Project, Initial Reports of the Deep Sea Drilling Project, U.S. Government Printing Office, XIII, 219-241, Https://Doi.Org/10.2*. PANGAEA. doi:10.1594/PANGAEA.868807

Sahabi, M., Aslanian, D., & Olivet, J. L. (2004). A new starting point for the history of thecentral Atlantic. *Comptes Rendus Geoscience*, *336*(12), 1041–1052.

Sallarès, V., Gailler, A., Gutscher, M. A., Graindorge, D., Bartolomé, R., Gràcia, E., … Zitellini, N. (2011). Seismic evidence for the presence of Jurassic oceanic crust in the central Gulf of Cadiz (SW Iberian margin). *Earth and Planetary Science*

*Letters*, *311*(1–2), 112–123. doi:10.1016/j.epsl.2011.09.003

Sallarès, V., Martínez-Loriente, S., Prada, M., Gràcia, E., Ranero, C., Gutscher, M. A., … Zitellini, N. (2013). Seismic evidence of exhumed mantle rock basement at the Gorringe Bank and the adjacent Horseshoe and Tagus abyssal plains (SW Iberia). *Earth and Planetary Science Letters*, *365*, 120–131. doi:10.1016/j.epsl.2013.01.021

Sallarès, V., & Ranero, C. R. (2019). Upper-plate rigidity determines depth-varying rupture behaviour of megathrust earthquakes. *Nature*, *576*, 96–101.

Sallarès, V., & Ranero, C. R. (2020). Shaking up geophysics. A new model for improved tsunami prediction. Retrieved 11 November 2020, from https://researchoutreach.org/wp-content/uploads/2020/08/Valenti-Sallares-and-Cesar-Ranero.pdf

Sandwell, D. T., Xiaohua, E. X., & Harper, H. (2020). SRTM15+: Global Bathymetry and Topographic at 15 arcseconds. Retrieved 13 November 2020, from https://topex.ucsd.edu/WWW_html/srtm15_plus.html

Santanach i Prat, P., & Masana, E. (2001). Prospects for Paleoseismology in Spain. *Acta Geologica Hispanica*, *36*(3), 193-196–196.

Sartori, R., Torelli, L., Zitellini, N., Peis, D., & Lodolo, E. (1994). Eastern segment of the Azores-Gibraltar line (central-eastern Atlantic) : An oceanic plate boundary with diffuse compressional deformation. *Geology*, *22*(6), 555–558. doi:10.1130/0091-7613(1994)022<0555:ESOTAG>2.3.CO;2

Satake, K. (2015). Tsunamis. *Treatise on Geophysics: Second Edition*, *4*, 477–504. doi:10.1016/B978-0-444-53802-4.00086-5

Scala, A., Lorito, S., Romano, F., Murphy, S., Selva, J., Basili, R., … Cirella, A. (2020). Effect of Shallow Slip Amplification Uncertainty on Probabilistic Tsunami Hazard Analysis in Subduction Zones: Use of Long-Term Balanced Stochastic Slip Models. *Pure and Applied Geophysics*, *177*(3), 1497–1520. doi:10.1007/s00024-019-02260-x

Scheffers, A. (2010). 12.5 Morocco, *2010*, 537–544.

Schettino, A., & Turco, E. (2009). Breakup of Pangaea and plate kinematics of the central Atlantic and Atlas regions. *Geophysical Journal International*, *178*(2), 1078–1097. doi:10.1111/j.1365-246X.2009.04186.x

Schlische, R. W., Withjack, M. O., & Olsen, P. E. (2002). Relative timing of CAMP, rifting, continental breakup, and inversion: Tectonic significance. In W. E. Hames (Ed.), *The Central Atlantic Magmatic Province: Insights From Fragments of Pangea* (Geophysica, pp. 33–59). Washington D.C.: AGU.

Scholz, C. H. (2002). The Mechanics of Earthquakes and Faulting. *The Mechanics of Earthquakes and Faulting*. doi:10.1017/cbo9780511818516

ScienceDirect. (2020). Response amplitude Operator. Retrieved 12 November 2020, from https://www.sciencedirect.com/topics/engineering/response-amplitude-operator

Selva, J., Tonini, R., Molinari, I., Tiberti, M. M., Romano, F., Grezio, A., … Lorito, S. (2016). Quantification of source uncertainties in Seismic Probabilistic Tsunami Hazard Analysis (SPTHA). *Geophysical Journal International*, *205*(3), 1780–1803. doi:10.1093/gji/ggw107

Serra, N., Ambar, I., & Käse, R. H. (2005). Observations and numerical modelling of the Mediterranean outflow splitting and eddy generation. *Deep Sea Research Part II: Topical Studies in Oceanography*, *52*(3), 383–408. doi:https://doi.org/10.1016/j.dsr2.2004.05.025

Serra, C.S., Martínez-Loriente, S., Gràcia, E., Urgeles, R., Vizcaino, A., Perea, H., … Zitellini, N. (2020). Tectonic evolution, geomorphology and influence of bottom currents along a large submarine canyon system: The São Vicente Canyon (SW Iberian margin). *Marine Geology*, *426*(May), 106219. doi:10.1016/j.margeo.2020.106219

Shanmugam, G. (2012). Chapter 4 - Bottom-Current Reworked Sands. In G. B. T.-H. of P. E. and P. Shanmugam (Ed.), *New Perspectives on Deep-water Sandstones* (Vol. 9, pp. 129–219). Elsevier. doi:https://doi.org/10.1016/B978-0-444-56335-4.00004-7

Shepard, F. P. (1981). Submarine canyons_multiple causes and long-time persistence.

*Petroleum Geologist Bulletin*, *65*, 1062–1077.

Sibuet, J.C., Srivastava, S. P., & Spakman, W. (2004). Pyrenean orogeny and plate kinematics. *Journal of Geophysical Research: Solid Earth*, *109*(B8), 1–18. doi:https://doi.org/10.1029/2003JB002514

Silva, P. F., Roque, C., Drago, T., Belén, A., Henry, B., Gemma, E., … Vázquez, J. T. (2020). Multidisciplinary characterization of Quaternary mass movement deposits in the Portimão Bank ( Gulf of Cadiz , SW Iberia ). *Marine Geology*, *420*, 1–20. doi:10.1016/j.margeo.2019.106086

Silva, S., Terrinha, P., Matias, L., Duarte, J. C., Roque, C., Ranero, C. R., … Zitellini, N. (2017). Micro-seismicity in the Gulf of Cadiz: Is there a link between micro-seismicity, high magnitude earthquakes and active faults? *Tectonophysics*, *717*, 226–241. doi:10.1016/j.tecto.2017.07.026

Smith, W. H. F., & Sandwell, D. T. (1997). Global Sea Floor Topography from Satellite Altimetry and Ship Depth Soundings. *Science*, *277*, 1956–1962. doi:10.1126/science.277.5334.1956

Somers, M. L., Carson, R. M., Revie, J. A., Edge, R. H., Barrows, B. J., & Andrews, A. G. (1978). GLORIA II-an improved long range sidescan sonar. In *Processings of the Institute of Electrical Engineering on Offshore Instrumentation and Communications, Oceanology International Technical Session* (pp. 16–24). London: London, BPS Publications Ltd.

Somoza, L., Gardner, J. M., Díaz-del-Río, V., Vázquez, J. T., Pinheiro, L. M., Hernández-Molina, F. J., & parties, T. shipboard scientific. (2002). Numerous methane gas-related sea floor structures identified in Gulf of Cadiz. *Eos, Transactions American Geophysical Union*, *83*(47), 541–549. doi:https://doi.org/10.1029/2002EO000371

Speckbacher, R., Behrmann, J. H., Nagel, T. J., Stipp, M., & Mahlke, J. (2012). Fluid flow and metasomatic fault weakening in the Moresby Seamount detachment, Woodlark Basin, offshore Papua New Guinea. *Geochemistry, Geophysics, Geosystems*, *13*(11), 24. doi:https://doi.org/10.1029/2012GC004407

Srivastava, S. P., Schouten, H., Roest, W. R., Klitgord, K. D., Kovacs, L. C., Verhoef,

J., & Macnab, R. (1990). Iberian plate kinematics: a jumping plate boundary between Eurasia and Africa. *Nature*, *344*(6268), 756–759. doi:10.1038/344756a0

Stampfli, G. M., & Borel, G. D. (2002). A plate tectonic model for the Paleozoic and Mesozoic constrained by dynamic plate boundaries and restored synthetic oceanic isochrons. *Earth and Planetary Science Letters*, *196*, 17–33.

Stanley, D. J. (1982). La plate-forme continentale du portugal et les provinces adjacentes: Analyse géomorphologique. *Geo-Marine Letters*, *2*(1), 109. doi:10.1007/BF02462809

Stein, S., & Okal, E. A. (2005). Speed and size of the Sumatra earthquake. *Nature*, *434*(7033), 581–582. doi:10.1038/434581a

Stich, D., Serepelloni, E., Mancilla, F., & Morales, J. (2006). Kinematics of the Iberia–Maghreb plate contact from seismic moment tensors and GPS observations. *Tectonophysics*, *426*, 295–317. doi:10.1016/j.tecto.2006.08.004

Stich, D., Mancilla, F. de L., & Morales, J. (2005). Crust-mantle coupling in the Gulf of Cadiz (SW-Iberia). *Geophysical Research Letters*, *32*(13), 1–4. doi:10.1029/2005GL023098

Stich, D., Martín, R., & Morales, J. (2010). Moment tensor inversion for Iberia-Maghreb earthquakes 2005-2008. *Tectonophysics*, *483*(3–4), 390–398. doi:10.1016/j.tecto.2009.11.006

Stow, D. A. V, Faugères, J.C., & Gonthier, E. (1986). Facies distribution and textural variation in Faro Drift contourites: Velocity fluctuation and drift growth. *Marine Geology*, *72*(1), 71–100. doi:https://doi.org/10.1016/0025-3227(86)90100-3

Stow, D. A. V, & Tabrez, A. R. (1998). Hemipelagites: processes, facies and model. *Geological Society, London, Special Publications*, *129*(1), 317 LP – 337. doi:10.1144/GSL.SP.1998.129.01.19

Sultan, N., Gaudin, M., Berne, S., Canals, M., Urgeles, R., & Lafuerza, S. (2007). Analysis of slope failures in submarine canyon heads: An example from the Gulf of Lions. *Journal of Geophysical Research: Earth Surface*, *112*(1). doi:10.1029/2005JF000408

Susagna i Vidal, M. T., & Goula i Suriñach, X. (1999). *Atles sísmic de Catalunya* (Vol. 1. Catàleg).

Swapna, M., & Srivastava, K. (2014). Effect of Murray ridge on the tsunami propagation from Makran subduction zone. *Geophysical Journal International*, *199*(3), 1430–1441. doi:10.1093/gji/ggu336

Sylvester, A. G. (1988). Strike-slip faults. *GSA Bulletin*, *100*(11), 1666–1703. doi:10.1130/0016-7606(1988)100<1666:SSF>2.3.CO;2

Szitkar, F., Dyment, J., Petersen, S., Bialas, J., Klischies, M., Graber, S., … Murton, B. J. (2019). Detachment tectonics at Mid-Atlantic Ridge 26°N. *Scientific Reports*, *9*(1), 1–8. doi:10.1038/s41598-019-47974-z

Talley, L. D., Pickard, G. L., Emery, W. J., & Swift, J. H. (2011). Atlantic Ocean. In L. D. Talley, G. L. Pickard, W. J. Emery, & J. H. B. T. D. P. O. (Sixth E. Swift (Eds.), *Descriptive Physical Oceanography* (6th ed., pp. 245–301). Boston: Academic Press. doi:https://doi.org/10.1016/B978-0-7506-4552-2.10009-5

Tarbuck, E. J., Lutgens, F. K., & Tasa, D. (2005). *Ciencias de la Tierra* (8th ed.). Pearson Prentice Hall.

Tendürüs, M., Van Wijngaarden, G. J., & Kars, H. (2010). Long-term effect of seismic activities on archaeological remains: A test study from Zakynthos, Greece. *Special Paper of the Geological Society of America*, *471*(October), 145–156. doi:10.1130/2010.2471(13)

Terrinha, P., Matias, L., Vicente, J., Duarte, J., Luís, J., Pinheiro, L., … Víctor, L. M. (2009). Morphotectonics and strain partitioning at the Iberia-Africa plate boundary from multibeam and seismic reflection data. *Marine Geology*, *267*(3–4), 156–174. doi:10.1016/j.margeo.2009.09.012

Terrinha, P., Pinheiro, L. M., Henriet, J. P., Matias, L., Ivanov, M. K., Monteiro, J. H., … Rovere, M. (2003). Tsunamigenic-seismogenic structures, neotectonics, sedimentary processes and slope instability on the southwest Portuguese Margin. *Marine Geology*, *195*(1–4), 55–73. doi:10.1016/S0025-3227(02)00682-5

Thomson, J. & Weaver, P. P. E. (2009) An AMS radiocarbon methods to determine the

emplacement time of recent deep-sea turbidites. *Sedimetary Geology, 267* (3-4), 156-174.

Thorpe, S. A. (1975). Variability of the Mediterranean undercurrent in the Gulf of Cadiz. *Deep-Sea Research*, *23*, 711–727.

Tinterri, R., Civa, A., Laporta, M., & Piazza, A. (2020). Chapter 17 - Turbidites and turbidity currents. In N. Scarselli, J. Adam, D. Chiarella, D. G. Roberts, & A. W. B. T. R. G. and T. (Second E. Bally (Eds.) (pp. 441–479). Elsevier. doi:https://doi.org/10.1016/B978-0-444-64134-2.00016-X

Tonini, R., Basili, R., Maesano, F. E., Tiberti, M. M., Lorito, S., Romano, F., … Volpe, M. (2020). Importance of earthquake rupture geometry on tsunami modelling: the Calabrian Arc subduction interface (Italy) case study. *Geophysical Journal International*, *223*(3), 1805–1819. doi:10.1093/gji/ggaa409

Torelli, L., Sartori, R., & Zitellini, N. (1997). The giant chaotic body in the Atlantic Ocean off Gibraltar: New results from a deep seismic reflection survey. *Marine and Petroleum Geology*, *14*(2), 125–134. doi:10.1016/S0264-8172(96)00060-8

Tortella, D., Torne, M., & Pérez-Estaún, A. (1997). Geodynamic Evolution of the Eastern Segment of the Azores-Gibraltar Zone: The Gorringe Bank and the Gulf of Cadiz Region. *Marine Geophysical Research*, *19*(3), 211–230. doi:10.1023/A:1004258510797

Toyos, M. H., Medialdea, T., León, R., Somoza, L., González, F. J., & Meléndez, N. (2016). Evidence of episodic long-lived eruptions in the Yuma, Ginsburg, Jesús Baraza and Tasyo mud volcanoes, Gulf of Cádiz. *Geo-Marine Letters*, *36*(3), 197–214. doi:10.1007/s00367-016-0440-z

Tozer, B., Sandwell, D. T., Smith, W. H. F., Olson, C., Beale, J. R., & Wessel, P. (2019). Global Bathymetry and Topography at 15 Arc Sec: SRTM15+. *Earth and Space Science*, *6*(10), 1847–1864. doi:https://doi.org/10.1029/2019EA000658

Tucholke, B., Sawyer, D., & Sibuet, J. C. (2007). Breakup of the Newfoundland–Iberia rift. *Geological Society, London, Special Publications*, *282*(1), 9–46.

Turcotte, D., & Schubert, G. (2002). *Geodynamics*. (Cambridge University Press, Ed.).

Urgeles, R., & INSIGHT Cruise Party. (2019). *ImagiNg large SeismogenIc and tsunamiGenic structures of the Gulf of Cadiz with ultra-High resolution Technologies (INSIGHT-Leg2)*. Barcelona.

USGS. (2020). GLORIA Mapping Program. Retrieved 12 November 2020, from https://coastalmap.marine.usgs.gov/gloria/

Vidal, J. (2016). Registros de paleotsunamis en las costas del litoral atlántico de la provincia de Huelva: antecedentes del maremoto de 1755. *IERD*, 29–35.

Viekman, B. E., Wimbush, M., & Van Leer, J. C. (1989). Secondary circulations in the bottom boundary layer over sedimentary furrows. *Journal of Geophysical Research: Oceans*, *94*(7), 9721–9730. doi:https://doi.org/10.1029/JC094iC07p09721

Vizcaino, A, Gràcia, E., Pallàs, R., Terrinha, P., Diez, S., Dañobeitia, J., & D, M. (2005). Active tectonic and sedimentary processes along the Sao Vicente Canyon (SW Iberian Margin): High-Resolution Imaging. *European Geosciences Union 2005*, *7*(1), 7707. Retrieved from file:///C:/VHD/VHBiblio%5CGulfofCadiz%5CVH05-2594.pdf

Vizcaino, A. (2009). *Processos sedimentaris d 'edat Holocena al marge sud-oest de la Península Ibèrica: aplicació a paleosismologia marina*. Universitat de Barcelona. PhD Thesis.

Vizcaino, A., Gràcia, E., Pallàs, R., Garcia-Orellana, J., Escutia, C., Casas, D., … Dañobeitia, J. (2006). Sedimentology, physical properties and age of mass transport deposits associated with the Marquês de Pombal Fault, Southwest Portuguese Margin. *Norsk Geologisk Tidsskrift*, *86*(3), 177–186.

Vogt, P. R. Ã., & Jung, W. Y. (2004). The Terceira Rift as hyper-slow , hotspot-dominated oblique spreading axis : A comparison with other slow-spreading plate boundaries. *Earth and Planetary Science Letters*, *218*, 77–90. doi:10.1016/S0012-821X(03)00627-7

Volpe, M., Lorito, S., Selva, J., Tonini, R., Romano, F., & Brizuela, B. (2019). From regional to local SPTHA: efficient computation of probabilistic tsunami inundation maps addressing near-field sources. *Natural Hazards and Earth System Sciences*,

*19*(3), 455–469. doi:10.5194/nhess-19-455-2019

Wallace, R. E. (1981). Active Faults, Paleoseismology, and Earthquake Hazards in the Western United States. *Earthquake Prediction*. doi:https://doi.org/10.1029/ME004p0209

Weaver, P. P. E., Wynn, R. B., Kenyon, N. H., & Evans, J. (2000). Continental margin sedimentation, with special reference to the north-east Atlantic margin. *Sedimentology*, *47*(s1), 239–256. doi:https://doi.org/10.1046/j.1365-3091.2000.0470s1239.x

Williamson, A. L., Rim, D., Adams, L. M., LeVeque, R. J., Melgar, D., & González, F. I. (2020). A Source Clustering Approach for Efficient Inundation Modeling and Regional Scale Probabilistic Tsunami Hazard Assessment. *Frontiers in Earth Science.* Retrieved from https://www.frontiersin.org/article/10.3389/feart.2020.591663

Wilson, T. (1963). Evidence from Islands on the Spreading of Ocean Floors. *Nature*, *197*(4867), 536–538. doi:10.1038/197536a0

Wood, N. (2011). Understanding Risk and Resilience to Natural Hazards. Retrieved 30 October 2020, from https://pubs.usgs.gov/fs/2011/3008/fs2011-3008.pdf

Wood, N., Peters, J., Wilson, R., Sherba, J., & Henry, K. (2020). Variations in community evacuation potential related to average return periods in probabilistic tsunami hazard analysis. *International Journal of Disaster Risk Reduction*, *50*, 101871. doi:https://doi.org/10.1016/j.ijdrr.2020.101871

Yamashita, T., & Sato, R. (1974). Generation of tsunami by a fault model. *Journal of Physics of the Earth*, *22*(4), 415–440. doi:10.4294/jpe1952.22.415

Yeo, I. A., Devey, C. W., LeBas, T. P., Augustin, N., & Steinführer, A. (2016). Segment-scale volcanic episodicity: Evidence from the North Kolbeinsey Ridge, Atlantic. *Earth and Planetary Science Letters*, *439*, 81–87. doi:https://doi.org/10.1016/j.epsl.2016.01.029

Yilmaz, O. (2001). *Seismic Data Analysis*. Society of Exploration Geophysicists.

Yoerger, D. R., Bradley, A. M., Jakuba, M., Tivey, M. A., German, C. R., Shank, T. M.,

& Embley, R. W. (2007). Mid-ocean ridge exploration with an autonomous underwater vehicle. *Oceanography*, *20*(SPL.ISS. 4), 52–61. doi:10.5670/oceanog.2007.05

Zamora, N., Catalan, P. A., Gubler, A., & Carvajal, M. (2021). Microzoning Tsunami Hazard by Combining Flow Depths and Arrival Times. *Frontiers in Earth Science*. doi:10.3389/feart.2020.591514

Zenk, W. (1975). On the Mediterranean outflow west of Gibraltar. *'Meteor' Forschungs Ergebunisse, 16*, 23–34.

Zitellini, N., Gràcia, E., Matias, L., Terrinha, P., Abreu, M. A., De Alteriis, G., … Diez, S. (2009). The quest for the Africa-Eurasia plate boundary west of the Strait of Gibraltar. *Earth and Planetary Science Letters*, *280*(1–4), 13–50. doi:10.1016/j.epsl.2008.12.005

Zitellini, N., Mendes, L. A., Cordoba, D., Danobeitia, J., Nicolich, R., Pellis, G., … Ruiz, A. Z. (2001). Source of 1755 lisbon earthquake and tsunami investigated. *Eos*, *82*(26), 285–291. doi:10.1029/EO082i026p00285-01

Zitellini, N., Rovere, M., Terrinha, P., Chierici, F., Matias, L., Victor, L. M., … Vigliotii, L. (2004). Neogene through quaternary tectonic reactivation of SW Iberian passive margin. *Pure and Applied Geophysics*, *161*(3), 565–587. doi:10.1007/s00024-003-2463-4

Zitellini, Nevio, Chierici, F., Sartori, R., & Torelli, L. (1999). The tectonic source of the 1755 Lisbon earthquake and tsunami. *Annali Di Geofisica*, *42*(1), 49–55. doi:10.4401/ag-3699

# ANNEXES

# Annex 1: Data to perform the tsunami simulations

Data are available at the file "Fault_meshes.ts" in the *figshare repository*: https://figshare.com/s/02e19886d2ded8ec9145

Fault_meshes.ts: coordinates of the simple fault planes for the Gorringe Bank fault, Lineament South fault, Marquês de Pombal fault, Horseshoe fault, North Coral Patch fault and South Coral Patch fault; and the coordinates of the vertex of each triangle that constitute the 3D fault planes of the Marquês de Pombal fault, Horseshoe fault, North Coral Patch fault and South Coral Patch fault.

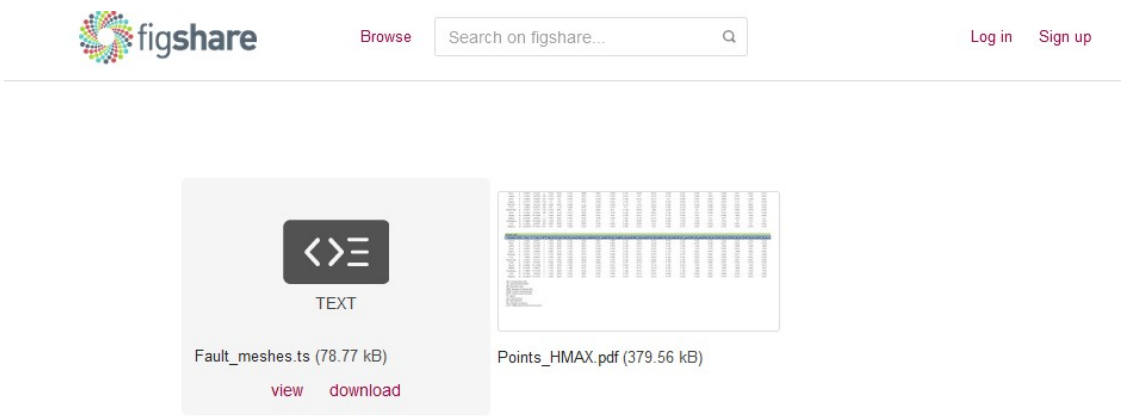


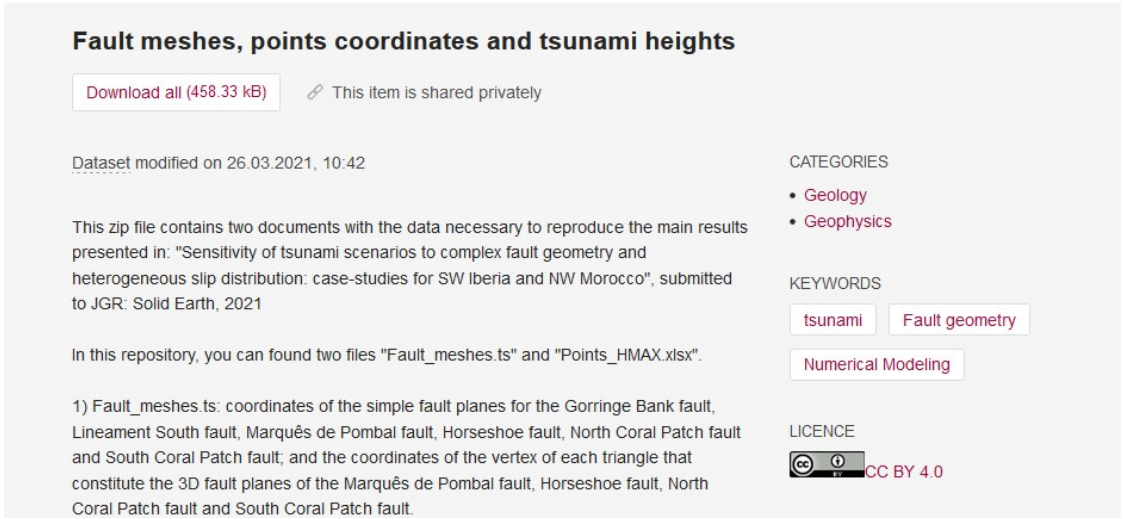

# Annex 2: Scientific article

**Serra, C.S.,** Martínez-Loriente, S., Gràcia, E., Urgeles, R., Vizcaino, A., Perea, H., Bartolome, R., Pallàs, R., Lo Iacono, C., Diez, S., Dañobeitia, J., Terrinha, P., Zitellini, N. (2020): Tectonic evolution, geomorphology and influence of bottom currents along a large submarine canyon system: The São Vicente Canyon (SW Iberian margin). *Marine Geology,* 426: 106219. https://doi.org/10.1016/j.margeo.2020.106219

Marine Geology 426 (2020) 106219

Contents lists available at ScienceDirect

Marine Geology

journal homepage: www.elsevier.com/locate/margo

# Tectonic evolution, geomorphology and influence of bottom currents along a large submarine canyon system: The São Vicente Canyon (SW Iberian margin)

Cristina S. Serra[a,b,*], Sara Martínez-Loriente[a,c], Eulàlia Gràcia[a], Roger Urgeles[a], Alexis Vizcaino[a], Héctor Perea[a,d], Rafael Bartolome[a], Raimon Pallàs[b], Claudio Lo Iacono[a,e], Susana Diez[f], Juanjo Dañobeitia[f], Pedro Terrinha[g,h], Nevio Zitellini[i]

[a] Institut de Ciències del Mar, CSIC, 08003 Barcelona, Spain
[b] Dpt. Geodinàmica de la Terra i l'Oceà, Univ. Barcelona, 08028 Barcelona, Spain
[c] Irish Centre for Research in Applied Geosciences, UCD School of Earth Sciences, Dublin 4, Ireland
[d] Dept. de Geodinámica, Estratigrafía y paleontología, Facultad de Ciencias Geológicas, Universidad Complutense de Madrid, 28040 Madrid, Spain
[e] Marine Geoscience, National Oceanography Centre, Southampton SO14 3ZH, UK
[f] Unitat de Tecnologia Marina, UTM-CSIC, 08003 Barcelona, Spain
[g] Instituto Português do Mar e da Atmosfera, IPMA, 1749-077 Lisboa, Portugal
[h] IDL - FCUL, Edf. C1 - Piso 1- Campo Grande - 1749-016, Lisboa, Portugal
[i] CNR-National Research Council of Italy, ISMAR-Marine Science Institute in Bologna, 40129 Bologna, Italy

ARTICLE INFO

*Keywords:*
Submarine canyon
Thrust faults
Bottom currents
Sedimentary pathways
Sidescan-sonar
Seismic reflection

ABSTRACT

A multi-scale dataset consisting of multi-beam echo-sounder, 2D multi-channel seismic and sidescan sonar (TOBI) data allows us to identify a large variety of morphologies originating from sedimentary and tectonic processes along the São Vicente Canyon (SVC), which is the largest submarine canyon developed in the external part of the Gulf of Cadiz. The SVC is located in one of the most seismogenic areas of Western Europe. The convergence between the Eurasian and African plates has controlled the formation and evolution of the canyon. The SVC is tectonically controlled by three main thrust faults: the Marquês de Pombal Fault, the São Vicente Fault and the Horseshoe Fault. No major rivers feed sediment to the canyon head, but the main sediment source is related to the dismantling of canyon flanks and the MOW (Mediterranean Overflow Water). This current contributes sediments by two different processes: a) conturites deposition at the head and flanks of the SVC that periodically fail into the canyon; and b) the coarser-grained and denser sediment of the MOW might be trapped at the head of the canyon and could develops into hyperpycnal flows. The SVC is characterized by retrogressive erosion being submarine landslide deposits and scars the main seafloor morphologies. The tectonic and stratigraphic interpretation of seismic profiles indicate that the SVC is a clear example of a diachronous and segmented canyon developed since the Late Miocene in an area of present-day active plate tectonics. This study investigates the interaction between active tectonics, the dynamics of submarine canyons and the resulting geomorphologies.

## 1. Introduction

Submarine canyons are major sediment pathways that link shallow continental shelf areas to the deep sea. They play an important global role in the development of continental margins. Submarine canyons not only act as conduits for sediments, but also they play a role as main transport corridor for associated nutrients, organic carbon, litter and pollutants travelling from the continental shelves to the abyssal plains (Amblas et al., 2012; Lastras et al., 2009; Micallef et al., 2014; Pierdomenico et al., 2019; Shepard, 1981). Erosion and sediment remobilization induced by sediment-laden gravity flows (e.g. turbidity currents), which travel from the head and flanks of the canyon towards the deep oceanic basins (Lewis and Barnes, 1999), are the main factors in the generation of submarine canyons. Temporary sediment accumulations near the canyon head may become unstable due to a number of factors, such as over-steepening, earthquake-triggered deformation,

* Corresponding author at: Institut de Ciències del Mar, CSIC, 08003 Barcelona, Spain.
*E-mail address:* csserra@icm.csic.es (C. S. Serra).

https://doi.org/10.1016/j.margeo.2020.106219
Received 10 January 2020; Received in revised form 28 April 2020; Accepted 30 April 2020
Available online 07 May 2020

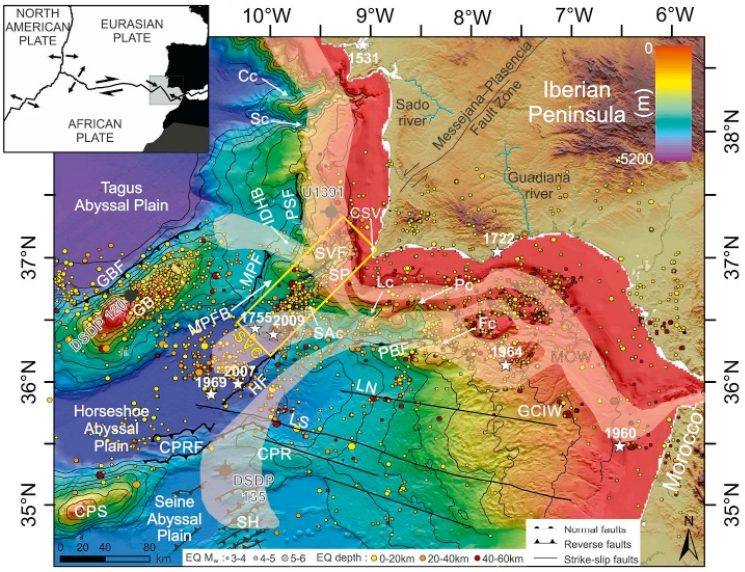


**Fig. 1.** Bathymetric map of the Gulf of Cadiz with the location of the main faults (after Martínez-Loriente et al., 2013, 2018). Yellow circles correspond to epicenter locations for the period 1400–2020 (Instituto Geográfico Nacional [IGN] catalogue; http://www.ign.es/ign/layout/sismo.do). Earthquakes locations according to Lozano et al., 2019 and Stich et al., 2006. Inset: Plate tectonic setting of the SW Iberian margin at the boundary between the Eurasian and African Plates. The grey rectangle corresponds to the area depicted in Fig. 1. Cc: Cascais canyon; CPR: Coral Patch Ridge; CPRF: Coral Patch Ridge Faults; CPS: Coral Patch Seamount; CSV: Cape São Vicente; Fc: Faro canyon; GB: Gorringe Bank; GBF: Gorringe Bank Fault; GCIW: Gulf of Cadiz Imbricated Wedge; HF: Horseshoe Fault; IDHB: Infante Don Henrique Basin; Lc: Lagos canyon; LN: Lineament North; LS: Lineament South; MPF: Marquês de Pombal Fault; MPFB: Marquês de Pombal Fault Block; PBF: Portimão Bank Fault; Pc: Portimão canyon; PSF: Pereira de Sousa Fault; SAc: Sagres canyon; Sc: Setúbal canyon; SH: Seine Hills; SP: Sagres Plateau; SVC: São Vicente Canyon; SVF: São Vicente Fault. (For interpretation of the references to colour in this figure legend, the reader is referred to the web version of this article.)

sediment liquefaction and basal erosion of canyon flanks (Arzola et al., 2008). However, other flows such as hyperpycnal flows that generated submarine slope failures at the canyon head, and dense shelf water cascading (Canals et al., 2006; Palanques et al., 2006; Puig et al., 2014) may cause erosion, and transport of large sediment volumes along the entire canyon.

The onset of canyon development and its subsequent evolution is determined by a number of factors, including sediment sources and the resulting sedimentary and erosive processes that shape the canyon floor and their flanks (Amblas et al., 2011). Sediments may derive from fluvial sources (i.e. most existing canyons are directly fed by rivers, particularly during sea level low-stands) (Mauffrey et al., 2017) or along-shore currents (Piper et al., 2009). In addition, structural control has also been proposed (Micallef et al., 2014).

The São Vicente Canyon (SVC) is the largest submarine canyon in the SW Iberian margin (Fig. 1), transporting sediment from the shelf break (~200 m water depth, where the SVC head is located) to the Horseshoe Abyssal Plain (4900 m at the SVC mouth), although no major river feeds sediment to its head. The SVC is located in a convergent setting placed between the Eurasian and African plates, which greatly control its dynamics. In this work, we use a multi-scale dataset and different analysis techniques to describe the tectonic, sedimentary and erosional processes linked to the canyon, and to propose a conceptual model to discuss the emplacement, age and evolution of the SVC. This study improves the knowledge on the origin and interplay between active tectonics, the dynamics of submarine canyons, and the resulting geomorphologies.

## 2. Geological setting

The SVC is located on the external part of the Gulf of Cadiz (SW Portuguese margin), along the Eurasian-African plate boundary. Present-day tectonic deformation is mainly driven by NW-SE trending convergence, with an estimated velocity of 3.8–5.6 mm $a^{-1}$ (Neres et al., 2016; Nocquet and Calais, 2004) (Fig. 1).

The SW Iberian margin has undergone a complex geodynamic evolution that includes three rifting phases during the Mesozoic (i.e., the opening of the Central Atlantic and the western Alpine-Tethys spreading system in the Early Jurassic, followed by the first stage of the North Atlantic opening in the Lower Cretaceous) and a Neogene-to-present-day convergence (Martínez-Loriente et al., 2014; Sallarès et al., 2013, 2011). The latest Neogene convergence stage, mainly trending NNW-SSE (Schettino and Turco, 2009), resulted in the emplacement of large allochthonous masses during the Tortonian (Gràcia et al., 2003a; Iribarren et al., 2007). As a result of the Neogene collision, Mesozoic extensional faults were reactivated and new fault systems appeared in weakened areas. There are two main families of active faults: a) NE-SW trending reverse faults; and b) WNW-ESE trending dextral strike-slip faults (Gràcia et al., 2003a, b; Martínez-Loriente et al., 2018, 2014, 2013; Terrinha et al., 2009, 2003) (Fig. 1).

The SW Iberia is an area of low to intermediate magnitude earthquakes ($M_w$ < 5.5), occasionally punctuated by high-magnitude seismic activity (Buforn et al., 1995; Martínez-Loriente et al., 2018, 2013; Stich et al., 2005) (Fig. 1), with focal mechanisms indicating compressional stress and/or strike-slip regime (Buforn et al., 1995; Stich et al., 2005). This area is also the source of the largest historical and instrumental earthquakes in Western Europe, including the earthquakes and tsunamis of the 26 January 1531 Tagus Estuary tsunami (MSK = X), the 27 December 1722 Tavira tsunami, ($M_w$ 6.5) and the 1 November 1755 Lisbon earthquake ($M_w \geq 8.5$) (Baptista and Miranda, 2009) events (Fig. 1). This last earthquake caused extensive destruction in Portugal, southern Spain and western Morocco (Baptista and Miranda, 2009; Barkan et al., 2009; Gràcia et al., 2010). In recent times, earthquakes of considerable magnitude have nucleated in the study area on the 28 February 1969 ($M_w$ 7.9–8.0), 12 February 2007 ($M_w$ 6.0), and 17 December 2009 ($M_w$ 5.5) (Stich et al., 2006; Lozano et al., 2019) (Fig. 1).

The physiography of the Portuguese margin is characterized by the presence of numerous large submarine canyons, such as the Faro, Portimão and Lagos canyons in the south (Mulder et al., 2006; Vizcaino et al., 2005), and the Cascais, Lisbon, Setúbal and Nazaré canyons in the west of Portugal (Arzola et al., 2008; Lastras et al., 2009; Oliveira et al., 2007; Terrinha et al., 2019) (Fig. 1). The oceanic circulation of the Gulf of Cadiz is dominated by the MOW (Mediterranean Outflow Water) (Fig. 1). The MOW is a salty, warm and poorly oxygenated submarine current that flows from the Strait of Gibraltar towards the Atlantic

following the slope and the Portuguese continental shelf (Hernández-Molina et al., 2003). Along its pathway, the MOW loses velocity and increases in depth. At the head of the SVC, the MOW generates associated sedimentary deposits such as contourites (Hernández-Molina et al., 2013).

The SVC extends from Cape São Vicente on the Portuguese coast to the Horseshoe Abyssal Plain, bounded by the Sagres Plateau and the Horseshoe Fault to the east, and by the Marquês de Pombal fault block to the west (Fig. 1). The SVC is located in a syncline fold in between two prominent anticlines (i.e., the Marques de Pombal block and the Sagres Palteau) (Vizcaino et al., 2005; Zitellini et al., 2001; Pereira and Alves, 2013) and is mainly dominated by the NE-SW-trending reverse Horseshoe Fault (Martínez-Loriente et al., 2018) (Fig. 1). Alternatively, some authors propose that the SVC is linked with the prolongation offshore of the Messejana–Plasencia Fault Zone (Pereira and Alves, 2013). The sedimentary inputs to the SVC are mainly fed by along-the-shelf sediment transport sources (i.e., the MOW) (Mastbergen and Van Den Berg, 2003). Most of the sediments travelling along the SVC are deposited in the Horseshoe Abyssal Plain (Gràcia et al., 2010).

## 3. Data and methods

The multi-scale dataset used in this work includes existing swath-bathymetry, sidescan sonar (TOBI) and multi-channel seismic (MCS) data (Fig. 2). Swath bathymetric data in the Gulf of Cadiz was acquired during 20 different marine cruises, from 2001 to 2009, using different multibeam echosounder systems. Ten European contributors collaborated to complete the bathymetric map of the Gulf of Cadiz, the "SWIM" compilation published by Zitellini et al. (2009) (Figs. 1, 2). Sidescan sonar data (Figs. 2, 5, 6, 7) were acquired on board the RV *Hesperides* during the "HITS" (*High Resolution Imagining of Tsunamigenic Structures of the Southern Iberian Margins*) survey (Gràcia et al., 2003a, 2006) by using the TOBI (Towed Ocean Bottom Instrument) side-scan sonar vehicle (Flewellen et al., 1993). The sidescan sonar system used a 30 kHz sonar frequency on a vehicle towed 200 to 500 m above the sea-floor to generate images with 6 m along-track resolution (Blondel and Murton, 1997). The data used for this study consisted of four 6-km-wide parallel tracks covering most of the São Vicente Canyon. In this study, swath-bathymetry and side-scan sonar data were analysed using the ArcGIS 10 commercial package.

The sinuosity index of the SVC has been calculated using the ratio of curvilinear to straight length (Leopold and Wolman, 1957). The volume of the eroded material by the SVC has been determined by calculating the difference in elevation between a spline-smoothed grid where the canyon topography was removed, therefore simulating the slope without canyon incision (Fig. S1) and the grid of the actual slope (Fig. S1).

The Multi-channel seismic (MCS) data available for this study consists of 17 profiles acquired with different configurations during different marine surveys (Fig. 2). The "AR" profiles, belonging to the 1992 ARRIFANO cruise, were acquired with the R/V OGS EXPLORA (Zitellini et al., 1999). This survey used an airgun array of 32 guns with a total capacity of 4880 cubic inches (c.i.) and a 3-km-long streamer with 120 channels and 50 m shooting interval (Zitellini et al., 1999). The AR data was processed with spiking deconvolution, spherical divergence correction, NMO correction, finite-difference wave-equation migration and time variant band-pass frequency filter (Zitellini et al., 2009). The "BS" profiles from the BIGSETS survey were acquired on board the R/V URANIA during November 1998 (Zitellini et al., 2001). The seismic source consisted of an array of two GI-guns with a total volume ranging

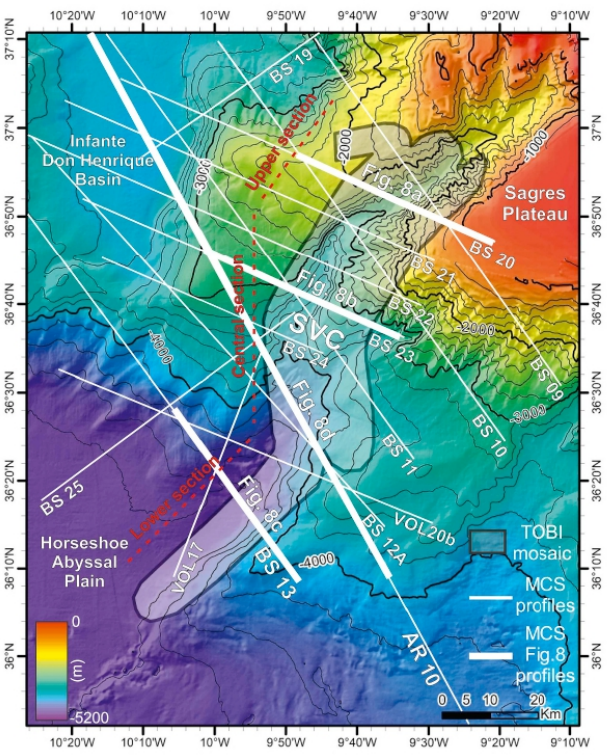


**Fig. 2.** Bathymetric map of the study area in the SW Portuguese Margin. The grey area depicts the TOBI sidescan sonar mosaic of the São Vicente Canyon (SVC) acquired during the HITS-2001 survey (Gràcia et al., 2003a). White lines label the multichannel seismic (MCS) profiles used in this study and acquired during the BIGSETS-1998 (BS), ARRIFANO-1992 (AR) and VOLTAIRE-2004 (VOL) surveys (e.g. Zitellini et al., 2001, 2004; Terrinha et al., 2003). Thick white lines represent the seismic sections shown in Fig. 8.

from 150 to 465 c.i. The seismic signal was recorded with a 1.2 km-long streamer of 48 channels and 25, 37 and 50 m shooting interval (Zitellini et al., 2004, 2001). The processing of BIGSETS MCS data consisted in spiking deconvolution, velocity analysis every 2.5 km, NMO correction, spherical divergence correction and finite-difference wave-equation time migration using stacking velocities reduced by 10% (Zitellini et al., 2004). The "VOL" profiles correspond to the 2002 VOLTAIRE survey carried out on board the R/V URANIA. In this survey, 2 GI guns totalling 210 c.i. were shot every 50 m and a 600 m-long, 48 channel streamer was used (Terrinha et al., 2009). The MCS VOLTAIRE dataset was processed with trace editing, shot delay removal, amplitude recovery, predictive deconvolution, velocity analysis every 200 CMPs, NMO correction, stack, bandpass-frequency filtering and time migration using stacking velocities reduced by 10%. The analysis and geological interpretation of the 17 MCS profiles used in this study were carried out using the "IHS Kingdom Suite" seismic interpretation software.

In this work, the seismostratigraphic units defined by Martínez-Loriente et al. (2013) were correlated throughout the seismic network of profiles shown in Fig. 2 (see supplementary material Fig. S2). These units were defined based on the DSDP (Deep Sea Drilling Project) Site 135 (Hayes et al., 1972) and correlated with those previously defined in the area (Tortella et al., 1997; Hayward et al., 1999; Medialdea et al., 2004). In addition, the tectonic and stratigraphic analysis carried out by Martínez-Loriente et al. (2018) along three MCS profiles crossing the mouth of the SVC has been used in this work as a reference. Hernández-Molina et al. (2015) defined four Quaternary subunits based on IODP (International Ocean Discovery Program) Site 339 results (Hernández-Molina et al., 2013). The lack of seismic data connecting the Site 339 to the study area, prevents a confident age assignment to the four unconformities identified within the youngest unit in the seismic dataset used in this work (i.e., subunit Ia; see Supplementary Material Figs. S2, S3).

## 4. Results

### 4.1. Geomorphology and acoustic character of the São Vicente Canyon

The SVC is a 157 km-long canyon connecting the continental shelf, at 200 m water depth, to the Horseshoe Abyssal Plain at 4900 m water depth (Figs. 1, 2). The sinuosity (winding), is 1.12 and its average axial slope is 1.8º (Fig. 3). The path of the SVC is characterized by several changes in orientation and slope. Accordingly, the canyon has been divided in three main sections, from north to south: 1) the upper section (canyon head) is 60 km-long, trends N50, and extends from the continental shelf from water depth of 200 m to 3200 m (Fig. 3a); 2) the central section is 54 km–long, trends N20 in the northern part and N160 in the southern end, covering the area located between 3200 m and 4400 m water depth (Fig. 3b); and 3) the lower section is 43 km-long, trends N30 (parallel to the Horseshoe Fault), and extends from 4400 m to 4900 m water depth towards the canyon mouth in the Horseshoe Abyssal Plain (Fig. 3c).

A significant characteristic of the SVC is that the longitudinal bathymetric profile of the canyon axis (Fig. 4d) presents a rectilinear morphology with a rather constant slope and, therefore, does not appear to be in equilibrium. Generally, bathymetric profiles that are in equilibrium, similarly to rivers on land, show a logarithmic longitudinal-profile (Amblas et al., 2012). However, the longitudinal profile of the SVC shows a rather linear morphology (Fig. 4d) although the flanks are clearly asymmetric and its height and slope vary along the canyon (profiles across the canyon in Fig. 4a, c) (Fig. 3). On the TOBI mosaic, the canyon floor and the lower part of the flanks display heterogeneous high-backscatter acoustic facies (i.e., shown as white and light grey in Figs. 5, 7). In contrast, the canyon flanks and part of the hanging-wall blocks of the Marquês de Pombal Fault (MPF), Horseshoe Fault (HF) and São Vicente Fault (SVF) outside the canyon, are characterized by homogenous dark grey to black colour (i.e., low-acoustic backscatter). The uppermost head-scarps of the flanks in the upper and central sections are homogeneous showing high acoustic backscatter facies.

#### 4.1.1. The upper section of the SVC

The SVC head shows a semi-circular shape cut by three main tributary canyons that converge at 36º59'N (2000 m water depth) (Figs. 2, 3a). At this location, the flanks steepen and the V-shaped thalweg becomes narrower (3 km) (Figs. 3a, 4a). Along the canyon, the slope is roughly constant at 1.02° (Fig. 3a). In this section of the canyon the flanks are characterized by gradients ranging from 9.7° to 26.6°, and a rugged topography. The flanks present a network of rectilinear gullies (rectilinear erosive landforms usually generated in land that has been remobilized) topped by semi-circular-shape erosional scarps (from 1 to10 kms of diameter) and minor flow pathways (maximum slope lines that can channel flows) that are oriented subparallel to the maximum slope direction and their gradients reach up to 24° (Fig. 3a).

The slope diagram (Fig. 3a), the topographic profiles (Fig. 4a) and the acoustic backscatter signal (Fig. 5) indicate that the NW flank of the canyon is rougher than the SE flank. Although both flanks show a number of gullies and other minor flow pathways, these are more abundant on the NW flank. The gullies and minor flow pathways (13–14 km-length) appear more incised in the SE flank than in the NW one (Figs. 2, 3, 4d), as the rocky substrate outcrops on the lower part of the SE flank.

The scars are about 1–4 km-wide on both flanks. However, the SE flank shows a single generation of scars, whereas in the NW flank there is evidence for at least two generations of scars. The first generation is located on the uppermost part of the NW flank. The second generation is longer and develops at mid-elevation, disrupting the minor flow pathways from the first generation of scars. The scars on both flanks, but particularly those of the NW flank, are characterized by submarine landslide deposits (up to 5 km-long and 4 km-wide) (Fig. 5).

The most striking feature in the TOBI mosaic is the ENE-WSW trending high-backscatter band, corresponding to the canyon floor (Fig. 5). The acoustic character of the canyon floor is highly heterogeneous, and shows the following features: a) multiple channels along the axis; b) grooves > 1 km-long, pervasive lineaments parallel to the canyon axis carved by sediment transport, of low to medium backscatter areas (grey to light-grey colours); c) sediment accumulation, areas of very-high backscatter along the axis; d) stratification, low backscatter lineaments showing acoustic shadows on the lower part of the eastern flank; and e) old terrace, low-backscatter semi-circular area with gentle slope, located on the internal side of a meander attached to the canyon east flank (area in green in Fig. 5b).

#### 4.1.2. The central section of the SVC

Along this section, the canyon axis shows an average slope of 1.02°, whereas its flanks show slopes steeper than 26.6° on the upper part, which gradually decreases southward to 14° (Fig. 3). In the middle of this section, the canyon cross section progressively changes from V-shaped to U-shaped (Figs. 3b, 4b). On the upper part of this central section, the canyon is incised 1000 m on the west flank and 800 m on the eastern one (Fig. 4b). Moving south along the canyon, these values decrease to less than 500 m on the west flank and 300 m at the east one.

Three main tributary canyons converging towards the main canyon can be recognized on the eastern flank of the slope by medium-high backscatter values in the TOBI mosaic (Figs. 3b, 6). The canyon located further north is oriented E-W, whereas the other two canyons are oriented NE-SW and NW-SE respectively, being the three > 15 km-long. Both flanks of this section show evidence for stratification, middle to low backscatter lineaments along the canyon and large scars, although less abundant than in the upper section. Some of these scars have associated submarine landslide deposits in the TOBI mosaic. The largest submarine landslide deposit located in the north of this section, is

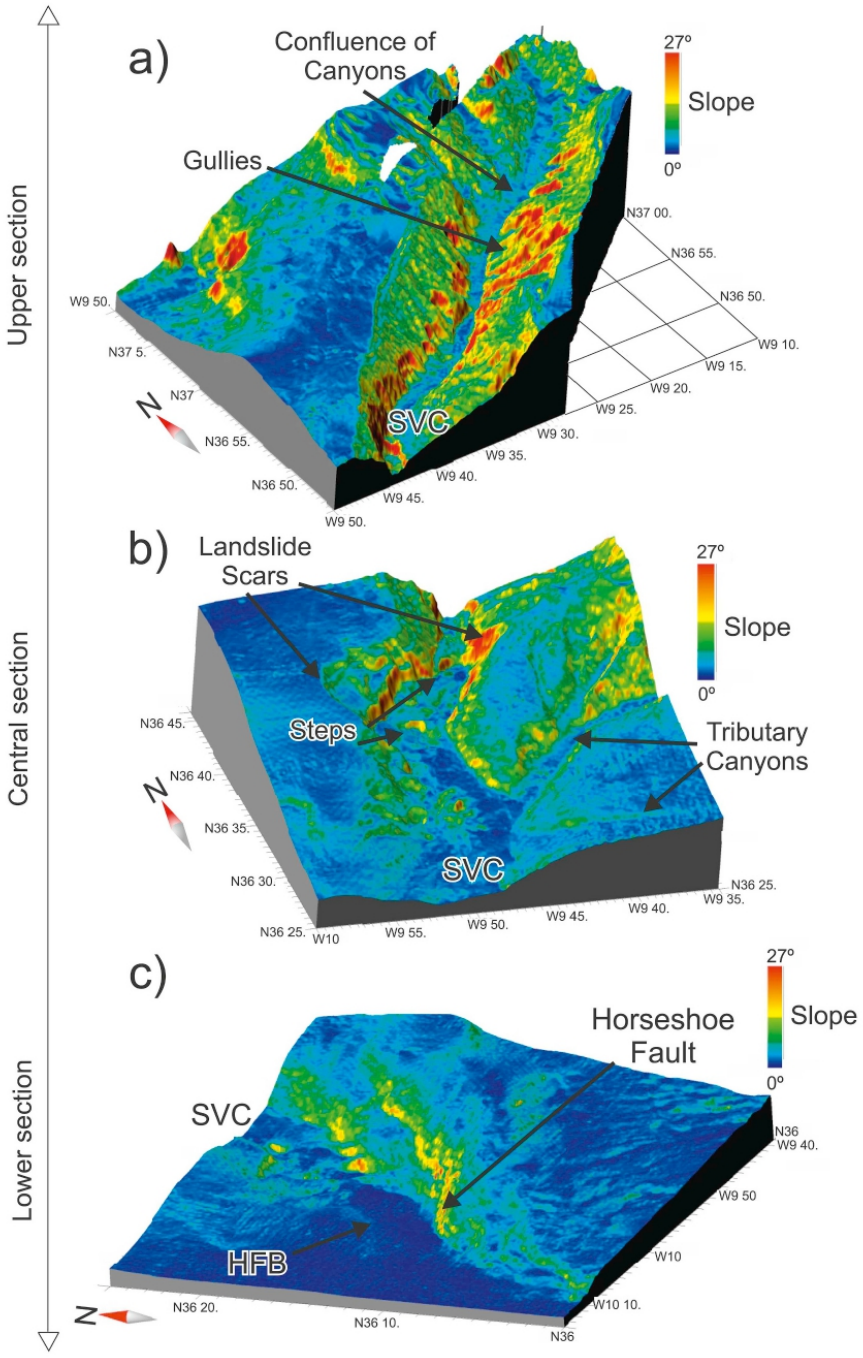


**Fig. 3.** Slope maps superimposed on the 3D bathymetry of the São Vicente Canyon (SVC). The slope is represented as percentages in dark blue for the lowest slope (0%) and red for the highest slope (≥ 50%). a), b) and c) correspond to the Upper, Central and Lower sections of the canyon. HFB: Horseshoe Fault Basin. (For interpretation of the references to colour in this figure legend, the reader is referred to the web version of this article.)

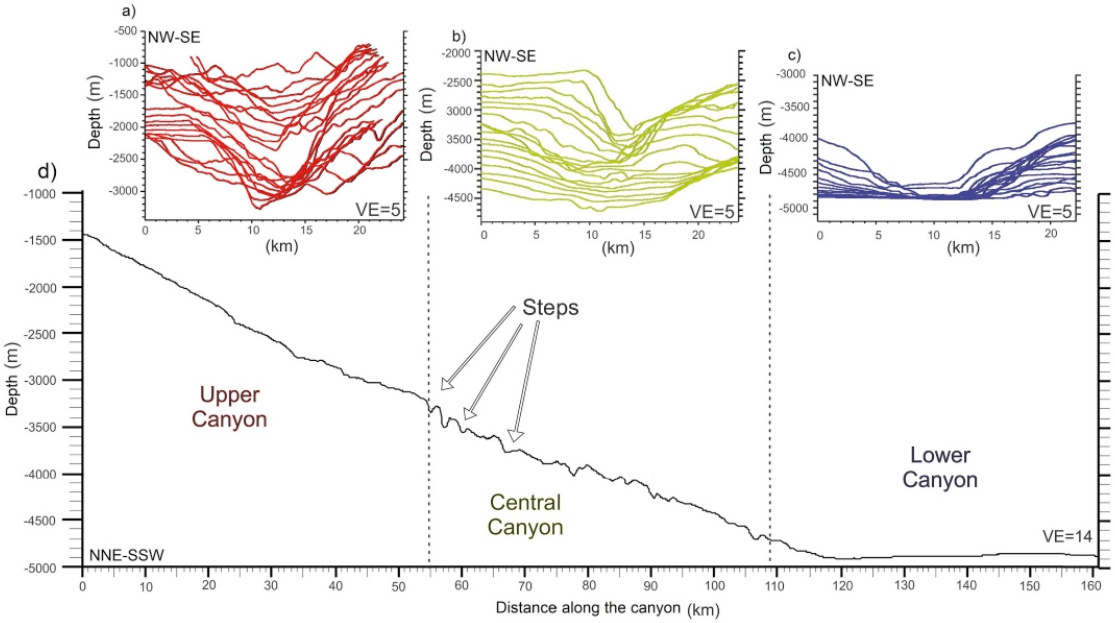


**Fig. 4.** Northwest-southeast oriented bathymetric profiles across the São Vicente Canyon at the Upper, Central, and Lower sections (a, b, and c, respectively); and d) Bathymetric longitudinal profile along the São Vicente Canyon axis.

associated to a semi-circular scar of ~ 3 km in diameter and is characterized by > 0.5 km-long high-backscatter patches. Long scars, such as those located on the central section of the NW flank are elongated (> 4 km-long) and characterized by low backscatter.

The canyon floor of this section shows several features similar to those described along the upper section of the canyon (Figs. 5, 6), including: a) a middle-grey backscatter signal that corresponds to the tributary canyons; b) grooves (erosive structures) that particularly stand out in areas of very high backscatter within the canyon floor (i.e., rock outcrops); c) high backscatter areas (light blue areas in the Fig. 6) along the canyon axis and canyon west flank that correspond to sediment accumulations; and d) scours (semi-circular negative relief perpendicular to the flow direction), which may attain a diameter of ~2 km and an elevation of 200 m (namely "steps" in the longitudinal profile on Figs. 3b, 4d and "scours" in Fig. 6).

#### 4.1.3. The lower section of the SVC

In this area, the SVC displays a wide U-shaped valley with a 7-km-wide flat canyon floor, low slope axis of 0.9° (Fig. 3c) and low angle flanks (mean slope less than 14°) in comparison to the upper and central canyon sections (Figs. 3, 4). The slope of the western flank flattens to the south towards the Horseshoe Abyssal Plain, whereas the slope of the eastern flank increases, reaching mean values of 16.7° and locally up to 26.6° (Fig. 3c). In this lower section, both the SW flank and the Horseshoe Abyssal Plain display a homogeneous low-backscatter facies and the SW flank presents a large number of canyon-parallel lineaments (stratification).

In the TOBI mosaic (Fig. 7), the canyon floor shows high-backscatter facies that progressively decrease towards the south (Martínez-Loriente et al., 2018). In this section, the canyon does not show a well-developed channel, rather it fades into the Horseshoe Abyssal Plain. The main features in this area include: a) high backscatter patches (probably outcrops), b) canyon-parallel, pervasive grooving (0.5–1 km-length) at the north-eastern part of the canyon floor, and c) low backscatter, 1 km-long comet-like, irregular scours along the main channel.

### 4.2. Seismo-stratigraphy of the São Vicente Canyon

Seismic horizons have been interpreted based on previous chronostratigraphic information (Fig. S2) (Hayes et al., 1972; Hernández-Molina et al., 2015; Martínez-Loriente et al., 2018, 2013). They have been correlated through the network of vintage and recent MCS profiles, and include the following units: Plio-Quaternary (Ia), Middle Miocene - Pliocene (Ib), Horseshoe gravitational unit (HGU-Ic), Upper Oligocene - Middle Miocene (Id), Upper Cretaceous - Early Eocene (II), Cretaceous (III), Lower Cretaceous (IV), Upper Jurassic (V) and basement (VI) (Fig. 8).

#### 4.2.1. Pliocene-Quaternary (Ia)

Unit Ia is characterized by middle frequency and middle amplitude continuous reflectors. This unit shows lateral continuity and is interrupted near the SVC, which completely erodes the Plio-Quaternary unit in the upper and central sections of the canyon axis (Fig. 8a, b). On the canyon flanks, gully incision and tributary canyons erode the uppermost part of this unit (Fig. 8a). The maximum thickness of unit Ia is 1.2 s TWTT (Two Way Travel Time) in the upper section of the canyon, which progressively decreases to 0.1 s TWTT towards the lower section. In the upper section of the SVC, mainly on the SE flank, contourite geometries can be distinguished (low-aspect, lenticular sedimentary bodies). Within this unit, we identify four discontinuities that may correspond to Late Quaternary (LQD), Mid Pleistocene (MPD), Early Quaternary (EQD) and Late Pliocene (LPD) discontinuities (Figs. S2, S3) described by Hernández-Molina et al. (2015, 2013) based on the IODP Site U1391 (Fig. 1).

#### 4.2.2. Middle Miocene-Pliocene (Ib)

Unit Ib is characterized by middle frequency, middle amplitude and continuous reflectors. The thickness of this unit is variable along and

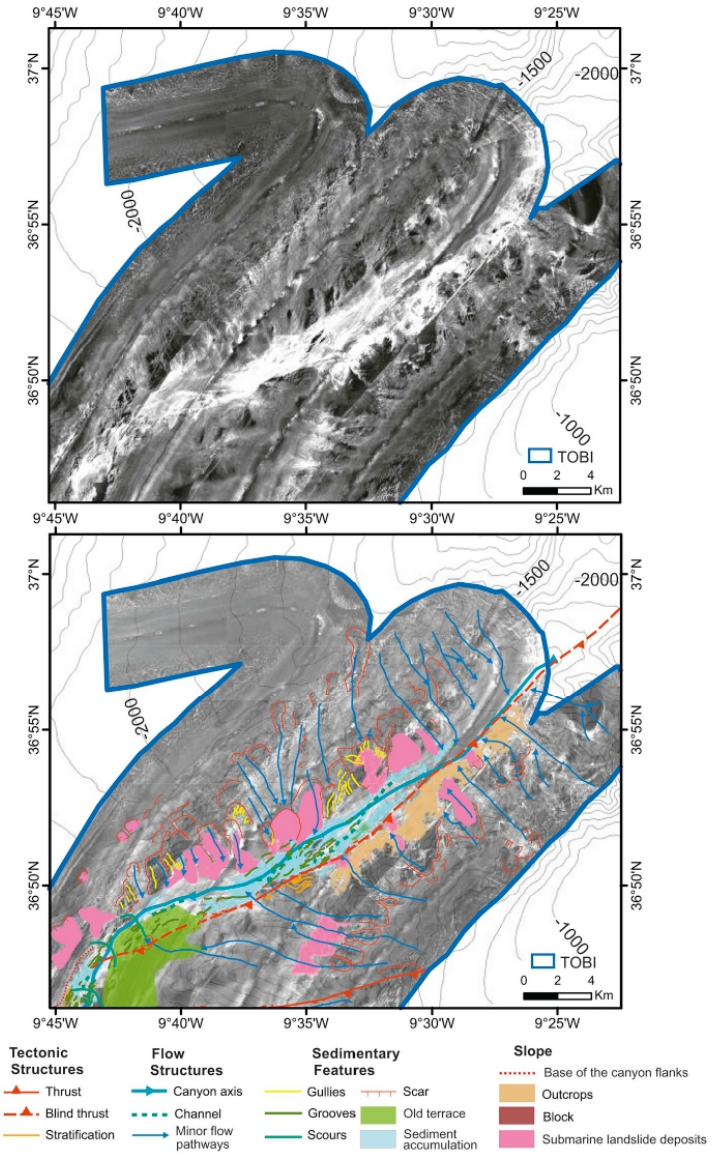


**Fig. 5.** a) TOBI sidescan sonar image of the Upper section of the São Vicente Canyon. b) Interpreted TOBI mosaic of the same area identifying flow structures, tectonic structures, slope structures, and sedimentary features.

across the SVC (Fig. 8), with a maximum thickness of 0.7 s TWTT below the canyon axis in the lower section, that progressively thins towards the flanks. This unit shows onlaps towards the Marquês de Pombal anticline fold and also towards the Horseshoe Fault hanging-wall block (Fig. 8d), so we can distinguish multiple progressive unconformities in the central and lower sections (Fig. 8b, Fig. S3). The incision of the canyon causes the total erosion of Unit Ib on the SVC axis of the upper section, whereas is only partially eroded in the central section. Both top and base of Unit Ib are unconformities.

#### *4.2.3. Horseshoe Gravitational Unit (HGU-Ic)*

The Horseshoe Gravitational Unit (HGU-Ic) is a wedge-shaped allochthonous body formed by stacked debris-flow that originates from the westward migration of the Gulf of Cadiz Imbricated Wedge (GCIW) and was emplaced during the Upper Miocene (Tortonian) (Gràcia et al., 2003b; Iribarren et al., 2007; Torelli et al., 1997) (Fig. 8c, d). The HGU is characterized by high-amplitude chaotic seismic facies with numerous diffractions and hyperbolic reflections. Only a few internal reflectors can be identified. The top and bottom are defined by

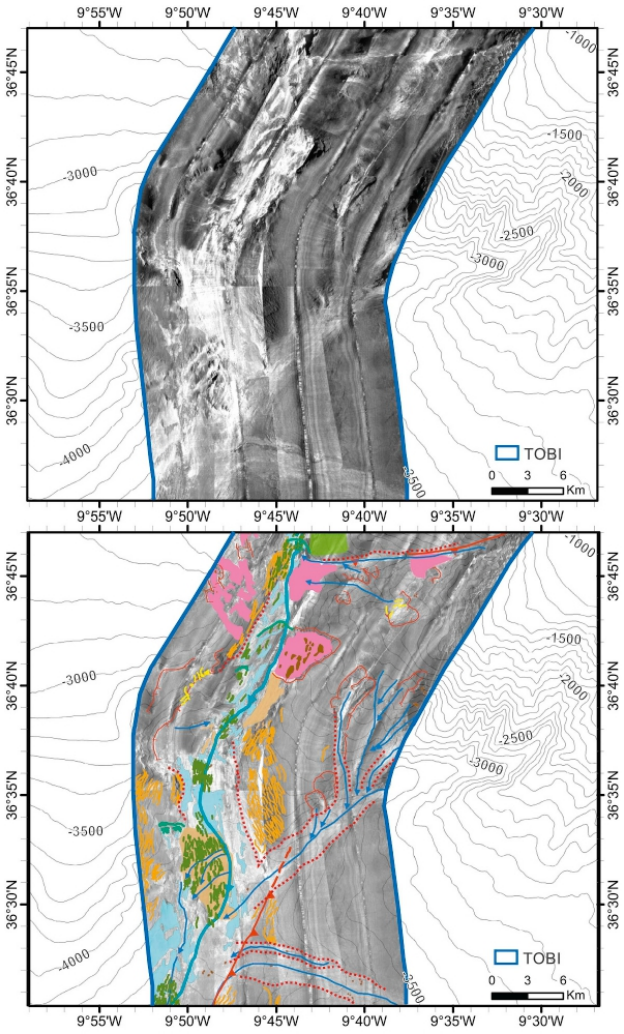


**Fig. 6.** a) TOBI sidescan sonar image of the Central section of São Vicente Canyon. b) Interpreted TOBI mosaic of the same area labelling the main features of the area. See legend in Fig. 5.

unconformities (Fig. 8c, d). The HGU fills the Horseshoe Valley and the Horseshoe Abyssal Plain, where it pinches out towards the edges of the valley (Martínez-Loriente et al., 2013). Therefore, the HGU can only be identified at the lower section of the canyon, where it reaches a maximum thickness of 1.3 s TWTT. In this section, the HGU partially or totally eroded the underlying Unit Id.

#### 4.2.4. Upper Oligocene-Middle Miocene (Id)

Unit Id is characterized by high-amplitude and low-frequency continuous reflectors. In the upper and central sections of the canyon, Unit Id lies directly below Unit Ib and reaches a maximum thickness of 0.5 s TWTT (Fig. 8a). In contrast, in the lower section of the SVC Unit Id lies below the HGU, which partially eroded its top. In this section, the top corresponds to an erosive surface generated by excavation and erosion during the emplacement of the HGU.

#### 4.2.5. Upper Cretaceous-Lower Eocene (II) and Cretaceous (III)

The seismic facies of Units II and III show similar characteristics (Fig. 8). Both have low-frequency and high-amplitude continuous reflectors. The contacts between both units and underlying unit (IV) are concordant. The top of Unit II is composed by a prominent unconformity marked by a high-amplitude reflector that corresponds to a regional sedimentary hiatus from Lower Eocene to Upper Oligocene (Hayes et al., 1972; Martínez-Loriente et al., 2013). Both units onlap the top of the basement (Fig. 8a, b). Their thickness is relatively uniform with a maximum value for Unit II of 0.45 s TWTT and 0.4 s TWTT for Unit III that reached the hanging wall of the Marquês de Pombal Fault. The minimum thickness for Unit II is 0.1 s TWTT below the HGU in the lower section of the canyon (Fig. 8c, d), and of 0.2 s TWTT for Unit III below the SVC at the central section (Fig. 8b). These units infill graben structures of the basement generated as a result of Mesozoic rifting (Martínez-Loriente et al., 2018).

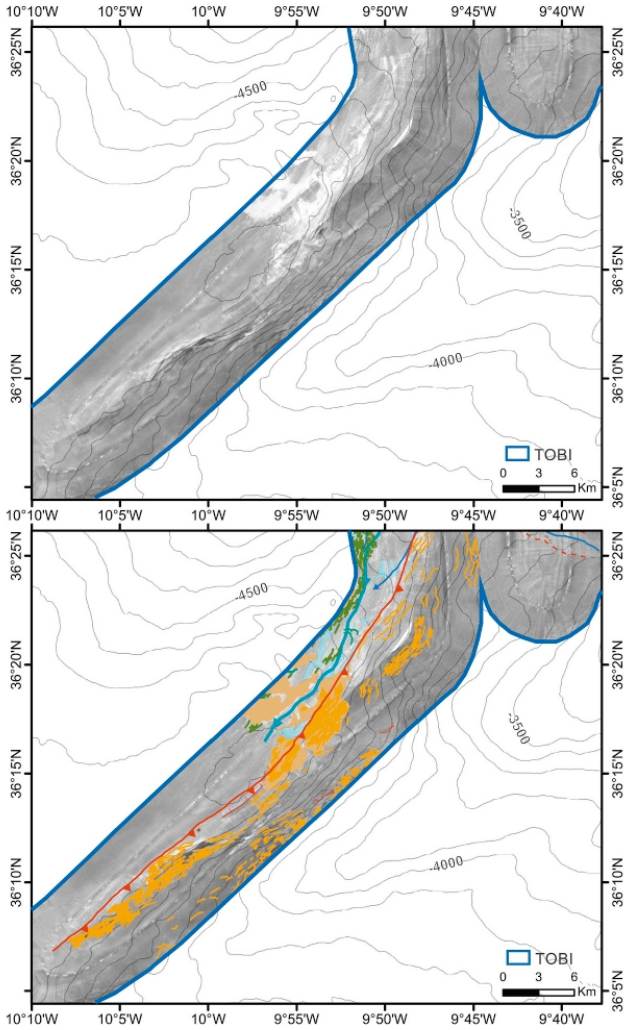


**Fig. 7.** a) TOBI sidescan sonar image of the Lower section of São Vicente Canyon. b) Interpreted TOBI mosaic of the same area identifying the main elements of this sector. See legend in Fig. 5 (modified from Martínez-Loriente et al., 2018).

#### 4.2.6. Lower Cretaceous (IV) and Upper Jurassic (V)

The Lower Cretaceous Unit IV and Upper Jurassic Unit V show semi-transparent and transparent seismic facies with low frequency and low amplitude reflectors (Fig. 8). The contact between these units is concordant and can be identified by parallel reflectors onlapping the top of basement highs (Fig. 8a, b, d). Unit IV reaches a maximum thickness of 0.5 s at the hanging wall of the Marquês de Pombal Fault. Unit V directly overlies the basement (i.e. discordant contact) and fills pre-existent half-graben depressions (Fig. 8d). Accordingly, the thickness of Unit V is highly variable, reaching a maximum value of 0.7 s (TWTT) at the lower section of the canyon (Fig. 8c, d).

#### 4.2.7. Basement (VI)

The Basement (Unit VI) is interpreted as composed of: a) thinned continental crust in the area of the SVC, Sagres Plateau and the hanging wall of the Marquês de Pombal Fault Block; b) oceanic crust at the southern half of the lower section of the SVC; and c) serpentinized exhumed mantle at the footwall of the Marquês de Pombal Block (Martínez-Loriente et al., 2014). This heterogeneous composition results in differences on the tectonic architecture of the basement. In the upper and central sections of the SVC, as well as in the MPF block, the MCS profiles reveal tilted basement blocks bounded by large, old normal faults (Fig. 8a, b, d). In contrast, at the Infante Don Henrique Basin the basement structure is completely different, and peridotite ridges have been identified (Fig. 8d).

### 4.3. Tectonic structures across and along the São Vicente Canyon

The strata across the SVC are folded by two anticlines bounding a synclinal (Fig. 8c, d), partially eroded by the incision of the SVC. The synclinal and anticlinal folds are more pronounced and well-defined in the lower section of the canyon, whereas their morphology is attenuated towards the upper section (Fig. 8).

The anticline located on the western flank of the canyon is

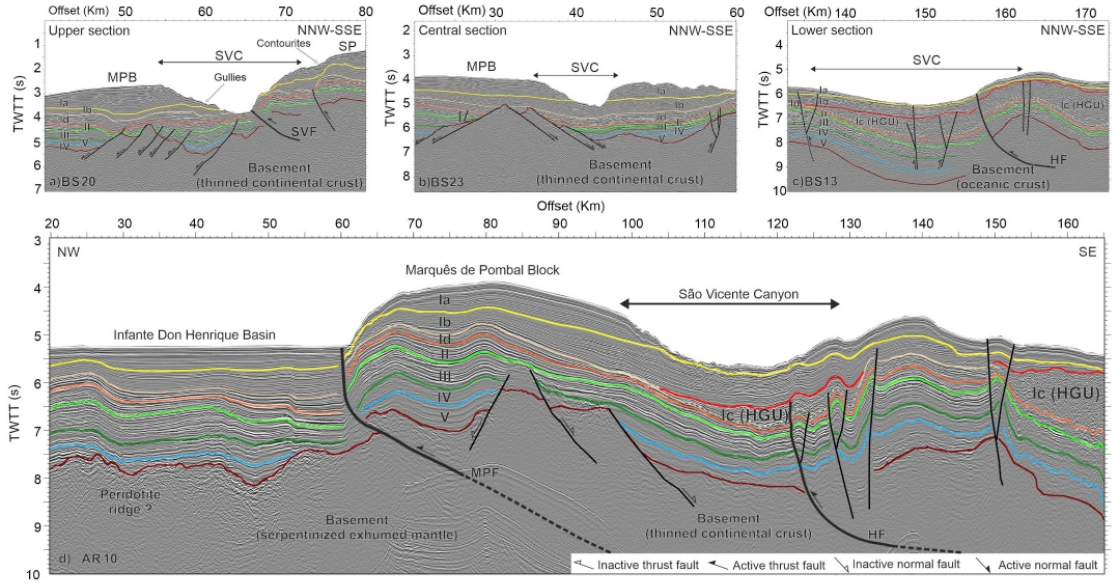


**Fig. 8.** Interpreted sections of 4 multichannel seismic profiles in time across the three sections of the São Vicente Canyon. See location in Fig. 2. Stratigraphy from Martínez-Loriente et al., 2013 (see Fig. S2). Ia = Plio-Quaternary; Ib = Middle Miocene - Pliocene; Ic-HGU = Horseshoe gravitational unit; Id = Upper Pligocene - Middle Miocene; II = Upper Cretaceous - Lower Eocene; III = Cretaceous; IV = Lower Cretaceous; V = Upper Jurassic; VI = Basement; HF: Horseshoe Fault; MPF: Marquês de Pombal Fault; MPB: Marquês de Pombal Block; IDHB: Infante Don Henrique Basin; SP: Sagres Plateau; SVF: São Vicente Fault; SVC: São Vicente Canyon; TWTT: Two-way travel time. VE (vertical exaggeration) = 2.

controlled by the west-verging monocline thrust Marquês de Pombal Fault (MPF) (Fig. 8d) and corresponds to the hanging wall of this active reverse fault (Gràcia et al., 2003a, 2010). The MCS profiles (Fig. 8d) show that the sedimentary sequence rises and tilts towards the SVC axis. The eastern flank of the upper section of the SVC seems to be controlled by the São Vicente Fault (SVF). The west-verging SVF is an NNE-SSO trending thrust that affects all the seismo-stratigraphic units until the seafloor (Ia) (Fig. 8a). Towards the SSW, the SVF becomes a blind-thrust along the canyon axis, which progressively attenuates and disappears (Fig. 8b).

The lower section of the SVC (Fig. 8c, d) is dominated by the presence of the west-verging Horseshoe Fault (HF), which is also oriented parallel to the canyon axis trending NE-SW. In this section, the south-eastern flank of the canyon corresponds to the hanging-wall block of the HF, whereas the canyon floor corresponds to the footwall block. Minor folds are observed in the hanging-wall block near the HF as a fault-propagation-fold (Fig. 8c, d). Flexure at the frontal part of the HF thrust generates accommodation space in the footwall, which is progressively filled by sediments transported downstream in the canyon. The HF can be easily identified in the MCS profiles (Fig. 8c, d), as well as in the TOBI mosaic (Fig. 7). In the lower section of the canyon, the HF cuts and displaces the entire seismo-stratigraphic sequence (Fig. 8c) (Martínez-Loriente et al., 2018). However, in the lower part of the SVC central section, the HF only cuts the sedimentary cover until the HGU (Tortonian age) and folds the uppermost units, acting as an active blind-thrust (Fig. 8d). In the middle part of the central section of the SVC, the HF cannot be identified neither in the MCS profiles nor in the TOBI mosaic (Figs. 7, 8b) (Martínez-Loriente et al., 2018).

## 5. Discussion

### 5.1. Sedimentary processes along the São Vicente Canyon

The highly variable TOBI backscatter evidences Present activity of the canyon. If the identified sedimentary morphologies were relict structures, a thin layer of hemipelagic sediment would homogenize the backscatter while preserving the morphology. Therefore, the TOBI mosaics show that the SVC is a significantly active pathway for sediment transport. Combining the TOBI mosaics and the morphological characteristics of the canyon reveals a predominance of submarine mass-wasting and erosive processes can be envisaged (Figs. 3, 5, 6, 7). These processes are widespread in the canyon flanks characterized by homogenous light-grey colours to low backscatter with dark grey acoustic facies. The retrogressive erosion is prevalent in the upper section of the canyon, with steep slopes favouring the incision of gullies along the canyon walls. These gullies often are topped by circular head-scarps where retrogressive erosion occurs. These landslide scars are often coalescent and form a sinuous array of unstable features following the main canyon path. Erosion is practically non-existent in the lower section of the SVC (Fig. 3).

Of relevance is the NW flank of the SVC, characterized by a large number of submarine landslides deposits and two generations of landslide scars (Figs. 5, 6). The lower landslide scars postdate the upper landslide scars, in contrast with the overall retrogressive and erosional setting of the canyon. The lower landslide scars (i.e., the second generation) suggest a recent rearrangement of the NW flank. Such rearrangement may result from changes in the base level of the SVC, which tries to come closer to a new equilibrium. In support of this hypothesis most of the deposits associated with the upper landslide scars cannot be recognized as they have been likely eroded. Conversely, the deposits associated with the lower landslide scars can be identified and have not yet been remobilized. The NW flank is located at the

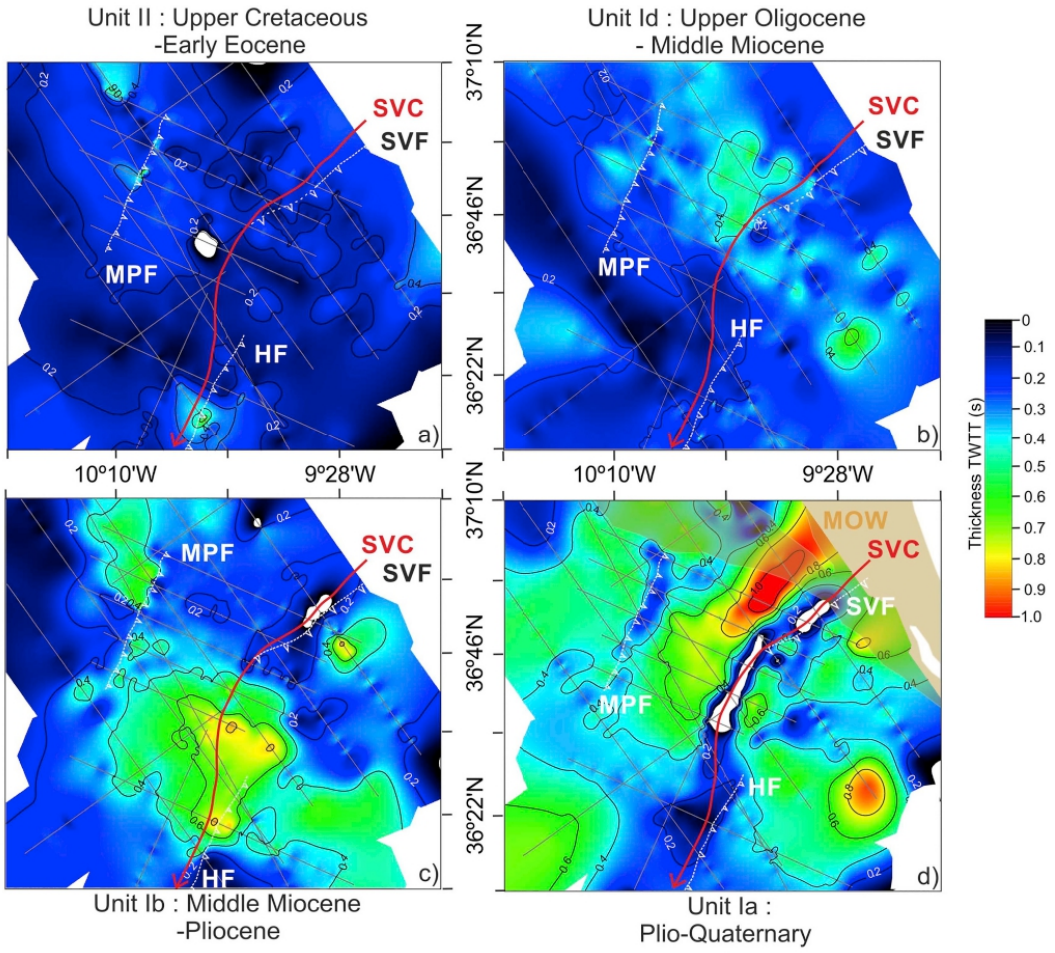


**Fig. 9.** Isochore maps that illustrate the variation in thicknesses of the different stratigraphic units over time: a) Upper Cretaceous – Early Eocene (Unit II); b) Upper Oligocene – Middle Miocene (Unit Id); c) Middle Miocene – Pliocene (Unit Ib); and d) Plio-Quaternary (Unit Ia). HF: Horseshoe Fault; MOW: Mediterranean Outflow Water; MPF: Marquês de Pombal Fault; SVC: São Vicente Canyon; SVF: São Vicente Fault; TWTT: Two-way travel time, in seconds.

hanging wall of the Marquês de Pombal Fault (Fig. 8a), that acts as a barrier and hinders the progression of the axial canyon incision. Mass-wasting processes seem to be particularly active in the NW flank of the canyon, although the length of the flank is shorter and slope gradients are gentler than those in the SE flank. One of the most seismically active areas of the SW Iberian margin is the SVC (Fig. 1), where the so-called São Vicente earthquake cluster nucleates (Geissler et al., 2010; Grevemeyer et al., 2017; Stich et al., 2005). Some authors suggest that the MPF is the tectonic source of the SVC cluster, which nucleates along the canyon at 20–40 km depth (Geissler et al., 2010; Grevemeyer et al., 2017; Martínez-Loriente et al., 2018; Silva et al., 2017). Consequently, seismicity is of special relevance to the occurrence of submarine mass movements in the SVC. The slope of the canyon axis significantly decreases in the lower section of the canyon, where submarine mass movements and turbidity currents also reduce velocity and erosive capacity (Fig. 3). In this section, erosive structures are almost non-existent and the canyon shows a broad U-shaped profile, also suggesting that there is a change in the dynamics of the canyon and a reduction in erosive capacity.

The high backscatter values in the TOBI mosaic along the canyon thalweg indicate the sediment accumulation of gravel and sand (coarse-grained deposits) (Blondel and Murton, 1997), which provide evidence of the high-energy sediment transport activity along the canyon floor (Figs. 5-7). The accumulation of gravels and sands is scarce and discontinuous and can probably attest to the presence of lag-deposits from sediment gravity flows periodically funnelled along the canyon. The medium-high backscatter values of the three main tributary canyons may suggest current activity. If the tributary canyons were inactive, they would be covered by a thin layer of hemipelagic sediments and their backscatter would be rather low.

Finally, we also recognize erosive bedforms (i.e., grooves and scours) along the central section of canyon thalweg. Scours form semi-circular steps (stepped scours or cyclic steps, which can be erosive, depositional or mixed) perpendicular to the canyon axis (Fig. 4d) partially filled by coarse-grained sediment, as observed in the high-backscatter areas in the TOBI sidescan sonar mosaic (Fig. 6). Stepped scours (upstream-migrating bed-forms), have been interpreted to result from supercritical turbidity currents (Covault et al., 2017) (Figs. 5,6).

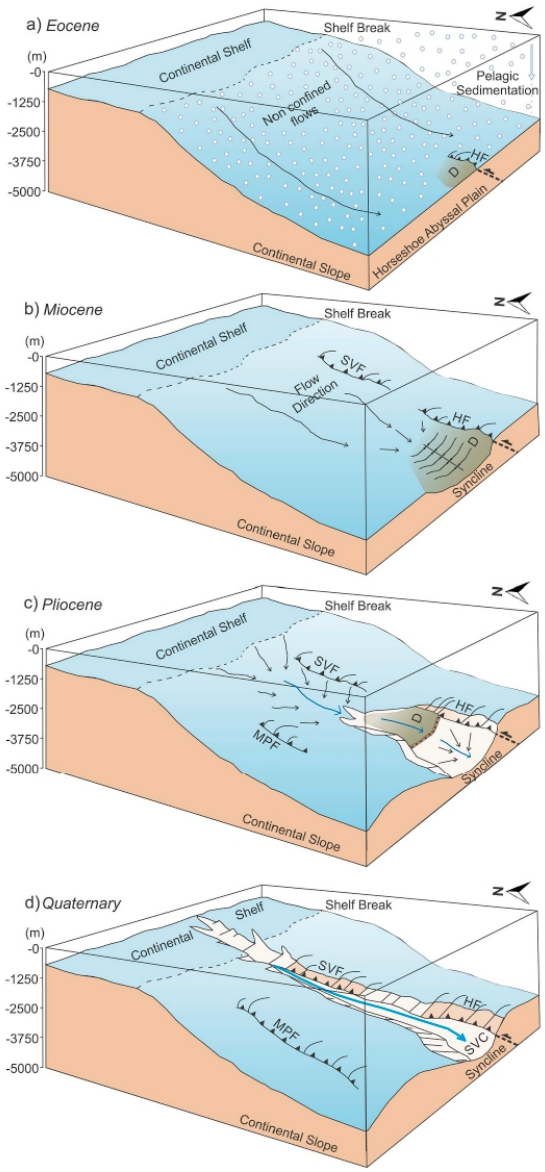


**Fig. 10.** Formation and evolution model of the São Vicente area from the Upper Cretaceous to the Plio-Quaternary, including the São Vicente Fault (SVF), the Horseshoe Fault (HF) and Marquês de Pombal Fault (MPF). D: Depocentre; M.M.-P.: Middle Miocene-Pliocene; P-Q: Plio-Quaternary; U.C.-E.E.: Upper Cretaceous-Early Eocene; U.O.-M.M.: Upper Oligocene-Middle Miocene; SVC: São Vicente Canyon.

Migration and growth of these cyclic steps takes place when the higher-density basal layer of the hyperpycnal flows interacts with the seabed triggering a hydraulic jump downstream of the base of the step (Hughes Clarke, 2016). Masson et al. (2004) suggested that this type of scour formation requires minimum current speeds between 1.0 and 2.5 m/s.

### 5.2. Sediment sources of the São Vicente Canyon

One of the main characteristics of the SVC is that there is no significant fluvial system onshore that could feed sediments to the canyon head (Fig. 1). The main rivers close to the SVC are the Sado River (located 140 km to the north) and the Guadiana River (located 170 km to the east). Both rivers have an adjacent submarine canyon system that trap and distribute their sediments. Therefore, the direct contribution of sediments from the continent to the SVC is relatively low. Thus, the question is, being the canyon disconnected from the onshore main drainages, which are the mechanisms that provide sediments to maintain it active and growing?

Isochore maps show that sediments were mainly accumulated in the central and lower sections of the SVC since the Middle Miocene (Fig. 9c), apparently related to the uplift of the HF hanging wall block and the generation of depositional space in the subsiding footwall block. It seems plausible to consider that the main sediment sources along the SVC are the materials provided by the erosion of canyon flanks through gullies, tributary canyons and submarine mass movements that generate submarine landslide deposits, which are abundant in the upper and central sections of the canyon. Arzola et al. (2008) also proposed similar processes of flanks dismantling for other canyon systems along the Portuguese coast, such as the Nazaré and Setúbal canyons. The total volume eroded by the SVC is 1219 $km^3$ (Fig. S1).

Nevertheless, there could also be secondary sediment sources feeding both the main SVC and their three tributary canyons. The submarine canyons developed along the Portuguese coast incise the continental shelf (the SVC at the shelf break) and work as traps for sediment transported by bottom currents along the shelf and upper-slope. This is particularly significant in the oceanographic framework of the Gulf of Cadiz, with a complex environment dominated by the Mediterranean Outflow Water (MOW) (Fig. 1). Along its pathway from the Straits of Gibraltar towards the West Iberian Margin, the MOW decreases in velocity, temperature and salinity (Hernández-Molina et al., 2015). This favours the sedimentary deposits (i.e., contourites) at the head and flanks of the canyons such as the SVC (Hernández-Molina et al., 2003) (Figs. 1, 8a, b). The contourites on the upper section of the SVC are deposited in water depths up to 1400 m. At this depth, the sediment transported by the MOW is sand-rich (Hernández-Molina et al., 2015). The TOBI images show coarse-grained sedimentary deposits in the upper and central sections of the SVC that could have been partially deposited by the MOW. Thus, the SVC acts as a sediment trap. The coarser-grained and denser sediment of the MOW is trapped at the head of the canyon, which could eventually evolve into hyperpycnal flows that would down into the canyon and could form steps at the canyon bed. The relatively high seismicity of the area (Fig. 1) triggers periodic failure of sediments accumulated at the edge or within the canyon, which are subsequently transported along the SVC to the Horseshoe Abyssal Plain, as previously described.

### 5.3. Timing of formation and evolution of the São Vicente Canyon and neighboring areas

The SVC is located in a syncline between two reverse fault-controlled anticlines related to the SVF, HF and MPF thrust faults, which suggests a strong structural control on its development (Figs. 1, 8, 9, 10). Their trend (NE-SW) is compatible with the present-day African-Eurasian plate convergence (NW-SE) (Martínez-Loriente et al., 2013, 2018). Our multidisciplinary dataset gives us some insights about the timing of formation and evolution of these reverse faults and neighboring areas.

The Upper Cretaceous to Early Eocene period (Unit II) was a tectonic quiescence phase in the SVC area and the low-rate sedimentation along the SVC area was rather constant, except in the current mouth of the canyon (Figs. 8, 9a, 10a). Here, the isochore map reveals a small depocentre that may be related to the uplift of the HF or to the filling of

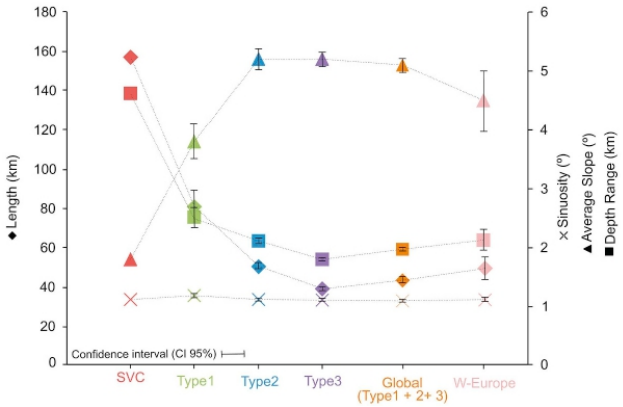


**Fig. 11.** Plot of the mean statistics of the submarine canyons in order of length (km), slope (°), sinuosity (°), and depth range (km). Classification of canyons according to Harris and Whiteway (2011). Morphometric parameter averages (see in supplementary material Table S1) of the submarine canyons in Western Europe and global average of canyon types from Harris and Whiteway (2011).

an old rifting structure.

In the lower section of the SVC, the sedimentary record of Unit Id (Upper Oligocene to Middle Miocene) is eroded in the Tortonian due to the emplacement of the allochthonous HGU (Unit Ic). Therefore, the related isochore map (Fig. 9b) does not provide relevant information about the tectonic activity and sedimentation in this zone of the study area. However, the AR10 seismic profile (Fig. 8d) shows that the HGU is not present in the hanging wall of the HF at the intersection between the central and lower sections of the SVC. This evidence suggests that the lowermost section of the canyon is controlled by the HF and their activity started just before emplacement of the HGU. Thus, this is the oldest section of the SVC of Middle or Late Miocene age (Fig. 10b). The isochore map of Unit Id shows a small depocentre at the footwall of the current MPF and in the southern segment of the SVF (i.e., the upper section of the SVC) (Fig. 9a, b). According to the seismic data, these would correspond to the filling of pre-existing rifting structures (Fig. 8a, b).

MCS profiles show that within Unit Ib (Middle Miocene to Pliocene) there are various unconformities, onlapping reflectors, and thin chaotic units at the central and lower sections of the SVC (Fig. 8). In addition, the isochore map (Fig. 9c) reveals a clear depocenter located in the same area. These evidences suggest a contemporaneous sedimentation and progressive folding and uplift of the HF and MPF, which also generated accommodation space. This corresponds to the central segment of the canyon of Pliocene age (Fig. 10c). Unit Ib is locally eroded in the upper section (Fig. 9c), but there is no clear evidence that this unit has been eroded by the SVC at that time (Fig. 8a). The isochore map also shows a depocenter in the footwall of the northern segment of the MPF (Fig. 9c). The growth-strata configuration identified in the seismic data (Fig. 8d) suggests synchronous sedimentation with the uplift of the fault. This tectonic activity would have generated accommodation space in the footwall block that may been filled by sediments coming from the surrounding morpho-structural highs (e.g., Marquês de Pombal and Gorringe Bank).

The Quaternary deposits are slightly folded both in the hanging-wall block of the MPF and in the upper and lower sections of the canyon. This evidence suggests that the Pliocene folding is currently active (Fig. 8a, c, d). This is not the case in the central section of the canyon, where seismic data shows the unfolded Plio-Quaternary Unit (Unit Ia) and no major tectonic structure can be identified (i.e., the lateral prolongation of the SVF or the HF) (Fig. 8b). The isochore map shows Unit Ia fully eroded along the canyon axis in the upper and central sections, and a highly diminished thickness in the lower section (Fig. 9d). The fairly rectilinear profile along the canyon axis (Fig. 4d) suggests that it has not yet reached its long-term equilibrium profile (e.g. Amblas et al., 2011). Evidence for significant erosion is observed in the upper and central sections of the canyon (Fig. S1) most likely indicate that the canyon is trying to reach equilibrium. This observation provides further evidence about the relatively young age of the SVC. The isochore map shows three depocentres, one of them associated with the footwall block of the MPF (Fig. 9d). This observation may indicate that during this period the maximum activity or development of the MPF took place. Therefore, the incision of the SVC may have started at the Pliocene being maximum at the same time that the maximum development of the MPF (Fig. 10d). Accordingly, this may suggest that the MPF plays an important role in the depositional dynamics of the canyon. All these observations indicate that the canyon likely developed in the late Quaternary from the central section, where erosion is largest and retrograded via mass movements on its flanks to its upper section and outer continental shelf (Fig. 10c, d). The incision along the SVC axis makes the flanks unstable, which enhances retrogression and widening of the canyon (Baztan et al., 2005). Mass movements triggered by turbidity currents would have favoured the incision of the canyon and its progression towards the Horseshoe Abyssal Plain.

The isochore map of Unit Ia also shows two depocentres located on both sides of the SVC, at the Marquês de Pombal Block and the Sagres Plateau (Fig. 9d). These depocentres result from sediment contribution by geostrophic currents. This favours the sediment deposition on the head and flanks of the SVC (Hernández-Molina et al., 2003), which acts as a sediment trap for the MOW sediments.

Summarizing, the growth of the three faults (MPF, HF and SVF) has conditioned the entire existence of the canyon, from its orientation to its incision and width. The initial uplift of the HF generated a depocentre, which became an embryonic canyon with the subsequent evolution of the SVF and the MPF (Fig. 10). These structures are currently active, and their uplift conditions the incision and activity of the canyon (permanently in disequilibrium).

### 5.4. Local and global relevance of the São Vicente Canyon

Comparing the morphometric parameters (i.e., length, head depth, mouth depth, width, and S index and incision) of the SVC with the average in the global inventory of large submarine canyons (Harris and Whiteway, 2011) it turns out that, the SVC parameters are significantly larger (at least in terms of length and depth range) (Table S1, Fig. 11). A similar relationship can be found when comparing with the average of those parameters in submarine canyons of Western Europe (Table 1, Table S1, Fig. 11). According to the submarine canyon classification by Harris and Whiteway (2011), three different submarine canyons typologies can be distinguished: a) **Type 1**, shelf-incision with connection to a major river system; b) **Type 2**, shelf-incision without a connection to a major river system; and c) **Type 3**, blind canyons. The

**Table 1**
Morphometric parameters of the canyons in the west and southwest Iberian margin.

| Canyon | *Straight length (km)* | *Depth at the head (mbsl)* | *Mouth depth (mbsl)* | *Width (km)* | *S Index* | *Tectonic control* | *Max. Incision (m)* | *River connection* | *Information Source* | *Canyon type*[a] |
|---|---|---|---|---|---|---|---|---|---|---|
| Cascais | 61.5 | 175 | 4600 | 4.2–28 | 1.44 | Unknown | 1800 | No | Lastras et al., 2009 | Type 2 |
| Setúbal-Lisbon | 145.8 | 150 | 4800 | 7.8–40 | 1.2 | Lower Tagus fault zone and Grândola fault | 2200 | Tagus and Sado rivers | Lastras et al., 2009 | Type 1 |
| São Vicente | 157 | 200 | 4900 | 1.5–3.5 | 1.12 | MPF, SVF, HF | 2000 | No | This study | Type 2 |
| Sagres | 41.7 | 1300 | 4200 | 1.26–2.89 | 1.06 | Unknown | 300 | No | This study | Type 3 |
| Lagos | 56 | 760 | 3600 | 2.46–12.4 | 1.16 | Unknown | 1500 | No | (Marchès et al., 2007) & this study | Type 3 |
| Portimão | 134.7 | 100 | 4000 | 2.3–5.7 | 1.125 | Portimão Fault | 1600 | Unknow | (Marchès et al., 2007) & this study | Type 2 |
| Faro | 48 | 1300 | 2700 | 4.9–11.8 | 1.16 | Unknown | 700 | No | This study | Type 3 |

[a] According to the classification by Harris and Whiteway (2011).

SVC belongs to the Type 2 by definition, even though its morphometric parameters are closer to Type 1 (Fig. 11).

Table 1 shows the comparison between the morphometric parameters of different canyon systems of the West Iberian margin (i.e., Cascais, Setúbal and Lisbon canyons) with the canyons systems of the Southwest Iberian margin (i.e., São Vicente, Sagres, Lagos, Portimão and Faro canyons). The São Vicente, Setubal-Lisbon and Portimão canyons, the three being controlled by faults, have the longest straight length. Together with the Cascais Canyon, they have also the greatest depth range. In addition, their depth at the head is shallower and they all incise the continental shelf. In contrast, the Sagres and Faro canyons are shorter, less incised and their head is located on the slope. Among the compared canyons, the only canyon with a clear river connection, the Setubal-Lisboa Canyon belonging to type 1, is the wider canyon. However, the São Vicente and Portimão canyons also show morphometric parameters such as length, incision, head and mouth depth typical of submarine canyons fed by a large river, despite they have no clear connection to a fluvial system. Finally, when observing the trace of the MOW (Fig. 1), it is evident that the heads of submarine canyons of south and west Iberia coincide with the trace of the MOW, which may interact with other submarine canyons as it does with the SVC. The SVC has an important sedimentary contribution from the MOW current; therefore it could be classified as a new type of canyon, which is strongly influenced by bottom currents and also by active tectonic structures (faults). Despite some authors classify the Gulf of Cadiz as a passive margin (Harris and Whiteway, 2011), it has been demonstrated that it is an active margin that hosts the Present-day Eurasia-Africa plate boundary (e.g., Bartolome et al., 2012; Gràcia et al., 2003a, 2010; Martínez-Loriente et al., 2013, 2014, 2018; Sallarès et al., 2013; Terrinha et al., 2003; Zitellini et al., 2004, 2009).

Some of the world's largest submarine canyons that do not have a river connection are associated to active margins with subduction zones. In this context, the base level of these canyons is constantly changing. Therefore, the submarine canyons are not in equilibrium and are constantly incising and growing due to retrogressive erosion.

Some examples are the submarine canyons located on the Pacific plate subduction margin, such as the Bering canyon, 400 km-long (Harris and Whiteway, 2011); the Navarin canyon, 250 km-long (Carlson and Karl, 1988); the Zhemchug canyon, 196 km-long (Carlson and Karl, 1988); the Pribilof canyon, 145 km-long (Normark and Carlson, 2003); and the Monterey canyon, 111 km-long (Carlson and Karl, 1988); as well as submarine canyons associated to the subduction system of the Caribbean plate, such as the Great Bahama canyon, 175 km-long (Andrews et al., 1970). Thus, the SVC is a clear example of how a large submarine canyon may develop within an active and slow seismogenic margin.

## 6. Conclusions

A multiscale view of the SVC region using multibeam echo-sounder data, 2D multi-channel seismic profiles and sidescan sonar data allows us to carry out an accurate morpho-sedimentary and tectonic study of the processes occurring in the area. The SVC is the largest submarine canyon of the SW Iberian margin. The upper and the central sections of the SVC are deeply entrenched in the continental slope. The upper section shows a V-shape that progressively changes to a U-shape in the central section, whereas the lower section connects to the Horseshoe Abyssal Plain.

On the basis of its physiography and morphology, at present the SVC is not in equilibrium and shows erosive dynamics. In the upper and central sections of the canyon, retrogressive erosion and dismantling of the flanks predominate, indicating that the canyon evolved from bottom-up. Submarine landslide deposits and landslide scars are the main processes that allowed bottom-up evolution of the canyon. The material resulting from the dismantling of the flanks and the MOW sedimentary deposits are the main sediment source, as the canyon is not

fed by rivers. The MOW contributes material through two different processes: a) it deposits contourites on the flanks and head of the upper section of the canyon that periodically fail into the canyon; and b) the coarser-grained and denser sediment of the MOW might be trapped at the head of the canyon and could generates hyperpycnal flows. Erosion by these hyperpycnal and other sediment gravity flows forms steps at the canyon bed on its way to the mouth of the canyon. Most sediment gravity flows likely originate from destabilization of canyon flanks and contourites deposits by frequent seismic events in this area.

The origin of the canyon is fully tectonic. Initial uplift of the HF developed a synclinal fold at the base of the continental slope during an NNW-SSE trending compressive stage (late Miocene). This topographic relief, latter enhanced by evolution of the SVF and MPF, favoured the development of an embryonic canyon. During the Pliocene, the embryonic canyon developed towards the continental shelf by means of retrogressive mass-failures induced by the tectonic uplift and steep slope gradient. Full canyon development took place coinciding with the period of maximum activity of the MPF in the Quaternary. Therefore, the SVC is a diachronous and segmented canyon. Currently, the SVC shows a strong structural control and is conditioned by three main active faults (i.e., the MPF, the SVF and the HF).

## Declaration of Competing Interest

The authors declare that they have no known competing financial interests or personal relationships that could have appeared to influence the work reported in this paper.

## Acknowledgements

The authors are grateful for funding from MINECO through projects HITS (AC 2011), IMPULS (REN 2003-05996/MAR), ESF-EUROCORES "EuroMargins" (REN2002-11234-E MAR), SWIM (AE MCYT-DGI 2006), INSIGHT (CTM2015-70155-R), a MINECO FPI-2016 grant (ref. BES-2016-078877) to Cristina S. Serra (ICM-CSIC), and a MICINN "Juan de la Cierva-2017" grant (ref. 33838) to Sara Martínez-Loriente (ICM-CSIC). We thank Doug Masson, Russell Wynn, Chris Flewellen and the TOBI Team from the National Oceanography Centre (NOC, UK) for their assistance throughout the "HITS-2011" (PI E. Gràcia) data collection on board the RV "Hesperides". We are also indebted to Tim Le Bas (NOC, UK) for assisting O.G., J.G. and E.G. in processing the TOBI sidescan sonar data. MCS data were acquired during the RIFANO, BIGSETS and VOLTAIRE cruise (PI N. Zitellini). Grup Recerca Consolidat: 2017 SGR 1662.

## Appendix A. Supplementary data

Supplementary data to this article can be found online at https://doi.org/10.1016/j.margeo.2020.106219.

## References

Amblas, D., Gerber, T.P., Canals, M., Pratson, L.F., Urgeles, R., Lastras, G., Calafat, A.M., 2011. Transient erosion in the Valencia Trough turbidite systems, NW Mediterranean Basin. Geomorphology 130, 173–184. https://doi.org/10.1016/j.geomorph.2011.03.013.

Amblas, D., Gerber, T.P., De Mol, B., Urgeles, R., Garcia-Castellanos, D., Canals, M., Pratson, L.F., Robb, N., Canning, J., 2012. Survival of a submarine canyon during long-term outbuilding of a continental margin. Geology 40, 543–546. https://doi.org/10.1130/G33178.1.

Andrews, J., Shepard, F., Hurley, R., 1970. Great Bahama Canyon. Geol. Soc. Am. Bull. 81, 1061–1078.

Arzola, R.G., Wynn, R.B., Lastras, G., Masson, D.G., Weaver, P.P.E., 2008. Sedimentary features and processes in the Nazaré and Setúbal submarine canyons, west Iberian margin. Mar. Geol. 250, 64–88. https://doi.org/10.1016/j.margeo.2007.12.006.

Baptista, M.A., Miranda, J.M., 2009. Revision of the portuguese catalog of tsunamis. Nat. Hazards Earth Syst. Sci. 9, 25–42. https://doi.org/10.5194/nhess-9-25-2009.

Barkan, R., ten Brink, U.S., Lin, J., 2009. Far field tsunami simulations of the 1755 Lisbon earthquake: Implications for tsunami hazard to the U.S. East Coast and the Caribbean. Mar. Geol. 264, 109–122. https://doi.org/10.1016/j.margeo.2008.10.010.

Bartolome, R., Gràcia, E., Stich, D., Martínez-Loriente, S., Klaeschen, D., de Lis Mancilla, F., Lo Iacono, C., Dañobeitia, J.J., Zitellini, N., 2012. Evidence for active strike-slip faulting along the Eurasia-Africa convergence zone: Implications for seismic hazard in the southwest Iberian margin. Geology 40, 495–498. https://doi.org/10.1130/G33107.1.

Baztan, J., Berné, S., Olivet, J.L., Rabineau, M., Aslanian, D., Gaudin, M., Réhault, J.P., Canals, M., 2005. Axial incision: the key to understand submarine canyon evolution (in the western Gulf of Lion). Mar. Pet. Geol. 22, 805–826. https://doi.org/10.1016/j.marpetgeo.2005.03.011.

Blondel, P., Murton, B., 1997. Handbook of the Seafloor Sonar Imagery. West Sussex, England.

Buforn, E., Sanz de Galdeano, C., Udías, A., 1995. Seismotectonics of the Ibero-Maghrebian region. Tectonophysics 248, 247–261. https://doi.org/10.1016/0040-1951(94)00276-F.

Canals, M., Puig, P., De Madron, X.D., Heussner, S., Palanques, A., Fabres, J., 2006. Flushing submarine canyons. Nature 444, 354–357. https://doi.org/10.1038/nature05271.

Carlson, P.R., Karl, H.A., 1988. Development of large submarine canyons in the Bering Sea, indicated by morphologic, seismic, and sedimentologic characteristics. Bull. Geol. Soc. Am. 100, 1594–1615. https://doi.org/10.1130/0016-7606(1988)100<1594:DOLSCI>2.3.CO;2.

Covault, J.A., Kostic, S., Paull, C.K., Sylvester, Z., Fildani, A., 2017. Cyclic steps and related supercritical bedforms: Building blocks of deep-water depositional systems, western North America. Mar. Geol. 393, 4–20. https://doi.org/10.1016/j.margeo.2016.12.009.

Flewellen, C., Millard, N., Rouse, I., 1993. TOBI, a vehicle for deep ocean survey. Electron. Commun. Eng. J. 5, 85–93. https://doi.org/10.1049/ecej:19930015.

Geissler, W.H., Matias, L., Stich, D., Carrilho, F., Jokat, W., Monna, S., Ibenbrahim, A., Mancilla, F., Gutscher, M.A., Sallars, V., Zitellini, N., 2010. Focal mechanisms for sub-crustal earthquakes in the Gulf of Cadiz from a dense OBS deployment. Geophys. Res. Lett. 37, 7–12. https://doi.org/10.1029/2010GL044289.

Gràcia, E., Dañobeitia, J., Vergés, J., Bartolomé, R., Córdoba, D., 2003a. Crustal architecture and tectonic evolution of the Gulf of Cadiz (SW Iberian margin) at the convergence of the Eurasian and African plates. Tectonics 22https://doi.org/10.1029/2001tc901045. n/a-n/a.

Gràcia, E., Dañobeitia, J.J., Vergés, J., Team, P., 2003b. Mapping active faults offshore Portugal (36°N-38°N): Implications for seismic hazard assessment in the SW Iberian margin. Geology 31, 83–86. https://doi.org/10.1130/0091-7613(2003)031<0083.

Gràcia, E., Pallàs, R., Soto, J.I., Comas, M., Moreno, X., Masana, E., Santanach, P., Diez, S., García, M., Dañobeitia, J., Bartolomé, R., Farrán, M., Gómez, M., Alpiste, M.J.R., Lastras, G., Wilmott, V., Perea, H., Blondel, P., Gómez, O., Bullock, L., Jacobs, C., Rouse, I., White, D., Whittle, S., Terrinha, P., Gafeira, J., Roque, C., 2006. Active faulting offshore SE Spain (Alboran Sea): Implications for earthquake hazard assessment in the Southern Iberian margin. Earth Planet. Sci. Lett. 241, 734–749. https://doi.org/10.1016/j.epsl.2005.11.009.

Gràcia, E., Vizcaino, A., Escutia, C., Asioli, A., Rodés, Á., Pallàs, R., Garcia-Orellana, J., Lebreiro, S., Goldfinger, C., 2010. Holocene earthquake record offshore Portugal (SW Iberia): testing turbidite paleoseismology in a slow-convergence margin. Quat. Sci. Rev. 29, 1156–1172. https://doi.org/10.1016/j.quascirev.2010.01.010.

Grevemeyer, I., Lange, D., Villinger, H., Custódio, S., Matias, L., 2017. Seismotectonics of the Horseshoe Abyssal Plain and Gorringe Bank, eastern Atlantic Ocean: Constraints from ocean bottom seismometer data. J. Geophys. Res. Solid Earth 122, 63–78. https://doi.org/10.1002/2016JB013586.

Harris, P.T., Whiteway, T., 2011. Global distribution of large submarine canyons: Geomorphic differences between active and passive continental margins. Mar. Geol. 285, 69–86. https://doi.org/10.1016/j.margeo.2011.05.008.

Hayes, E., Pimm, A.C., Beckmann, P., Benson, W., Berger, W., Roth, P., Supko, P., 1972. Initial Reports of the Deep Sea Drilling Project. Government Printing Office, Washington D.C.

Hayward, N., Watts, A.B., Westbrook, J.K., Collier, J.S., 1999. A seismic reflection and GLORIA study of compressional deformation in the Gorringe Bank region, eastern North Atlantic. Geophys. J. Int. 138 (3), 831–850. https://doi.org/10.1046/j.1365-246x.1999.00912.x.

Hernández-Molina, J., Llave, E., Somoza, L., Fernández-Puga, M.C., Maestro, A., León, R., Medialdea, T., Barnolas, A., García, M., Díaz del Río, V., Fernández-Salas, L.M., Vázquez, J.T., Lobo, F., Alveirinho Dias, J.M., Rodero, J., Gardner, J., 2003. Looking for clues to paleoceanographic imprints: a diagnosis of the Gulf of Cadiz contourite depositional systems. Geology 31, 19–22. https://doi.org/10.1130/0091-7613(2003)031<0019:LFCTPI>2.0.CO;2.

Hernández-Molina, J., Stow, D., Alvarez-Zarikian, C., Expedition IODP 339 Scientists, 2013. IODP Expedition 339 in the Gulf of Cadiz and off West Iberia: decoding the environmental significance of the Mediterranean outflow water and its global influence. Sci. Drill. 16, 1–11. https://doi.org/10.5194/sd-16-1-2013.

Hernández-Molina, F.J., Sierro, F.J., Llave, E., Roque, C., Stow, D.A.V., Williams, T., Lofi, J., Van der Schee, M., Arnáiz, A., Ledesma, S., Rosales, C., Rodríguez-Tovar, F.J., Pardo-Igúzquiza, E., Brackenridge, R.E., 2015. Evolution of the gulf of Cadiz margin and Southwest Portugal contourite depositional system: Tectonic, sedimentary and paleoceanographic implications from IODP expedition 339. Mar. Geol. 377, 7–39. https://doi.org/10.1016/j.margeo.2015.09.013.

Hughes Clarke, J., 2016. First wide-angle view of channelized turbidity currents links migrating cyclic steps to flow characteristics. Nat. Commun. 7, 11896. https://doi.org/10.1038/ncomms11896.

Iribarren, L., Vergés, J., Camurri, F., Fullea, J., Fernàndez, M., 2007. The structure of the Atlantic-Mediterranean transition zone from the Alboran Sea to the Horseshoe Abyssal Plain (Iberia-Africa plate boundary). Mar. Geol. 243, 97–119. https://doi.

org/10.1016/j.margeo.2007.05.011.
Lastras, G., Arzola, R.G., Masson, D.G., Wynn, R.B., Huvenne, V.A.I., Hühnerbach, V., Canals, M., 2009. Geomorphology and sedimentary features in the Central Portuguese submarine canyons, Western Iberian margin. Geomorphology 103, 310–329. https://doi.org/10.1016/j.geomorph.2008.06.013.
Leopold, L., Wolman, M., 1957. River channel patterns - braided, meandring and stright. U. S. Geol. Surv. Prof. Pap. 4, 39–85 (282-B).
Lewis, K.B., Barnes, P.M., 1999. Kaikoura Canyon, New Zealand: active conduit from near-shore sediment zones to trench-axis channel. Mar. Geol. 162, 39–69. https://doi.org/10.1016/S0025-3227(99)00075-4.
Lozano, L., Cantavella, J.J., Barco, J., 2019. A new 3-D P-wave velocity model for the Gulf of Cadiz and adjacent areas derived from controlled-source seismic data: application to non-linear probabilistic relocation of moderate earthquakes. Geophys. J. Int. 1–57. https://doi.org/10.1093/gji/ggz562. ggz562.
Marchès, E., Mulder, T., Cremer, M., Bonnel, C., Hanquiez, V., Gonthier, E., Lecroart, P., 2007. Contourite drift construction influenced by capture of Mediterranean Outflow Water deep-sea current by the Portimão submarine canyon (Gulf of Cadiz, South Portugal). Mar. Geol. 242, 247–260. https://doi.org/10.1016/j.margeo.2007.03.013.
Martínez-Loriente, S., Gràcia, E., Bartolome, R., Sallarès, V., Connors, C., Perea, H., Lo Iacono, C., Klaeschen, D., Terrinha, P., Dañobeitia, J.J., Zitellini, N., 2013. Active deformation in old oceanic lithosphere and significance for earthquake hazard: Seismic imaging of the Coral Patch Ridge area and neighboring abyssal plains (SW Iberian margin). Geochem. Geophys. Geosyst. 14, 2206–2231. https://doi.org/10.1002/ggge.20173.
Martínez-Loriente, S., Sallarès, V., Gràcia, E., Bartolome, R., Dañobeitia, J.J., Zitellini, N., 2014. Seismic and gravity constraints on the nature of the basement in the Africa-Eurasia plate boundary: New insights for the geodynamic evolution of the SW Iberian margin. J. Geophys. Res. Solid Earth 119, 127–149. https://doi.org/10.1002/2013JB010476.
Martínez-Loriente, S., Gràcia, E., Bartolome, R., Perea, H., Klaeschen, D., Dañobeitia, J.J., Zitellini, N., Wynn, R.B., Masson, D.G., 2018. Morphostructure, tectono-sedimentary evolution and seismic potential of the Horseshoe Fault, SW Iberian Margin. Basin Res. 30, 382–400. https://doi.org/10.1111/bre.12225.
Masson, D.G., Wynn, R.B., Bett, B., 2004. Sedimentary environment of the Faroe-Shetland and Faroe Bank Channels, north-East Atlantic, and the use of bedforms as indicators of bottom current velocity in the deep ocean. Sedimentology 51, 1207–1241. https://doi.org/10.1111/j.1365-3091.2004.00668.x.
Mastbergen, D.R., Van Den Berg, J.H., 2003. Breaching in fine sands and the generation of sustained turbidity currents in submarine canyons. Sedimentology 50, 625–637. https://doi.org/10.1046/j.1365-3091.2003.00554.x.
Mauffrey, M.A., Urgeles, R., Berné, S., Canning, J., 2017. Development of submarine canyons after the Mid-Pleistocene transition on the Ebro margin, NW Mediterranean: the role of fluvial connections. Quat. Sci. Rev. 158, 77–93. https://doi.org/10.1016/j.quascirev.2017.01.006.
Medialdea, T., Vegas, R., Somoza, L., Vázquez, J.T., Maldonado, A., Díaz-del-Río, V., Maestro, A., Córdoba, D., Fernández-Puga, M.C., 2004. Structure and evolution of the "Olistostrome" complex of the Gibraltar Arc in the Gulf of Cadiz (eastern Central Atlantic): evidence from two long seismic cross-sections. Mar. Geol. 209 (1–4), 173–198. https://doi.org/10.1016/j.margeo.2004.05.029.
Micallef, A., Mountjoy, J.J., Barnes, P.M., Canals, M., Lastras, G., 2014. Geomorphic response of submarine canyons to tectonic activity: Insights from the Cook Strait canyon system, New Zealand. Geosphere 10, 905–929. https://doi.org/10.1130/GES01040.1.
Mulder, T., Lecroart, P., Hanquiez, V., Marches, E., Gonthier, E., Guedes, J.C., Thiébot, E., Jaaidi, B., Kenyon, N., Voisset, M., Perez, C., Sayago, M., Fuchey, Y., Bujan, S., 2006. The western part of the Gulf of Cadiz: Contour currents and turbidity currents interactions. Geo-Marine Lett. 26, 31–41. https://doi.org/10.1007/s00367-005-0013-z.
Neres, M., Carafa, M.M.C., Fernandes, R.M.S., Matias, L., Duarte, J.C., Barba, S., Terrinha, P., 2016. Lithospheric deformation in the Africa-Iberia plate boundary: improved neotectonic modeling testing a basal-driven Alboran plate. J. Geophys. Res. Solid Earth 121, 6566–6596. https://doi.org/10.1002/2016JB013012.
Nocquet, J.M., Calais, E., 2004. Geodetic measurements of crustal deformation in the Western Mediterranean and Europe. Pure Appl. Geophys. 161, 661–681. https://doi.org/10.1007/s00024-003-2468-z.
Normark, W.R., Carlson, P.R., 2003. Giant submarine canyons: is size any clue to their importance in the rock record? Spec. Pap. Geol. Soc. Am. 370, 175–190. https://doi.org/10.1130/0-8137-2370-1.175.
Oliveira, A., Santos, A.I., Rodrigues, A., Vitorino, J., 2007. Sedimentary particle distribution and dynamics on the Nazaré canyon system and adjacent shelf (Portugal). Mar. Geol. 246, 105–122. https://doi.org/10.1016/j.margeo.2007.04.017.
Palanques, A., Durrieu de Madron, X., Puig, P., Fabres, J., Guillén, J., Calafat, A., Canals, M., Heussner, S., Bonnin, J., 2006. Suspended sediment fluxes and transport processes in the Gulf of Lions submarine canyons. The role of storms and dense water cascading. Mar. Geol. 234, 43–61. https://doi.org/10.1016/j.margeo.2006.09.002.
Pereira, R., Alves, T.M., 2013. Crustal deformation and submarine canyon incision in a Meso-Cenozoic first-order transfer zone (SW Iberia, North Atlantic Ocean). Tectonophysics 601, 148–162. https://doi.org/10.1016/j.tecto.2013.05.007.
Pierdomenico, M., Casalbore, D., Chiocci, F.L., 2019. Massive benthic litter funnelled to deep sea by flash-flood generated hyperpycnal flows. Sci. Rep. 9, 5330. https://doi.org/10.1038/s41598-019-41816-8.
Piper, D.J.W., Normark, William, R., 2009. Processes that initiate turbidity currents and their influence on turbidites: a marine geology perspective title. J. Sediment. Res. 79, 347–362.
Puig, P., Palanques, A., Martín, J., 2014. Contemporary sediment-transport processes in submarine canyons. Annu. Rev. Mar. Sci. 6, 53–77. https://doi.org/10.1146/annurev-marine-010213-135037.
Sallarès, V., Gailler, A., Gutscher, M.A., Graindorge, D., Bartolomé, R., Gràcia, E., Díaz, J., Dañobeitia, J.J., Zitellini, N., 2011. Seismic evidence for the presence of Jurassic oceanic crust in the central Gulf of Cadiz (SW Iberian margin). Earth Planet. Sci. Lett. 311, 112–123. https://doi.org/10.1016/j.epsl.2011.09.003.
Sallarès, V., Martínez-Loriente, S., Prada, M., Gràcia, E., Ranero, C., Gutscher, M.A., Bartolome, R., Gailler, A., Dañobeitia, J.J., Zitellini, N., 2013. Seismic evidence of exhumed mantle rock basement at the Gorringe Bank and the adjacent Horseshoe and Tagus abyssal plains (SW Iberia). Earth Planet. Sci. Lett. 365, 120–131. https://doi.org/10.1016/j.epsl.2013.01.021.
Schettino, A., Turco, E., 2009. Breakup of Pangaea and plate kinematics of the Central Atlantic and Atlas regions. Geophys. J. Int. 178, 1078–1097. https://doi.org/10.1111/j.1365-246X.2009.04186.x.
Shepard, F.P., 1981. Submarine canyons_multiple causes and long-time persistence. Pet. Geol. Bull. 65, 1062–1077.
Silva, S., Terrinha, P., Matias, L., Duarte, J.C., Roque, C., Ranero, C.R., Geissler, W.H., Zitellini, N., 2017. Micro-seismicity in the Gulf of Cadiz: is there a link between micro-seismicity, high magnitude earthquakes and active faults? Tectonophysics 717, 226–241. https://doi.org/10.1016/j.tecto.2017.07.026.
Stich, D., de Mancilla, F.L., Morales, J., 2005. Crust-mantle coupling in the Gulf of Cadiz (SW-Iberia). Geophys. Res. Lett. 32, 1–4. https://doi.org/10.1029/2005GL023098.
Stich, D., Serepelloni, E., Mancilla, F., Morales, J., 2006. Kinematics of the Iberia–Maghreb plate contact from seismic moment tensors and GPS observations. Tectonophysics 426, 295–317. https://doi.org/10.1016/j.tecto.2006.08.004.
Terrinha, P., Pinheiro, L.M., Henriet, J.P., Matias, L., Ivanov, M.K., Monteiro, J.H., Akhmetzhanov, A., Volkonskaya, A., Cunha, T., Shaskin, P., Rovere, M., 2003. Tsunamigenic-seismogenic structures, neotectonics, sedimentary processes and slope instability on the southwest Portuguese margin. Mar. Geol. 195, 55–73. https://doi.org/10.1016/S0025-3227(02)00682-5.
Terrinha, P., Matias, L., Vicente, J., Duarte, J., Luís, J., Pinheiro, L., Lourenço, N., Diez, S., Rosas, F., Magalhães, V., Valadares, V., Zitellini, N., Roque, C., Víctor, L.M., 2009. Morphotectonics and strain partitioning at the Iberia-Africa plate boundary from multibeam and seismic reflection data. Mar. Geol. 267, 156–174. https://doi.org/10.1016/j.margeo.2009.09.012.
Terrinha, P., Duarte, H., Brito, P., Noiva, J., Ribeiro, C., Omira, R., Baptista, M.A., Miranda, M., Magalhães, V., Roque, C., 2019. The Tagus River delta landslide, off Lisbon, Portugal. Implications for Marine geo-hazards. Mar. Geol. 416, 105983. https://doi.org/10.1016/j.margeo.2019.105983.
Torelli, L., Sartori, R., Zitellini, N., 1997. The giant chaotic body in the Atlantic Ocean off Gibraltar: New results from a deep seismic reflection survey. Mar. Pet. Geol. 14, 125–134. https://doi.org/10.1016/S0264-8172(96)00060-8.
Tortella, D., Torne, M., Perez-Estaun, A., 1997. Geodynamic evolution of the eastern segment of the Azores–Gibraltar Zone: The Gorringe Bank and Gulf of Cadiz region. Mar. Geophys. Res. 19, 211–230.
Vizcaino, A., Gràcia, E., Pallàs, R., Terrinha, P., Diez, S., Dañobeitia, J.D.M., 2005. Active tectonic and sedimentary processes along the Sao Vicente Canyon (SW Iberian Margin): High-Resolution Imaging. Eur. Geosci. Union 7, 7707.
Zitellini, N., Chierici, F., Sartori, R., Torelli, L., 1999. The tectonic source of the 1755 Lisbon earthquake and tsunami. Ann. Geofis. 42, 49–55. https://doi.org/10.4401/ag-3699.
Zitellini, N., Mendes, L.A., Cordoba, D., Danobeitia, J., Nicolich, R., Pellis, G., Ribeiro, A., Sartori, R., Torelli, L., Bartolome, R., Bortoluzzi, G., Calafato, A., Carrilho, F., Casoni, L., Chierici, E., Corela, C., Correggiari, A., Delia Vedova, B., Gracia, E., Jornet, P., Landuzzi, M., Ligi, M., Magagnoli, A., Marozzi, G., Matias, L., Penitenti, D., Rodriguez, P., Rovere, M., Terrinha, P., Vigliotti, L., Ruiz, A.Z., 2001. Source of 1755 Lisbon earthquake and tsunami investigated. Eos (Washington. DC). 82, 285–291. https://doi.org/10.1029/EO082i026p00285-01.
Zitellini, N., Rovere, M., Terrinha, P., Chierici, F., Matias, L., Victor, L.M., Corela, C., Ribeiro, A., Cordoba, D., Danobeitia, J.J., Grácia, E., Bartolomé, R., Nicolich, R., Pellis, G., Della Vedova, B., Sartori, R., Torelli, L., Correggiari, A., Vigliotii, L., 2004. Neogene through quaternary tectonic reactivation of SW Iberian passive margin. Pure Appl. Geophys. 161, 565–587. https://doi.org/10.1007/s00024-003-2463-4.
Zitellini, N., Gràcia, E., Matias, L., Terrinha, P., Abreu, M.A., De Alteriis, G., Henriet, J.P., Dañobeitia, J.J., Masson, D.G., Mulder, T., Ramella, R., Somoza, L., Diez, S., 2009. The quest for the Africa-Eurasia plate boundary west of the Strait of Gibraltar. Earth Planet. Sci. Lett. 280, 13–50. https://doi.org/10.1016/j.epsl.2008.12.005.

# Annex 3: Uninterpreted MCS profiles

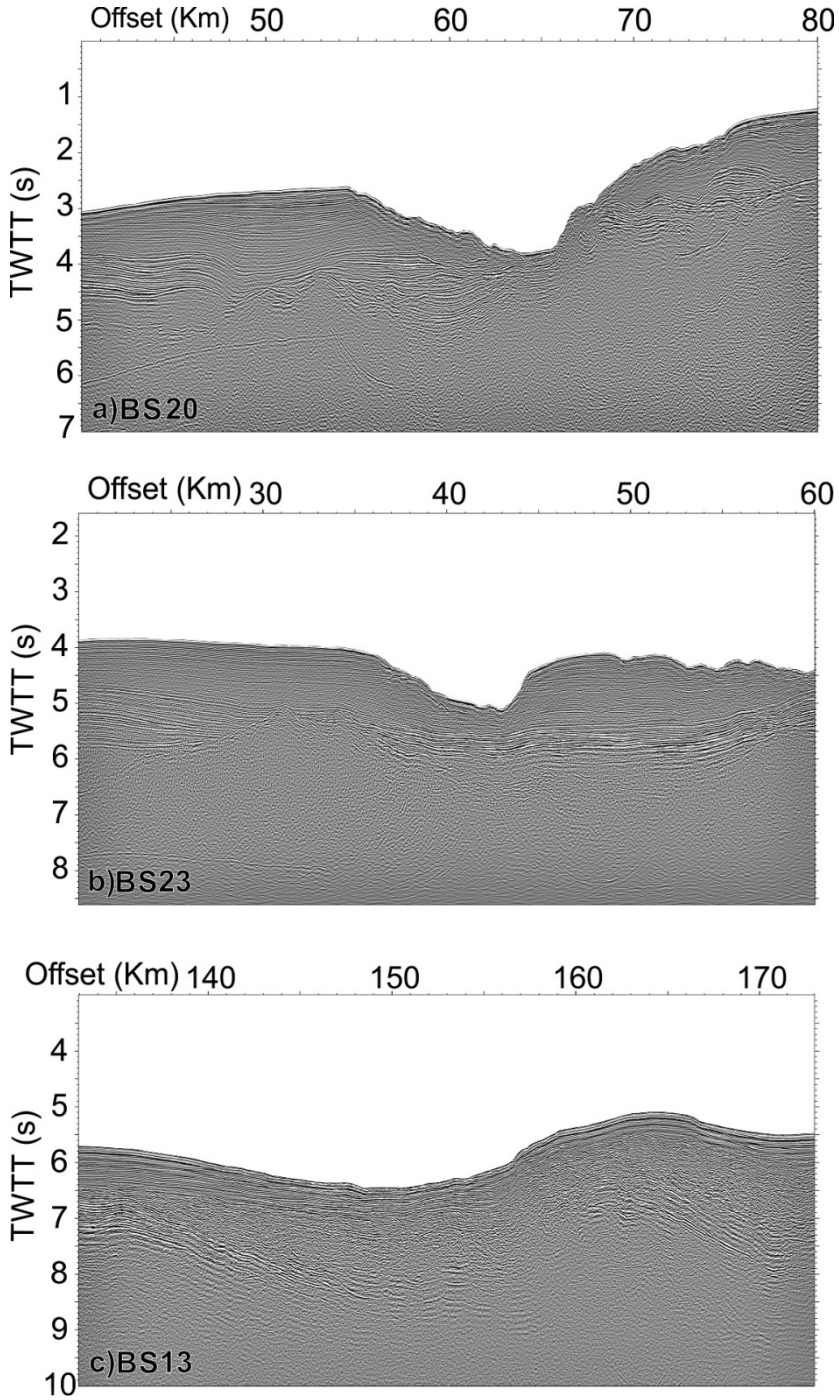

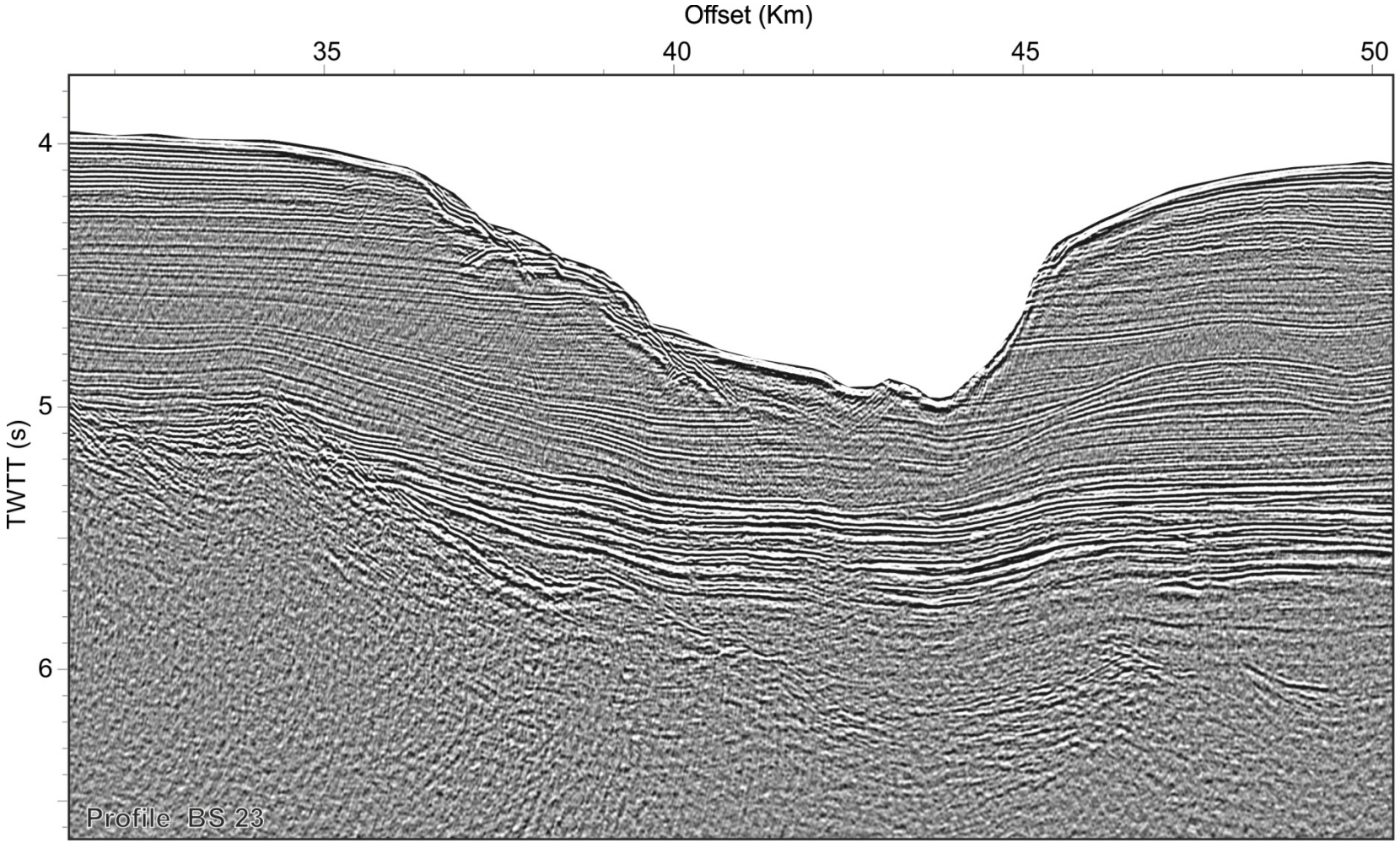
Offset (Km)
35
40
45
50
4
5
6
TWTT (s)
Profile BS 23

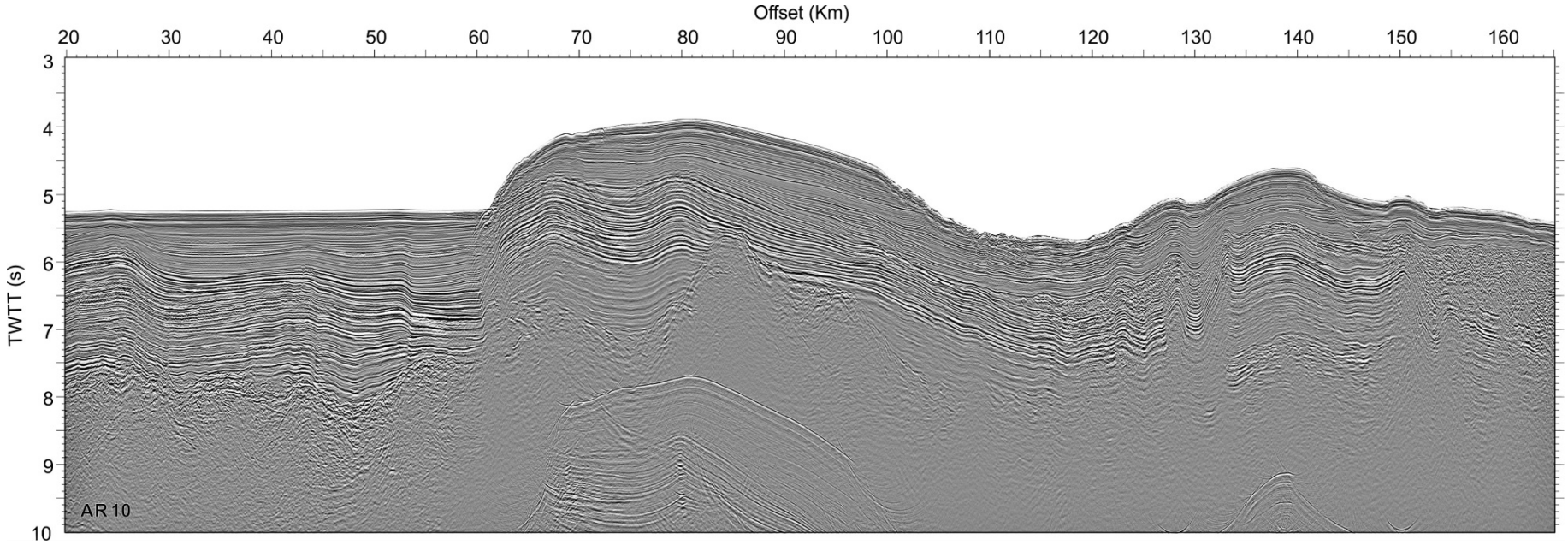
Offset (Km)
20
30
40
50
60
70
80
90
100
110
120
130
140
150
160
TWTT (s)
3
4
5
6
7
8
9
10
AR 10

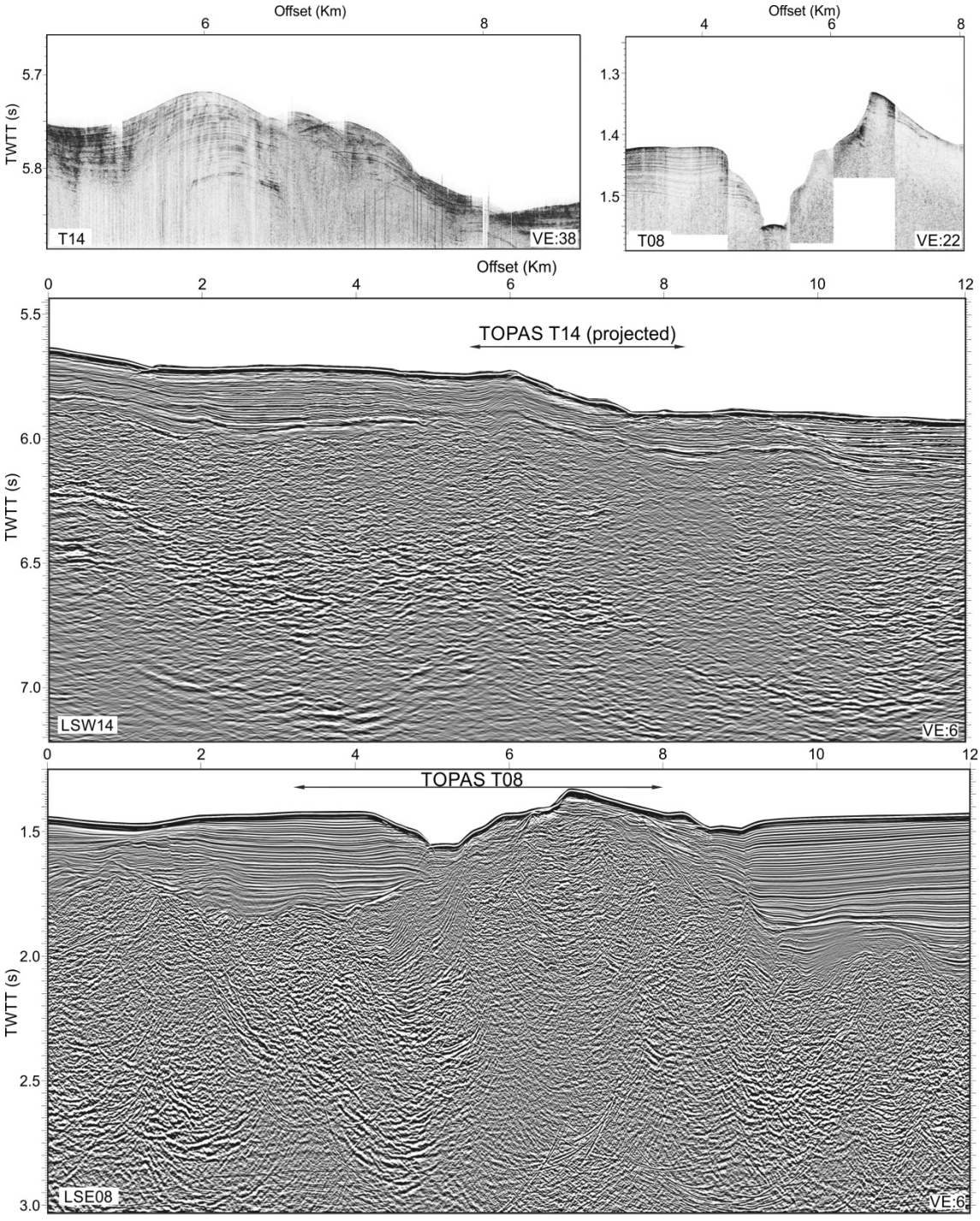
Offset (Km)
6
8
5.7
5.8
TWTT (s)
T14
VE:38
Offset (Km)
4
6
8
1.3
1.4
1.5
T08
VE:22
Offset (Km)
0
2
4
6
8
10
12
5.5
6.0
6.5
7.0
TWTT (s)
TOPAS T14 (projected)
LSW14
VE:6
0
2
4
6
8
10
12
TOPAS T08
1.5
2.0
2.5
3.0
TWTT (s)
LSE08
VE:6

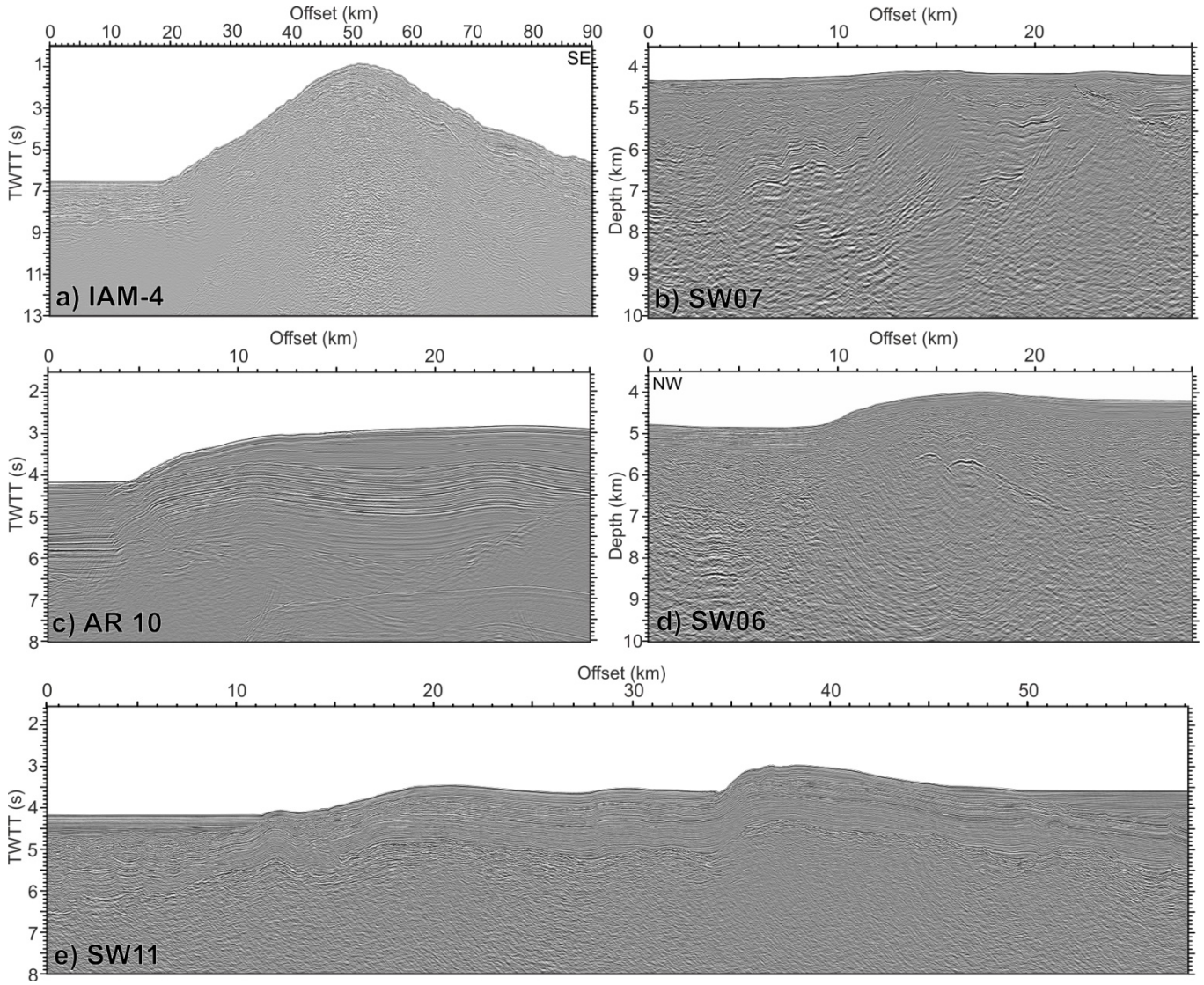
Offset (km)
0 10 20 30 40 50 60 70 80 90
SE
TWTT (s)
1 3 5 7 9 11 13
a) IAM-4
Offset (km)
0 10 20
Depth (km)
4 5 6 7 8 9 10
b) SW07
Offset (km)
0 10 20
TWTT (s)
2 3 4 5 6 7 8
c) AR 10
Offset (km)
0 10 20
NW
Depth (km)
4 5 6 7 8 9 10
d) SW06
Offset (km)
0 10 20 30 40 50
TWTT (s)
2 3 4 5 6 7 8
e) SW11

# Annex 4: Wave height for each coastal point and tsunami simulation

Wave height for each coastal point and tsunami simulation

| Location | ID | X Dec | Y Dec | D(1) | GB_PL | LS_PL | HF_PL_hom | MPF_PL_hom | NCPF_PL_hom | SCPF_PL_hom | HF_3D_hom | MPF_3D_hom | NCPF_3D_hom | SCPF_3D_hom | HF_PL_gauss | HF_3D_gauss | HF_3D_het_1 | HF_3D_het_2 | HF_3D_het_3 | HF_3D_het_4 | HF_3D_het_5 |
|---|---|---|---|---|---|---|---|---|---|---|---|---|---|---|---|---|---|---|---|---|---|
| Fisterra | 1 | -9.2948 | 42.8875 | 2.03 | 0.239 | 0.047 | 0.109 | 0.032 | 0.023 | 0.058 | 0.111 | 0.039 | 0.027 | 0.059 | 0.141 | 0.137 | 0.146 | 0.137 | 0.133 | 0.161 | 0.125 |
| Porto | 2 | -8.6707 | 41.1216 | 2 | 0.365 | 0.101 | 0.157 | 0.048 | 0.031 | 0.078 | 0.161 | 0.058 | 0.037 | 0.079 | 0.191 | 0.196 | 0.21 | 0.199 | 0.19 | 0.233 | 0.177 |
| Lisboa | 3 | -9.3485 | 38.6798 | 1.95 | 0.874 | 0.363 | 0.642 | 0.232 | 0.139 | 0.338 | 0.643 | 0.27 | 0.159 | 0.352 | 0.885 | 0.969 | 1.015 | 0.884 | 0.837 | 1.192 | 0.853 |
| Sines | 4 | -8.8824 | 37.9507 | 2.33 | 0.745 | 0.6 | 0.597 | 0.231 | 0.136 | 0.309 | 0.596 | 0.272 | 0.153 | 0.4 | 0.828 | 0.933 | 0.916 | 0.803 | 0.757 | 1.2556 | 0.821 |
| Sagres | 5 | -8.9775 | 37.0078 | 1.76 | 0.7 | 2.93 | 1.117 | 0.272 | 0.224 | 0.616 | 1.435 | 0.27 | 0.265 | 0.984 | 0.986 | 0.713 | 0.793 | 0.959 | 1.25 | 2.12 | 0.818 |
| Portimao | 6 | -8.5829 | 37.1178 | 1.86 | 0.644 | 0.839 | 0.448 | 0.32 | 0.166 | 0.418 | 0.313 | 0.39 | 0.197 | 0.443 | 0.674 | 0.716 | 0.722 | 0.573 | 0.576 | 0.883 | 0.736 |
| Faro | 7 | -7.8866 | 36.9631 | 1.56 | 0.67 | 1.15 | 0.286 | 0.095 | 0.063 | 0.179 | 0.3 | 0.127 | 0.058 | 0.203 | 0.324 | 0.387 | 0.382 | 0.348 | 0.341 | 0.448 | 0.345 |
| Punta Umb. | 8 | -6.9533 | 37.1717 | 1.78 | 0.323 | 0.637 | 0.18 | 0.04 | 0.041 | 0.11 | 0.189 | 0.054 | 0.04 | 0.094 | 0.165 | 0.2 | 0.199 | 0.197 | 0.205 | 0.238 | 0.192 |
| Cadiz | 9 | -6.2942 | 36.5258 | 1.99 | 0.539 | 1.118 | 0.377 | 0.094 | 0.072 | 0.156 | 0.444 | 0.126 | 0.063 | 0.128 | 0.451 | 0.52 | 0.506 | 0.472 | 0.476 | 0.613 | 0.438 |
| Tanger | 10 | -6.06082 | 35.45404 | 3 | 0.492 | 0.455 | 0.415 | 0.095 | 0.09 | 0.18 | 0.748 | 0.116 | 0.117 | 0.172 | 0.693 | 1.06 | 1.16 | 0.994 | 1.025 | 1.295 | 0.693 |
| Rabbat | 11 | -6.87815 | 34.0032 | 1.9 | 0.996 | 0.437 | 0.893 | 0.105 | 0.109 | 0.293 | 1.041 | 0.149 | 0.123 | 0.249 | 1.055 | 1.196 | 1.31 | 1.277 | 1.216 | 1.283 | 1.21 |
| Casablanca | 12 | -7.46989 | 33.66566 | 1.52 | 1.589 | 0.725 | 1.116 | 0.151 | 0.16 | 0.5 | 1.281 | 0.208 | 0.186 | 0.499 | 1.432 | 1.518 | 1.577 | 1.512 | 1.4 | 1.45 | 1.743 |
| Safi | 13 | -9.23642 | 32.4639 | 2.47 | 0.961 | 0.442 | 0.212 | 0.069 | 0.165 | 0.481 | 0.202 | 0.088 | 0.22 | 0.482 | 0.435 | 0.398 | 0.392 | 0.322 | 0.247 | 0.4 | 0.432 |
| Madeira | 14 | -16.82205 | 32.76931 | 2.97 | 0.35 | 0.205 | 0.268 | 0.164 | 0.123 | 0.292 | 0.405 | 0.163 | 0.14 | 0.289 | 0.375 | 0.567 | 0.652 | 0.578 | 0.569 | 0.638 | 0.523 |

Green's Law

| Location | ID | X Dec | Y Dec | D(1) | GB_PL | LS_PL | HF_PL_hom | MPF_PL_hom | NCPF_PL_hom | SCPF_PL_hom | HF_3D_hom | MPF_3D_hom | NCPF_3D_hom | SCPF_3D_hom | HF_PL_gauss | HF_3D_gauss | HF_3D_het_1 | HF_3D_het_2 | HF_3D_het_3 | HF_3D_het_4 | HF_3D_het_5 |
|---|---|---|---|---|---|---|---|---|---|---|---|---|---|---|---|---|---|---|---|---|---|
| Fisterra | 1 | -9.2948 | 42.8875 | 1 | 0.285 | 0.056 | 0.130 | 0.038 | 0.027 | 0.069 | 0.132 | 0.047 | 0.032 | 0.070 | 0.168 | 0.164 | 0.174 | 0.164 | 0.159 | 0.192 | 0.149 |
| Porto | 2 | -8.6707 | 41.1216 | 1 | 0.434 | 0.120 | 0.187 | 0.057 | 0.037 | 0.093 | 0.191 | 0.069 | 0.044 | 0.094 | 0.227 | 0.233 | 0.250 | 0.237 | 0.226 | 0.277 | 0.210 |
| Lisboa | 3 | -9.3485 | 38.6798 | 1 | 1.033 | 0.429 | 0.759 | 0.274 | 0.164 | 0.399 | 0.760 | 0.319 | 0.188 | 0.416 | 1.046 | 1.145 | 1.199 | 1.045 | 0.989 | 1.409 | 1.008 |
| Sines | 4 | -8.8824 | 37.9507 | 1 | 0.920 | 0.741 | 0.738 | 0.285 | 0.168 | 0.382 | 0.736 | 0.336 | 0.189 | 0.494 | 1.023 | 1.153 | 1.132 | 0.992 | 0.935 | 1.551 | 1.014 |
| Sagres | 5 | -8.9775 | 37.0078 | 1 | 0.806 | 3.375 | 1.287 | 0.313 | 0.258 | 0.710 | 1.653 | 0.311 | 0.305 | 1.133 | 1.136 | 0.821 | 0.913 | 1.105 | 1.440 | 2.442 | 0.942 |
| Portimao | 6 | -8.5829 | 37.1178 | 1 | 0.752 | 0.980 | 0.523 | 0.374 | 0.194 | 0.488 | 0.366 | 0.455 | 0.230 | 0.517 | 0.787 | 0.836 | 0.843 | 0.669 | 0.673 | 1.031 | 0.860 |
| Faro | 7 | -7.8866 | 36.9631 | 1 | 0.749 | 1.285 | 0.320 | 0.106 | 0.070 | 0.200 | 0.335 | 0.142 | 0.065 | 0.227 | 0.362 | 0.433 | 0.427 | 0.389 | 0.381 | 0.501 | 0.386 |
| Punta Umb. | 8 | -6.9533 | 37.1717 | 1 | 0.373 | 0.736 | 0.208 | 0.046 | 0.047 | 0.127 | 0.218 | 0.062 | 0.046 | 0.109 | 0.191 | 0.231 | 0.230 | 0.228 | 0.237 | 0.275 | 0.222 |
| Cadiz | 9 | -6.2942 | 36.5258 | 1 | 0.640 | 1.328 | 0.448 | 0.112 | 0.086 | 0.185 | 0.527 | 0.150 | 0.075 | 0.152 | 0.536 | 0.618 | 0.601 | 0.561 | 0.565 | 0.728 | 0.520 |
| Tanger | 10 | -6.06082 | 35.45404 | 1 | 0.648 | 0.599 | 0.546 | 0.125 | 0.118 | 0.237 | 0.984 | 0.153 | 0.154 | 0.226 | 0.912 | 1.395 | 1.527 | 1.308 | 1.349 | 1.704 | 0.912 |
| Rabbat | 11 | -6.87815 | 34.0032 | 1 | 1.169 | 0.513 | 1.048 | 0.123 | 0.128 | 0.344 | 1.222 | 0.175 | 0.144 | 0.292 | 1.239 | 1.404 | 1.538 | 1.499 | 1.428 | 1.506 | 1.421 |
| Casablanca | 12 | -7.46989 | 33.66566 | 1 | 1.764 | 0.805 | 1.239 | 0.168 | 0.178 | 0.555 | 1.422 | 0.231 | 0.207 | 0.554 | 1.590 | 1.686 | 1.751 | 1.679 | 1.554 | 1.610 | 1.935 |
| Safi | 13 | -9.23642 | 32.4639 | 1 | 1.205 | 0.554 | 0.266 | 0.087 | 0.207 | 0.603 | 0.253 | 0.110 | 0.276 | 0.604 | 0.545 | 0.499 | 0.491 | 0.404 | 0.310 | 0.501 | 0.542 |
| Madeira | 14 | -16.82205 | 32.76931 | 1 | 0.459 | 0.269 | 0.352 | 0.215 | 0.161 | 0.383 | 0.532 | 0.214 | 0.184 | 0.379 | 0.492 | 0.744 | 0.856 | 0.759 | 0.747 | 0.838 | 0.687 |

GB: Gorringe Bank fault
LS: Lineament South fault
HF: Horseshoe fault
MPF: Marquês de Pombal fault
NCPF: North Coral Patch fault
SCPF: South Coral Patch fault
PL: planar
hom: homogeneous
het: heterogeneous
Dec: decimal coordinates
(1) D: Depth (meters below the sea level)

Data are available at the file "Points_HMAX.pdf" in the *figshare repository*: https://figshare.com/s/02e19886d2ded8ec9145

## Annex 5: Horseshoe fault tsunami simulations

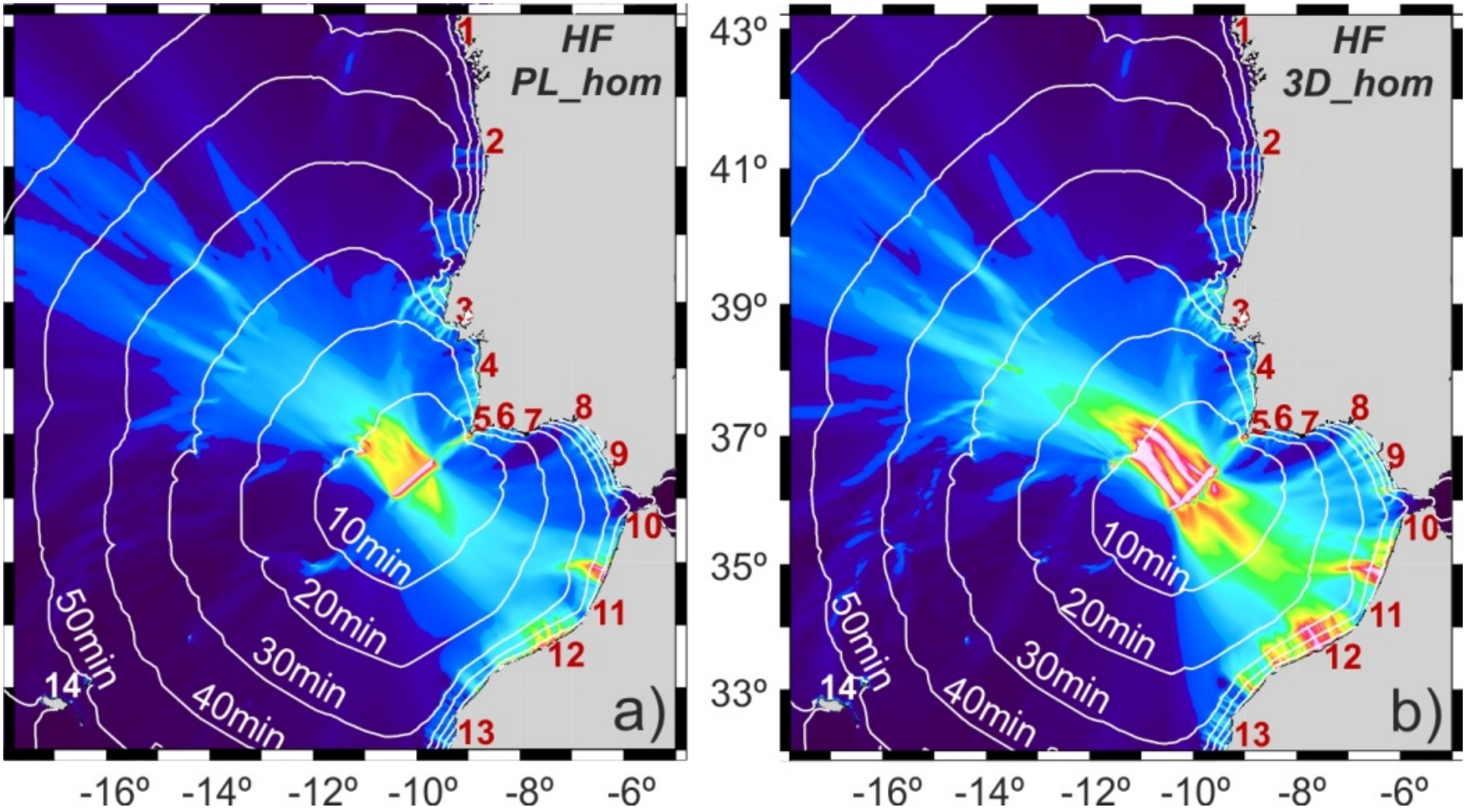

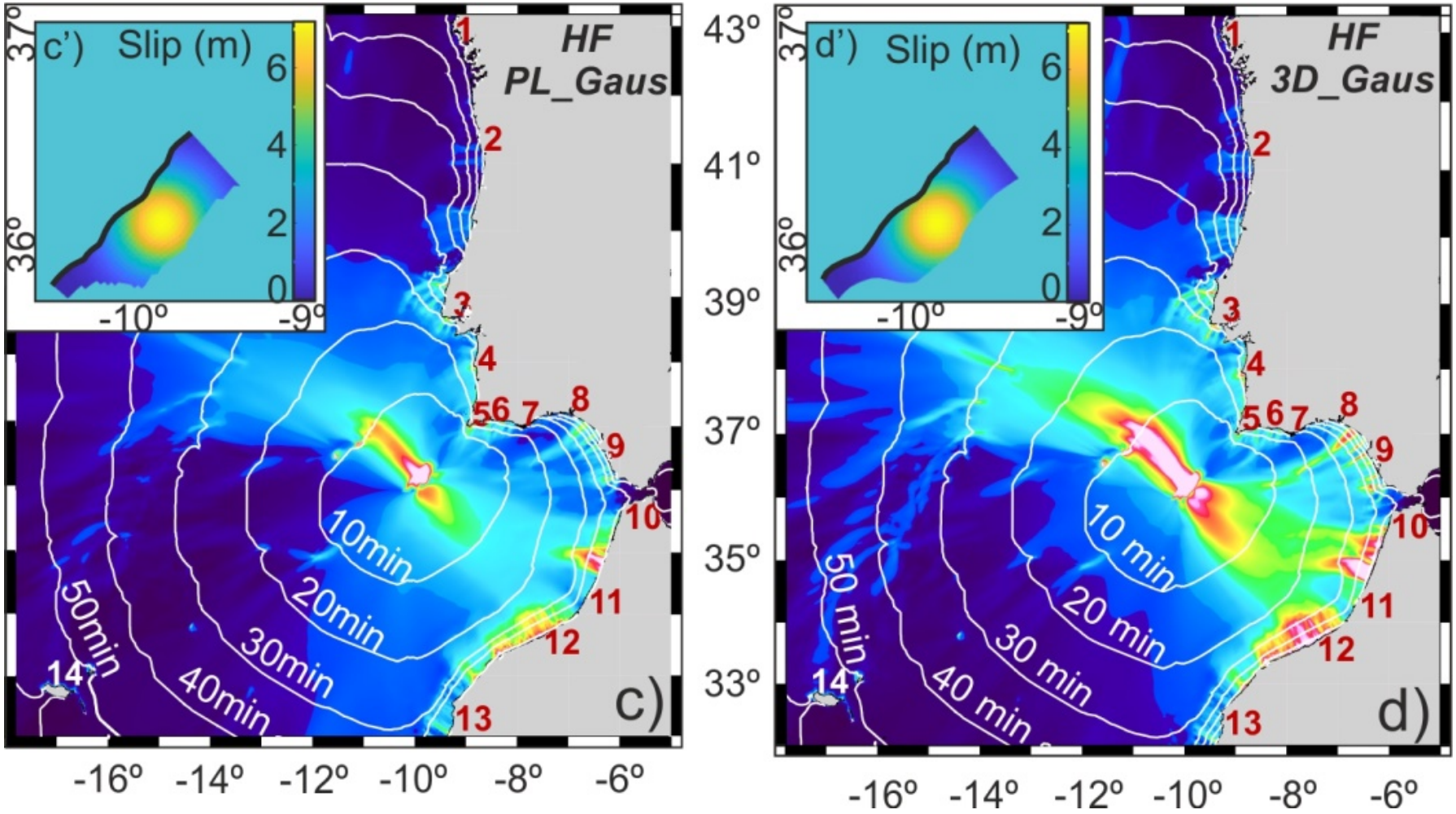
c')
Slip (m)
6
4
2
0
-10°
-9°
HF
PL_Gaus
37°
36°
1
2
3
4
5
6
7
8
9
10
11
12
13
14
10min
20min
30min
40min
50min
c)
-16°
-14°
-12°
-10°
-8°
-6°
d')
Slip (m)
HF
3D_Gaus
43°
41°
39°
37°
35°
33°
10 min
20 min
30 min
40 min
50 min
d)

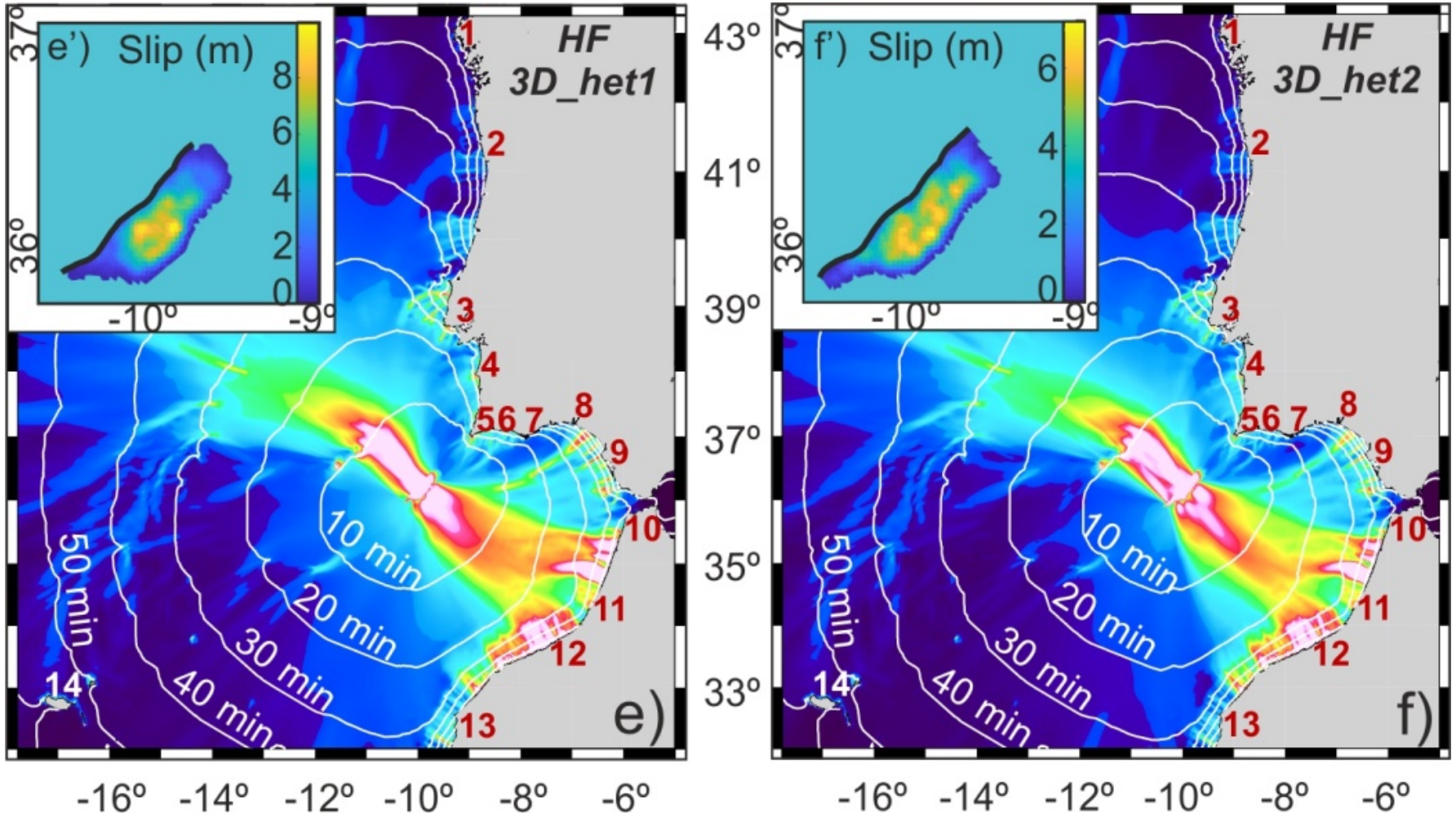
e') Slip (m)
8
6
4
2
0
HF
3D_het1
1
2
3
4
56 7
8
9
10
11
12
13
14
10 min
20 min
30 min
40 min
50 min
e)
f') Slip (m)
6
4
2
0
HF
3D_het2
f)
37°
36°
43°
41°
39°
37°
35°
33°
-10°
-9°
-16° -14° -12° -10° -8° -6°

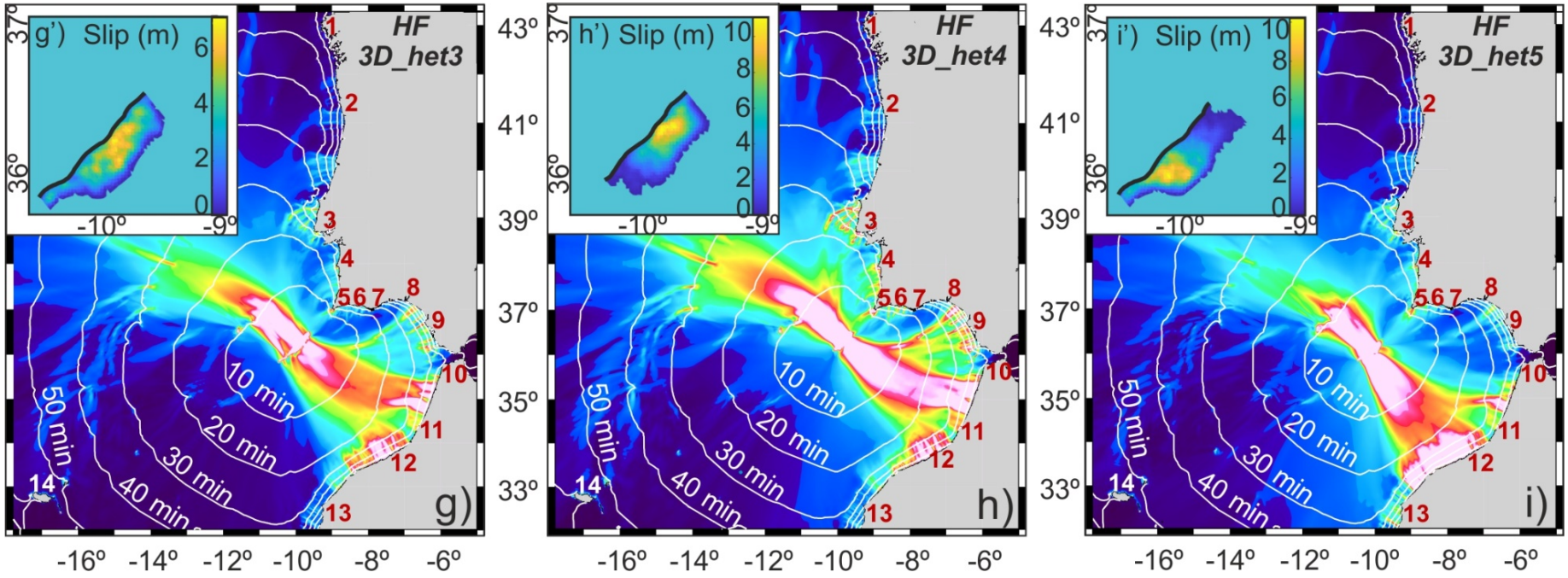
g') Slip (m)
HF
3D_het3
h') Slip (m)
HF
3D_het4
i') Slip (m)
HF
3D_het5
10 min
20 min
30 min
40 min
50 min
g)
h)
i)